uOttawa

L'Université canadienne
Canada's university

FACULTÉ DES ÉTUDES SUPÉRIEURES ET POSTOCTORALES

uOttawa

L'Université canadienne
Canada's university

FACULTY OF GRADUATE AND POSDOCTORAL STUDIES

Gavin Post

AUTEUR DE LA THÈSE / AUTHOR OF THESIS

M.A.Sc. (Civil Engineering)

GRADE / DEGREE

Department of Civil Engineering

FACULTÉ, ÉCOLE, DÉPARTEMENT / FACULTY, SCHOOL, DEPARTMENT

The Measurement of Reynolds Stresses in a Model River Bend using Acoustic Doppler Velocimeters

TITRE DE LA THÈSE / TITLE OF THESIS

Dr. C. Rennie

DIRECTEUR (DIRECTRICE) DE LA THÈSE / THESIS SUPERVISOR

Dr. I. Nistor

CO-DIRECTEUR (CO-DIRECTRICE) DE LA THÈSE / THESIS CO-SUPERVISOR

EXAMINATEURS (EXAMINATRICES) DE LA THÈSE / THESIS EXAMINERS

Dr. Paul Simms

Dr. Sai Vanapalli

Dr. R. Droste

Gary W. Slater

Le Doyen de la Faculté des études supérieures et postdoctorales / Dean of the Faculty of Graduate and Postdoctoral Studies

The Measurement of Reynolds Stresses in a Model River Bend using Acoustic Doppler Velocimeters

Gavin Charles Post

Thesis submitted to the
Faculty of Graduate and Postdoctoral Studies
In partial fulfillment of the requirements
For the Master of Applied Science degree in Civil Engineering

The Ottawa-Carleton Institute for Civil Engineering
Department of Civil Engineering
Faculty of Engineering
University of Ottawa

Your file Votre référence
ISBN: 978-0-494-49265-9
Our file Notre référence
ISBN: 978-0-494-49265-9

Acknowledgments

I want to thank Richard Suttie, my long lost friend who showed me how to never give up regardless of the obstacle. His spirit guided me through my most trying hours. This thesis is dedicated to him.

I want to thank the University of Ottawa for an incredibly enriching experience. Having had the opportunity over the last four years to play the combined role of designer, manufacturer, Technical Officer, and student, I have learned more than these pages could hope to present. Specifically, I would like to thank Dr. Colin Rennie for the autonomy he granted me throughout the duration of this flume build, and his close support during these last few months. I would also like to thank Dr. Ioan Nistor, my co-supervisor, whose support and insight into my thesis was greatly appreciated.

Very special thanks go to the Mechanical Engineering Department machine shop staff, specifically John Perrins for his dedication to this project, and Dr. William Hallett for his granting me unprecedented access to the machine shop. Special thanks also go to James MacDermid, Mike Burns, Leo Denner and Brent Cotter whose craftsmanship and insight into the significant roadblocks overcome during the build was a key factor in seeing this project through to fruition.

Lastly, I would also like to thank my whole family for their endless guidance, love and support.

Abstract

This thesis reports the first two experiments in long term study of the distribution of Reynolds stresses in a model river bend, as well as the development and procedural details of the model river bend itself. The open channel flume measures 18.2 m along the centerline, and is 1 m wide with a uniform 0.3 m deep mobile sand bed. With a 12.2 m straight approach, a 135 bend with 1.5 m constant radius, followed by a straight exit section, this bend is considered to be sharply curved.

The first experiment was conducted with a channel slope of 0.044% which, for the 0.2 m flow depth resulted in clear water scour conditions in the bend with a planned dimensionless boundary shear stress, τ_*, of 0.035. For the second experiment, the slope was increased to 0.064% to ensure movement in the straight approach section which required sediment circulation. Dimensionless boundary shear stress for the second test was selected to be 0.05.

Following development of equilibrium bed topography in the first test, a total of 609 time-series measurements lasting 2 minutes each were taken at a wide distribution throughout the entire bend. Two Vectrino ADVs were used for velocity measurements operating at a sampling frequency of 200Hz and the ability of these sensors to directly measure 3D Reynolds stress is a key aspect of this study. With a noted lack of data on Reynolds stresses for which to calibrate turbulent flow models, this thesis is designed to identify these stresses. Through the examination of the mean flow properties and verifying that the measurements are correct, the discovery of two zones of high streamwise-vertical Reynolds stress are reported, one at the beginning of the scour hole formation, and the other at the tip of the downstream point bar. For this thesis the results from the first experiment will be examined in detail, and the second will be discussed only from a qualitative point of view since all measurements could not be completed.

Table of Contents

Chapter 3 Methods

Chapter 4 Results

Appendix B

Appendix C (enclosed CD)

List of Symbols

a	acceleration
b_i	velocity in the direction of the bistatic axis
c	speed of sound
d	depth of sand bed at a given point
e_{ij}	rate of strain tensor
f	Darcy-Weisbach friction factor, acoustic operating frequency of ADVs
f'	grain roughness component of f
f''	form roughness component of f
g	acceleration due to gravity,
g_i	acceleration due gravity in the i-direction
h	flow depth
k	turbulent kinetic energy
k_s	roughness height
l	Prandlts' mixing length
l_x	micro scale length
m	bed roughness coefficient for determining z_o, mass
n	Manning's coefficient of roughness, noise, cross stream direction (cylindrical coordinates)
r	channel bend centerline radius of curvature
s	streamwise direction (cylindrical coordinates)
u	turbulent fluctuations in the streamwise direction
v	cross stream turbulent fluctuations
v_{amb}	maximum measureable velocity along the bistatic axis
w	channel width, vertical turbulent fluctuations
x	streamwise direction (facing downstream)
y	cross stream direction
z	vertical direction
z_{rel}	vertical location measured from the sand bed
z_o	elevation of zero velocity
C_{11}	autocorrelation function
D_s, D_{50}	characteristic particle diameter
E	water surface elevation
F	force

H	head on V-Notch weir
L_m	characteristic length (model)
L_p	characteristic length (prototype)
L_x	integral length scale
N	noise
P	pressure
Q_T	total flow
R	hydraulic radius, correlation coefficient
R_*	boundary Reynolds number, particle Reynolds number
R_{11}	Eularian time-coefficient
S	streamwise channel slope
S_{11}	Power spectrum
T	coordinate transformation matrix for ADVs
T_E	integral time scale
U	streamwise instantaneous velocity
U_*	friction velocity, turbulent shear velocity
$\overline{U}_i$	mean velocity in the i-direction
$\overline{U}_{0.2}$	mean velocity at 0.2h
$\overline{U}_{0.8}$	mean velocity at 0.8h
V	cross-stream instantaneous velocity
VZ_l	vertical velocity measured along the streamwise axis
VZ_l	vertical velocity measured along the cross-stream axis
W	vertical instantaneous velocity
γ	specific weight of water
γ_s	specific weight of bed particles
δ	boundary layer thickness
δ_o	thickness of laminar sublayer
δ_{ij}	Kroenecker delta
θ	Doppler phase shift for a pulse pair
κ	von Karman's constant
λ	wavelength, dune length, Taylors' microlength
μ	coefficient of viscosity
ρ	density

σ	standard deviation of data
σ_{ij}	stress on i-plane in j-direction
τ	total shear stress, time lag
τ_*	dimensionless boundary shear stress
τ_{*c}	critical dimensionless boundary shear stress
τ_c	critical shear stress
τ_o	shear stress at the bed
$(\tau_s)_o$	downstream boundary shear stress (in cylindrical coordinates)
$(\tau_n)_o$	cross stream boundary shear stress (in cylindrical coordinates
τ_E	micro-time scale
χ_i	body force per unit mass in the x_i direction
ω	frequency
Π	Coles wake strength parameter

List of Abbreviations

ADV	acoustic Doppler velocimeter
ADVP	acoustic Doppler velocity profiler
CFD	computational fluid dynamics
DNS	direct numerical simulation
GUI	graphical user interface
RMS	root mean square
LDV	laser Doppler velocimeter
NSE	Navier-Stokes equation
PIV	particle imaging velocimetry
SNR	signal to noise ratio
NaN	not at number
WES	U.S. Army Engineer Waterways Experiment Station

List of Figures

List of Tables

Chapter 1 Introduction

1.1 Introduction

The understanding of many complex systems in nature is still beyond our present level of knowledge. Analyzing a highly complex system requires both sensible and radical assumptions to make the identification of a unique solution possible. Three-dimensional (3D) systems are often reduced to one or two-dimensional (2D) systems to simplify analysis, using different techniques. These solution methods are both theoretically and empirically derived, and consequently the accuracy of the results they produce can vary significantly from the expected values. This is true for the case of river hydraulics as the dynamic complexity of real river behaviour proves to be among the most difficult problems addressed by hydraulic engineers today. With the reality of climate change and the consequent effects on our hydrologic cycles expanding into being global in scale, we are experiencing an increased intensity of atmospheric events and associated flooding. Thus, understanding and predicting these phenomena may help us as a society to avoid loss of life and infrastructure.

In turbulent flow, the "random" movement of individual particles is due to changes in pressure and temperature. As a starting point, a scale of analysis is considered where an individual fluid element is sufficiently small to neglect density changes, but large enough to neglect molecular attraction. Making the assumption that the fluid within the element is incompressible allows the use fundamental laws of mass and motion to describe their behaviour.

As the spatial scale of interest increases, the additional factors which need to be accounted for are inter-dependent, but fluctuate independently over time. River flow is affected primarily by general channel properties such as flow depth and channel slope; their product provides an estimation of total shear force while internal viscous and boundary friction form flow resistance. All of these factors change with time due to sediment transport and attempting to take them into consideration together requires a massive number of calculations even with simplifications. However, advancements in computer processing power over the last decade have made complex 3D computational analyses such as direct numerical simulation (DNS) relatively easy (Wilcox 2000). These numerical solutions, however, are highly sensitive to initial input conditions, and have only been proven to be successful with turbulent flows at low Reynolds numbers.

Considering that a majority of point velocity measurements are classically at best 2D, using these data for model verification is problematic as the Reynolds stresses require 3D velocimetry for direct measurement. However, the development of acoustic velocimetry techniques over the past 10 years has made non-intrusive, 3D measurements possible in a wide range of field and laboratory settings.

It is the purpose of this thesis to contribute to the understanding of the fundamental inter-related unsolved problems in river hydraulics of turbulence, flow resistance, and sediment transport. By directly measuring the distribution of 3D Reynolds stresses throughout a model river bend, verification of numerical models for turbulent flow is possible. There are no such data in the literature and thus the experiments reported in this thesis are the first to determine the distribution of Reynolds Stresses in a river bend using Acoustic Doppler Velocimeters (ADVs) for velocity measurements. A model river bend has been developed for these purposes shown in Fig. 1-1.

The first experiment was conducted at clear water conditions, meaning that there was little or no movement of sand grains in the approach section, and local scour was created in the bend section due to the presence of the bend alone. Sediment which was carried out of the flume was not recirculated. For the second experiment, live-bed conditions were created by increasing the slope of the flume slightly, which, for the same water depth increases shear stress at the bed. With an increase in shear past the critical value for our selected bed material, movement of the sand grains in the approach section was achieved and a recharge of material into the scour zone results. Due to the higher rate of sediment transport in live bed conditions, it is necessary to recirculate bed material from the outlet to the flume entrance, which is difficult to do effectively. A novel system was created to separate sand from water and required adjustment for which the run had to be stopped, and thus ADV measurements were not possible for this second experiment. However, its inclusion in this thesis is primarily to report the performance of the model and the effect of changing channel slope.

A total of 609 individual time series measurements were made in the first experiment resulting in over 1.4 M individual velocity measurements. The use of the Vectrino+ ADV allowed high frequency measurements (200 Hz) with few erroneous measurements. We will show here that the flow structures calculated from the data are highly congruous with known data, which lends credibility to observations and conclusions made from the data. Most notably are two loci of high principal Reynolds stress, one at the inception point of the scour hole and the other just downstream of the point bar tip.

The primary objective of this thesis is to make a large spatial grid of ADV measurements which provide direct measurement of 3D Reynolds stresses. This is especially important as these stresses play a key role in numerical simulation of turbulent flow, without which, calibration and validation of these 3D models is not possible. Furthermore, an examination of flume performance is made in terms of predicted sediment transport rates. Procedures were also developed and documented in Appendix A for successful use of the flume and related equipment.

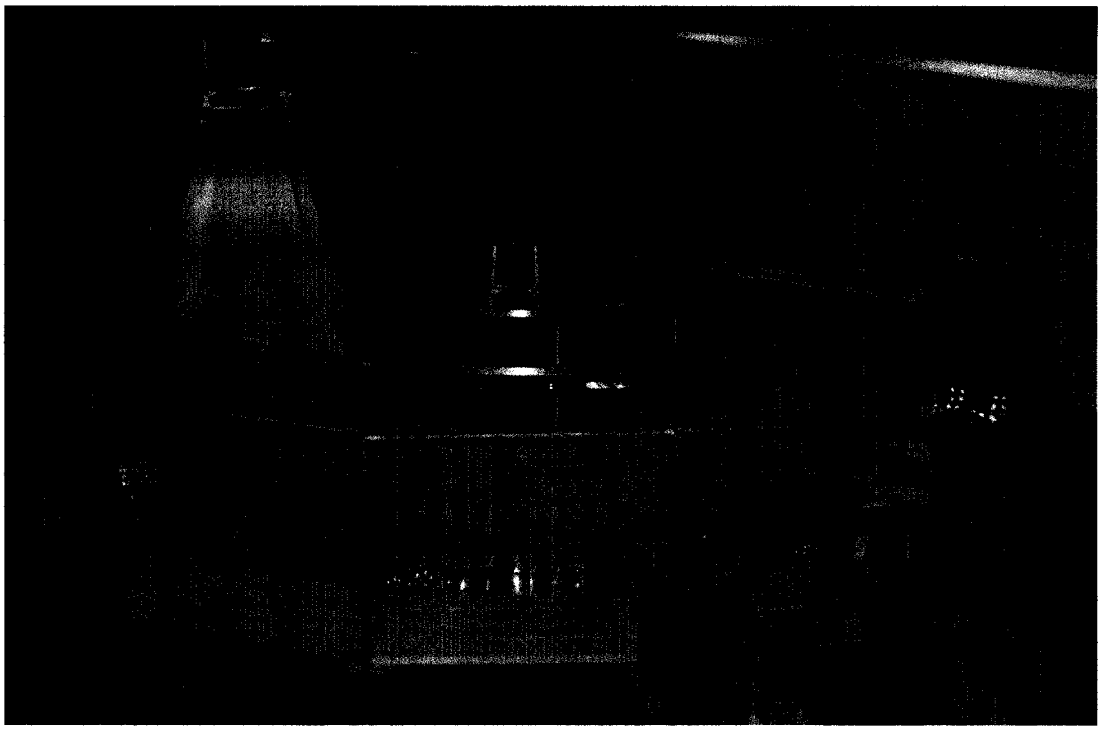

Figure 1-1. Model river bend

Chapter 2 Theoretical Framework

2.1 Introduction

The study of flow in river bends follows an understanding of turbulence, flow resistance and sediment transport. This section presents aspects of each of these subjects that are relevant to this thesis: incompressible fluid mechanics, 2D open channel flow theory, roughness and flow resistance, sediment transport, ADV measurement, the analysis of time-series data, and finally flow in river bends.

The right hand rule system with z vertical is employed throughout this thesis (Fig. 2-1). The bottom river-right corner of the flume entrance is considered the origin with coordinates (0, 0, 0). In terms of basic velocity, U, V, and W, are used to represent instantaneous velocity in the x, y and z-direction respectively. Vertical locations with respect to the bed are denoted by z, while d indicates sand bed depth, and h is flow depth.

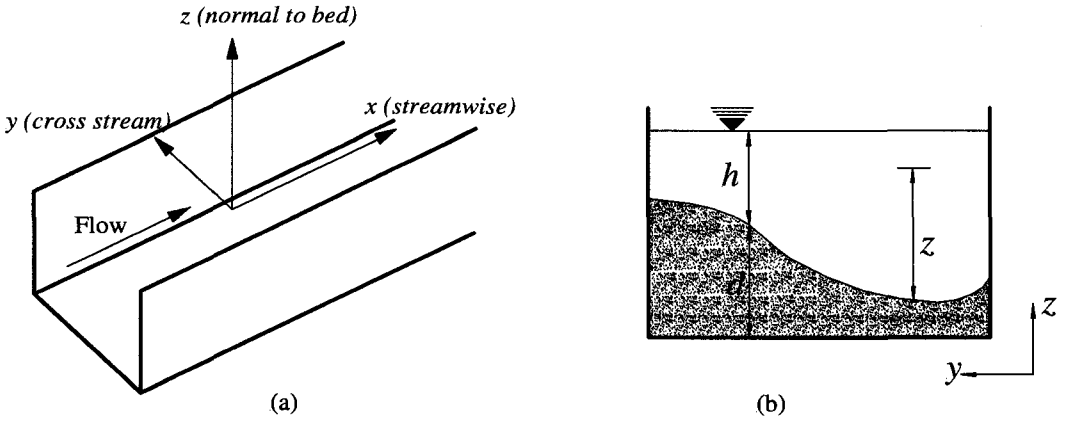

Figure 2-1. Coordinate system in (a) 3D and (b) 2D

2.2 Governing Equations for Incompressible Fluid Flow

2.2.1 Continuity and Navier-Stokes Equation

The derivation of governing equations for fluid flow can be presented differently depending on the author and the sign convention used. In this discussion vector notation will be used as often as possible to reduce "equation clutter", a useful explanation of this notation is provided in Rouse (1959).

For the analysis of water as a fluid, an important assumption is that it is incompressible and non-diffusive. In other words, an assumption is made that density, ρ, is constant. Newton's second law of motion, and the conservation (or continuity) of mass are the governing equations for fluid flow.

To begin this analysis, consider a control volume which is small, but large enough that molecular forces can be ignored. Thus, the concept of mass continuity can be developed with the assumption that the rate of mass flow into the control volume equals the mass flow out of the control volume. Again, by making the assumption that density is constant, the continuity equation is expressed as

$$\nabla \bullet \overline{U}_i = 0 \tag{2.1}$$

A differential form of Newton's second law of motion is most popularly known as the Navier-Stokes equation (NSE). Understanding that these equations are the work of a succession of different researchers (Navier, Cauchy, Poisson, St. Venant and finally Stokes), the name is derived from the first and last individuals to contribute to their form presented here (Rouse 1959). The NSE takes into consideration body forces on the control volume, convective accelerations, gravity, as well as the normal and shear stress and their resultant rate of strain of the control volume. In tensor notation the sum of forces on the fluid element can be expressed as

$$(\Delta\forall)\left(\frac{\partial \sigma_{ij}}{\partial x_j} + \chi_i \rho\right) \tag{2.2}$$

where χ_i is body force per unit mass in the x_i direction, $\rho\Delta\forall$ is mass and lastly σ_{ij} is stress on i-plane in the j-direction. Acceleration is considered in both time and space since a particle passing through the control volume in steady, non-uniform flow will undergo a spatial (convective) acceleration. Thus, the material or Langrangian derivative of velocity is taken, which in vector notation is:

$$\frac{\Delta u_i}{\Delta t} = \frac{\partial u_i}{\partial t} + u_i \bullet \nabla u_i \tag{2.3}$$

The term ($u_i \bullet \nabla u_i$) represents the convective accelerations which are non-linear terms, meaning, for example, that a doubling of velocity will not necessarily result in a doubling of acceleration.

Equations 2.2 and 2.3 are now substituted into the basic formulation of Newton's second law, $F = ma$. Note that the only body force considered is gravity, leaving out other forces such as centrifugal and Coriolis. With this we have the force-momentum equation, expressed as,

$$\left(\frac{\partial \sigma_{ij}}{\partial x_j} + g_i \rho\right) = \rho\left(\frac{\partial u_i}{\partial t} + u_i \bullet \nabla u_i\right) \tag{2.4}$$

Given channel slope which forms an angle, θ, to a horizontal datum and since the coordinate system considers the streamwise direction (facing downstream), x, to be parallel with the channel bottom, acceleration due to gravity, g, needs to be resolved into each coordinate direction where g_i indicates the effect of gravity in the i-direction. This leads to,

$$g_i = \left(g\sin\theta\vec{i}, 0\vec{j}, -g\cos\theta\vec{k}\right) \tag{2.5}$$

Now take into consideration two parallel plates separated by laminar flow in a Newtonian viscous fluid (Fig. 2-2); the rate of viscous strain is linearly proportional to the viscous stress leading to the following relation in 1D;

$$\tau = \mu\frac{du}{dz} \tag{2.6}$$

Where μ is the coefficient of viscosity and τ is shear stress. In 3D, we can define a "stress tensor" which describes the state of stress on the sample volume under consideration. The notation for τ_{ij} is such that the first subscript represents the plane in which the stress acts and the second is the direction of action. Noting that repeated subscripts represent normal stresses we can define the stress tensor as such,

$$\tau_{ij} = \begin{bmatrix} \sigma_x & \tau_{xy} & \tau_{xz} \\ \tau_{yx} & \sigma_y & \tau_{yz} \\ \tau_{zx} & \tau_{zy} & \sigma_z \end{bmatrix} \tag{2.7}$$

Noting that $\tau_{xy} = \tau_{yx}$, $\tau_{yz} = \tau_{zy}$, and $\tau_{xz} = \tau_{zx}$. Finally we need to relate the stresses to the rate of strain. With the implementation of Stokes hypothesis which for incompressible flows can be written as,

$$\sigma_{ij} = -P\,\delta_{ij} + 2\mu e_{ij} \tag{2.8}$$

where δ_{ij} is the Kronecker delta defined by Eqn. 2.9, and e_{ij} is the rate of strain tensor defined by Eqn. 2.10.

$$\delta_{ij} = \begin{Bmatrix} 0 & for\ i \neq j \\ 1 & for\ i = j \end{Bmatrix} \tag{2.9}$$

$$e_{ij} = \frac{1}{2}\left(\frac{\partial u_i}{\partial x_j} + \frac{\partial u_j}{\partial x_i}\right) \tag{2.10}$$

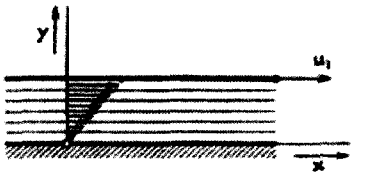

Figure 2-2. Velocity distribution between two plates in a viscous fluid (Rouse 1959)

This leads finally to the NSE for Newtonian, incompressible fluids written as,

$$\rho\left(\frac{\partial u_i}{\partial t}+u_j\frac{\partial u_i}{\partial x_j}\right)=-\nabla P+\mu\nabla^2 U_i+\rho g_i \tag{2.11}$$

This non-linear, partial differential equation cannot be solved analytically, with 4 equations and 4 unknowns. While DNS of the full equation has been achieved for simple flows with low Reynolds numbers, solutions are highly susceptible to initial and boundary conditions. This is analogous to the "butterfly effect" in which a system's complexity is verging on being chaotic. Taking this into consideration, as well as the constantly changing boundary shape and conditions in river hydraulics, DNS for these situations is still not possible.

2.3 Turbulence

2.3.1 General Considerations

Turbulent flow differs from laminar flow in that a precise definition of the velocity for a given location and time is not possible. The fluid particles move in an extremely irregular manner which might be considered as a heterogeneous secondary motion superimposed on the mean flow pattern (Rouse 1959). More recently Hinze (1975, cited in Wilcox 2000) offered the following statement which documents the development of our understanding:

"Turbulent fluid motion is an irregular condition of flow in which the various quantities show a random variation with time and space coordinates, so that statistically distinct average values can be discerned." In other words, for an incompressible flow both velocity and pressure differ with time and space, and thus, through periodic measurements in a single location, mean values can be computed. Hence turbulent structures in steady flows are analyzed more effectively using these long duration averages. By introducing the time-dependent aspects of turbulent flow and including them in the analysis, statistical methods are employed to help quantify the characteristics of the random fluctuations."

In addition to averaging values, Fourier analysis of a time history for a turbulent flow reveals a wide range of frequencies and wavelengths which give an indication of time and length

scales of turbulent structures. In reality, turbulence is a cascading process; a large eddy transfers kinetic energy to smaller ones. As this cascading process continues, the eddy size decreases until their energy is dissipated finally into heat through the effect of viscosity. There are many tangible examples of the turbulent cascade of scales, such as effluent from a smokestack or, a decidedly morose yet effective example is the plume from the detonation of nuclear warheads in the ocean (Fig. 2-3).

The main plume stays relatively columnar due to the incredible upward mean flow velocities, and with its outer edges shearing against the surrounding air, plumes develop and push outward decreasing in speed and size consistently until their energy is exhausted. The following rhyme from Richardson (1922) neatly expresses this physical picture of developed turbulence:

"Big whorls have little whorls,
Which feed on their velocity;
And little whorls have lesser whorls,
And so on to viscosity (in a molecular sense)."

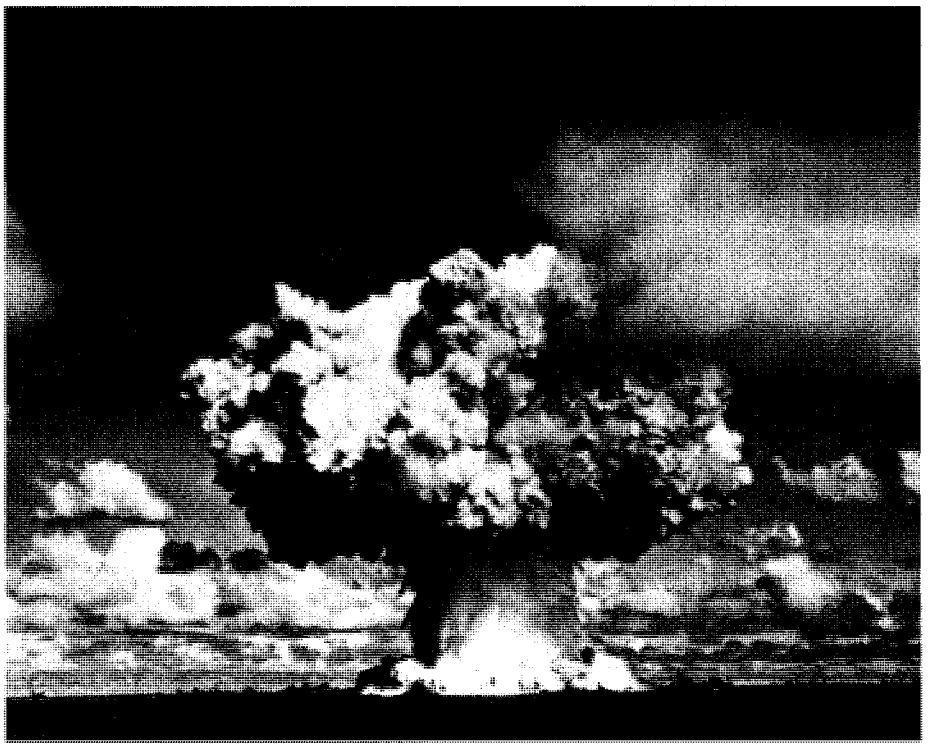

Figure 2-3. Nuclear warhead testing (www.thevintageplayhouse.com/atomicbomb.htm)

2.3.2 Reynolds Averaged Navier-Stokes Equations

The most important contribution of Osborne Reynolds is the application and extension of the NSE to turbulent flow (Rouse and Ince 1957). He assumed that for turbulent flows instantaneous velocity, U_i, and pressure, P, can be described as the summation of time-averaged mean values and their respective fluctuations, written as

$$\begin{aligned} U_i(t) &= \overline{U}_i + u_i \\ P(t) &= \overline{P} + p_i \end{aligned} \tag{2.12}$$

Where u_i and p_i are the instantaneous fluctuations of velocity and pressure respectively. Over bars are used in Eqn. 2.12 to represent time averaged values. This relationship is substituted into the continuity equation and the NSE (Eqns. 2-1 and 2-11) to give the Reynolds averaged continuity equation,

$$\frac{\partial \overline{U}_i}{\partial x_i} = 0 \tag{2.13}$$

and the Reynolds averaged Navier-Stokes equation (RANS),

$$\overline{U}_j \frac{\partial \overline{U}_i}{\partial x_j} = -\frac{1}{\rho}\frac{\partial \overline{P}}{\partial x_i} + \frac{1}{\rho}\frac{\partial}{\partial x_k}\left(\mu \frac{\partial \overline{U}_i}{\partial x_k} - \rho \overline{u_i u_k}\right) + \rho g_i \tag{2.14}$$

This form of the Navier-Stokes equation is less sensitive to initial conditions as it is based on mean values. It should be noted that Reynolds averaging introduces new terms into the Navier-Stokes equation, specifically the Reynolds stresses $\overline{u_i u_k}$, which represent the time averaged rate of momentum transfer due to turbulence. Wilcox (2000) points out that the identification of this parameter is an essential step in being able to calculate all mean-flow properties of a turbulent flow, and in his words is "the fundamental problem of turbulence".

2.3.3 Reynolds Stresses

The nine products $\overline{u_i u_k}$ are commonly known as the Reynolds stresses, and form the symmetric tensor as follows

$$\overline{u_i u_k} = \begin{bmatrix} \overline{u^2} & \overline{uv} & \overline{uw} \\ \overline{vu} & \overline{v^2} & \overline{vw} \\ \overline{wu} & \overline{wv} & \overline{w^2} \end{bmatrix} \tag{2.15}$$

Reynolds stresses exchange momentum between the turbulence and the mean flow, even though the mean of turbulent fluctuations is zero (if measured over a sufficiently long period). These are actually acceleration terms and are grouped with terms for viscous stress in the RANS.

This is simply a device for illustrating the net effect that these fluctuations have on the flow in lieu of the instantaneous viscous stresses which disappeared through the averaging process. Although these apparent mean stresses may be quite large in comparison with the mean viscous shear, they cannot account for the dissipation of energy; the entire energy of the flow, both mean and turbulent, is eventually dissipated through the action of viscosity (Rouse 1959).

Through the addition of the Reynolds Stress tensor, 6 unknown quantities have been added as a result of the averaging process, with no new equations. Along with the original three velocity unknowns and the single pressure unknown, this totals 10 unknowns, and only four equations have been presented. Thus the problem is known as a "closure problem", and requires models such as the eddy viscosity or κ-ε model to make a solution possible.

2.3.4 Reynolds Stress Profile

By taking Eqn. 2.14 in the z-direction for 2D flow, and integrating in the z-direction results in,

$$\frac{P}{\rho} = (h-z)g\cos\theta + \left(\overline{w_s^2} - \overline{w^2}\right) \tag{2.16}$$

Where w_s is the magnitude of fluctuations of w at the water surface; the value of which reduces to zero because of the effect of a free surface. The first term on the right hand side of Eqn. 2.16 is the hydrostatic pressure distribution; the second term indicates the contribution of turbulence to the mean pressure (Nezu and Nakagawa 1993). Combining Eqns. 2-14 and 2-16 (in the x-direction now) and integrating yields,

$$\frac{\tau}{\rho} \equiv -\overline{uw} + \nu\frac{\partial U}{\partial z} = U_*^2\left(1-\frac{z}{h}\right) \tag{2.17}$$

and,

$$\frac{\tau_o}{\rho} \equiv U_*^2 = gh\left(\sin\theta - \cos\theta\frac{dh}{dx}\right) \equiv ghS \tag{2.18}$$

The term U_* is used throughout this thesis and is defined differently depending on the author. It is termed friction velocity, shear velocity, or turbulent shear velocity. Also, τ_o is shear stress at the bed. From Eqn. 2.17 we can see that total shear stress varies linearly from the value τ_o at the bed to zero at the free surface (Fig. 2-4). Total stress is the summation of the Reynolds Stress and viscous stress.

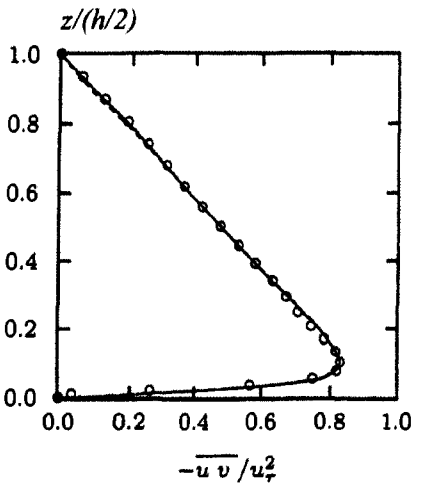

Figure 2-4. Principal Reynolds stress distribution (Wilcox 2000)

2.3.5 Boundary Layer Development

When water enters a channel, any non-smooth element at the channel entrance creates a disturbance. If the flow is uniform and stable, the velocity distribution will vary along the channel length until reaching a definite pattern known as a fully developed turbulent boundary layer. A good example in most laboratory cases is the transition from inlet structure to a test channel. Directly at the channel entrance flow is laminar and the zone of laminar boundary layer development length corresponds to line AB in Fig. 2-5. Above line ABC, velocity theoretically does not change with depth and the region below ABC is known as the boundary layer, defined here as δ. The thickness of the boundary layer is difficult to define accurately and is dependent on the roughness of the channel boundary.

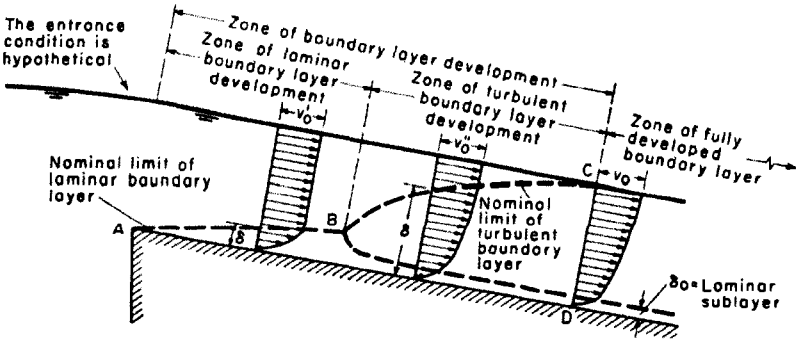

Figure 2-5. Development of the boundary layer in an open channel with an ideal entrance condition (Chow 1959)

The region below line ABD is known as the laminar sublayer, δ_o, within which, flow is laminar. Since the thickness of δ_o is much smaller compared to δ, and while the velocity distribution in this region is theoretically parabolic, it is normally estimated as linear for simplicity.

Individual roughness elements or protrusions will form small eddies at their top, which are dampened in the laminar flow region. As velocity increases along the channel, eddies continue to develop, and at point B they reach the top of the laminar flow region. Downstream of point B, eddies are strong enough to generate turbulence along line BC, and a turbulent boundary layer is developed. As we will show in the next section, the velocity distribution in this region is known to be approximately logarithmic. The thickness of the boundary layer, δ, for most applications, can be assumed to be equal to flow depth, h, if the flow is uniform and stable as seen in Fig. 2-6. This is an important concept for hydraulic modeling of river flow.

When numerically modeling a river reach, a fully developed turbulent boundary layer exists throughout said reach, unless some significant obstruction causes flow separation. Hence, when conducting experiments such as the ones outlined for this thesis, a check for fully developed turbulent boundary layer is essential in assuring natural conditions have been properly simulated.

It is said that a fully developed turbulent boundary layer will occur at a distance downstream from the channel entrance of approximately 320 to 400 times the hydraulic radius (Simons and Senturk 1992). Kirinoto and Graf (1994) demonstrated that estimating this length at $40h$ is acceptable.

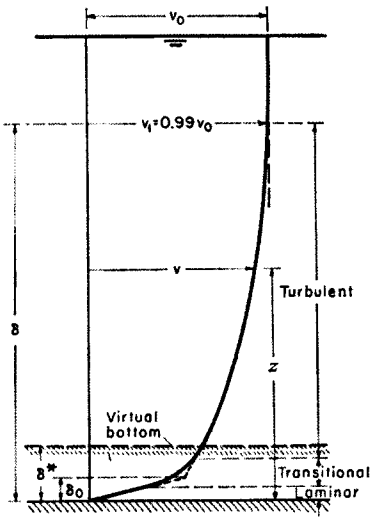

Figure 2-6. Velocity distribution over a smooth channel (Chow 1959)

2.3.6 Turbulent Velocity Distribution

2.3.6.1 The Law of the Wall

In 1926, Prandtl developed an equation in which the shear stress at any point in a turbulent flow moving over a solid surface can be calculated by,

$$\tau = \rho l^2 \left(\frac{du}{dz}\right)^2 \tag{2.19}$$

or,

$$\sqrt{\frac{\tau}{\rho}} = l\left(\frac{du}{dz}\right) = U_* \tag{2.20}$$

The parameter l is known as mixing length and is the length in which turbulent fluctuations are confined. Prandtl introduced two assumptions. First, the mixing length is assumed to be proportional to depth, and secondly, that the shear stress is constant, therefore $\tau = \tau_o = \tau_{xy}$ which allows substitution of U_*. By combining Eqns. 2.19 and 2.20 from above, we have,

$$U_*^2 = l^2 \left(\frac{du}{dz}\right)^2 \tag{2.21}$$

Now, the assumption of the mixing length can be expressed as,

$$l = \kappa z \tag{2.22}$$

where κ is known as von Kármán's universal constant, which, when substituted into Eqn. 2.20 yields,

$$\frac{du}{dz} = \frac{\sqrt{\tau/\rho}}{\kappa z} \tag{2.23}$$

and by integration gives,

$$\frac{u}{U_*} = \frac{1}{\kappa} \ln z + C \tag{2.24}$$

This is known as the Prandtl-von Kármán's equation, the law of the wall, or the log-law, and dictates that the velocity profile is log linear with distance to the surface. Based on experiments made by Nikuradse, values of κ and C (constant of integration) have been, in many cases, assumed to be 0.41 and 8.5 respectively for rough channels. Note that these values can vary slightly depending on the boundary and flow conditions.

2.3.6.2 The Wake and Power Laws

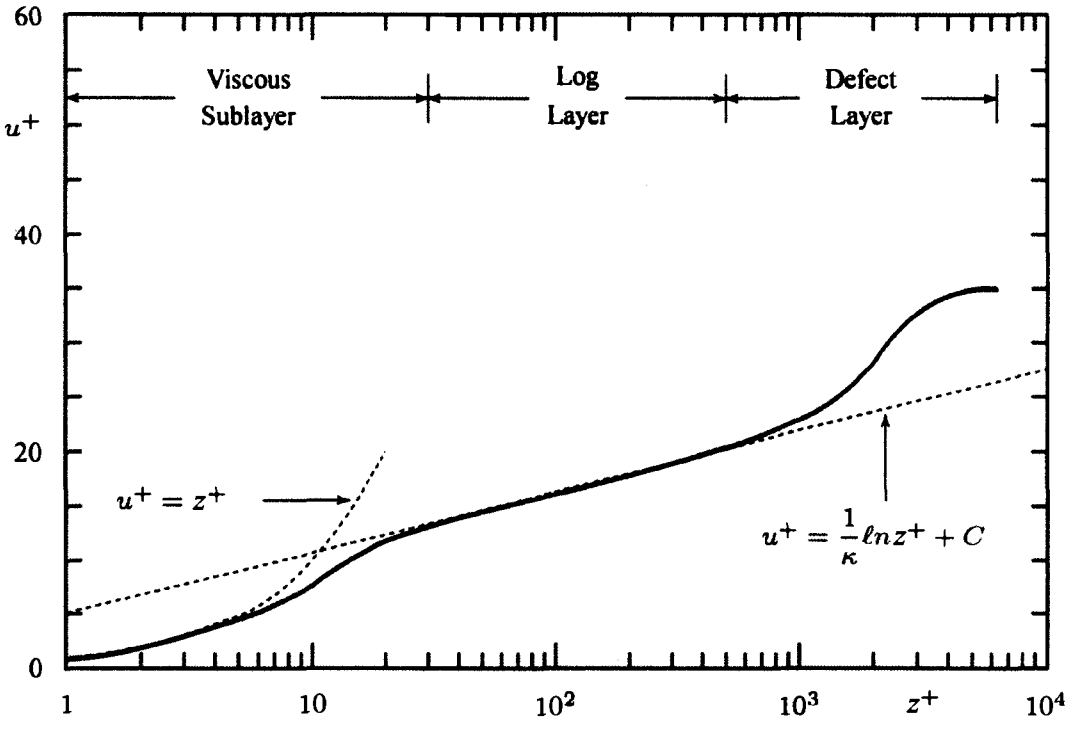

Figure 2-7. Typical velocity profile for a turbulent boundary layer (Wilcox 2000)

Wilcox (2000) presents a typical velocity profile for a turbulent boundary layer (Fig. 2-7). In this diagram z^+ and u^+ are dimensionless length and velocity scales, respectively:

$$u^+ \equiv \frac{u}{U_*} \tag{2.25}$$

and,

$$z^+ \equiv \frac{U_* z}{\nu} \tag{2.26}$$

While a velocity distribution has already been presented, Fig. 2-7 is considered to be a more accurate representation with the major difference being the deviation away from the law of the wall in the region near the surface. This region is known as the "defect layer". Nezu and Nakagawa (1993) point out that the law of the wall is only valid where $z/h < 0.2$. To account for the deviation in the defect layer, Coles (1956) empirically determined a wake function and added this to Eqn. 2.24 to yield,

$$\frac{u}{U_*} = \frac{1}{\kappa}\ln z + C + \frac{2\Pi}{\kappa}\sin^2\left(\frac{\pi z}{2h}\right) \tag{2.27}$$

where Π is Coles' wake strength parameter which is a function of pressure. This concept is analogous to the velocity-dip phenomenon where we see the effect of a free surface on velocity and turbulent fluctuations. While there are several other methods proposed to determine velocity in the "outer region", Nezu and Nakagawa (1993) point out that this wake function appears to be the most acceptable extension of the log-law. Rennie et al. (2002) found in the field that the log-law held all the way to the surface. Near the bed, however, roughness elements (considering most natural channels are made up of non-homogenous particles) induce a "wake layer" which vertically displaces the log-law as well as the Reynolds stress distribution (Nowell and Church 1979).

Contrary to the idea of a segmented profile, it is also argued that turbulent boundary layer profiles can be more accurately represented over the entire flow depth as a power-law. This is expressed in Wilcox (2000) as,

$$\frac{U}{U_*} = \left(\frac{z}{\delta}\right)^{1/n} \tag{2.28}$$

where n is an integer value between 6 and 8.

It is worthwhile to note that all relationships discussed thus far have been determined in a channel with solid boundary without sediment transport.

2.4 Roughness

2.4.1 General Considerations

Generally speaking, roughness is difficult to accurately determine since it is essentially a function of flow obstruction, ranging from viscous skin friction on the surface to accelerations due to the presence of bars and dunes. Regardless of the source, fluid flow is constantly losing energy primarily from internal friction. Consider again Fig. 2-2 where two plates are separated by an incompressible fluid; were there no shear resistance, these plates would accelerate at a constant rate.

The concept of internal shear being the fundamental contributor to fluid resistance is complicated in channel flow due to the addition of boundary friction which makes evaluation more complex. In natural rivers, the characteristics of the boundary are highly variable and changing with time and therefore accurate predictions of roughness can be difficult.

2.4.2 Manning's Formula

The most widely employed uniform flow equation for open channel flow is that presented by Irish engineer Robert Manning in 1889. Its most widely used form is as follows,

$$\overline{U} = \frac{1}{n} R^{2/3} S^{1/2} \tag{2.29}$$

Where R is the hydraulic radius in m, S is channel slope, and n is the coefficient of roughness, specifically known as *Manning's n*.

While R and S are tangible relations, n has no exact selection method. Many studies have been conducted to help assist the calculation of n through making assumptions and conducting experiments for a variety of simplified conditions. The complicated nature of roughness is inherent in defining a value of n, especially in natural channels. Roughness then is due to, and a function of (Simons and Senturk 1992):

1. the depth of flow,
2. the sediment transport (bed load, suspended load and wash load),
3. the geometry of the cross-section,
4. channel irregularity or the geometric pattern of scouring and silting in the channel,
5. the size of bed material,
6. floating debris,
7. the type and extent of vegetation on the banks,
8. the water temperature,
9. ice cover,
10. wind direction and magnitude.

Thus, in a real channel, no single value of n can be applied to an entire reach. The estimation of n for a given situation can be done several different ways. Regardless, the most important aspect of this decision is sound engineering judgement that experience brings. Works are available (Chow 1959; Graf 1971; Hicks and Mason 1999) which report measured n values for a host of varied natural and experimental conditions. While not directly applicable to laboratory studies, empirical equations have been developed for the prediction of n for varied natural conditions.

Of importance here is Stickler's (1923) empirically derived equation for determining Manning's n based on grain size alone,

$$n = \frac{D_{50}^{1/6}}{21.1} \tag{2.30}$$

The flume used for experiments to develop Eqn. 2.30 had sand glued to the bottom and the walls and thus this relation should be used with caution. However, it is used for our purposes to give an initial idea of roughness for our chosen grain size.

2.4.3 Estimation of Boundary Resistance from Measured Velocity Profiles

The law of the wall was presented in Eqn. 2.24. A particularly useful aspect of that relation is in the determination of roughness parameters. Kuelegan (1938) brought the constant of integration, C into the log term to yield,

$$\frac{u}{U_*} = \frac{1}{\kappa} \ln\left(\frac{z}{z_o}\right) \tag{2.31}$$

where z_o is known as the elevation of zero velocity. This can be thought of as an upward projection of the boundary surface due to roughness elements. Also, z_o is equivalent to δ_o which was presented earlier for boundary layer development. For our purposes, $z_o = \delta_o = mk_s$ where m depends on bed roughness, which was found experimentally to be approximately equal to 1/30 for rough surfaces. This leads to a useful form of the equation,

$$U = \frac{U_*}{\kappa} \ln z + \frac{U_*}{\kappa} \ln\left(\frac{30}{k_s}\right) \tag{2.32}$$

from which U_* and k_s can be determined from a linear regression of U versus $\ln z$, where k_s is the roughness height.

2.4.4 Grain and Form Roughness

In rivers, total roughness or friction is the summation of grain resistance and form resistance. Grain resistance is due to boundary resistance which includes viscous skin friction and wake loss due to flow separation behind individual particles. Form resistance is attributed to flow separation and subsequent eddy losses from bedforms (Bray and Davar 1987) but can also be considered to include all losses not accounted for in grain roughness.

Using the Darcy-Weisbach friction factor expressed as

$$\frac{1}{\sqrt{f}} = \frac{U}{\sqrt{8gRS}} \tag{2.33}$$

and,

$$f = \left[2.03 \log\left(\frac{12.2R}{k_s} \right) \right]^{-2} \tag{2.34}$$

Here, a value of grain roughness is estimated, k_s, which was determined by Nikuradse (1933) to be equivalent to the D_{50} of the bed material for uniform sediment. For gravel-bed rivers, Millar (1999) concluded after analysing 176 sets of data that using $k_s = 5.9D_{50}$ yields a root mean square (RMS) error between calculated and observed values of f of 25%. Bray and Davar (1987) give a value different value, $k_s = 6.84D_{50}$, which, if nothing else, shows that no unified approach has been adopted.

After Einstein and Barbarossa (1952) we illustrate the concept of segmented friction by

$$f = f' + f'' \tag{2.35}$$

where f' and f'' are grain and form components of friction respectively. In a straight, plane-bed with no bed form development, $f'' = 0$ and the flow resistance is due to grain roughness only. Millar (1999) points out that form resistance cannot be measured directly and still remains an open subject in literature. Alternately, grain roughness can determined through

$$f' = \left[2.03 \log\left(\frac{12.2R}{k_s'} \right) \right]^{2} \tag{2.36}$$

In this case, since we are trying to analyze grain roughness alone, following Millar (1999), Nikuradses' original definition that $k_s' = D_{50}$ is most commonly used.

2.5 Sediment Transport

2.5.1 Beginning of Motion

It is well known that the river bottom imposes drag forces on river flow. If that drag force is less than a critical value, bed material remains motionless and can be treated as a fixed boundary for analysis. Near the critical value, we see only a few particles moving on the channel bottom. The critical value is subject to the investigator's interpretation (Buffington and Montgomery 1997). As shear stress increases past this critical value, more particles begin to move and their movement becomes less individual. At even higher rates of shear, particles can be entrained and suspended in the flow.

Typical gravel-bed rivers are composed of a broad range of sediment sizes, varying from fine sands to cobbles. Of course, if the forces on a particle are unbalanced the particle will move. The forces holding the particle in place are the submerged weight, and grain-to-grain frictional

interaction. On the other hand, fluid drag and lift due to dynamic pressure variation over the particle force the particle out of place. Very small sand particles can translate in a hopping motion termed saltation, while larger particles roll and slide along the bed. This variability leads to sorting of the material through armouring and formation of particle clusters, and depending on local magnitude of shear, different structures can form. Note that all of these movements are greatly affected by turbulent fluctuations and time-dependent analysis is complicated because particle movement often involves long rest periods. (Knighton 1998)

Determining exactly where the threshold of motion exists for certain particles has been researched for many decades. The beginning of motion for a bed of well sorted particles can be determined using the widely accepted Shields diagram shown in Fig. 2-8.

The Shields parameter is also known as the dimensionless critical shear stress, τ_*, and is represented by,

$$\tau_* = \frac{\tau_c}{(\gamma_s - \gamma)D_s} \tag{2.37}$$

where γ_s is the specific weight of the particle, γ is the specific weight of water, D_s is the characteristic particle diameter which is normally estimated as D_{50}, and τ_c is critical shear, defined as,

$$\tau_c = \rho U_{*,c}^2 \tag{2.38}$$

Again, U_*, c is the critical turbulent shear velocity, where

$$U_* = \sqrt{\tau_o / \rho} \tag{2.39}$$

The Chezy depth-slope relation is most commonly used to estimate the shear stress exerted on the bed, τ_o, in uniform flow which is represented by,

$$\tau_o = \gamma RS \tag{2.40}$$

Shields related dimensionless critical shear to particle Reynolds number, R_* which is represented here as,

$$R_* = \frac{U_* D_{50}}{\nu} \tag{2.41}$$

Thus, the Shields diagram is employed in this thesis to indicate flow conditions and more specifically the channel slope required for incipient motion given the characteristic particle diameter.

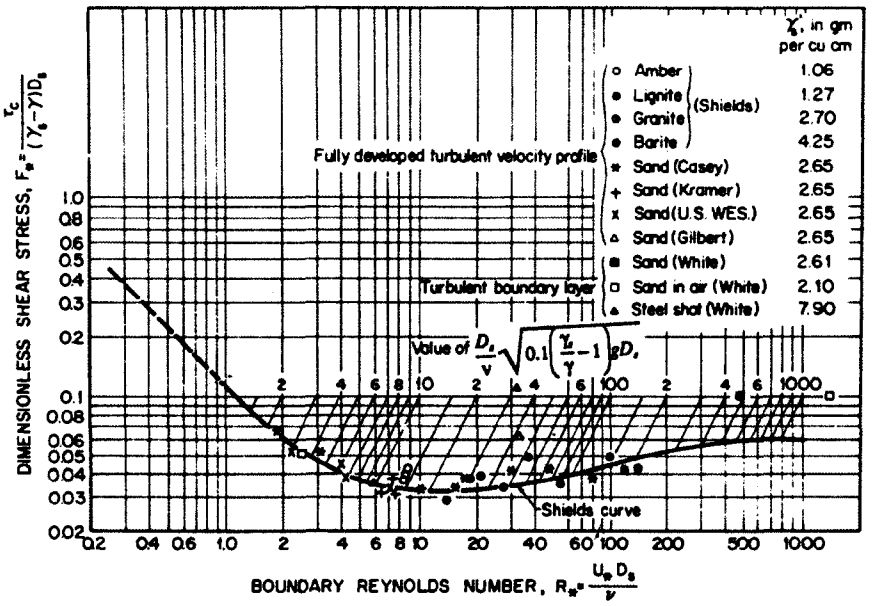

Figure 2-8. Shields diagram (Simons and Senturk 1992)

2.5.2 Bedforms and Equilibrium

Again, when shear stress exceeds a critical value, bed material is transported. Temporal and spatial variations of turbulent structures cause local increases in shear, resulting in an accumulation of individual grains into distinct configurations known as bedforms. The geometry of bedforms depends on flow characteristics which in turn are influenced by those forms, resulting in complex feedback relationships (Knighton 1998). Referring back to the relationship between grain and form roughness (Eqn. 2.35) if flow depth, and consequently total friction remain constant, form roughness increases as bedforms develop which results in a decrease in grain roughness. Thus, a river adjusts its roughness through the development of bedforms which ultimately stabilizes the channel. If flow rate is constant over a sufficiently long period, bedform readjustment decreases in magnitude until finally the equilibrium of forces acting on each particle is reached. This is commonly referred to as equilibrium.

While equilibrium is important for the experiments conducted for this thesis, it rarely exists for very long, if at all, in natural channels. The following excerpt from Knighton (1998) gives a good description of the complex action-reaction nature of natural channels:

"True stability never exists in natural rivers, which frequently change their position and which must continue to pass a range of discharges and sediment loads. However, they can become relatively stable in the sense that, if disturbed, they will tend to return approximately to

their previous state and the perturbation is damped down. Provided the controlling variables remain relatively constant in the mean, a natural river may develop characteristic or equilibrium forms, recognizable as statistical averages associated with single-valued relationships to the control variables."

Knighton (1998) presents a succinct diagrammatic representation of the interaction of flow intensity and roughness in terms of their capacity for sediment transport, along with the profile shapes and flow features to expect local to the bedform as a function of transport rate (Fig. 2-9). Noting that this diagram was developed from experimental results produced in a test channel as presented by Simons and Richardson (1966), it is good reference for the analysis of the experiments reported in this thesis. The following commentary on bedform structure and formation will give the most attention to dunes as they are the only expected bedform for this thesis.

Below the threshold of motion, a plane bed is said to exist when there are no depressions larger than the largest grains of the bed material. Bedforms from previous high flow events may still be present, but at this lower flow, are not changing. The roughness height, k_s for plane bed is reported to range from $1.25D_{35}$ to $5.1D_{84}$ (van Rijn 1982) with a typical value of $3D_{90}$. Note that the subscripts represent percent finer on a typical grain size distribution plot.

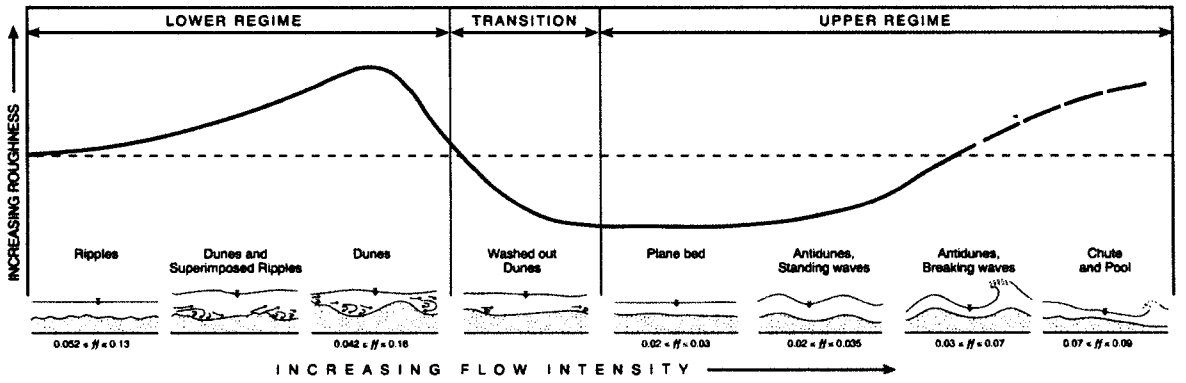

Figure 2-9. Experimental bedform development in sand bed rivers as function of friction factor (Knighton 1998)

Based on their shape, resistance to flow, and mode of sediment transport, bedforms are classified into upper and lower flow regimes. As shear increases from the plane bed, subcritical state, in the lower flow regime we see ripples begin to form. Ripples are usually less than 40 mm in height and 0.6 m in wavelength, both of which are primarily a function of particle size (Raudkivi 1997). Since ripples are a function of near bed flow conditions, their size is

independent of depth. Their shape is roughly triangular in profile, with gentle upstream and steep downstream slopes (Knighton 1998). These are not significant to these tests since the sediment used for these studies, D_{50} = 1.1 mm, is larger than 0.6 mm which Knighton (1998) points out as being the approximate threshold particle size for ripple formation. Figure 2-10 shows a phase diagram for bedforms as a function of characteristic particle diameter, or D_{50}, and dimensionless boundary shear stress, τ_* which shows that dunes form directly after lower regime plane bed in material larger than 0.6 mm.

With higher bed shear, ripples are washed out and dunes form or in material larger than 0.6 mm, dunes follow directly after plane bed motion. Dunes are generally larger than ripples and differ mainly in that they scale with flow depth and ripples can be superimposed on relict dunes from past events (Knighton 1998). While dune height is variable, Yalin (1992) proposed that

$$\lambda \approx 6h \tag{2.42}$$

where λ is wavelength, and h is flow depth. Knighton (1998) gives a range of 4 to 8 times the flow depth for λ, and suggests dune height can be as much as a third of the flow depth. In the laboratory, dunes tend to extend across the full width of the channel which is a result of narrow width to depth ratios. Yalin (1992) based his argument on the premise that burst length (a concept we will cover in turbulence measurement) or the streamwise distance between the birth and decay of a macroturbulent eddy, will control dune wavelength as is shown as (e) in Fig. 2-11.

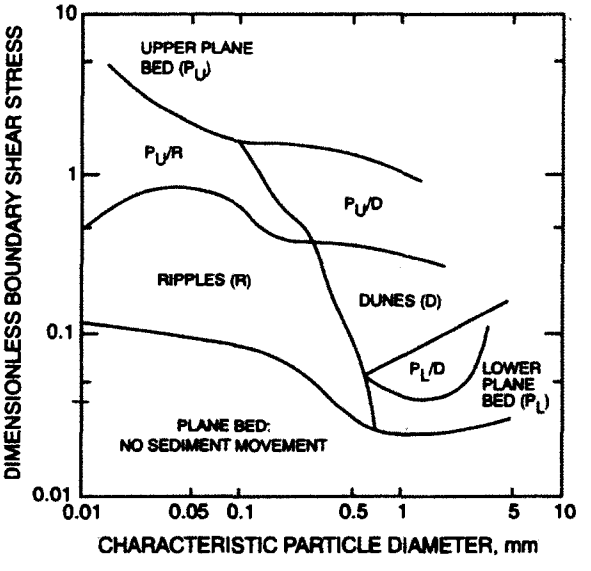

Figure 2-10. Bedforms defined in terms of grain size and boundary shear stress (Allen 1983, cited in Knighton 1998)

Dunes then become washed out in the "transition zone" out until upper plane bed is reached in the upper flow regime where we see a large reduction in form roughness and a consequent increase in grain roughness. This upper-stage plane bed is characterized by intense bed-load transport, which prevents the patterns of erosion and deposition required for the formation of bedforms. As flow intensity increases we see the formation of dunes again, this time known as anti-dunes.

While anti-dunes only differ marginally in shape from their lower flow regime counterpart in that they are more symmetrically triangular in profile, in this case the water surface is in phase with the dune formation. This is due to the presence of standing waves which are a function of the flow being supercritical (Simons and Senturk 1992), and thus the location of anti-dunes may actually move upstream which lead Gilbert (1914) to name them anti-dunes (Simons and Senturk 1992).

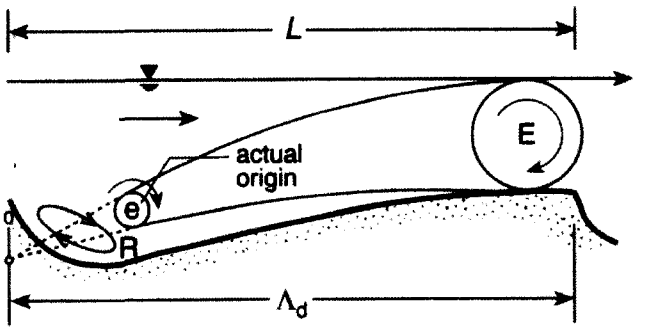

Figure 2-11. Dune formation as a function of eddy production (Yalin 1992)

2.6 The Measurement of Turbulence

Turbulence is dominated by large, energy bearing eddies (Wilcox 2000). Generation of turbulence occurs when main flow energy is extracted by large eddies, which is ultimately due to shear. Following the Chezy depth-slope relation for total bed shear stress, total shear is a function of flow depth, and thus the length scale, or size, of the largest eddies we expect in open channel flow are less than or equal to the flow depth. Dissipation of turbulent energy occurs at a very small scale where fluid viscosity can change kinetic energy into heat. The rate of small eddy diffusion is controlled by the rate at which they receive energy from the larger eddies. However, even at the largest scales, the process is not perfectly efficient, and some energy is dissipated (Rouse 1959). For example, when larger eddies coalesce with one another energy is transferred to the larger eddy (Nezu and Nakagawa 1993).

When we introduced turbulence, the concept of time and length scales was briefly introduced. In this section we present the metrics by which turbulence is discussed and how we obtain and calculate them. For example, Reynolds number will give an indication of the level of turbulence for a given flow, but not an actual size or strength of turbulent fluctuations. Since pressure is difficult to measure in fluid flow, numerous periodic velocity measurements are made at different fixed points in the flow.

2.6.1 Eulerian and Lagrangian Measurements

Eulerian measurements are those made at a fixed point, which, if we are interested in determining eddy sizes (time scales), must be made over a sufficiently long duration that the period of oscillations is discernable. Eulerian measurements, then, require a longer time series, and faster sampling rate than the period of oscillations in the flow due to the larges eddies.

Here, velocity measurements are made at each location for two minutes, which is commonly accepted as a suitable duration for turbulent velocimetry in fluvial environments (Nikora and Goring 1998; Buffin-Belanger and Roy 2005).

Lagrangian measurements are those in which the sample volume travels at the same velocity as the mean flow and are required if a direct analysis of the spatial size of an eddy (length scale) is desired. Eulerian measurements are commonly converted using Fourier transforms to analyze time and length scales.

2.6.2 Mean Statistics

Through determining mean values of velocity and pressure, as was Reynolds' approach in deriving his version of the continuity and RANS equations, a series of descriptive terms for turbulent flow can be developed. The parameters based on mean values which are of particular concern to this thesis are turbulent intensity, Reynolds stress, and turbulent kinetic energy. These parameters are based on mean velocity fluctuations and do not require a continuous time series for analysis. Note that these indicators do not give any indication of the time or length scales of flow oscillations or eddy sizes.

By taking the RMS of turbulent fluctuations, $\sqrt{\overline{u_i^2}}$, the effect of positive and negative fluctuations is removed, providing a clearer average than would be revealed by their mean. While this measure is used consistently in the literature and for this thesis, it is more sensible to use the mean of absolute fluctuations, $\left|\overline{u}\right|$, for describing the mean of turbulent fluctuations in data taken with acoustic velocimetry. Erroneous measurements or noise can cause a significant "spike" in

the data, which, when squared and summed with the rest of the data set, can result in fluctuations which are biased high.

Turbulent boundary layer flow is usually anisotropic (stronger velocity fluctuation in the streamwise direction, or in other words, flow is axes dependent) and in such a manner that $\sqrt{\overline{u^2}} > \sqrt{\overline{v^2}} > \sqrt{\overline{z^2}}$ is in a ratio of 9:7:5 (Nezu and Nakagawa 1993). Also, because these values are based on 1D measurement, early experimental values are likely to be quite accurate which is useful for analysis (Nezu and Nakagawa 1993).

Relative turbulent intensity is a 1D description of how intense the turbulent fluctuations are, shown here in the x, y, and z axes respectively, as (from Rennie MatLab code).

$$\hat{u} \equiv \frac{\sqrt{\overline{u^2}}}{\overline{U}}, \qquad \hat{v} \equiv \frac{\sqrt{\overline{v^2}}}{\overline{V}}, \qquad \hat{w} \equiv \frac{\sqrt{\overline{w^2}}}{\overline{W}} \tag{2.43a, b, c}$$

This definition differs from the more classic way of normalization where each coordinate is normalized by mean downstream velocity, $\overline{U}$, defined in Wilcox (2000), or shear velocity, U_* (Nezu and Nakagawa 1993). It is felt that the definition used here is more effective for flow in bends as helical flow does not tend to necessarily have mean flow following the channel geometry (Rennie, pers. comm.).

The Reynolds stresses (Eqn. 2.15) are the most commonly sought indicators of turbulence in hydraulics research. Again, these give an indication of the exchange of momentum between the main flow and turbulence, and as such, the distribution of Reynolds stress is of primary importance to this thesis. Streamwise-vertical Reynolds stress is commonly referred to as principal Reynolds stress, and from straight channel flow theory it provides a clear picture of stress on the bed. As we will see, however, for flow in river bends the core of maximum velocity becomes helical in nature, shifting about the channel centerline. Thus, using principal Reynolds stress for shear on the bed is less reliable. The methods for estimating bed shear in bends will be discussed in Section 2.8.1

Turbulent kinetic energy, k, is a 3D representation of the amount of turbulent kinetic energy that exists at a single point. It is defined as

$$k = \frac{1}{2}\left(\overline{u^2} + \overline{v^2} + \overline{w^2}\right) \tag{2.44}$$

2.6.3 Correlation Functions and Spectral Analysis

There are two equivalent approaches to determine time and length scales from Eulerian velocity measurements. In the time domain correlation functions are useful, and in the frequency domain spectral analysis techniques are employed. A comprehensive discussion of the principles

and techniques inherent in these expansive fields is outside the scope of this thesis. Rather a basic summary of the most commonly used approaches in open-channel turbulence research are presented here. Spectral analysis calculations are employed in this thesis, however, there are also qualitative deductions one can make from visually examining a plot of spectral density.

2.6.3.1 Correlation Functions

Deviating from the classical definition of turbulence where individual particle motion is purely stochastic and turbulence is isotropic; the actual motion of each particle is also a function of the movement of its neighbour. Townsend (1976) points out that to describe the organization of the flow we require mean values of the functions of flow variables for two or more particles at two or more positions. Given a continuous time series of velocity fluctuations at a point, *u(t)*, correlations are calculated for the observed fluctuations that are separated by a time lag, τ (not to be confused with shear stress, and this notation is used only in this section of the thesis). Thus, the correlation function, $C_{11}(\tau)$, is defined as,

$$C_{11}(\tau) = \overline{u(t)\,u(t+\tau)} \tag{2.45}$$

where the subscripts 11 mean autocorrelation, or the comparison of u to u. It is also possible to calculate cross-correlations using this relationship, but it is less prevalent in the literature. If velocities tend to be similar when they are separated by a time lag, τ, then $C_{11}(\tau)$ will have a positive value, if there is no relation between separate velocities, $C_{11}(\tau)$ tends to zero. Regardless, Eqn. 2.45 is evaluated at all possible values of τ, from zero to half the duration of the time series (i.e., up to the Nyquist frequency, $f_{Nyquist}$). The values are commonly normalized resulting in what is known as the Eulerian time-correlation coefficient (Wilcox 2000), and is defined as,

$$R_{11}(\tau) = \frac{C_{11}(\tau)}{\overline{u^2}} = \frac{\overline{u(t)u(t+\tau)}}{\overline{u^2}} \tag{2.46}$$

and by definition $R_{11} = 1$ when $\tau = 0$. For large values of τ we expect the fluctuations to be uncorrelated so then $R_{11} = 0$ when $\tau \rightarrow \infty$. This relationship is normally plotted with $R_{11}(\tau)$ versus (τ) as in Fig. 2-12.

The intersection of the line with the axis in Fig. 2-12 is an indication of the largest time lag where data still show a correlation with each other, or the largest time lag for the generation of eddies. The integral time scale, T_E, is found by integrating Eqn. 2.46 from zero to infinity as such,

$$T_E = \int_0^\infty R_{11}(\tau)\, d\tau \tag{2.47}$$

The integral time scale is a measure of the time scale for the largest period oscillations in the flow. In other words, T_E is the time scale over which there is some organization in the flow and therefore, velocities at lags up to T_E will be similar to each other. Note that instead of integrating to infinity, common practice is to integrate to where correlation goes to zero, as shown in Fig. 2-13.

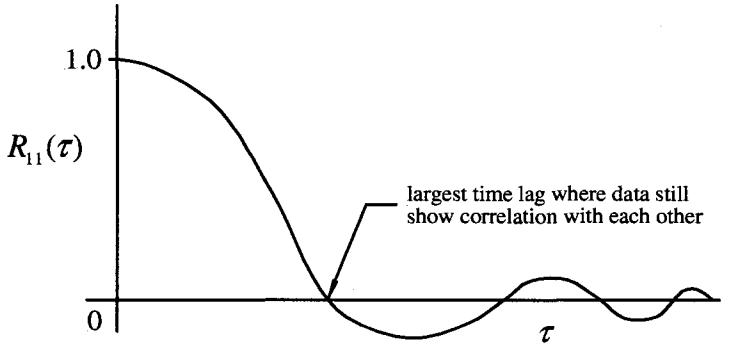

Figure 2-12. A typical Eulerian time-correlation coefficient plot

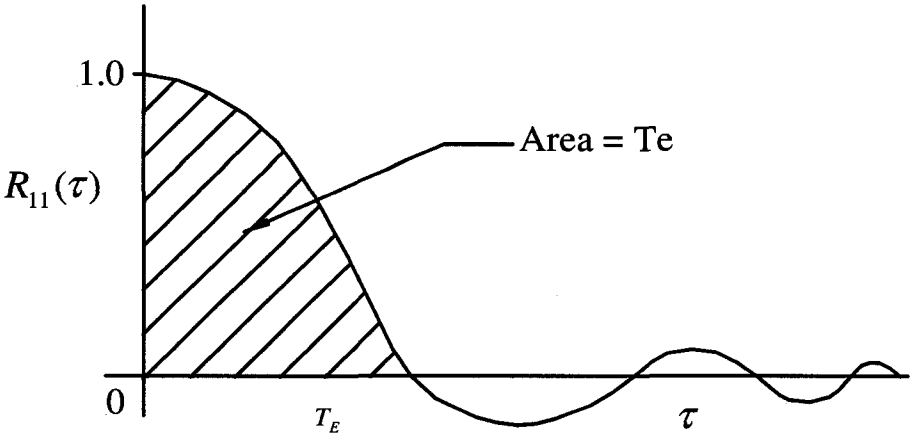

Figure 2-13. Definition sketch of integral time scale, T_E

From the shape of this curve another time scale can be determined for small time displacements which prove to correlate. This is the result of the small dissipating eddies and is known as the microtime scale, τ_E, defined here as,

$$\tau_E \equiv \sqrt{\frac{-2}{\left(\partial^2 R_{11}/\partial\tau^2\right)_{\tau=0}}} \tag{2.48}$$

Taylor's frozen field hypothesis is invoked to determine length scales from time series. If the relative turbulence intensity is not large (<0.25) then one can assume that the Taylor microscale, λ, is related to the microtime scale by

$$\lambda = \overline{U}\tau_E \tag{2.49}$$

Advection speed of the eddy will equal the mean velocity and the Taylor microscale is a product of the mean velocity and the micro-time scale. Because the Taylor microscale is generally too small to characterize large eddies, and too large to characterize small eddies, it has been ignored in most turbulence modelling research (Wilcox 2000). The same deduction can be used to define an integral length scale, L_x, where,

$$L_x = \overline{U}T_E \tag{2.50}$$

The conceptualization of Eqn. 2.50 reveals why this parameter is interesting to researchers. Since flow is considered in which relative turbulent intensity is much less than the mean velocity in a given direction, velocity fluctuations are small in comparison to the advection velocity, and the turbulence field is considered "frozen" as it passes the point of measurement. With this it can be stated that Eulerian measurements are identical to what would be observed with Lagrangian measurements which, since they require incredibly controlled movement of equipment, are rare in research outside of particle imaging velocimetry (PIV).

2.6.3.2 Spectral Analysis

Generally speaking, the information resulting from the autocorrelation function (Eqn. 2.46) can be converted to the frequency domain using a Fast Fourier Transform. The Fourier Transform of the autocorrelation function is:

$$S_{11}(\omega) = \frac{1}{2\pi}\int_{-\infty}^{\infty} e^{-i\tau\omega} C_{11}(\tau)\, d\tau \tag{2.51}$$

where ω is frequency in Hz. Here the autocorrelation function is multiplied by a cos curve, then integrated over all time lags, τ, to find the spectral energy, S_{11}, at a given frequency. Thus, cos curves of different frequencies are fit to the time series and summed finding the frequencies of oscillations that exist in the time series.

Kolmogorov's law is used not only as a way to visually check the acceptability of measurements, but also for noise estimations which is discussed later in this chapter. In between the upper and lower extremes of eddy production and dissipation is the intermediary region

known as the inertial subrange. In this region eddies are small enough that we can assume that their movement is random and isotropic (Nezu and Nakagawa 1993), but are still cascading into smaller eddies. Here, the direct effects of turbulence production (production range) and also dissipation through viscosity (viscous range) can be ignored. Kolmogorov showed by dimensional analysis that the energy in the inertial subrange should be a -5/3 power of frequency (Wilcox 2000). Figure 2-14 is a plot of spectral density versus frequency which shows the turbulent energy at different frequencies. Note that the line fitted to the section in the inertial subrange follows the -5/3 slope. Wilcox (2000) explains the importance of Kolmogov's hypothesis succinctly;

"The Kolmogorov -5/3 law is so well established that, as noted by Rogallo and Moin (1984), theoretical and numerical predictions are regarded with scepticism if they fail to reproduce it. It's standing is as important as the law of the wall."

Thus in analyzing velocity measurements, a plot of power spectra in the streamwise and vertical directions should show a -5/3 slope in the inertial subrange.

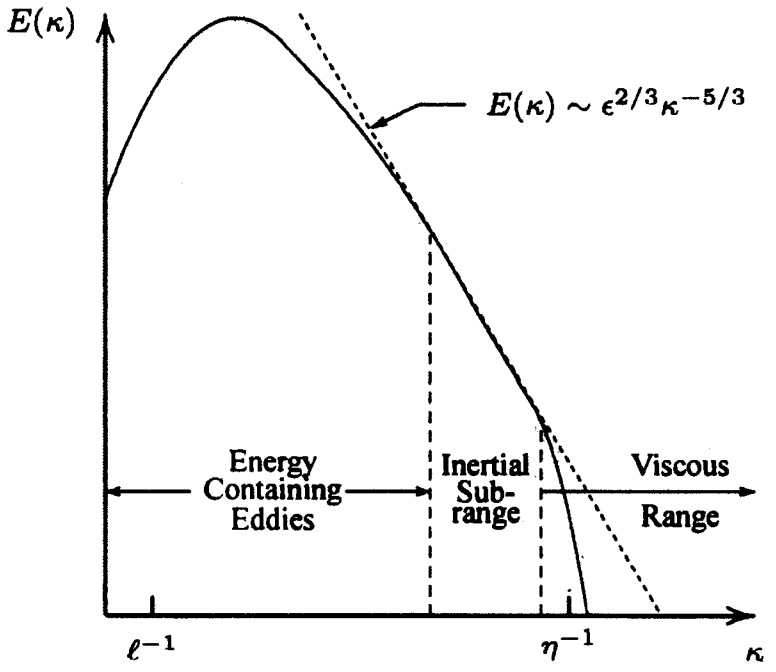

Figure 2-14. Energy spectrum for a turbulent flow (log-log scales) (Wilcox 2000)

2.7 Acoustic Doppler Velocimetry

With the advent of acoustic velocimetry and the refinements made over the last 15 years, we now have at our disposal robust and versatile velocimetry equipment for use in both the field and laboratory. For this thesis, we are using multiple ADVs, and more specifically the Nortek Vectrino+, which are capable of measurement frequencies up to 200Hz. The ADV was originally developed by the U.S. Army Engineer Waterways Experiment Station (WES) as a replacement for the sensitive Laser Doppler Velocimeter (LDV). With low cost, easy operation, and accurate measurements of mean and turbulent velocities in 3D, ADVs represent a turning point in hydraulics research.

While the original ADVs produced by Sontek and Nortek were popular and successful, two major problems were apparent. Due to bulky shapes, flow disturbance in the region very near the transducers created error. Also, seeding was often required to have enough particulate within the sample volume to produce an adequate return signal. The Nortek Vectrino ADV utilizes a smaller transducer and streamlined receiver arms along with advances in electronics, manufacture and design.

Older velocimeters used a multiplexed receiver circuit and amplifier to listen rapidly to each of the three receivers in sequence. The Vectrino uses a non-multiplexed receiver allowing sampling of all four receivers simultaneously (Rusello et al. 2006).

2.7.1 Operating Principle

The concept of the Doppler Effect can be illustrated by imagining standing beside a train track with the train approaching. The pitch (frequency) of its whistle blasts increases until the moment the train passes, and then the sound instantly becomes lower. This can be explained by considering that the rapidly approaching source of sound carries the individual phases of the waves forward so the crests and troughs succeed each other more rapidly (Born 1965). The ADV operates on pulse-to-pulse coherent Doppler shift where a pair of acoustic pulses are emitted from a central transmitting transducer with a sound wave frequency of 10 Mhz (in the case of the Nortek Vectrino). Scattered sound is received by four different receiving transducers (Fig. 2-15). The phase shift between the two pulses is utilized to estimate the Doppler frequency shift. A pulse travels down through the water column to the sample volume 50 mm below the emitter. Sound is then reflected from within the sample volume by ambient particles in the water, which are either naturally present in suspended sediment, or through seeding techniques. Since these particles follow the fluid motion with negligible inertial lag, their velocity is assumed to be identical to the fluid velocity. Note that signal strength increases with the amount of particulate

present within the sample volume. The reflected sound or backscatter is now at a different frequency which is a function of how quickly the particles are passing through the sample volume. The difference in the emitted and received frequency is known as the Doppler shift frequency (Song and Chiew 2001).

Figure 2-15. Two ADVs deployed in developed sand bed conditions

Because there are different transmitting and receiving transducers ADVs are called "bistatic", meaning that the measuring axis is the bisector of the send and receive axes. The Nortek Vectrino is one of the first ADVs to use four receiving transducers. The fourth receiver is used for making a redundant second measure of vertical velocity, which is useful for error calculation. The velocity in the sample volume in the direction of each of the bistatic axes (b_1, b_2, b_3, b_4) is calculated by:

$$b_i = \frac{c\left(\overline{d\theta/d\tau}\right)}{4\pi f} \tag{2.52}$$

where c is the speed of sound, θ is the Doppler phase shift for a pulse pair, τ is the time between pulses in a pulse pair, and f is the acoustic operating frequency. The mean value in Eqn. 2.52 is present because θ measurements from several pulse pairs are averaged for each sample. Since the pulses are emitted at a constant rate, as the sampling frequency increases, the amount of

averaging decreases for each measurement. For the Nortek Vectrino ADVs used in this thesis sampling frequency is adjustable using the Nortek Vectrino+ software, and the maximum sampling rate for the Vectrino is 200 Hz. This represents a significant increase in sampling rate than had been used by previous researchers.

The maximum streamwise velocity that can be measured is also adjusted using the Nortek Vectrino+ software. This control changes the time lag between acoustic pulses, τ, which is related to the maximum measureable velocity along the bistatic axis, v_{amb}, by,

$$v_{amb} = \pm \frac{c}{4 \tau f} \tag{2.53}$$

As τ increases, the range of measureable velocities decreases as the pulses will be more likely to decorrelate and phase ambiguities can occur. While short lags are more robust and allow measurement of more dynamic and higher velocities, they introduce more parasitical noise into the velocity signal because less spectral resolution is achieved with small lags. The user can select from ± 0.03, 0.10, 0.30, 1.0, 2.5, or 4.0 m/s, depending on the expected velocities. Selecting the lowest expected velocity range for a given flow is desired as it provides a balance between measurement robustness, accuracy, and minimizing noise (Rusello et al. 2006).

Lastly, the values for velocity corresponding to the orthogonal coordinate system (x, y, z_1, and z_2) are calculated automatically by the Vectrino+ software employing a sensor-specific coordinate transformation matrix, T (Voulgaris and Trowbridge 1998). For example,

$$[u_i] = T [b_i] \tag{2.54}$$

2.7.2 Noise

Because of the echoes from the flume bed or water surface, or other sources of experimental or electronics noise, the received signal can be distorted. The quantification of noise level is known as the signal to noise ratio (SNR), and is one of the main means of judging the quality of velocity measurements. Generally, the higher the SNR, the higher the correlation and the more reliable the velocity measurement will be (Rusello et al. 2006). In this case the term correlation refers to the autocorrelation function for pulse pairs, which is calculated continuously during data collection. Manufacturers recommend that correlations should be above 70% (Sontek) and SNR above 15 dB (Nortek), to ensure accurate velocity measurements.

In the section on spectral analysis, we explained that velocity measurements should display a -5/3 slope in the inertial subrange of a power spectrum plot (Fig. 2-14). The same is true for the power spectrum plots for ADV measurements in the streamwise and vertical directions (Rennie and Hay, in revision) However, if noise is high (low SNR), then noise dominates the

signal. This has especially proven to be the case for the high frequency region of ADV measurements.

Eddies that are small in comparison to the sample volume are difficult to measure because of spatial aliasing and low turbulent energy, and thus we see deviation from the -5/3 slope at higher frequencies. Spectral plots of vertical velocity components are less susceptible to this deviation than horizontal because of the orientation of the probes to the sample volume (Nikora and Goring 1998). This deviation of the power spectra occurs typically at the "noise floor" shown in Fig. 2-16. The concept of a noise floor can be demonstrated by the fact that energy content of true random noise (Gaussian) is uniformly distributed, and thus its spectrum plots horizontal over all frequencies. Extensive studies of noise and reducing noise error have been undertaken by Blanckaert and Lemmin (2006). Here, the approach to quantifying noise (N) is adopted from Rennie and Hay (in revision) whereby a developed algorithm fits a -5/3 slope to the inertial subrange of the sample spectra and then integrates the deviations across the entire spectrum. The details of this procedure are outlined in Section 3.4.2 of this thesis. Rusello et al. (2006) conclude from their work that the noise floor for the Vectrino is not typically reached until approximately 50 Hz which shows a significant improvement in ADV technology.

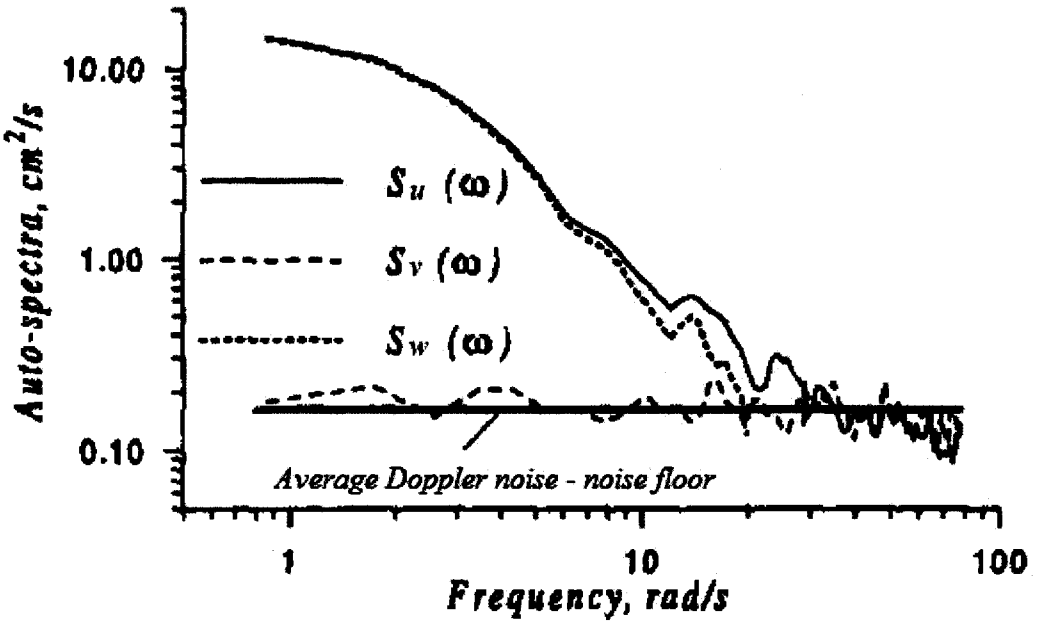

Figure 2-16. Example of Power spectra from an ADV measurement (Nikora and Goring 1998)

2.7.3 Near Bed Performance of ADVs

Recently, a study has been reported detailing a comparative study of the near-bottom performance of ADVs (Precht et al. 2006). Its focus is investigating the notion that the sampling volume size is larger than is stated by the software. This becomes problematic as we try to sample closer to the bed. If the sample volume is stated to be above the channel boundary, and is actually incorporating some of the non-moving boundary elements, then measured velocities are naturally skewed lower. As a useful consequence, SNR and signal amplitude become much higher than in the free flow under set conditions. It is noted that this comparative study was undertaken using the first generation of ADVs; with the updated design and circuitry, it is expected that the Nortek Vectrino works adequately close to the bed.

2.8 Flow and Turbulence in River Bends

This section is the most theoretically relevant to this thesis. To fully explain river bend phenomena and the results of the experiments reported here, a detailed understanding of turbulent structures both qualitatively and quantitatively, their interaction with the fluid in terms of viscous shear, and most dynamically their interaction with the developed bed are required. Thus far, this chapter has covered each of these topics independently. Past researchers have modified these more proven concepts from straight turbulent open channel flow in an attempt to understand the processes controlling the complex nature of river bend flow. Previous research has been limited by the limitations of classic velocimetry methods.

Also, engineers have made many attempts to develop empirical approaches for stable channel design, which predict that width must be less than six to ten times depth in order for the channel to remain stable, whereas most natural channels have width-to-depth (w/h) ratios larger than 10 and thus are unstable (Odgaard 1989). This instability leads to river meandering and migration.

Practically speaking, the main driving forces behind river bend research are bank erosion through natural meandering tendencies and the restoration and preservation of wildlife habitat. While both are fundamentally a function of channel and flow stability, there are two categories of "stability theory". Bar theories examine the conditions for formation of alternating bars in straight channels, while bend theories examine the migration features of meandering flows (Odgaard 1989). Numerical models presently used for predicting river flow frequently use closure schemes developed for analysis of two-dimensional boundary layers, since only 2D data were accessible

for model calibration (Blanckaert and DeVriend 2005). As a consequence, these models are highly debated and limited in their applicability (Odgaard and Bergs 1989).

In terms of flow theory for this thesis, we are concerned with presenting the measured distribution of Reynolds stress throughout an entire model river bend. The data set produced from the first experiment of this thesis, however, contains a wealth of 3D flow information beyond Reynolds stresses alone, which there is a noted lack of in research (Odgaard 1989; Blanckaert and DeVriend 2005). Given that, this thesis is not intended to analyze bend flow modeling techniques or how these models attempt to explain the phenomena; rather the discussion here is an introduction to the more proven bend flow characteristics which will aid in explaining the experimental results and lending credibility for the further exploration of the data set.

2.8.1 Helical Flow and Secondary Currents

The concept of helical or secondary flow is the basis for understanding turbulent flow in bends. While exact numerical modeling of secondary circulation over a developed bed has eluded engineers due to the complexity of the problem and more importantly the scarcity of 3D velocity measurements from which to calibrate and verify computed results, secondary circulation is a thoroughly studied aspect of bend flow. Thus, presented herein is a summary of the mechanisms involved in the production and behaviours of secondary circulation.

As flow enters a bend it experiences an increased centrifugal force; to counter this force, the water surface slope begins to tilt toward the outside bend making flow depth deeper in the outside of the bend (Dietrich 1987). This change in surface slope creates differing downstream flow conditions on either side of the channel centerline. On the inside of the bend, where the water surface elevation is reduced, the streamwise slope increases. The reverse is true for the water surface at the outside of the bend. The vertical distribution of this centrifugal force increases with distance from the bed. Near the surface, both streamwise velocity and centrifugal forces are strong while near the bed, the flow is moving slower and the centrifugal force is lower. As a consequence of this imbalance, shown in Fig. 2-17, a strong helical circulation (or secondary circulation) current is produced with outward flow at the surface, and relatively weak inward flow at the channel bed (Corney et al. 2006). This helical motion causes sediment to be transported inward creating a varying cross-sectional slope, and in plan, typical bar-pool topography will develop.

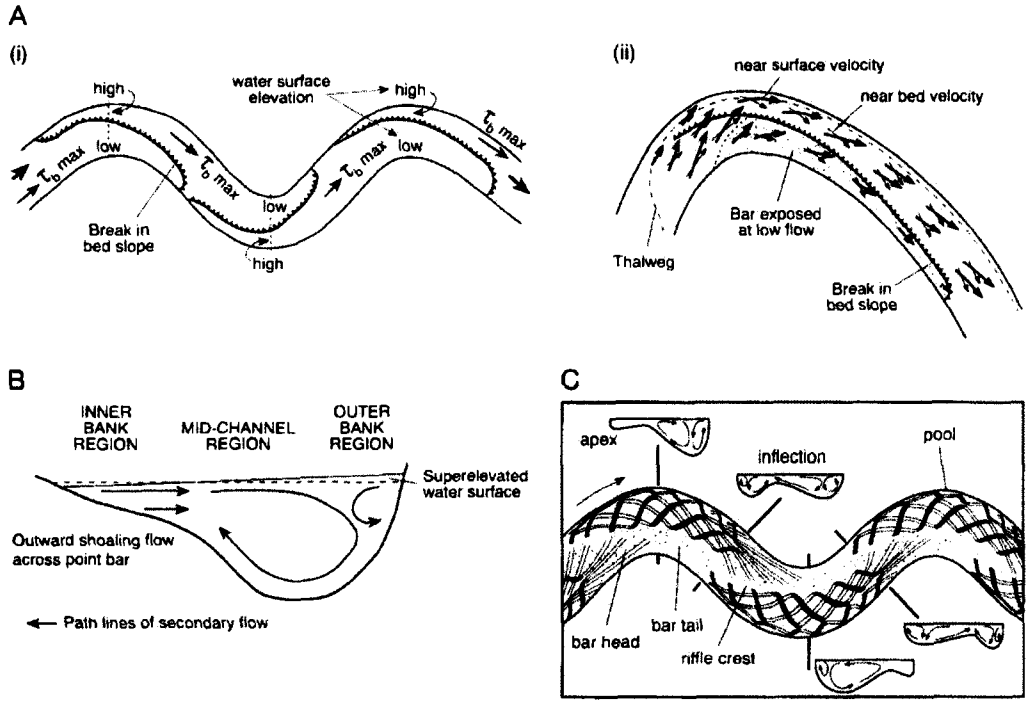

Flow pattern in meanders. (A) (i) Location of maximum boundary shear stress (τ_b), and (ii) flow field in a bend with a well-developed bar (after Dietrich, 1987). (B) Secondary flow at a bend apex showing the outer bank cell and the shoaling-induced outward flow over the point bar (after Markham and Thorne, 1992). (C) Model of the flow structure in meandering channels (after Thompson, 1986). Black lines indicate surface currents and white lines near-bed currents.

Figure 2-17. Flow pattern in meanders (Knighton 1998)

Past the apex in a natural channel, the curvature decreases progressively in the downstream direction, and the corresponding gradual reduction in centrifugal force causes the streamwise water surface slope to return to a normal level slope. Also the cross-section remains asymmetric (sloped) but the pool tends to shoal, and the point bar top to deepen (Dietrich and Smith 1983). The intent of this referenced research was to investigate the hypothesis that the spatial accelerations induced by the topographical changes are large in magnitude and strongly influence flow processes and the topography itself. At that time, the limitation to the development of a predictor was the inability to measure velocity in 3D.

In addition to the main helical vortex, Blanckaert and Graf (2001) were extremely interested in another secondary circulation cell in the upper part of the outer bank region (Fig. 2-18). While documented several times in earlier field studies (Bathurst et al. 1977; Dietrich and

Smith 1983), it was never explored in great detail again because of instrumentation limitations. Blanckaert had the benefit of an acoustic Doppler velocity profiler (ADVP) which is especially capable of measurements in this portion of the flow. This smaller circulation cell has an opposite sense of rotation than the center-region cell and consequently has a protective effect on the outer bank and the adjacent bottom. In this region there is also a reduction in turbulent activity which corresponds to a reduction in the bank shear stress.

Figure 2-18 also introduces a "cylindrical" coordinate system that follows the channel centerline which is more convenient for bend flow studies as natural rivers have a constantly varying curvature. In this coordinate system, s points downstream parallel to the centerline, n denotes the cross stream axis (positive toward left bank facing downstream), and z is the vertical direction.

In terms of shear stress, the increase of streamwise water surface slope on the inside of the bend leads to an increase in boundary shear stress, with its maximum value being just past the apex of the bend, as shown in Fig. 2-17a. Smith and McLean (1984) derived the following modifications of the RANS in terms of bed shear,

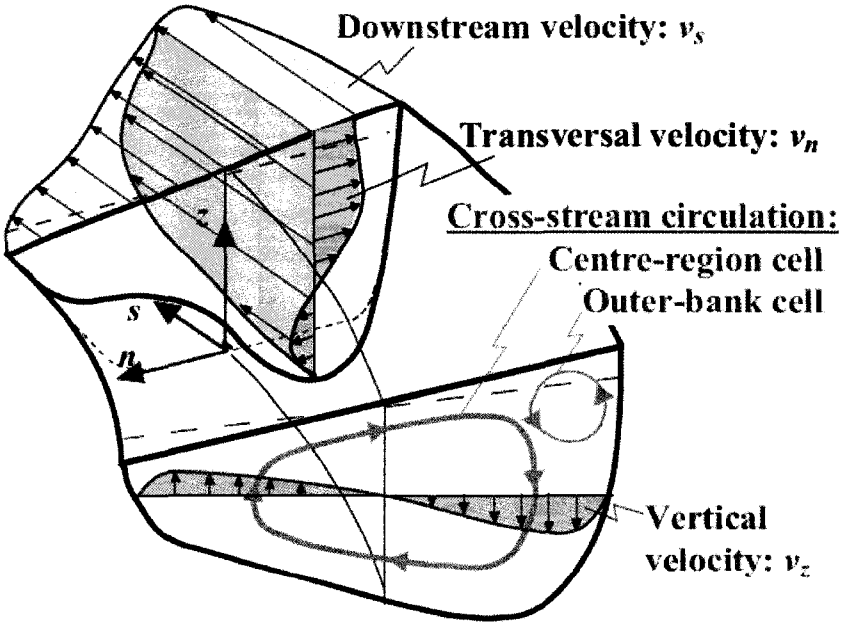

Figure 2-18. Definition sketch of curved open-channel flow in cylindrical coordinates (Blanckaert 2003)

$$(\tau_s)_o = \frac{-\rho g h}{1-N}\frac{\partial E}{\partial s} - \rho\frac{1}{1-N}\frac{\partial}{\partial s}<u_s^2>h - \rho\frac{\partial}{\partial n}<u_s u_n>h + \frac{2\rho<u_s u_n>h}{(1-N)r} \tag{2.55}$$

$$(\tau_n)_o = -\rho g h\frac{\partial E}{\partial n} - \rho\frac{<u_s^2>h}{(1-N)r} - \rho\frac{1}{1-N}\frac{\partial}{\partial s}<u_s u_n>h - \rho\frac{\partial}{\partial n}<u_s^2>h + \frac{\rho<u_s^2>h}{(1-N)r} \tag{2.56}$$

The terms $(\tau_s)_o$, and $(\tau_n)_o$, are the downstream and cross stream components of boundary shear stress; E is the elevation of the water surface, h is the depth of flow, g is the gravitational acceleration, and ρ is fluid density. The term N here is the ratio n/r, where r is the local radius of curvature of the centerline. This scale factor compares an arc length measured along the channel centerline to that measured along any other line of constant n (Dietrich 1987). The water surface elevation, E, at the bend apex can be approximated by the follow theoretical expression (Bridge 1992),

$$E = \frac{w\overline{U}^2}{gr} \tag{2.57}$$

2.8.2 Current Research

In the past 50 years, many physical studies have been undertaken on the topic of flow in bends. Figure 2-19 shows a list of bend studies analyzed by Blanckaert and Graf (2001); it is noteworthy, however, that the laboratory studies of Yen and Yen (1971), which are the comparative basis for the field work of Dietrich and Smith (1983), are not reported there. Excluding those that were conducted in a highly idealized rectangular cross-sectional flume, and field studies over natural topography (Dietrich 1983, Anwar 1986), this thesis is one of only three laboratory bend studies conducted with a mobile bed.

While an important contribution, the velocity measurements made by Odgaard (1984, 1988), were conducted using an electromagnetic current meter capable only of 2D measurement. Recently, with the advent of 3D velocimetry, is it possible to directly measure all three coordinate velocities along with the Reynolds stresses. As previously discussed, acoustic velocimetry and the high frequency time series measurements they produce can be analyzed for both their mean values and the statistics we derive from the individual measurements, as well as turbulent scales revealed from spectral analysis.

Along with the doctoral thesis reported by Blanckaert, this is the only study to measure 3D flow in a river bend over a developed sand bed. Velocimetry in that study was done through the use of an ADVP which is similar to the ADV only completely non-intrusive as it operates

through a clear flume wall. Utilizing this technology generated a high density of point measurements, but for only one cross-section of the flow.

In this thesis, 13 streamwise cross-sections with 5-12 measurements at each of 5 vertical profiles or plan points are examined for a total of 609 measurements throughout the entire bend. The research of Blanckaert studied only a small window in the outer half of one cross-section in the bend, which did not include near bed measurements. However, a high planar resolution of measurements was made in that small window. The experimental setup used by Blanckaert is shown in Fig. 2-20. The similarity with the experiments reported for the present thesis lies in the use acoustic velocimetry, and more importantly the ability to measure Reynolds stresses directly.

Literature	Cross section and channel bed	Planform	Flow regime	Size of measuring grid (approximately)	Number of vertical profiles in outer-bank region	Flow and turbulence measurements
Rozovskii (1957)	Rectangular: smooth bed rough bed Triangular	Single bend, 180°	Transition Rough turbulent Transition	$H/7 \times B/8$ $H/7 \times B/8$ $H/7 \times B/4$	2 2 1	v_s, v_n
Götz (1975)	Rectangular smooth bed	Single bend, 180°	Transition	$H/5 \times B/10$ (denser near banks and bottom)	2, 3, 4, 5 (for aspect ratios of 20, 10, 4.6, 2.9)	v_s, v_n
de Vriend (1979)	Rectangular smooth bed	Single bend, 180°	Transition	$H/10 \times B/10$	3	v_s, v_n
de Vriend (1981)	Rectangular rough bed	Single bend, 180°	Rough turbulent	$H/10 \times B/10$	3	v_s, v_n
Siebert (1982)	Rectangular smooth bed	Single bend, 180°	Transition	$H/5 \times B/4$ $z/H = 0.09, 0.66 \times B/3$	3 2	v_s, $\overline{v_s v_n}$ v_s, $\overline{v_j' v_k'}$
Dietrich and Smith (1983)	Natural topography; sand bottom	Meander, field study	Rough turbulent	$H/6 \times B/13$	<10	v_s, v_n
Steffler (1984)	Rectangular smooth bed	Single bend, 270°	Transition	$H/10 \times B10$ (denser near bottom)	2	v_s, v_n, $\overline{v_s'^2}$, $\overline{v_n'^2}$
Anwar (1986)	Natural topography; sand bottom	Single bend, 35°; field study	Rough turbulent	$H/4 \times B/15$	<7	v_s, $\overline{v_j'^2}$ $\overline{v_s' v_n'}$, $\overline{v_s' v_z'}$
Odgaard and Bergs (1988)	Natural bed topography, fixed inclined banks; sand bottom	Single bend, 180°	Transition	$H/10 \times B/8$	1	v_s, v_n
Muto (1997)	Rectangular smooth bed	Meander	Transition	$H/10 \times B/10$	5	v_j, $\overline{v_j' v_k'}$
Tominaga et al. (1999)	Rectangular smooth bed + different configuration with vegetation	Single bend, 60°	Transition	$H/10 \times B/18$ (bend outlet section) $H/5 \times B/18$ (other sections)	6	v_s, v_n, v_z
Present study	Natural bed topography, fixed vertical banks; sand bottom	Single bend, 120°	Rough turbulent	$H/22 \times B/33$	65	v_j, $\overline{v_j' v_k'}$

Note: H = averaged water depth; B = channel width; z = distance above bed; outer-bank region = region extending $2H$ from outer bank; v_j ($j = s, n, z$): mean velocities; $\overline{v_j' v_k'}$ ($j, k = s, n, z$): turbulent correlations.

Figure 2-19. Summary of experimental research on flow in open channel bends as printed in Blanckaert and Graf (2001)

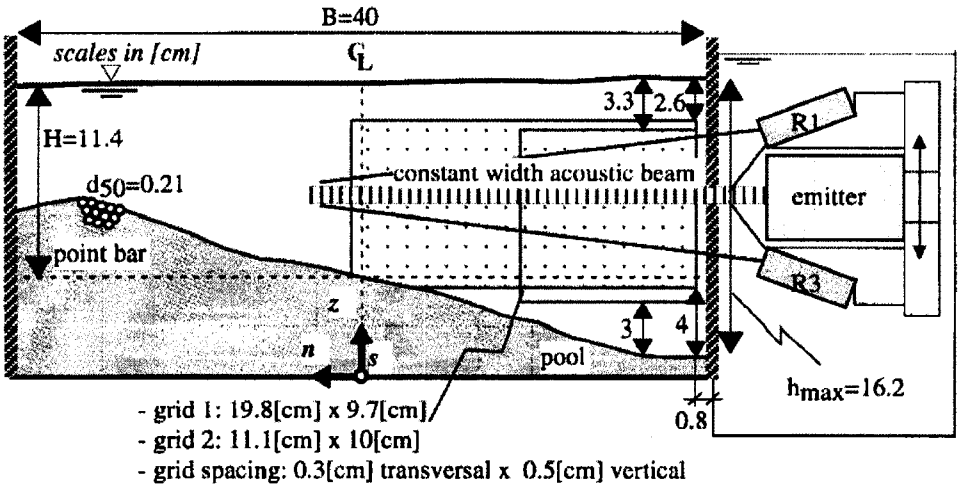

Figure 2-20. Definition sketch of experimental setup used by Blanckaert (Blanckaert 2003)

In the six years subsequent to the first and only reported experiment in 1999, Blanckaert published a host of papers, all of which form chapters of his thesis. In these chapters, bend specific topics of acoustic velocimetry, mean-flow and turbulence, secondary flow, momentum transport, turbulence structure, and turbulence characteristics are completely discussed, as well as analyzing the contribution to numerical modelling development his results provide.

It is noteworthy also that based on those experimental results, the first non-linear model to predict flow in the center cell region was proposed. The basis is the idea that advective momentum transport by the secondary circulation is a dominant mechanism with respect to the downstream velocity distribution. The hypothesis is then that advective momentum transport by the center-region cell causes an increase of downstream velocity in an outward direction and the flattening, or decreasing in the upper part of the downstream velocity profile and increasing lower portion. The outer-bank cell presumably prevents the increase in flow outward from impinging onto the outer bank. Thus, this additional cell stabilizes a region in between the outer bank and the center-region cell thereby keeping the core of high velocity at some distance from the outer bank (Blanckaert 2003). Note that these conclusions, especially the tendency of vertical downstream velocity profiles to flatten, are a function of the limited area with which the measurements took place.

Note that no debate is offered here as to the validity of results made therein as it is beyond the scope of this thesis to analyze and compare the results of these experiments completely considering the numerical simulation required. In the first of this series of papers produced by Blanckaert (Blanckaert and Graf 2001), however, a series of conclusions were made based on their initial findings as follows:

1. In the outer half section, the downstream velocity is higher than that for the straight channel flow. The core of maximum velocity is found well below the water surface in the outside of the bend.
2. The pattern of cross-section velocities contains two circulation cells seen in Fig. 2-18.
3. The magnitude of the principal Reynolds stresses are low in the outer bank region compared with straight channel flow resulting in outer bank shear stresses being lower than expected
4. Both the outer-bank cell and the reduced turbulent activity have a protective effect. The outer-bank cell keeps the core of maximum velocity away from the bank, whereas the reduced turbulence results in a reduced outer-bank shear stress.

These conclusions are useful for initial comparison and validation of Blanckaert's results to the present study. Before making any deductions about flow phenomena, however, the first step is to show that the measurements made are acceptably accurate. With that accomplished as a focal point of this thesis, and having produced a large volume of time series measurements, conclusions can be comfortably made.

In conclusion, this study is the first laboratory study looking at the 3D distribution of Reynolds stress throughout a model river bend using ADVs. A focus will be made in this thesis to prove the validity of the results through analysis of the time-series velocity measurements to determine whether the data commensurate of further analysis. Also, because these experiments are the first produced with the flume developed for this thesis, comments will be made on the performance for future research.

Chapter 3 Methods

3.1 Experimental Plan

Two experiments in a long duration study examining the distribution of Reynolds stresses at varying rates of sediment transport have been completed for this thesis. Keeping a constant depth of 0.2 m for both experiments, channel slope was varied to alter the rate, and regime of sediment transport. The first experiment was conducted at a slope of 0.044% which for the sediment size of 1.1 mm lies directly on the Shields curve (Fig. 2-8) and resulted in clear-water scour conditions. For the second experiment, channel slope was increased to 0.064% resulting in live-bed conditions. Clear-water scour conditions are those for which the structure alone causes local scouring in the bend, and few grains move in the straight approach. Live-bed scour conditions occur when critical shear for the bed material is exceeded, and thus transport exists throughout the entire channel which requires sediment recirculation for these experiments.

For the first experiment a total of 609, two minute ADV measurements and 2773 points measurements of the bathymetry throughout the bend were made producing a large amount of data. The second experiment was intended to analyze the predictive methods for channel slope used for both experiments, as well as to examine the performance of the more complicated sediment recirculation system. No velocity measurements were taken during the second experiment. More discussions on this matter are offered later in the results chapter.

3.2 Apparatus

For the purposes of this study and future research, the construction of a river bend model has been completed. With the original planform dimensions and initial strength calculations of the model completed by Dr. Rennie, all design and manufacturing were completed by the author with the assistance of the combined Mechanical/Civil Engineering machine shop at the University of Ottawa. To ensure reproducibility of these experiments a detailed look into procedures for proper use is thus included. While fundamentally based on other flumes developed at the University of Ottawa, this tilting flume is significantly larger and more adjustable than its predecessors.

The primary design considerations were total cost of the system, the availability of space, and the pumping capabilities of the lab. Through using a combination of demolition, adaptation of existing infrastructure from decommissioned apparatus and available scrap materials, initial material cost was kept to a minimum and useable area was reclaimed. Also, precisely manufacturing the large-

scale flume required extensive adaptation of materials, equipment, and build techniques. In this thesis, design and manufacture details will only be included for aspects relevant to this study.

The sole structural component of the flume body is acrylic sheet (Plexiglas and Lexan). This material was chosen to ensure optical visibility at any point along the length of the flume. For sediment and turbulence research in open channel bends, this visibility offers an exceptional look into the transport processes and mechanisms, as well as providing a convenient method of non-invasive measurement of water depth at all points along the channel. A unique sediment re-circulation system was also developed to enable testing scenarios in live-bed conditions, which for open-channel bends there is a noted absence of in the literature. Under live-bed conditions this optical visibility is especially advantageous for watching transport processes occur.

The primary intent of these experiments is to study turbulent structures within sand bed channel bends at equilibrium conditions using acoustic velocimetry. The test channel was also designed to accommodate follow-up on recent "stream-barb" research conducted at the University of Ottawa (Minor et al. in press; Townsend and Matsuura 2004), as well as work in the emerging field of turbidity currents. An overall view of the test channel is shown in Fig. 3-1.

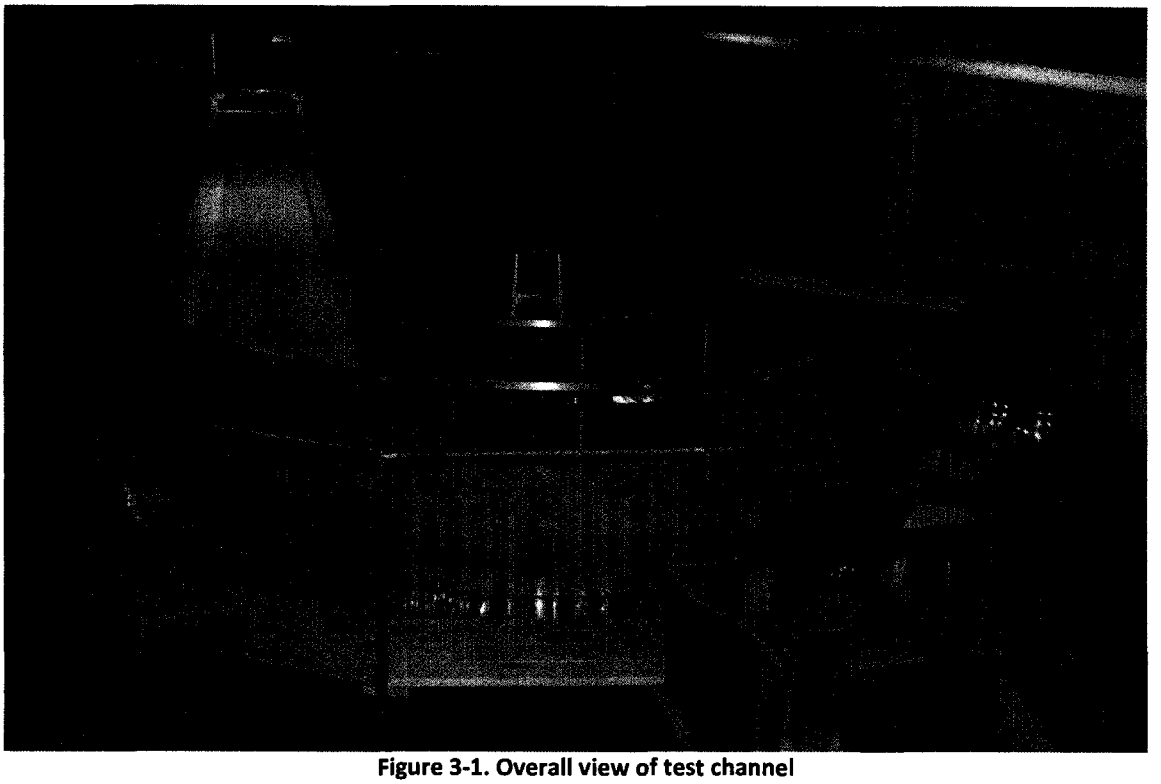

Figure 3-1. Overall view of test channel

3.2.1 Determination of Flume Dimensions

3.2.1.1 Width and Depth

Given the available space in the lab, a reasonable starting point was to select a flume width, w, of 1 m. With this width, a flow depth, h, for these tests was chosen to be 0.2 m, giving a width to depth ratio (w/h), of 5:1, and a hydraulic radius, R, of 0.143. This 5:1 ratio is considered to be a threshold value above which, results are more applicable to river engineering where w/h ratios are typically large. The selected depth was a trade-off between large w/h ratios for physical modelling of a river bend and sufficient depth for turbulent velocimetry. The sample volume for ADV measurements is located 0.05 m below the emitting transducer, which needs to be submerged approximately 7-10 mm for proper operation. Consequently, this will inhibit the accurate determination of the velocity profile over the upper 30% of the flow at the design depth of 0.2 m, which is equally important for turbulence measurements.

Given a 0.2 m flow depth being taken as the constant flow depth for these studies, and considering expected scour volumes based on previous research, a bed depth of 0.3 m was chosen. Now with 0.5 m total depth, an additional freeboard of 0.4 m is added to the flume wall for a total of 0.9 m. This added depth was selected to allow maximum flexibility of the system for other studies such as recently proposed turbidity current experiments. Figure 3-2 is a modification of the drawing used for the cross-sectional dimensions of both the bend and straight sections.

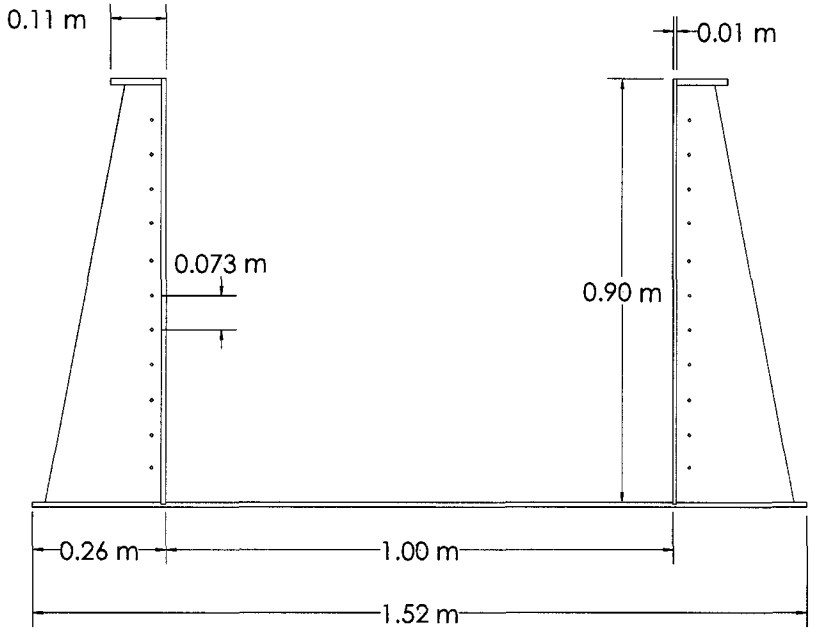

Figure 3-2. Cross-sectional dimensions (not to scale)

3.2.1.2 Planform Dimensions

For tests under uniform flow conditions, we need to allow development length for a turbulent boundary layer to form before entering the bend; for which a straight "approach" section is chosen. As outlined in the discussion on turbulent boundary layer development (Section 2.3.5) we introduced several reported estimation methods for development lengths. By the hydraulic radius relation outlined in Simons and Senturk (1992); for $R = 0.143$, minimum development length calculated using this relation, $l_{(1)min}$, is over 45 m. On the other extreme, the minimum development length based on experience and modelling is a more reasonable value of $l_{(2)min} = 40h$ results in a much lower estimation at 8 m which is acceptable for these tests. If future work is considered, and the fact that a flow depth of 0.3 m or more is advantageous for ADV measurements, 12 m of approach length would be required by this same deduction. With the availability of an existing 12.192 m (40 ft) tilting platform, a straight approach of the same length was selected. This comparison is shown in Table 3-1.

Table 3-1. Boundary layer development length calculations

h (m)	R (m)	$l_{(1)min}$ (m)	$l_{(2)min}$ (m)
0.2	0.143	40	8
0.3	0.188	60	12

For the bend section, a constant curvature bend with a centerline radius, r, of 1.5 m was chosen due mainly to space limitations. This gives a radius to width (r/w) ratio of 1.5, and radius to depth (r/h) ratio of 7.5 which is tighter than most natural river bend formations. Also, with a w/h ratio of 5, the flume is much narrower. In a wide bend with developed bed topography, however, the deepest part of the bed is in the outer portion of the flow, which consequently contains a majority of the flow (Odgaard 1984). To enable comparative work with previous research, a 135° bend section was chosen. The bend section is comprised of three separate 45° sections to enhance future adjustability.

Following the bend sections is a 2.4 m (8 ft) straight exit section. The use of an exit section allows the shear stress distribution to return to its centerline values; where, in theory, another bend of opposite sense would begin, ensuring the accurate representation of a river bend.

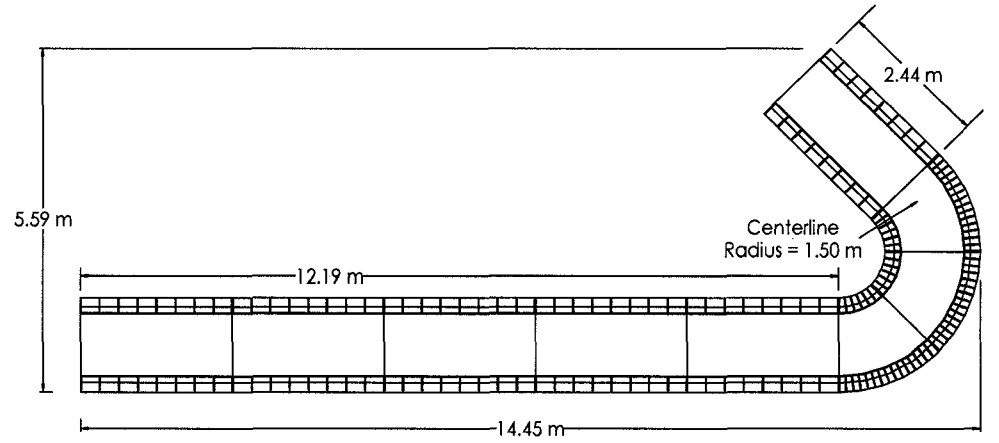

Figure 3-3. Planform flume dimensions (not to scale)

Shown in Fig. 3-3, the flume is 18.2 m in centerline length, with a 12.2 m straight approach section, followed by 135° bend section with a constant radius of 1.5 m, and lastly, a straight 2.4 m exit section. Again, cross-sectional dimensions are 1 m wide and 0.9 m deep including a sand depth of 0.3 m. For details on how to adjust the slope of flume, refer to Appendix A.1.

3.2.2 Selection of Sand Bed Material

Past sediment transport experiments conducted at the University of Ottawa used raw sand dredged from the Ottawa River which was laboriously sieved to specific grain size distributions. To save time, commercially available silica sand with an already determined grain size distribution (Fig. 3-4) was selected with a D_{50} of 1.1 mm. One particular important oversight was the shape of the grains. Using the Powers (1953) roundness index reference chart (Pye 1994) the Ottawa River fluvial is well-rounded and highly spherical, while silica particles are very angular with low spherity. These angular particles are more indicative of material recently weathered from a hill slope, which would normally occur in mountainous areas.

3.2.3 Flow Control and Measurement

3.2.3.1 Flowrates

The design of flowrates for these studies is bound by the flow depth with which we conduct the tests. Because we are keeping depth constant at 0.2 m, we can increase bed shear by increasing the slope and consequently the velocity and flowrate. The control structures and specifically the V-Notch weir were designed to manage the given flowrate. Through the estimation methods detailed in Section 3.3.2, a maximum expected flow rate of 0.085 m^3/s was determined.

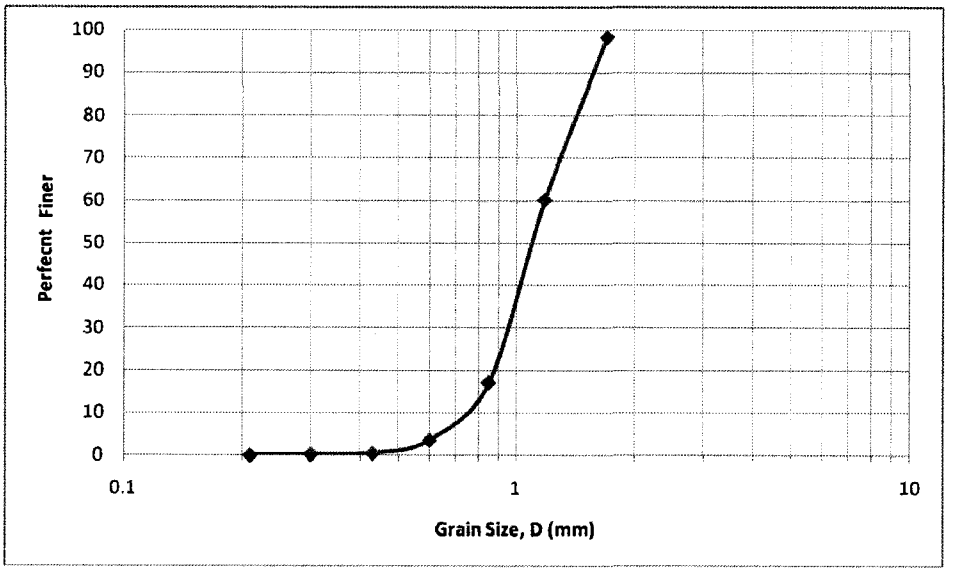

Figure 3-4. Grain size distribution for Granusil 2075 silica sand

3.2.3.2 Fresh Water Supply and Inlet Tank

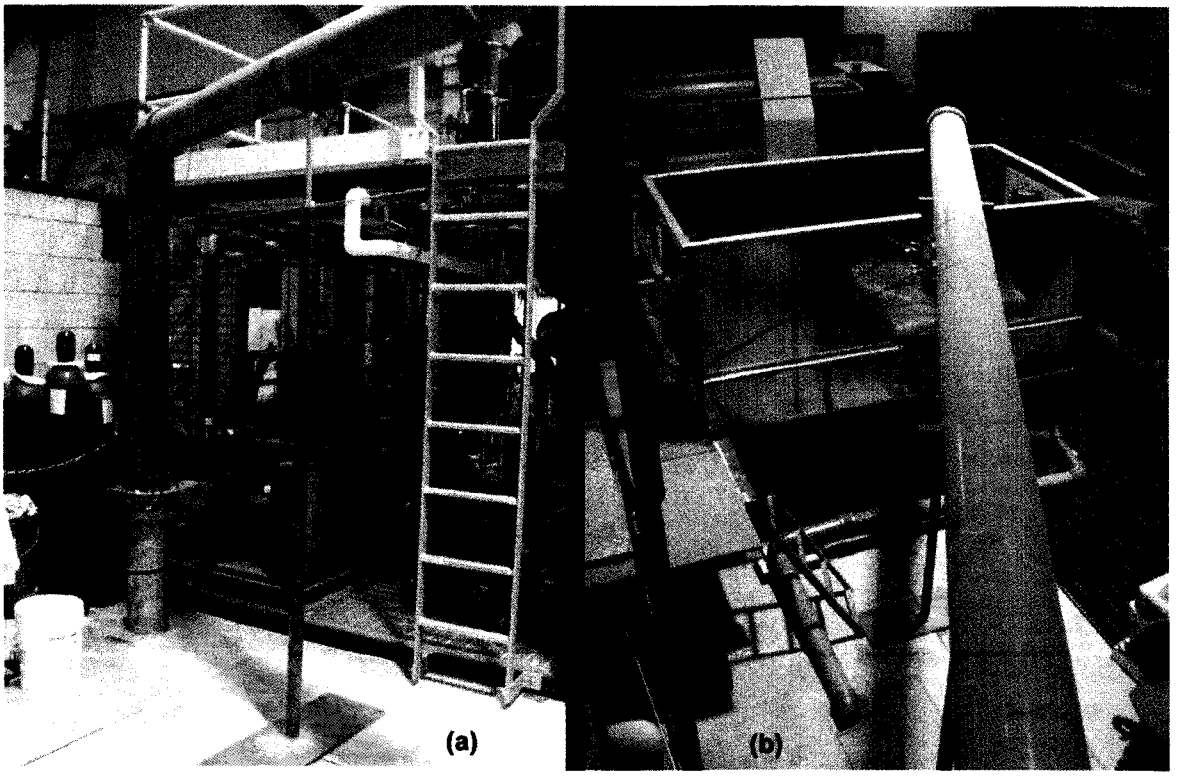

Figure 3-5. Water supply system: (a) existing water supply control valve and (b) bird's eye view of delivery system into inlet tank

Water is supplied to the flume via a 90 hp low-head centrifugal pump draws from a 300 m^3 sub-floor reservoir, delivering a maximum flow of 0.315 m^3/s, at 18.3 m of total dynamic head. Shown in the highlighted portion of Fig. 3-5a, the butterfly valve used to throttle flow for the 20. 3 cm (8") Schedule 80, Polyvinylchloride (SCH-80 PVC) delivery line is shown, as well as the vertical supports manufactured to support the horizontal delivery line. Figure 3-5b shows an aerial view of the inlet tank from the view of the supply line. The supply line and inlet tank structures were manufactured entirely from materials salvaged from past tests. Information on proper filling procedures have been documented in Appendix A.2

The inlet tank was manufactured by welding together a large aluminum tank, with dimensions of 1.22 m x 2.44 m x1.22 m (width x length x depth) on top of a smaller 1.22 m x 0.91 m x 0.91 m tank and is shown in Fig. 3-5b. In Fig. 3-6b, we show the T-shaped, perforated diffuser which is situated in the bottom of the tank, and the end of the distribution line. By utilizing the extra depth, entrained air is expelled, and the flow is allowed to stabilize. The highlighted region in Fig. 3-6a shows the drain valve on the PVC drain line. The entrance drain is located behind the supply line in Fig. 3-6b. The ball valve is used to drain the tank after tests, but more importantly to have slightly more control over the flow rate during the establishment of uniform flow. Ideally a gate valve would have been installed, but the excessive cost forced the use of the already available ball valve.

To further aid in the reduction of turbulence as the flow enters the test channel, a screen was fabricated to stabilize the flow (Fig 3-6c). The blue material is a 100 mm thick economy air filter made from natural fibres and is known as a "Hogs hair filter" by suppliers. It is attached with brass wire to a coarser stainless steel mesh (hidden in figure), all of which is supported by an aluminum frame welded from 38.1 mm (1.5") equal-leg angle.

Figure 3-6. Inlet tank details (a) overall view (b) perforated diffuser in bottom of tank (c) flow settler

3.2.3.3 Bend Section Drains

To eliminate the problem of temporary high shear events when draining the flume, a series of drains were installed in the bend section. Upon shutting down the flume, increases in shear stress past testing levels often occur. Shown in Fig. 3-7, these drains will help draw the water through the column of water ensuring established bedforms and bathymetry remains intact.

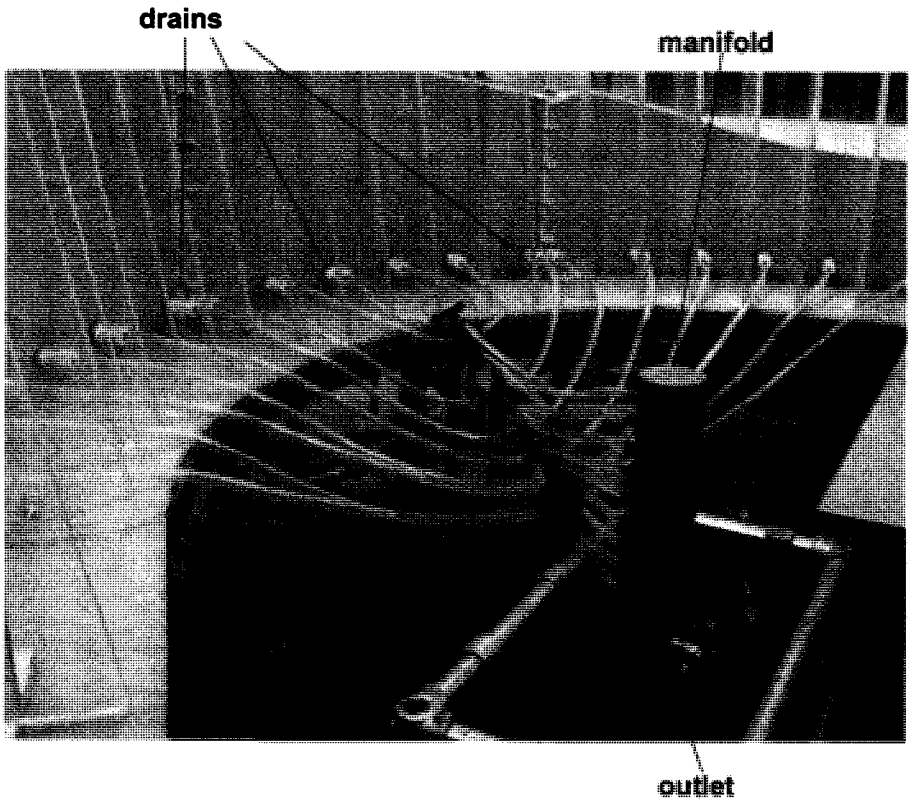

Figure 3-7. Bend section drains

3.2.3.4 Exit Gate

The most challenging portion of the build was the exit gate. As Fig. 3-8 shows, this gate is essentially two separate gates. The upper gate is intended for coarse flow adjustment, and the lower sluice gate is dual-purpose for downstream control of bed level as well as fine flow adjustments. The upper gate is controlled by an electric linear actuator and the gate rotates about a shaft to which it is bolted. On the other hand, the lower gate moves vertically upward from the bottom, similar to a typical sharp-crested weir.

Using a chain drive system, the gate height is adjusted via the hand wheel shown in Fig. 3-9b. This unique combination-gate design quickly solved the problem of limited space, and the tension-cable support system for the linear actuator which was bolted to the ceiling, outlet tank, and support frame, eliminated the need for a robust frame to support the full force of the flow (Fig. 3-9a).

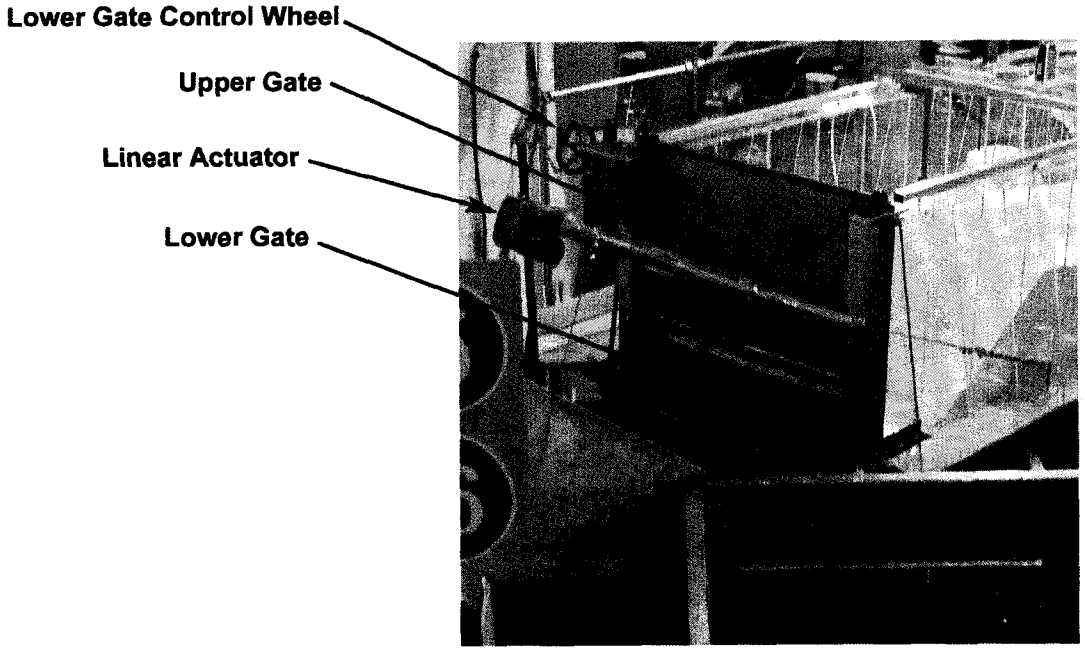

Figure 3-8. End gate overall view

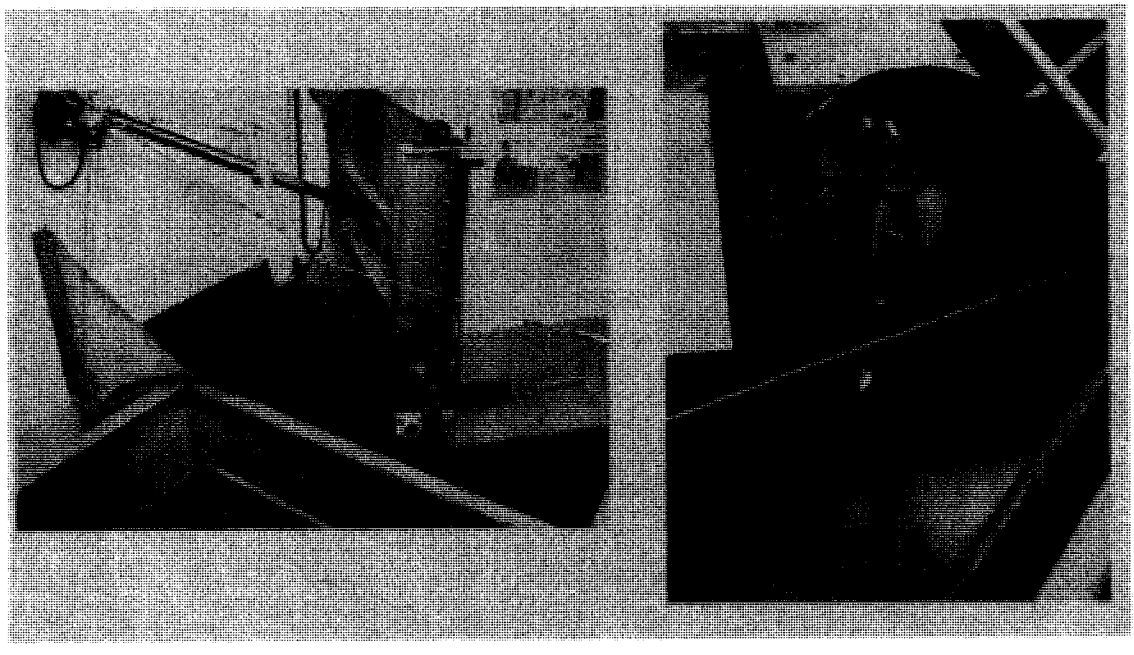

Figure 3-9. (a) Tension cable support system for linear actuator and (b) drive mechanism for bottom gate

3.2.3.5 Outlet Tank and Sediment Recirculation System

The outlet tank was also constructed by modifying existing aluminum tanks, and a two stage tank system was developed. In this case rather than weld the two tanks together, they were bolted due to the extra strength bolting provides over welding given the two tanks butt-up against each other.

The first stage tank measures 1.25 m x 1.83 m x 0.91 m, and is designed to channel sediment toward the submersible slurry pump which delivers the sand-water mix back to the channel entrance. Baffles were welded into this first stage tank creating a sloped surface for which the pump is at the lowest point; it is expected that the water will push the sand toward the pump (Fig. 3-10b). Shown in Fig. 3-10a, the pump is a 10 hp submersible slurry pump, model P-50CS-2 (manufactured by Stancor). Normally intended for use in drilling applications, the recessed impeller of this slurry pump reduces the pulverization of the sand grains. In these long duration tests, if the sediment is mechanically pulverized during the return process, a significant change in the grain size distribution can occur. This design is intended to avoid this source of error.

To ensure that sand was retrained in the first stage tank a stainless steel screen with a mesh size smaller than the smallest grains from the grain size distribution was placed at the entrance to the second stage tank (Fig. 3-10d, e). The details of the stainless steel bolting cloth used for the screen are outlined in Table 3-2. For easy removal, the outer frame is made to fit snugly in the opening between the two tanks, with the outer edge of the frame sealing to the tank wall using water pressure to keep it in place (Fig. 3-10c).

The second tank (Fig. 3-11) measures 2.44 m x 1.22 m x 1.22 m and is designed to first stabilize the flow via the diffuser plate installed in the tank, and secondly to measure the flow rate of the remaining flow that is not removed by the slurry pump in the first stage. This measurement is accomplished through the use of a 90° V-Notch weir. Lastly, a plywood "return box" was constructed to return the flow back to the reservoir. This box posed significant construction roadblocks due to the awkward space it needed to fit into, and the fact that it would be continuously exposed to moisture, which together made joint sealing difficult.

Table 3-2. Sand separation screen details

Wire thickness	0.011	mm
Screen aperture	0.029	mm
Open area	51.9	%

The return line for the slurry pump is constructed from 3" SCH-80 PVC pipe (Fig 3-12). Very near the first stage tank, a removable section of the PVC return line was installed to allow for modifications to the return line for troubleshooting. Here a gate valve was installed to allow for precise throttling of the return flow.

Figure 3-10. First stage tank details (a) submersible slurry pump (b) interior baffles (c) sediment separation screen (d) front side of screen (e) back side of screen

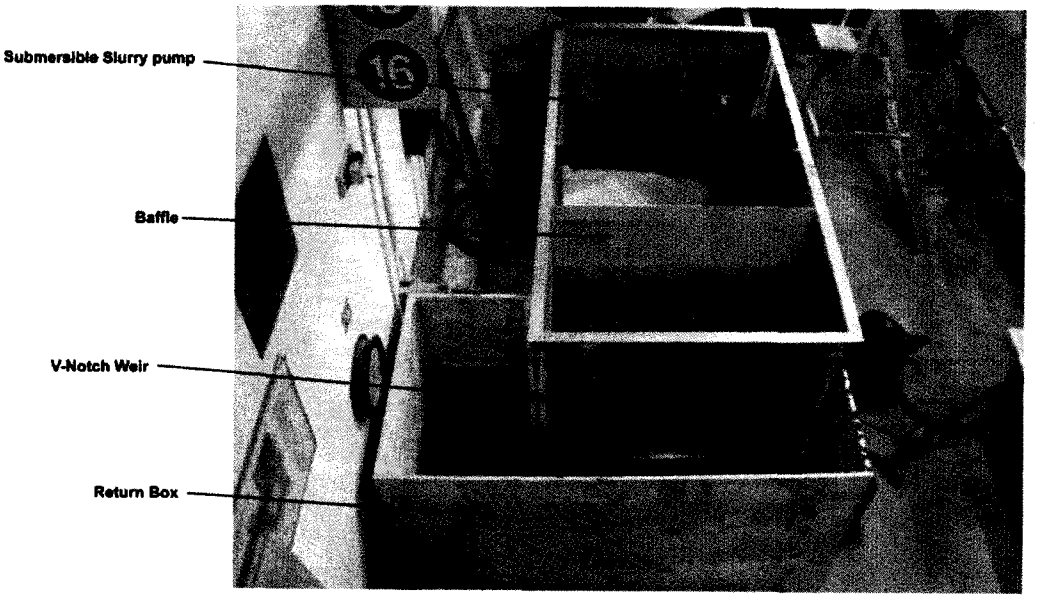

Figure 3-11. Aerial view of second stage outlet tank

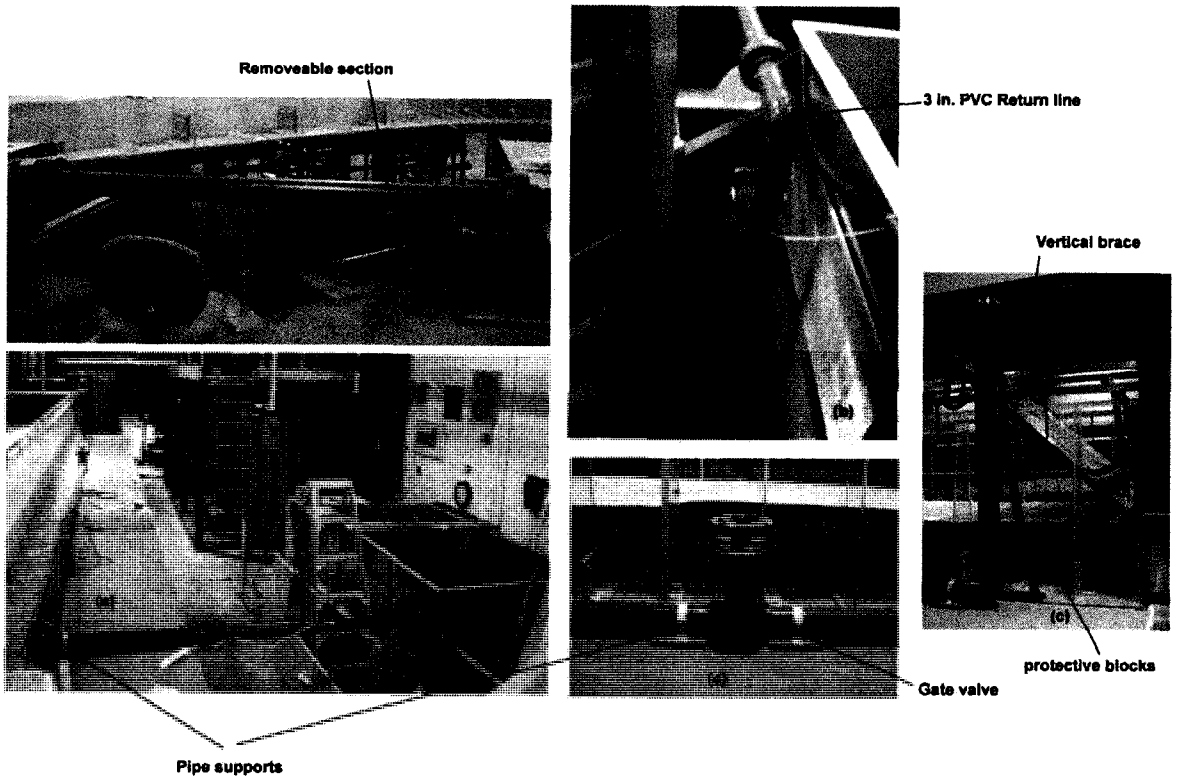

Figure 3-12. Sediment return line details (a) removable section for future modifications (b) return line origin at pump (c) outlet section (d) gate valve for throttling flow (e) overall view

A vertical brace was also installed to eliminate the flow induced moment at the outlet. The design of the "re-introduction" system is also meant to address some of the problems inherent to pumping a sand-water mixture into the flume. Considering the importance of boundary layer development, the system is designed using a reinforced aluminum sheet with 15 mm holes drilled in a grid pattern. Held at an adverse slope to the flow, the sand will be uniformly distributed in the cross-stream as gravity carries it down the sheet and the flow will push the grains through the different openings. This arrangement also helps to eliminate large scale turbulent structures; however, a consequence of the returned flow spraying downward into the main flow is a jet which can scour bed material. To address this issue, a series of cement blocks are placed on a sheet of standard geo-textile and levelled to follow the same slope as the rest of the bed (Fig. 3-12c).

3.2.4 Measurement

The following is a description of the equipment and methods used for all measurements pertaining to the experiments reported here, excluding the TopCon Total Station and equipment rail levelling procedure discussed in Appendix A.1.3.

3.2.4.1 Depth Measurements

Flow depth, h, and the depth of the sand bed, d, are measured through the flume wall using a metric ruler. The clear acrylic walls of the flume prove advantageous as they allow non-intrusive measurement of both the water surface and sand bed elevations at the wall. For more precise measurement of the water surface, a point gauge was fabricated from existing materials for measurements accurate to 0.0001 m. Elevation of the dry sand bed is measured before and after tests using a Leica Systems Disto Pro4a laser altimeter.

3.2.4.2 Flow Measurement

A 90° V-Notch weir was manufactured and installed in the second stage of the outlet tank shown in Fig. 3-13c. Head on the weir is measured with the piezometers installed on the side of the second stage tank (Fig. 3-13d). The United States Bureau of Reclamation Water Measurement Manual (USBR 1997) outlines the geometric requirements for the proper installation of a weir so as to ensure the applicability of empirically derived flowrate relationships or "fully contracted conditions". Due to the limited space for flow development in the outlet tank, a standard weir calibration curve could not be employed. Thus, initial data for a calibration curve for the weir were gathered.

Once established, accurate flow measurement to within ± 2% is possible. For the entries to the calibration curve past and future, a Dynasonics TXFP ultrasonic flowmeter is attached to the fresh-water supply line (Fig. 3-13b), and a record kept over time to include a variety of measurements

for calibration. Flow rate was also measured using the ADVs during the test, and while this represents a more accurate method for measuring the flow rate, it is not possible to do so quickly while uniform flow was being established in the flume. This is especially important for tests when bed shear is below critical values and sediment recirculation is not used. For tests above critical bed shear, or live-bed conditions, the same Dynasonics flowmeter is attached to the sediment return line to measure the input of reintroduced flow. Under these conditions total flow is calculated by the summation of individual flowrates from the main supply line and the sediment return line taken separately.

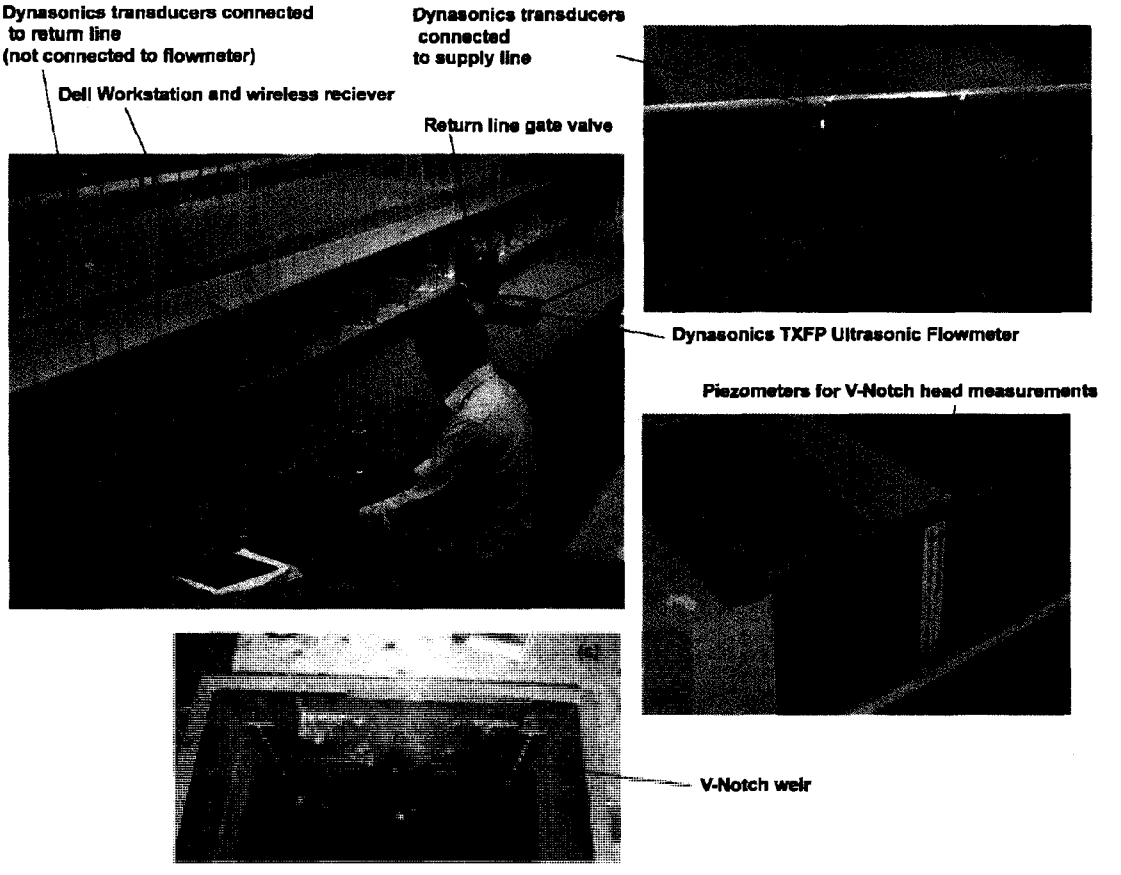

Figure 3-13. Flow measurement details: (a) overall view of set-up (b) Dynasonics transducers connected to supply line (c) V-Notch weir flow (d) Piezometers for reading V-Notch head

3.2.4.3 Acoustic Doppler Velocimeters (ADVs)

Two Nortek Vectrino ADVs were used for velocity measurements. This particular model of ADV addresses some of the issues that arose from the first generation of such instruments (Rusello et al. 2006). Of significance here is the capability of these ADVs to operate at sampling frequencies as high as 200 Hz. The provided Vectrino+ software is used for configuration, data capture, as well as the synchronous operation of multiple ADVs.

A series of preliminary trials using the ADVs in the test channel were completed to determine the optimal configuration for the tests (shown in Fig. 3-14). For these trials, sampling frequency, velocity range, transmit length, sample volume and power level were all varied systematically to find an optimized configuration for high correlation and SNR. Based on past personal work with these sensors a transmit length (or pulse length) of 1.8 mm and sample volume height of 5.5 mm were chosen. For turbulence measurements, the velocity range should be as low as possible to reduce error. For a selected velocity range the maximum vertical and streamwise velocities are displayed in the upper right hand corner of the configuration panel. With approximated streamwise velocities for tests being in the range of 0.5 m/s the ± 0.30 m/s setting for beam velocity was chosen.

Power level gives an indication of the strength of the emitted pulse. Contrary to past work, the high power setting (maximum power) yielded better results in the pre-trials than any other lower power setting. This setting has typically yielded a problematic increase in noise due to acoustic refraction within the water column. Lastly, and most noteworthy in terms of settings, was the effective use of the 200 Hz maximum sampling frequency which consistently returned the highest quality results. By high quality results, we infer that the correlation and SNR remain high while time series data is not spiky.

A Dell Precision Workstation is used for data acquisition and ADV operation. Although synchronization was used for taking measurements to save time during data collection, discussing the specific details of the configuration for synchronous use of multiple ADVs is not specifically relevant to this study, and thus, the reader is directed toward the instruction manual provided by Nortek for information.

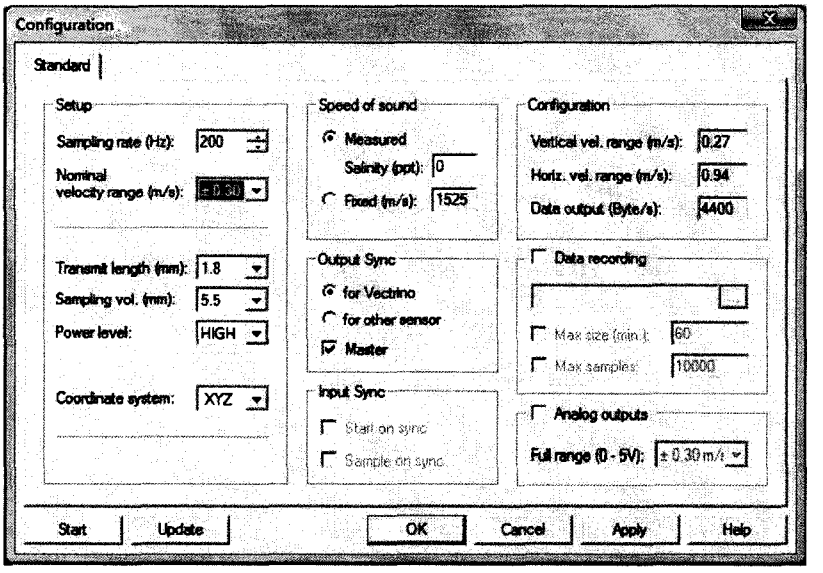

Figure 3-14. Vectrino+ ADV configuration panel

3.2.4.4 Manufacturing Errors in Vectrino Probes

It was noticed during testing that the probe tips for the Vectrino probes are rotated slightly clockwise. It was also noticed that sign convention used for the measurement axis of the probes is incorrect in the manual. The actual coordinate system is the one presented in Section 2.1, it follows that y is positive to the left.

To measure the rotation of the probe tips, a machinist's surface plate was used. The purpose of the surface plate is to have a very precise flat surface to work from. Each of the Vectrino probes has two flats milled from the Delryn housing for which the ADV can be precisely attached to a carriage. Vernier calipers were used to measure the tip to tip distance, and the ADV was placed on the surface plate. Shown in Fig. 3-15, a precision square was then placed against the probe tips and the skew was measured and rotation angle calculated. The results of these measurements are provided in Table 3-3.

Table 3-3. Rotation of Vectrino probe heads

Probe ID	*tip-to-tip (mm)*	*skew (mm)*	*rotation angle (°)*
N-7059	61.85	0.113	2.658
N-7047	61.31	0.0925	2.194
N-7055	61.44	0.1055	2.497

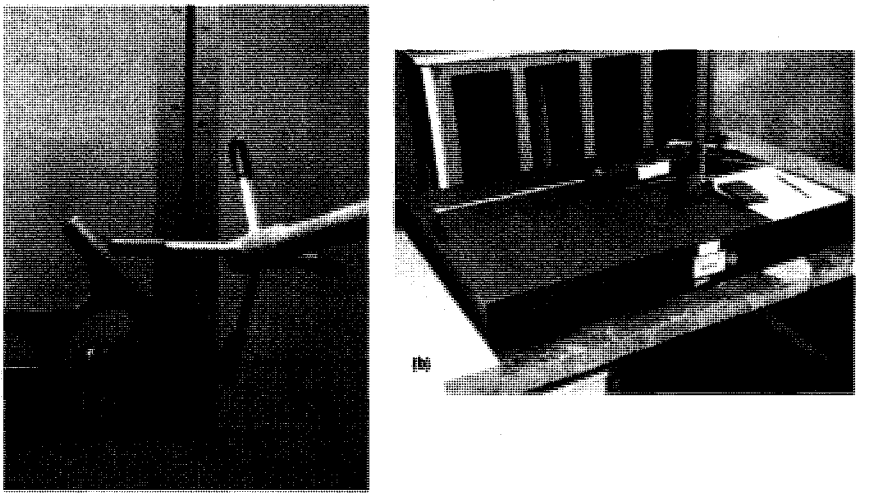

Figure 3-15. Measurement of probe rotation

3.2.4.5 ADV Carriage

For the purposes of carrying out the measurements required for this and other studies, the following is a description of an equipment carriage for three Nortek Vectrino ADVs. Using criteria for both present and future research objectives, a first stage in the development of an optimal configuration is designed.

The primary objective of material and equipment is to be not only accurate, but as sturdy as possible to eliminate error from instrument vibration. Also the carriage needs to have as smooth a movement as possible while keeping overall cost as low as possible. The best solution was determined to be the use of "Extruded Aluminum" components. The primary advantage of the extruded aluminum concept is fully interchangeable connections to enable a multitude of different connection possibilities with one capital investment. Material and connecters were ordered from the 80/20 company (www.8020.net). The main lateral cross-member (details in Fig. 3-16), shown in Fig. 3-17d, is a section of double wide 1530-Lite series extruded bar. The extra width aids in minimizing both overall stability issues and torsion effects from flow induced moment. Vertical members are constructed of 1.5" square 1515-Lite series bar. Linear bearing-brake kits (Fig. 3-17b) allow smooth vertical and horizontal movement and rigidity with the brake engaged. The assembly of the overall system required little machining, however, metric graduations have been engraved on both cross-members and vertical members for accurate location of each ADV. ADV holders were also manufactured with the idea of precise and secure location, with easy use for accurate relocation of the probes between tests (Fig. 3-17d). Plumb for vertical members was checked with the use of a spirit level routinely to avoid vertical error.

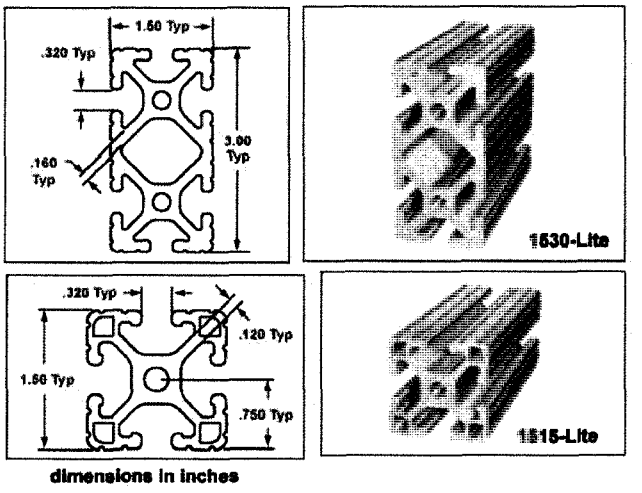

Figure 3-16. Extruded Aluminum details (http://download.8020.net/PDF/Section%209%20Fractional.pdf)

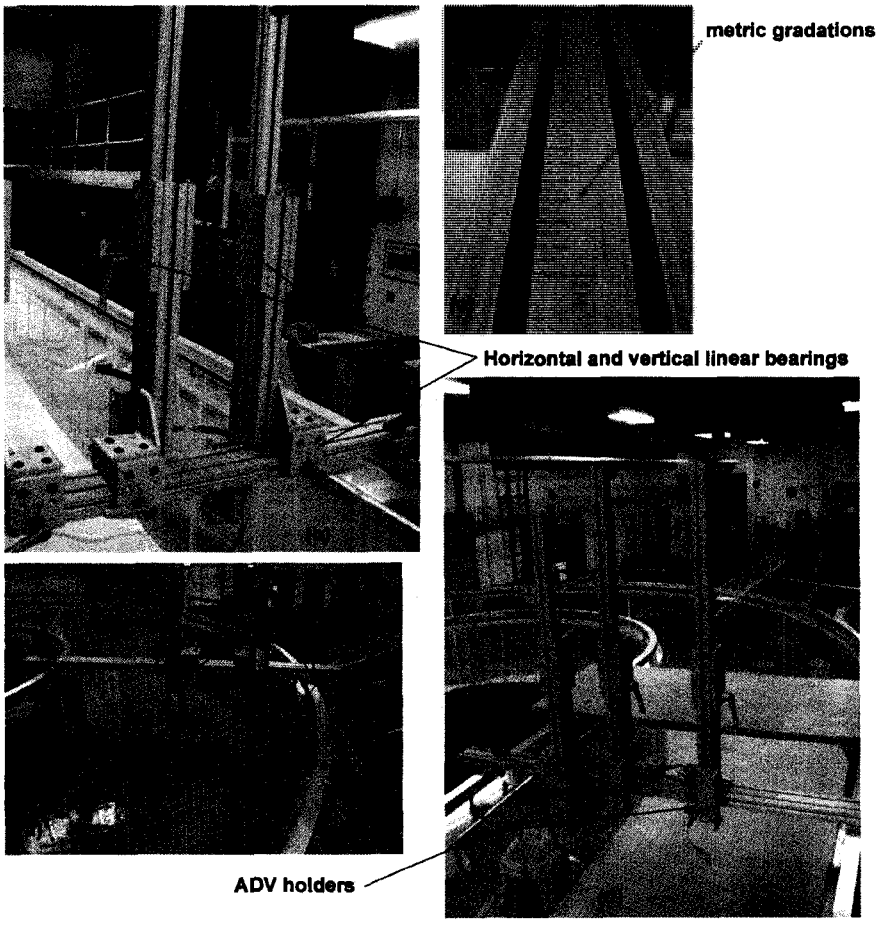

Figure 3-17. ADV carriage details (a) set-up overall view (b) horizontal and vertical connection (c) display of metric gradations (d) front view of carriage

3.2.5 Scaling Details

The most important aspect of a physical model is "similitude" between the model and prototype where the term prototype is given to the natural system which is to be modeled. For a model to be truly representative of the prototype, geometric, kinematic and dynamic similitude must be achieved. Geometric similitude is achieved when the model is geometrically similar to the prototype in that a length ratio, L_m/L_p (subscripts represent model, and prototype, respectively), is maintained for all physical dimensions. Kinematic similitude is achieved when velocities and accelerations are scaled correctly and dynamic similitude is achieved when the forces controlling the model and prototype are identical. Froude scaling is a term given to models in which Froude number is equivalent in model and prototype. These tend to be large scale models in which inertial forces caused by gravity control flow behaviour. On the contrary, smaller scaled models in which surface tension and viscosity control flow behaviour are termed Reynolds models. Froudian similarity is achieved when,

$$\left(\frac{V}{\sqrt{gh}}\right)_m = \left(\frac{V}{\sqrt{gh}}\right)_p \tag{3.1}$$

For the case of more complicated sediment transport models, the Shields' curve (Fig. 2-8) is used as it is assumed that a point on the curve fully describes the characteristics of a given flow with respect to the sediment transport, bedforms and resistance (Prashun 1992). Sediment similarity is assumed satisfied if $(R_*)_m = (R_*)_p$ or,

$$\left(\frac{U_* D_{50}}{\nu}\right)_m = \left(\frac{U_* D_{50}}{\nu}\right)_p \tag{3.2}$$

It is important to note that sediment similitude comes at the cost of dimensional similitude as channel roughness changes with factors such as bed load, formation and movement of bedforms as well as scour and deposition. However, by using Fig. 3-8 it is possible to achieve the same incipient motion in model and prototype. Table 3-4 gives a summary of the scaling considerations for the model used in this thesis.

For the 1 m channel width and 0.2 m flow depth, the dimensional scaling ratio of 5 gives a 5 m wide prototype with 1 m flow depth. Also the selected grain size of 1.1 mm is scales using the Shields' curve to be 5.6 mm.

Table 3-4. Summary of Froude scaling details

S	0.00044	
D_{50} model	1.1	mm
scale ratio	0.2	
model width	1	m
model depth	0.2	m
prototype width	5	m
prototype width	1	m
n prototype	0.02	
Q prototype	4.19	m^3/s
V prototype	0.84	m/s
Q model	0.075	m^3/s
V model	0.37	m/s
τ_{*c} prototype	0.048	
D_{50} prototype	5.6	mm
R_* prototype	3.65E+02	

3.3 Experimental Procedure

3.3.1 Introduction

The long term objective of this experimental program is to compare the distribution of Reynolds stress at varying rates of sediment transport utilizing multiple ADVs. The procedure followed for two of the first experiments in this long term study are reported here. The first test was run slightly below expected values for incipient motion, or clear-water conditions, and another at a slightly steeper slope resulting in live-bed conditions. For the latter test the sediment carried out of the flume was recycled from the main flow and reintroduced at the entrance of the flume. With flow depth for tests to be maintained precisely at 0.2 m channel slope was the only possible variable if subcritical uniform flow is to be maintained in all tests. The procedure presented here was followed for the two tests completed for this thesis.

3.3.2 Determination of Slope and Expected Flow Parameters

With a channel width of 1 m, a characteristic bed grain size, D_{50}, of 1.1 mm, and an exact flow depth of 0.2 m, the Shields diagram (Fig. 2-8) was used to determine the channel slope, S, for both experiments. First, Fig. 2-10 from Knighton (1998) was used to determine the critical dimensionless boundary shear stress, τ_{*c}, required for the desired regime of sediment transport. For a grain size of 1.1 mm Fig. 2-10 gives $\tau_{*c} = 0.035$ for incipient motion. Because we are interested in clear-water scour conditions, the goal for the first test is to produce slightly less shear than this estimation gives. Briefly, under these conditions, no grains move in the straight approach section, and scour in the bend is due solely to the turbulence created by the structure itself. However, as discussed

in the next section, the silica sand used for these tests is rather angular and it was thought this may require additional shear, so the critical value of 0.035 was used for slope determination of the first experiment.

Now turning to the techniques introduced for the beginning of motion (Section 2.5.1) the following relation was used to determine channel slope from the estimation of τ_{*c}:

$$S = \frac{\tau_{*c}(\gamma_s - \gamma)D_{50}}{\gamma R} \tag{3.3}$$

With this estimation of channel slope Eqn. 2.41 was used to determine the boundary Reynolds number, R_* and then the Shields diagram (Fig. 2-8) was employed to verify the proximity to the curve. In the process the bed shear, τ_o, and shear velocity U_* are estimated, which are useful for validation of the model. After the results from the first test showing only a few grains moving in the straight section this same procedure was also used to determine the slope for the second experiment.

Referring to Fig. 2-8 again, because the second experiment was to be conducted at live-bed conditions, and more specifically plane bed motion, a value of 0.05 was chosen for τ_* which should result in dune formation. Addressed in the discussion chapter of this thesis, calculated results from the first experiment gave lower values for shear than expected. As a result, it was felt that choosing a value slightly higher than expected would verify which measure is indeed more correct. Slope and the other parameters for both experiments are listed in Table 3-5.

Table 3-5. Relevant parameters for experiments based on Shields diagram

Run	D_{50} *(mm)*	*R (m)*	*S*	*Elev. change (m)*	τ_o *(N/m²)*	U_*	R_*	τ_{*c} *(N/m²)*
1	1.1	0.143	0.00044	0.0081	0.622	0.0250	27.46	0.0350
2	1.1	0.143	0.00064	0.0116	0.888	0.0298	32.82	0.0500

With flow depth and channel slope determined, mean velocity and flow needed to be calculated for the proper sizing of the flow supply, outlet control and flow measurement. Because we are ensuring uniform flow, Manning's formula (Eqn. 2.29) was used, however, a value of Manning`s n must be estimated. Based on reasonable values for the model conditions as per Chow (1959), a value of 0.02 for n was selected and compared against the value 0.0134 predicted by Strickler's formula (Eqn. 2.30). This comparison is shown in Table 3-6.

Table 3-6. Flowrate and velocity estimations for Run 1 from Manning's equation

S	*A* (m^2)	*R (m)*	*n*	*Q* (m^3/s)	*U (m/s)*
0.00044	0.20	0.143	0.0200	0.058	0.288
0.00044	0.20	0.143	0.0134	0.085	0.427

It is satisfactory to use the slope determined for the first experiment for sizing the flume. Live-bed testing will employ the use of the slurry pump which draws directly from the outlet tank so any additional flow over roughly 0.075 m^3/s will not be measured using the outlet tank but rather the Dynasonics flowmeter.

3.3.3 Establishment of Test Conditions

Procedural details for filling the flume and the establishment of uniform flow are provided in Appendix A.3 and A.4, respectively. With uniform flow established, and expected rates of sediment transport occurring, the flume bed must now be allowed to establish its equilibrium or developed bed. Generally speaking, the sand is scoured from the outside of the bend and deposited on the inside bend. Eventually, the bed is scoured to an equilibrium shape with no further movement of the grains. This is measured with the use of the small clear ruler placed on the outside wall of the exit section at the point of maximum scour (Fig. 3-18). For the first test conducted under clear-water scour conditions, this took approximately 48 hours. Comments on the second test are made in Section 4.3 this thesis.

Figure 3-18. Measurement of scour at near equilibrium conditions (outer bend wall)

3.3.4 ADV Measurements

3.3.4.1 Spatial Distribution of Measurement Locations

After equilibrium was achieved in the model, ADV measurements were then made. Considering that we are interested in the distribution of Reynolds stress throughout the entrance to the bend, the bend section itself, and the entire exit section, 13 cross-sections were measured. Choosing the resolution of measurements within each of those cross-sections becomes an optimization problem. Considering the work of Blanckaert (2001), an extremely tight resolution of measurements is made in the outer half of one cross-section, and a close look at near wall measurements is made. This is especially useful for turbulence theory, however, maybe not as interesting as the work of Dietrich to sedimentologists or river engineers. For these groups, a wide spatial distribution with a focus on bed shear and near bed measurements is optimal for explaining transport phenomena. Our approach, then, is to try to meet the needs of both groups and produce a multi-use data set for a variety of analyses. Figure 3-19 shows a plan view of all measurement locations or "plan points" along the channel length.

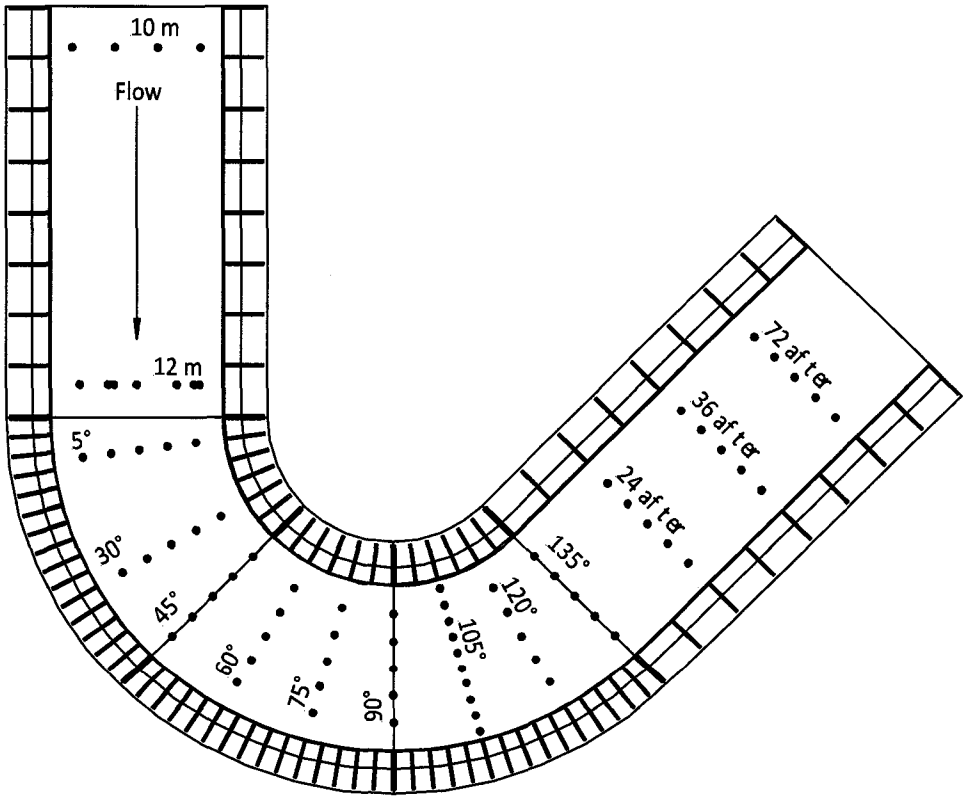

Figure 3-19. ADV measurement locations in plan view

The 10 m cross-section was divided into 4 equal area components for the purposes of accurate flow determination taken at 0.125, 0.375, 0.625 and 0.875 m measured from the right hand channel wall (facing downstream). Cross-sections past 10 m (x-direction) were planned to be divided into 5 lateral plan points again, from the channel right wall, which remained constant. These locations across the channel are at 0.166, 0.333, 0.500, 0.666, and lastly at 0.833 m. A tighter resolution of cross-stream measurements were taken at the 12 m and 105° cross-sections. At the 12 m mark an excess of plan point profiles were measured due to calculation error. This gives an irregular distribution of measurements, but was included to increase accuracy for later interpolation. The spacing at this section was 0.133, 0.166, 0.266, 0.500, 0.633, 0.666, and 0.833 m. The 105° section showed the greatest amount of sediment movement and the steepest cross-stream bed slope, and thus it was assumed that this would be the region with the greatest shear stress and turbulent energy. With 13 cross-sections, there are a total of 77 plan points, and at each plan point a vertical profile consisting of a variable number of measurements was taken.

3.3.4.2 Vertical Distribution of Measurement Points

Determining the spacing for vertical profiles was based primarily on the technique used to determine shear velocity, U_*, and roughness height, k_s, from Eqn. 2.32. For this analysis, velocity profiles are plotted on a logarithmic scale and thus a close spacing of measurements was employed near the bed which gradually increases as we move upward. For example at the deepest point in the bend, measurements were taken at 5, 10, 20, 40, 70, 100, 140, 180, 220, and 260 mm from the channel bottom depending on the depth at that location. Thus, for the straight approach section, which maintained a uniform 200 mm depth, the spacing would be 5, 10, 20, 40, 70, 100, and 140 mm. In addition to this regular pattern, a measurement was taken at the same elevation for all plan points at 60 mm below the water surface. Figure 3-20 shows an example of the vertical spacing of measurements; however, note that this is only an example of spacing. In total there are 609 velocity measurements each lasting 2 minutes, which was chosen to be able to measure the largest expected turbulence scales.

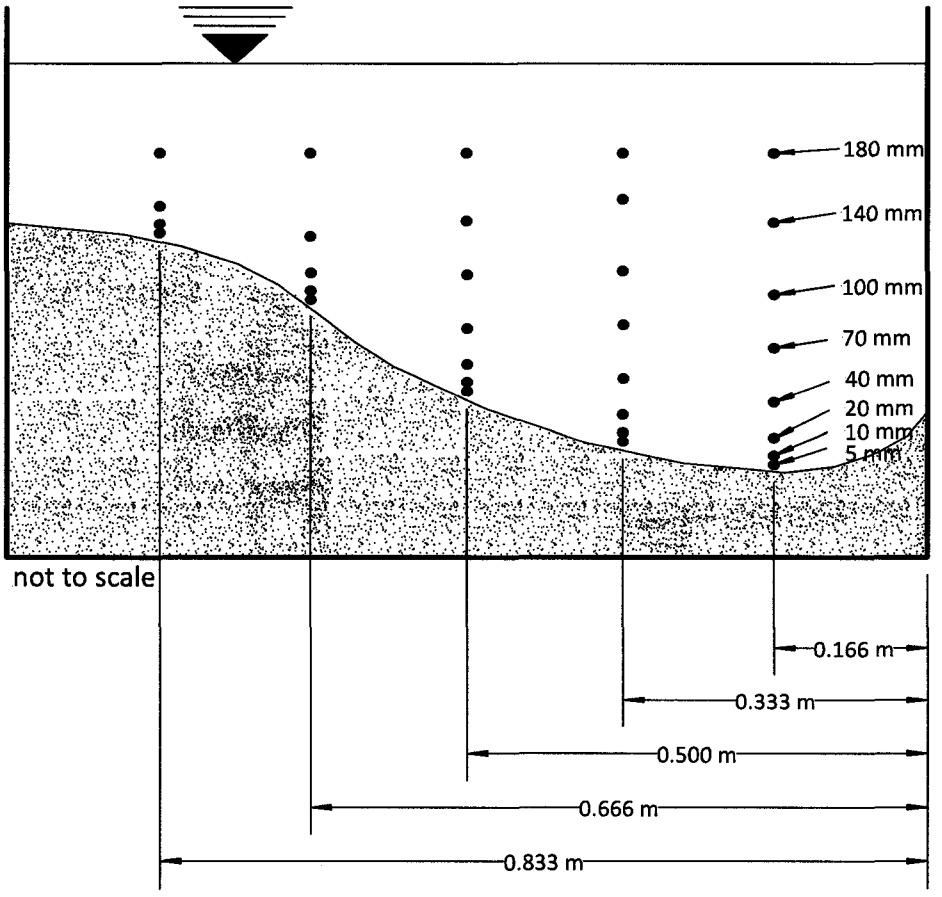

Figure 3-20. Schematic of ADV measurement locations (labels indicate distance from the bed)

3.3.4.3 Measurement Depth Identification

Seemingly straightforward, at times it is difficult to determine instrument height above the sand bed because of the acoustic refraction within the water column. This causes the sensor to show a doubling or halving of the actual depth value at many depths throughout the water column. Therefore, the metric gradations on the equipment carriage should be used in conjunction with the distance check feature of the Vectrino+ software (Fig. 3-21). By deduction, the correct value between the two is maintained. While the scales on the ADV carriage can be used for locating measurements, a more precise approach for computing purposes is done after the bed surface profile is measured. Actual sensor height, z_{abs}, is then located by adding the height of the bed, plus the height of the sensor above the bed. Other useful tips for ADV use are provided in Appendix A.6.

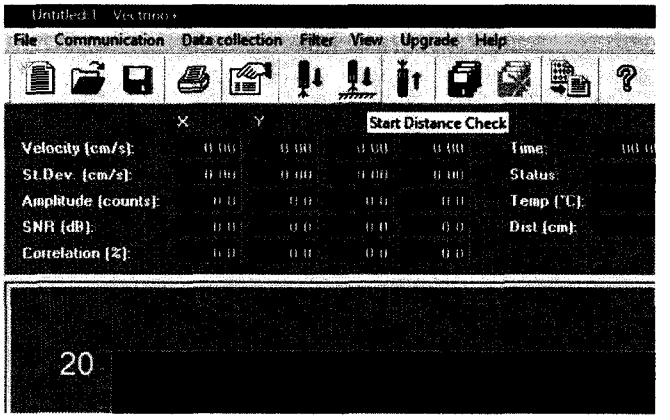

Figure 3-21. Distance check feature of Vectrino+ software.

3.3.5 Measurement of Sand Bed Profile

With the flume properly drained (details in Appendix A.5), elevation of the dry sand bed was measured after the first test using a Leica Systems Disto pro4a laser altimeter. Making a high spatial resolution of measurements in a short period of time is possible with this tool if data are uploaded to a spreadsheet using the provided serial cable and DISTO Transfer-PC software. By configuring the software to trigger the altimeter automatically, and to enter the values properly into the spreadsheet of your choice, the user is left to simply move the altimeter accurately between measurements. The recommended measurement interval is 2 seconds. For the these experiments, a much tighter resolution of bed measurements was made in comparison to ADV measurements because of this fast and easy procedure. In total then, 28 cross-sections were measured at a spacing of 10 mm between each, making for a total of 2772 individual point measurements.

3.4 Data Analysis

This section describes the procedures used to analyze raw ADV data, and the procedures used to interpolate measurements and develop the figures used for discussion in this thesis. First, an examination of the MatLab coding used to calculate mean values and the scales produced via spectral analysis of time series data is made. Also, a look at the interpolation methods used to transform individual point measurements of both bathymetry and velocity measurements into the volumetric representations produced for this thesis will be made. A flowchart summarizing the steps followed in the processing of ADV data is shown in Fig. 3-22.

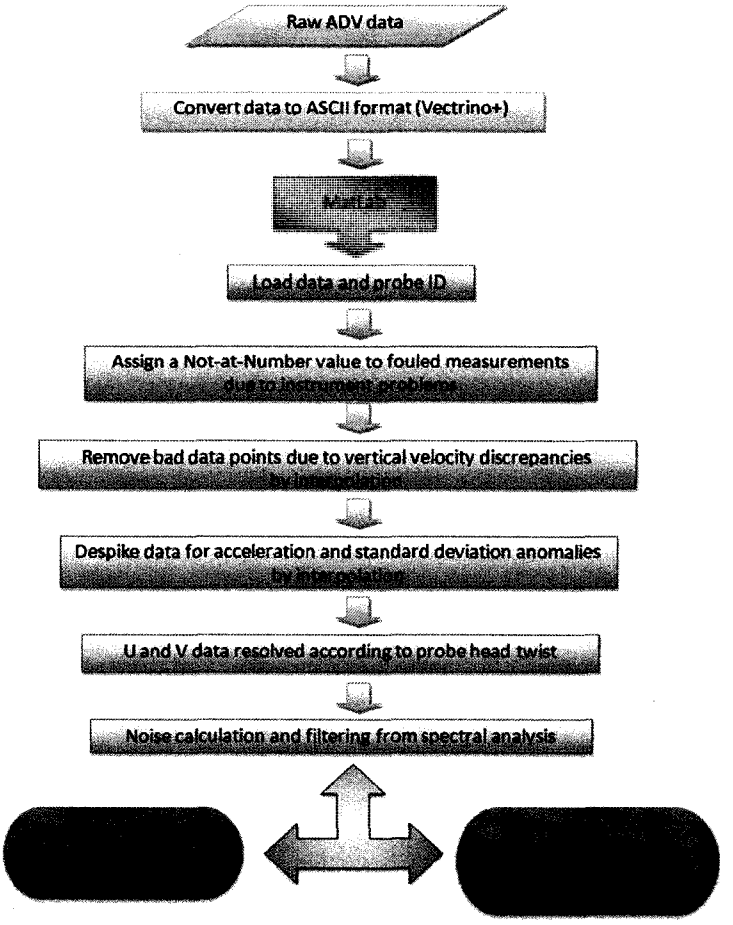

Figure 3-22. MatLab data process flowchart

3.4.1 Conversion of Raw ADV Data for Analysis

Raw time-series data from each of the 609 individual ADV measurements were analyzed using MatLab code. First, however, individual measurements produce files with a .vno extension, which need to be converted into ASCII data files (.dat) using the Vectrino+ software (data collection>data conversion). Note this can be done with a batch of files ensuring before conversion ensure that the velocity time check box is checked as this includes the timestamp for each measurement. The Vectrino+ conversion creates three types of files: an ADV file (.adv), an ASCII .dat file, and a header file (.hdr). While the ADV file is inconsequential to this discussion, the header file contains information about the measurement such as probe ID, probe depth, and water temperature. The MatLab code accesses these header files to pull relevant information from each measurement for analysis.

The ASCII data file which is output from the Vectrino+ conversion is organized into 18 self explanatory columns as follows:

1	Time step	
2	Ensemble counter	
3	Velocity (Beam1|X)	(m/s)
4	Velocity (Beam2|Y)	(m/s)
5	Velocity (Beam3|Z)	(m/s)
6	Velocity (Beam4|Z2)	(m/s)
7	Amplitude (Beam1)	(counts)
8	Amplitude (Beam2)	(counts)
9	Amplitude (Beam3)	(counts)
10	Amplitude (Beam4)	(counts)
11	SNR (Beam1)	(dB)
12	SNR (Beam2)	(dB)
13	SNR (Beam3)	(dB)
14	SNR (Beam4)	(dB)
15	Correlation (Beam1)	(%)
16	Correlation (Beam2)	(%)
17	Correlation (Beam3)	(%)
18	Correlation (Beam4)	(%)

For each two minute time series, with the sampling frequency at 200Hz, a total 23999 individual velocity measurements are taken. To gain perspective on the volume of data, for all 609 time-series, 20.3 hours or 14.6 million individual velocity measurements were made for the first experiment.

3.4.2 MatLab Analysis Procedure

The MatLab coding utilized in this thesis was produced by Dr. Rennie for use in his past experimental work. Several small changes were made to tailor his coding for these experiments, most notably to resolve measurements to account for the discovery of probe head axial rotation.

MatLab works by loading different M-files, which are modules called on by the batch file, which is also an M-file. The batch file "processVectrinobatch" is the main M-file where the list of filenames (in single quotations, one entry per line) is added before execution of the analysis. The batch file then calls on other M-files for various operations, the more significant portions of which are discussed here, and are included in Appendix B.

To load the data from each ASCII file, the batch file assigns a dummy variable name for each column of the data file and analyzes one measurement at a time. With variables loaded, the probe-ID is read from the header file, and the rotation of each head is identified.

The batch file then calls on "processVectrinocore". This initially hides bad data from instrument error by attaching a value of "Not-a-Number" (NaN) to measurements that failed. When a measurement fails due to instrument error a value is automatically entered which makes for easy

removal from time series. In the past Sontek has used a specific value of 3276.7, but also a value of 0 for velocity is any direction is considered bad. Nortek does not use a bad data flag, however, this coding is applicable to all types of ADVs, and was not altered.

For later comparison, the mean statistics introduced in Section 2.6.2 of this thesis are first calculated from the raw data, which requires that the mean values of velocity measurements be calculated. First, with erroneous measurements identified as NaN, the average of both vertical velocity measurements, Z_1 and Z_2, is taken. Next, the mean value of each velocity component $\overline{U_i}$ is calculated from the raw data while ignoring NaN values through the use of the "meanignoringNaN" M-file. The fluctuating component of the velocity due to turbulence, u_i, is also calculated by:

$$u_i = U_i - \overline{U_i} \tag{3.4}$$

and the three components of the Reynolds shear stresses are also then calculated by:

$$-\rho\overline{uw}, -\rho\overline{uv}, -\rho\overline{vw} \tag{3.5}$$

The RMS of turbulent fluctuations for each direction is calculated by:

$$\sqrt{\overline{u_i^2}} \tag{3.6}$$

All three components of relative turbulent intensity are also calculated:

$$\hat{u} \equiv \frac{\sqrt{\overline{u^2}}}{\overline{U}}, \qquad \hat{v} \equiv \frac{\sqrt{\overline{v^2}}}{\overline{V}}, \qquad \hat{w} \equiv \frac{\sqrt{\overline{w^2}}}{\overline{W}} \tag{3.7}$$

The last of these statistics to be calculated is turbulent kinetic energy, k, again introduced in Section 2.6.2:

$$k = \frac{1}{2}\left(\overline{u^2} + \overline{v^2} + \overline{w^2}\right) \tag{3.8}$$

One of the advantages of having two measures of vertical velocity for every measurement is that it provides another good indication of instrument error. Data are now filtered based on the difference between the two simultaneous vertical velocity measurements. If the difference between the two measurements is greater than 0.1 m/s, each of the component velocity measurements are replaced with a value interpolated from the measurement before and after the erroneous value, but in this case it is only for that component of the velocity (Nikora and Goring 1998).

Data are now "despiked", which removes large spikes in the time series which are determined erroneous for several reasons. First, we despike based on acceleration thresholds. Acceleration is calculated by dividing the difference in subsequent velocity measurements by the time-step between them. If this ratio is above $1.5g$ for any coordinate velocity, where g is acceleration due to gravity, then the values are removed by interpolating in the same manner. An example of time series before

and after filtering is shown in Fig. 3-23, which is a raw time series plot from one measurement made for this thesis.

Despiking is also done for those measurements which lie more than four standard deviations away from the local mean. This calls for another M-file "stdignoringNaN", which calculates the standard deviation of each velocity component time series again ignoring NaN values.

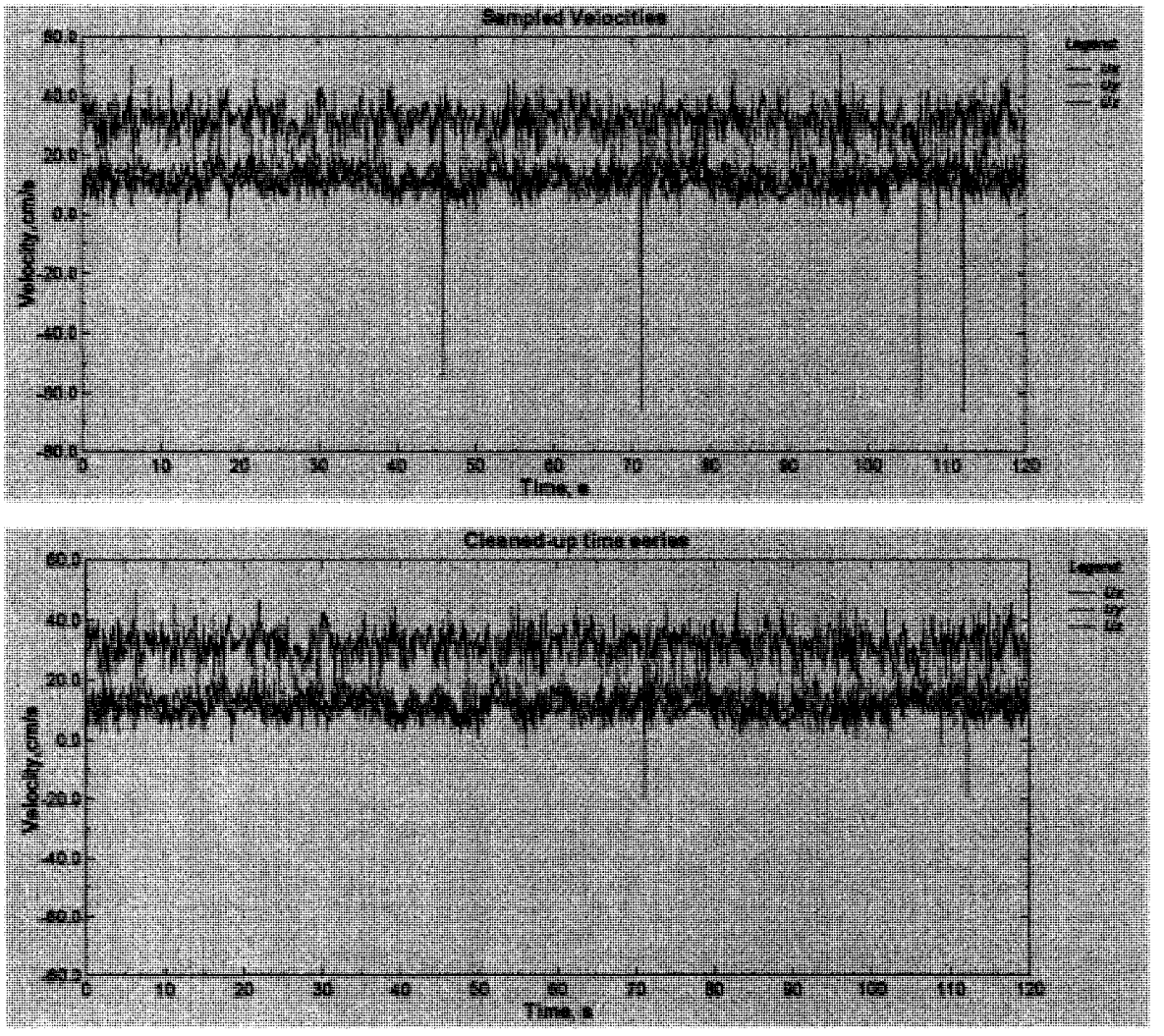

Figure 3-23. Example time series: (a) raw data and (b) after filtering (not rotated)

Vertical velocity is now averaged again from the despiked data, and then streamwise, U, and cross-stream, V, velocity components are rotated based on the twist of the probe head. These data are dubbed "despiked and rotated". The Reynolds stresses and mean statistics are calculated as previously discussed with the despiked and rotated time series and the batch file then calls for the "spectralVectrinofinalfiltnoisebatch" M-file. The concepts used for discussion of this M-file were introduced in Section 2.6.3.

Before the spectral analysis takes place, all NaN values are removed and interpolated by the "interpolateNaN" M-file because spectral analysis requires a complete time series. The spectrum of the time series is then calculated. In utilizing the fast Fourier transform to produce the power spectrum for the time series, a "windowing" method is used to divide the time series into a series of overlapping windows. Here, four "hanning" windows are used. This technique increases the accuracy of the high frequency measurements but reduces the size of the largest eddies which can be analyzed.

A noise level is then fit to the spectrum by first determining where the inertial subrange should be (starting at a safe estimate of 5 Hz) and then fitting a -5/3 slope to it by least squares curve fitting algorithms (Rennie and Hay, in revision). The equation for this sloped line is as follows:

$$S = a f^{-5/3} + n \tag{3.9}$$

Noise, N, in the vertical direction is calculated by integrating over the entire spectrum by the following relationship:

$$N = \sqrt{n \cdot f_{Nyqyuist}} \tag{3.10}$$

Where n is the distance from the fitted -5/3 slope that each measurement falls (noise) and $f_{Nyqyuist}$ is known as the Nyquist frequency. The Nyquist frequency is simply half the sampling frequency, and can be thought of as the largest frequency wave that can be analyzed.

Despiked and rotated data are now filtered based on a noise ratio which is determined as the noise divided by the mean absolute fluctuation in the velocity component:

$$NR = \frac{N}{\overline{|u|}} \tag{3.11}$$

If the calculated noise ratio is higher than 0.75, the calculated Reynolds stresses will likely be biased by noise and a lowpass Butterworth filter is applied.

With data filtered based on the noise ratio cut-off, power spectrum and noise calculations are completed again as well as Reynolds stresses and mean turbulent statistics. If data are not filtered these calculations should match the despiked and rotated data.

The last M-file called by processVectrinobatch is "Vectrinooutput". Here, turbulence scales are calculated from the correlation function introduced in Section 2.6.3.1. First, the correlation function, R is calculated from Eqn. 2.46.

Now, integral time scale, T_E, is calculated by Eqn. 2.47, and micro-time scale, τ_E, by Eqn. 2.42. Also, if turbulent intensity is less than 0.25, integral length scale, L_x, micro-length scale, l_x, and Taylors' micro-length, λ, are calculated by the relationships outlined in Section 2.6.3.1. Each of the component velocities is analyzed separately.

As a final step, processVectrinobatch now writes the results from all calculations to an output spreadsheet, and returns to start the entire process over for the next data file. For all 609 point measurements calculation time was approximately 4 hours using a powerful Dell Precision workstation (2.0 GHz Pentium M processor, 512Mb DDR2 RAM).

A second MatLab code was written to evaluate the quality of the ADV measurements. First the error between the two vertical velocity measurements is computed and averaged for each of the 23999 individual samples in a time series. As well, the average SNR and correlation values are computed for each component axes over the whole time series. These provide important indications of measurement accuracy.

3.4.3 Interpolation Methods

Interpolation methods are used to transform individual point measurements of both bathymetry and velocity measurements into the 3D volumetric presentations produced for this thesis. Surfer™ was used for the interpolation of bathymetry measurements, and Tecplot 360™ for the ADV measurements, and as such will be discussed separately.

3.4.3.1 Bathymetric Data Interpolation

Surfer is a powerful contouring, gridding, and surface mapping package for scientists and engineers capable of producing accurate 3D contour plots. It is used here only for its highly adjustable interpolation parameters available to the user. More specifically we are interested in the ability to control the shape of the variogram used for Kriging. Kriging is a geostatistical technique that will interpolate an unobserved location from observations at nearby locations. This is commonly used in many earth sciences to determine the elevations as a function of the geographic location. Our aim is to interpolate the 2773 point elevation measurements into a finely spaced mesh for use in Tecplot 360 as the boundary surface.

The first step is to determine the variogram for the bathymetric data. The variogram is a measure of how quickly things change on the average. The underlying principle is that two observations closer together are more similar than two observations farther apart. The computed

variograms used for this thesis are shown in Fig 3-24. Note that the variograms shown are only a radial slice of the 3D variogram grid, which can be thought of as a "funnel shaped" surface. This is necessary because it is difficult to draw the three-dimensional surface, let alone try to fit a three dimensional function (model) to it. By taking slices, it is possible to draw and work with the directional experimental variogram in a familiar form.

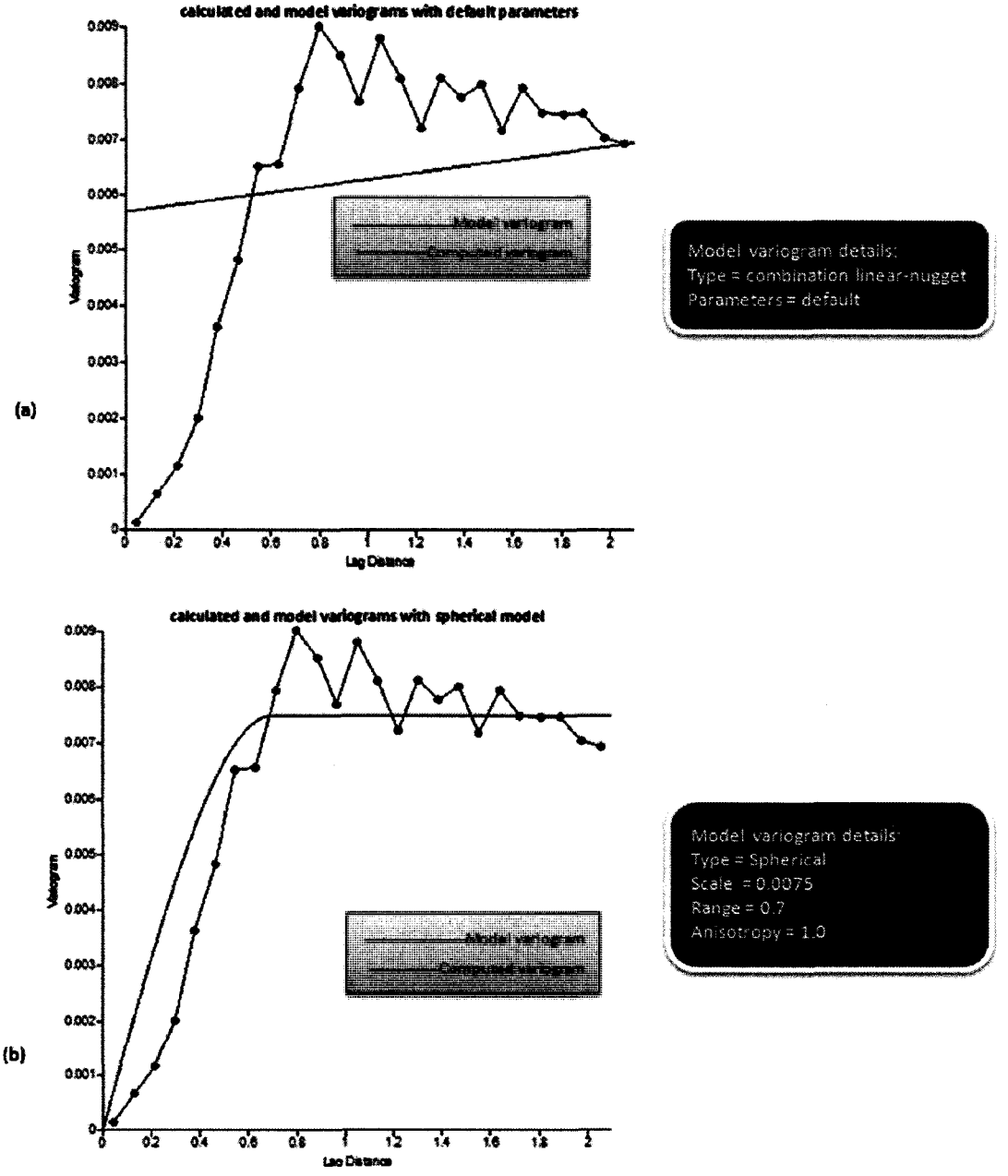

Figure 3-24. Variogram analysis of bathymetric data for Kriging (a) default model variogram (b) spherical variogram chosen for this study

With the experimental variogram computed, a model variogram is chosen which will then be used to execute the Kriging. In Surfer, it is possible to quickly adjust the variogram parameters to assess the fit to computed data. As shown in Fig. 3-24b, a spherical model was chosen which more closely represents the distribution of computed data. In creating a more accurate model, the user defines a variety of parameters that create a better fit.

The Nugget effect is used when error is expected in measurements and is represented by a vertical projection of the *y*-axis intercept of the model variogram (Fig. 3-24a). Specifying a nugget effect causes Kriging to become more of a smoothing interpolator, implying less confidence in individual data points versus the overall trend of the data. The chosen spherical model shows no nugget effect since we are confident in the bathymetry measurements. Next, the slope of the model variogram is altered by the range setting which is set to 0.7 m for our model. Scale changes the vertical scale and is set to 0.0075 m^2 to match computed data. Lastly an anisotropy value is assigned which changes the direction in which data are more likely to be independent. The bathymetric data is indeed anisotropic as you would expect for a river bottom. Streamwise elevation change is much smoother than cross-stream elevation changes. Also a much higher resolution of cross-stream measurements are made than streamwise. These two factors alone would lead to the effective use of anisotropy. However the orientation of these measurements changes in relation to the coordinate axes due to the channel bend. The parameters for the model variogram are summarized in Fig 3-24b.

With the model variogram selected, a grid file is computed from the raw bathymetry through Kriging with the model variogram. A spacing of 20 mm was used for this thesis, as finer grids were too calculation intensive for the computer. Because the developed grid is generated for the entire rectangular area chosen in the gridding options, the area outside of the flume walls now needs to be "blanked".

The blanking process transforms all grid data in a chosen area to be assigned an elevation value of 1.38E 10^8. A blanking file (.bln) is created in Surfer that is comprised of coordinates for the vertices (listed clockwise) of a polygon which are applied to the analysis surface. Care must be taken in determining the coordinates of the blanking file for two important reasons. First, a cross-over in the path of the blanking confuses the software; and second, the blanked area should extend slightly outside the frame of reference. The resultant grid is then output in ASCII data form.

Tecplot 360 comes equipped with a spreadsheet data loader which is used to load the ASCII bathymetry grid data, and create a 3D volume mesh or "prism-grid". In creating the prism grid, the number of vertical layers to use for grid formation is chosen. With a maximum depth of 0.5 m, 50 layers were chosen to be created. The water surface is also set at 0.5 m which eliminates those values blanked in Surfer.

3.4.3.2 Interpolation of Velocity Data

Tecplot 360 is intended primarily for the visualization of computational fluid dynamics (CFD) and other numerical model results. It is also capable of working with field or lab data and although the model variogram is less adjustable, Tecplot can perform 3D Kriging of an irregularly shaped grid of point measurements, which is the case for this thesis. An experimental variogram of the ADV data is also not available, which leaves the determination of variogram parameters to user experience and judgment.

ADV data is first loaded using the provided excel data loader and these point measurements can be interpolated into a "prism-grid" for graphing. The type of variogram model used for Kriging in Tecplot is not provided, and based on the graphical user interface (GUI), is assumed to be a linear variogram similar to Fig. 3-24a. The default value for "Range" of 0.3 means 30% of the spatial dimension of the grid was used, again because no variogram of the data itself is available. In Tecplot, "Zero Value" is analogous to the nugget effect discussed in Section 3.4.3.1. Based on the ongoing research of the water resources group at the University of Ottawa and their extensive use of this software recently, a value of 0.0075 m^2 was chosen. This was the lowest nugget where the interpolation would converge for similar work with field measurements. "Drift" is the overall trend in the data; it is assumed that no trend was present. Now, the number and location of points to include in each interpolation is chosen. "Point Selection" lets the user choose the way in which the interpolation looks for values near itself, and "Number of Points" determines how many points to use for interpolating. The selected octant choice takes the specified number of points from each of 8 equal angle sections around the point of interest. Increasing this number increases the amount of calculations the computer must do and slows exploration and manipulation of the resultant volume. Finally, with the velocity data and bathymetry grid file loaded 3D diagrams can be created using the export utility. Exported images should be in the Portable Network Graphics (.png) format as the anti-aliasing capability of this format reduces the jaggedness of contour lines and axes, producing high quality images with small file sizes.

Chapter 4 Results

4.1 Introduction

All results pertaining to the experimental plan reported in Section 3.1 of this thesis are presented here. This chapter will be divided into two sections, first the more successful first experiment will be detailed and later the second experiment is explained providing some useful insight into flume performance. The naming convention for measurement locations is as follows. Cross-sections taken in the straight approach section are named for their distance from the channel entrance (e.g., 10 m). Nomenclature for cross-sections taken in the bend is a function of rotation angle the cross-section makes with the bend entrance (e.g., 30°). Lastly, the straight, exit cross-sections are named with the imperial distance (in inches) they were taken after the bend exit (e.g., 24 after).

4.2 Experiment #1

4.2.1 Flowrates and Velocity Profiles

As a first step, the "normal" velocity profiles are shown in Fig. 4-1. Each velocity profile from different "plan points" are shown in different colours. For determination of flow rate and average velocity for the first experiment, the standard field measurement technique of averaging velocities at depths of $0.2h$ and $0.8h$ ($\overline{U}_{0.2}$, $\overline{U}_{0.8}$) for each of 4 equal area portions of the cross-section, and summing the flow from each to determine total flow, Q_T, was applied. For the 0.2 m flow depth, velocities were taken directly from measurements at $0.2h$. At $0.8h$, the fitted power curve equation, shown in the legend for Fig. 4-1, was used to determine the value shown. For Fig. 4-1, z_{rel}, is used to indicate the distance from the bed that measurements were made. A summary of these calculations is as shown in Table 4-1.

Table 4-1. Calculation of total flow and mean streamwise velocity from Fig. 4-1

Section	$\overline{U}_{0.8}$ *(m/s)*	$\overline{U}_{0.2}$ *(m/s)*	$\overline{U}_{0.8/0.2}$ *(m/s)*	Q *(m^3/s)*	Q_T *(m^3/s)*	*mean* $\overline{U}$ *(m/s)*
0.125 m	0.411	0.335	0.373	0.019	0.0788	0.394
0.375 m	0.466	0.395	0.430	0.022		
0.625 m	0.453	0.379	0.416	0.021		
0.875 m	0.396	0.320	0.358	0.018		

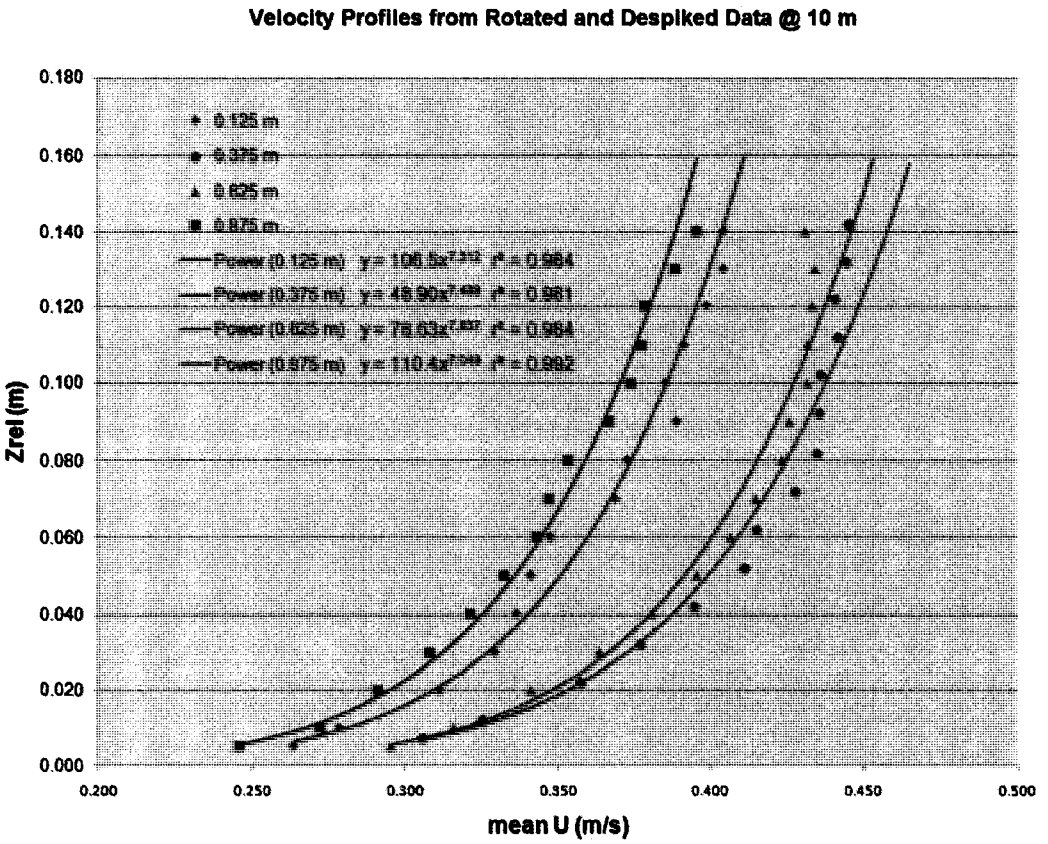

Figure 4-1. Mean streamwise velocity measured at 10 m (colours represent *y* location)

Power law trend lines, similar to those fit to the 10 m section profiles, were also fit to the 12 m section profiles. The equation for each profiles trend line is shown in the legend for Fig. 4-2. Also shown in Fig. 4-1, and Fig. 4-2, are the r^2 values for the fit of each line. This gives an indication of the accuracy of a trend line based on regression analysis and is known as the coefficient of determination. A maximum value of 1 is reached when there is perfect correlation between the ordinate and abscissa values.

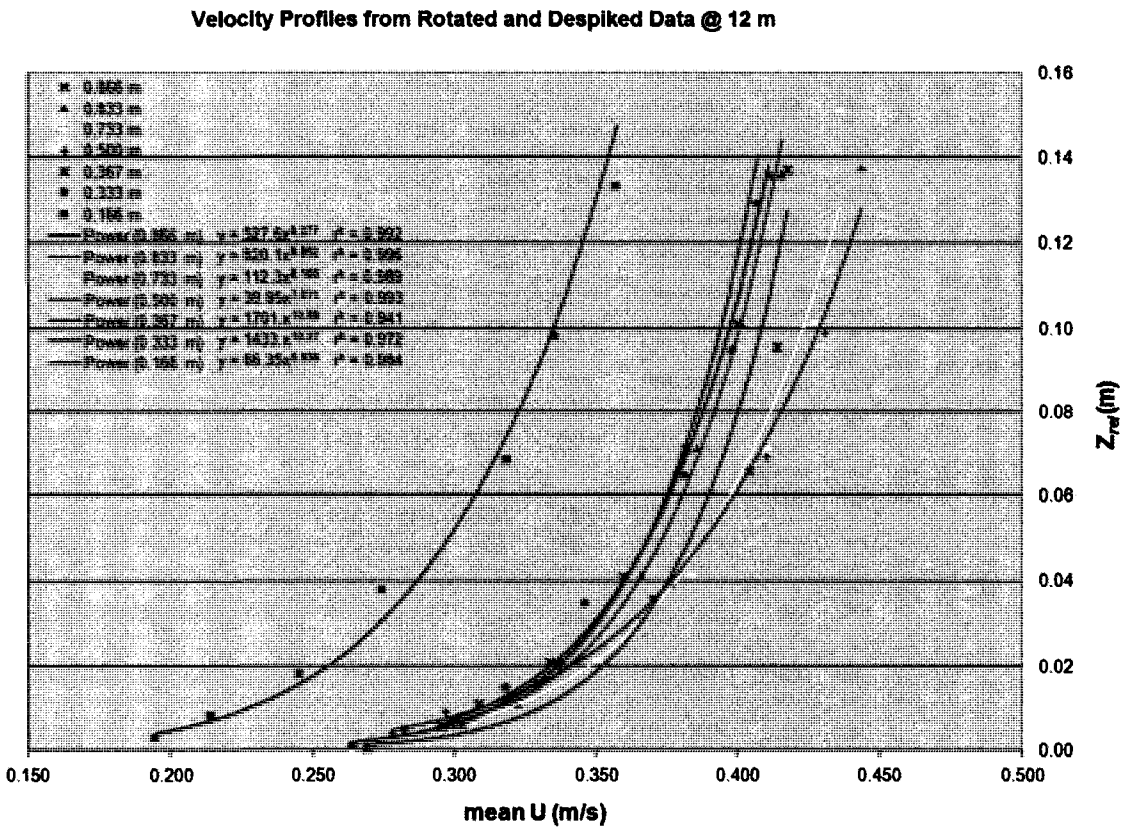

Figure 4-2. Mean streamwise velocity measured at 12 m (equations are for fit power law trend lines)

Total flow, Q_T, was also measured using the Dynasonics flowmeter discussed in Section 3.2.4.2. Readings at steady test flow varied between 0.0712 to 0.0720 m^3/s, so a value of 0.0716 m^3/s was chosen to represent this measurement. Head on the V-Notch weir was also measured to be 0.305 m at steady test flow. Total flow, while not used for validation, was calculated from the standard V-Notch weir equation (King and Brater 1952) with conversion to SI units,

$$Q_T = 2.53\left(\frac{H}{30.48}\right)^{2.47}\left(\frac{1\,m}{3.281\,ft}\right)^3 \tag{4.1}$$

where Q_T is total flow in m^3/s, and H is head on the weir in cm. A comparison of these measured flow rates is shown in Table 4-2.

Table 4-2. Comparison of flow measurements from Run 1

Method	$Q_T (m^3/s)$
velocity measurements	*0.0788*
Dynasonics	*0.0716*
V-Notch	*0.0715*

With several estimations of total flow rate, a log-linear plot of streamwise velocity was used for determination of roughness parameters (Fig. 4-3) using Eqn. 2.32. This concept allows use of the equation for a linear trend-line fit to semi-log profiles, $y = ax + b$ in the following manner,

$$a = \frac{U_*}{\kappa}, \qquad b = \frac{U_*}{\kappa} \ln\left(\frac{30}{k_s}\right) \tag{4.2}$$

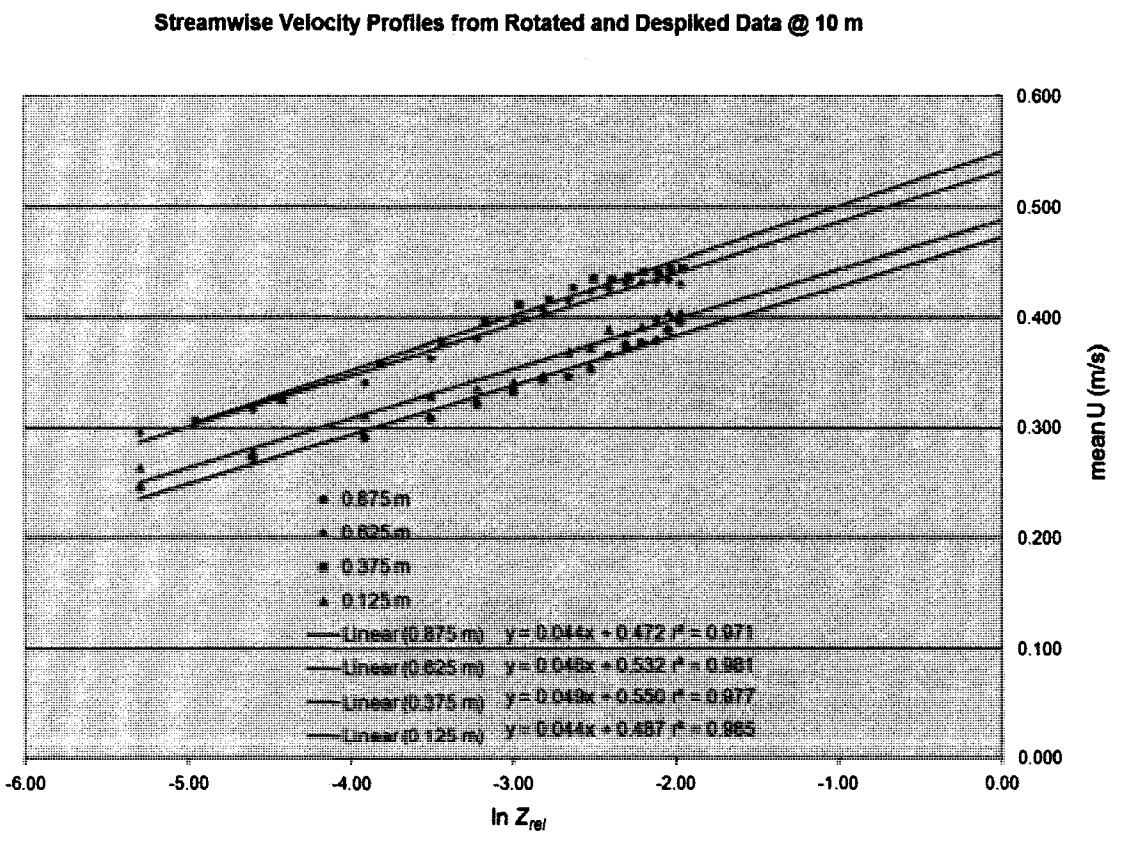

Figure 4-3. Log-linear plot of streamwise velocity profiles at 10 m

By taking von Karman's constant, κ, equal to 0.41 we can easily find boundary shear velocity, U_*, and roughness height, k_s. Also, an estimation of bed shear stress τ_o, can be made from Eqn. 2.20, and the Darcy-Weisbach friction factor from Eqn. 2.34. The summary of this group of calculations is shown in Table 4-3.

Table 4-3. Summary of computed roughness parameters at 10 m

Section	*a*	*b*	U_* *(m/s)*	k_s *(m)*	*f*	τ_o (N/m^2)
0.125 m	0.044	0.487	0.0180	0.00047	0.0190	0.325
0.375 m	0.049	0.550	0.0201	0.00040	0.0183	0.403
0.625 m	0.046	0.532	0.0189	0.00028	0.0169	0.355
0.875 m	0.044	0.472	0.0180	0.00066	0.0207	0.325
average			0.0188	0.00045	0.0187	0.352

The velocity profile for the 12 m cross-section plotted in a log-linear fashion is shown in Fig. 4-4. While this plot shows considerable deviations from linearity especially for measurements near the bed, and the fit linear trend lines show more deviation than for 10 m, shear stress was still calculated for comparison as summarized in Table 4-4.

Table 4-4. Summary of computed roughness parameters at 12 m

Section	*a*	*b*	U_* *(m/s)*	k_s *(m)*	*f*	τ_o (N/m^2)
0.866 m	0.037	0.482	0.0152	0.00007	0.01241	0.230
0.833 m	0.036	0.482	0.0148	0.00005	0.01157	0.217
0.733 m	0.044	0.524	0.0180	0.00020	0.01566	0.325
0.500 m	0.049	0.541	0.0201	0.00048	0.01915	0.403
0.367 m	0.029	0.471	0.0170	0.00020	0.01470	0.294
0.333 m	0.031	0.462	0.0175	0.00023	0.01527	0.310
0.166 m	0.044	0.433	0.0182	0.00028	0.01619	0.333
average			0.01724	0.00021	0.01499	0.302

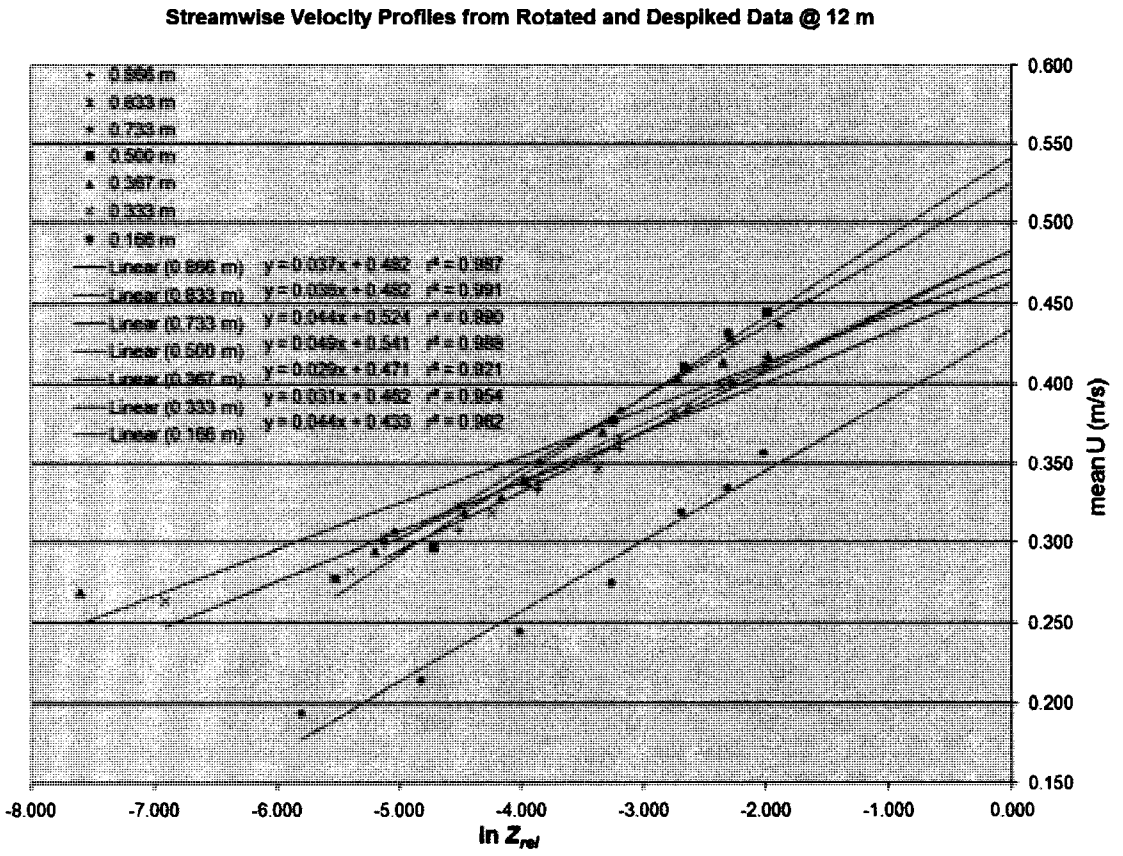

Figure 4-4. Log-linear plot of streamwise velocity profiles at 12 m

4.2.2 Boundary Layer Development

Shear stress at the bed, τ_o, can also be determined by extrapolating a fitted linear trend line to a plot of Principal Reynolds stress, $-\rho\overline{uw}$, as shown in Fig 4-5 for the 10 m cross-section and Fig. 4-6 for 12 m cross-section. In Fig. 4-5, the intercept of the linear trend line fitted to measured profiles, b, again where the expression $y = ax + b$ is used to assess boundary layer development. As shown in Fig. 2-4, Reynolds stress tends to zero at the free surface in a fully developed turbulent boundary layer, which was at h = 0.2 m for these experiments. The measured b/h, which should equal 1.0 for a fully developed boundary layer, is shown in Table 4-5. Also shown is the conversion of the trend line slope, a, into expected values of total shear, τ, for measured values at 10 m.

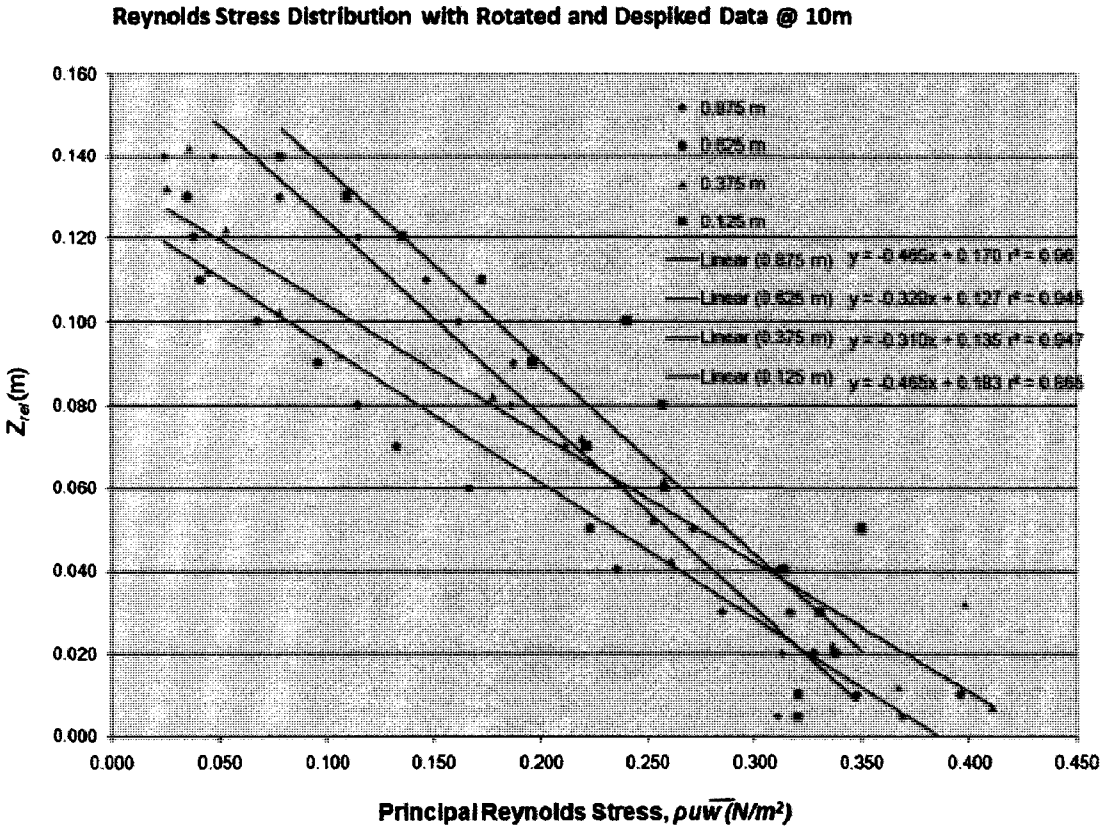

Figure 4-5. Measured Reynolds stress distribution at 10 m

Table 4-5. Summary of boundary layer development and calculated shear stress at 10 m

Section	*a*	*b*	*b/h*	τ (N/m^2)
0.125 m	-0.465	0.185	0.925	0.465
0.375 m	-0.310	0.135	0.675	0.310
0.625 m	-0.329	0.127	0.635	0.329
0.875 m	-0.472	0.170	0.850	0.472
average			0.771	0.394

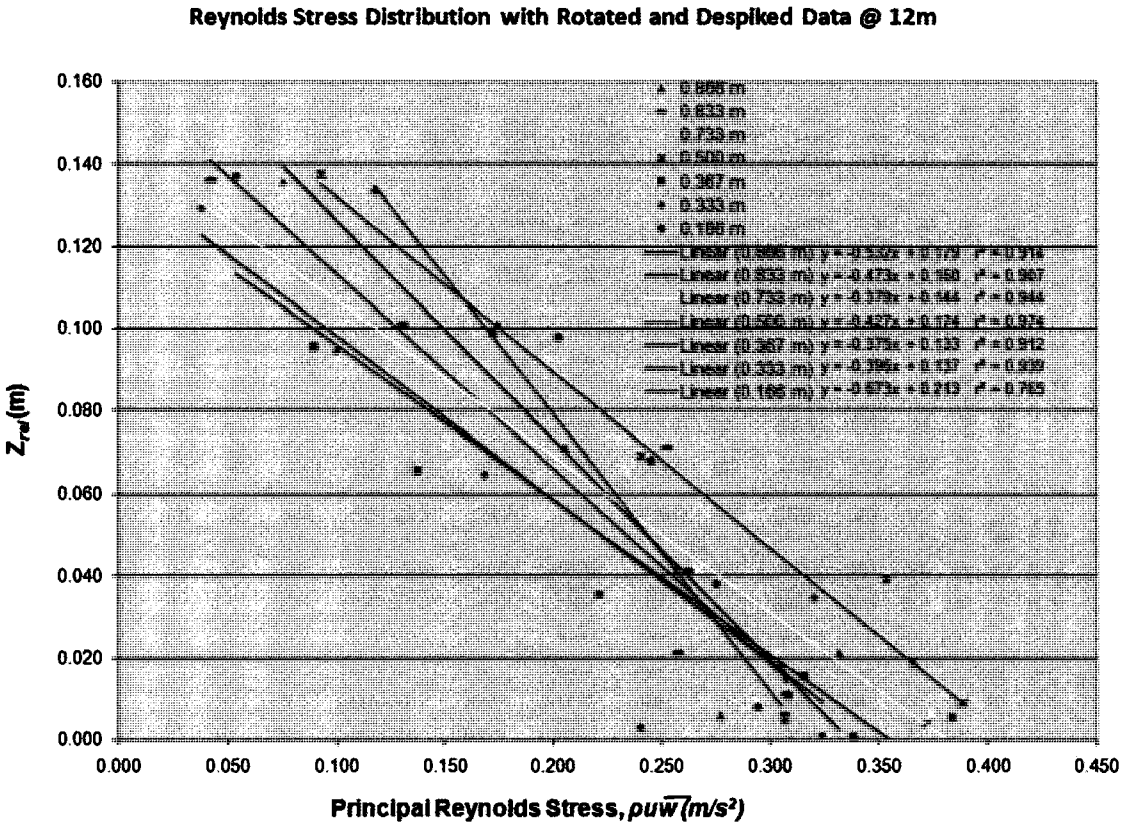

Figure 4-6. Measured Reynolds stress values at 12 m

Using the same process of analysis with the profiles of Principal Reynolds stress taken at 12 m as was used for the 10 m profiles, estimations of boundary layer development and bed shear are summarized in Table 4-6.

Table 4-6. Summary of boundary layer development and calculated shear stress at 12 m

Section	*a*	*b*	*b/h*	τ (N/m^2)
0.866 m	-0.532	0.179	0.895	0.532
0.833 m	-0.473	0.160	0.800	0.473
0.733 m	-0.379	0.144	0.720	0.379
0.500 m	-0.427	0.174	0.870	0.427
0.367 m	-0.375	0.133	0.665	0.375
0.333 m	-0.396	0.137	0.685	0.396
0.166 m	-0.673	0.213	1.065	0.673
average			0.813	0.465

4.2.3 Bathymetry

With the completion of ADV measurements, flow was stopped in the first test after 70 hours of total run time. With the flume drained, 2773 individual elevation measurements were made of the entire bed section using the procedure outlined in Section 3.3.5, and a 3D grid file was developed for loading into Tecplot 360. Presented first (Figure 4-8), is a surface map of the bathymetry, generated using the described Kriging parameters from Section 3.4.3.1. Expanded slightly in the z-direction, this gives a first look at the equilibrium bed conditions. As a complement to this and subsequent 3D images, a black and white contour drawing has been provided (Fig. 4-8). Figure 4-8 provides reference for the elevations and planform dimensions of bedform details which may be difficult to discern from Fig. 4-7.

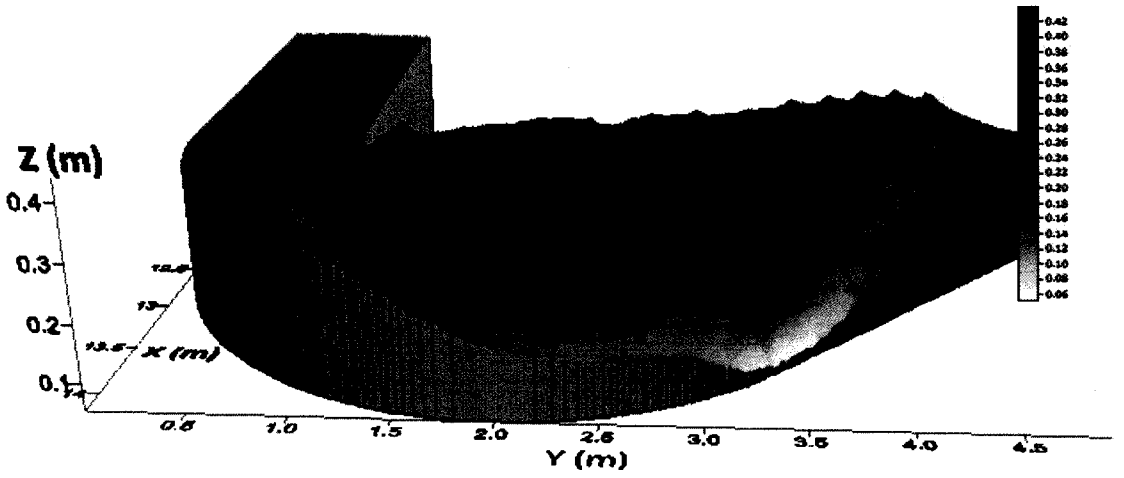

Figure 4-7. Kriging interpolated Run 1 bathymetry

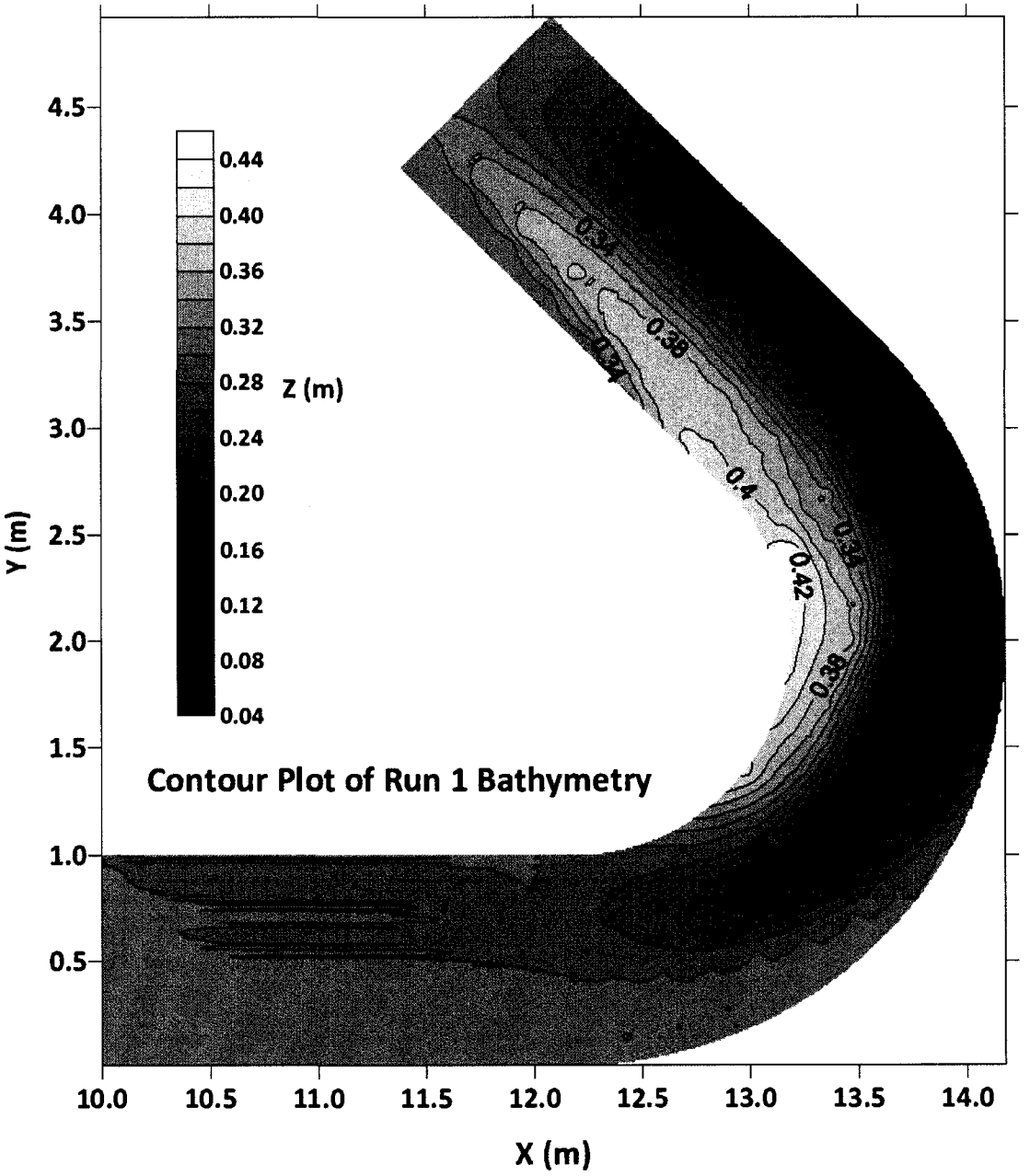

Figure 4-8. Contour plot of Run 1 bathymetry (z = 0.5 m was the water surface elevation)

To show a detailed look at equilibrium bathymetry a collage of photographs has been provided in Fig. 4-9. While lending validity to Fig. 4-7 by providing overall perspective, this collage also shows in better detail some of the ridges which developed on the slope of the point bar both on the upstream face (Fig. 4-9a, b) and the downstream face (Fig. 4-9c, d). Included in Appendix C is a video clip taken of the bathymetry which gives good perspective of the bathymetry through the bend.

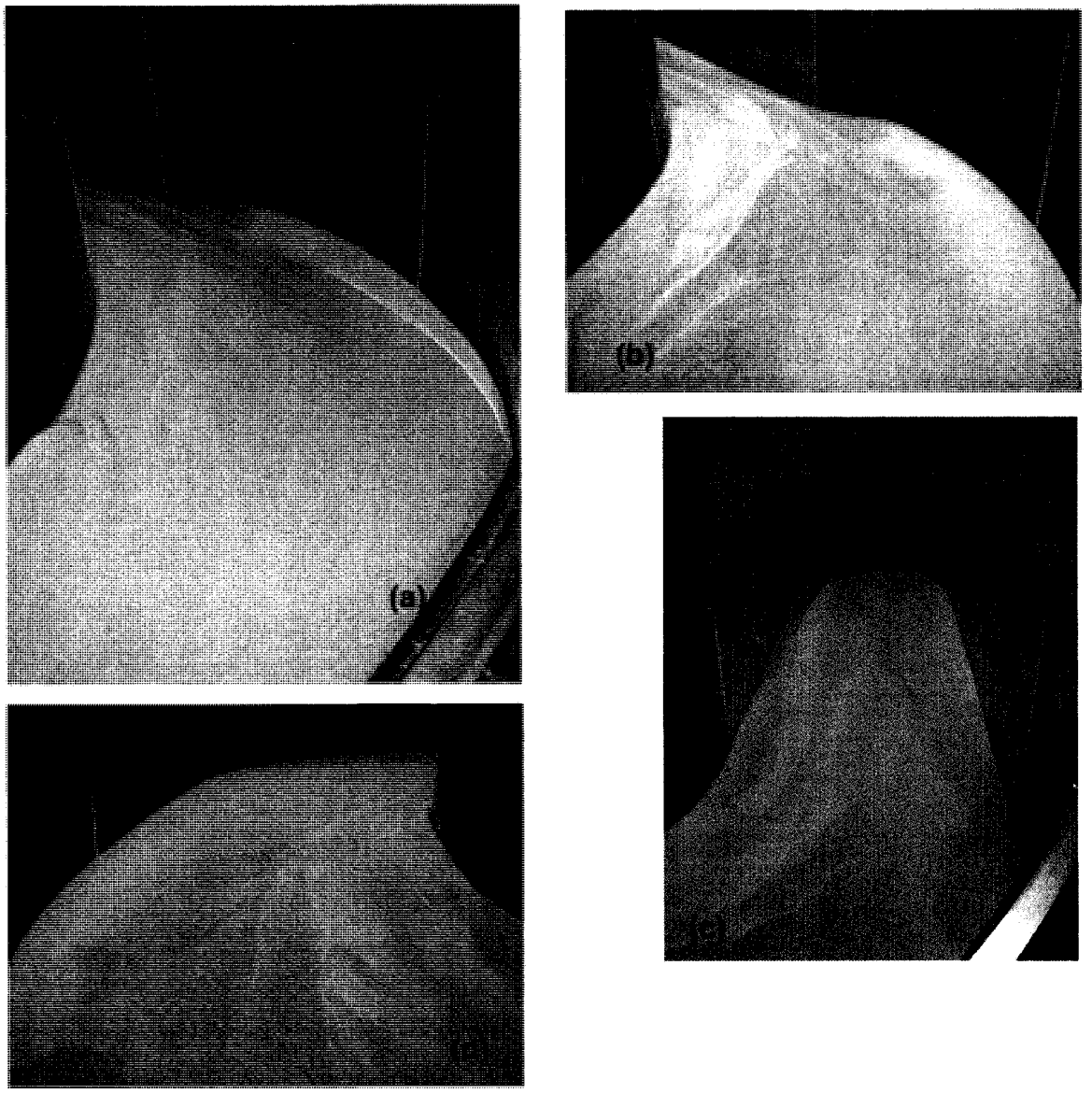

Figure 4-9. Bathymetry photo collage; (a) bend entrance viewed from upstream (b) further downstream showing point bar ridge features (c) outer bend and exit section view from bend apex (d) downstream point bar ridge detailing looking back upstream

4.2.4 Channel Slope and Sediment Transport Observations

As outlined in Section 3.3.2, the first experiment was run at clear-water scour conditions, and the second at higher bed shear, resulting in live-bed scour conditions, the difference being that there was no bed movement in the straight section for the clear-water test. To be specific, no organized movement of bed material was observed. When we reached full flow conditions, very few grains were

observed to move, thus, after the full 70 hours of run time, slight changes (± 1 mm) were measured very near the bend entrance. This can be seen in Figure 4-8Fig. 4-8, near coordinate (11, 0.5). Note that the contour line in that region represents 0.3 m was the starting elevation of the bed, and these slight changes caused the interpolation to generate "scribbles". A contour label was not included for 0.3 m in Fig. 4-8 as this created an enormous amount of labels on the plot because the software adds a label for each slope direction change.

There was, however, some movement in the approach section near the bend entrance as shown in Fig. 4-10a, although it was due primarily to procedural error. As a result of a brief period of high shear from opening the exit gate too much during the establishment of uniform flow, local scouring at the transition from the protective entrance blocks and the bed material occurred. Fortunately, over the 65-70 hours of run time following this episode of high shear, the sediment "slug" did not reach the bend section, and clear-water scour conditions were maintained.

For the bend section, observed maximum scour occurred directly after the bend exit on the outside of the channel. This scour hole very nearly impinged on the solid flume bottom scouring to a maximum of 0.25 m, which would have fouled the experiment. A photograph showing this maximum scour is shown in Fig. 4-11, where it should be noted that although the clear scale on the flume wall shows 20 mm, it is sitting atop a structural reinforcement strip not discussed in this thesis that projects the ruler vertically upward.

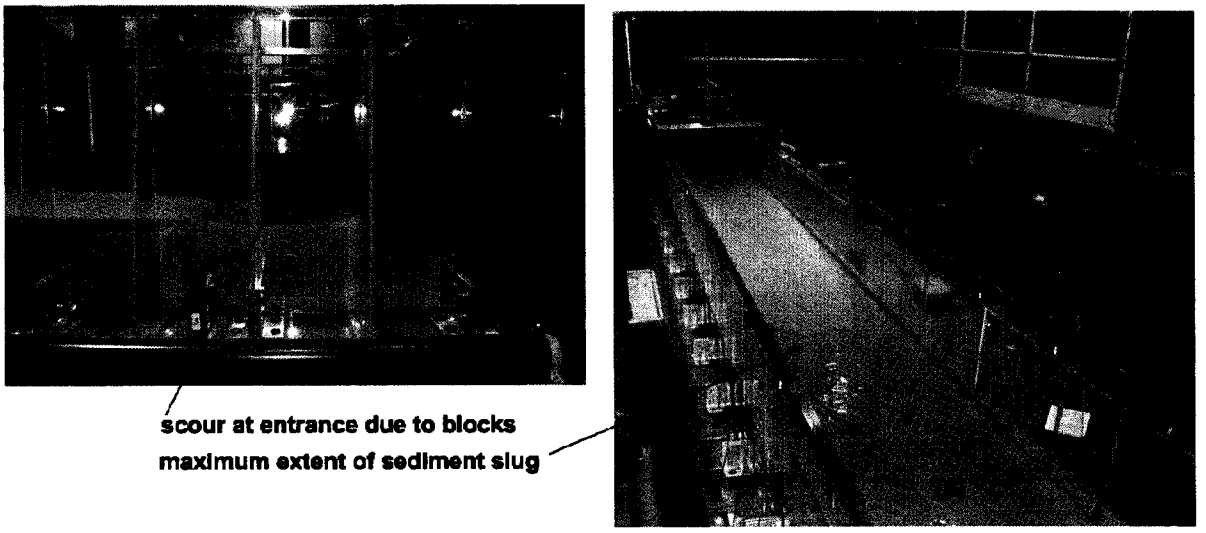

Figure 4-10. Sediment "slug" observed during Run 1; (a) genesis point, (b) maximum extent after 70 hours

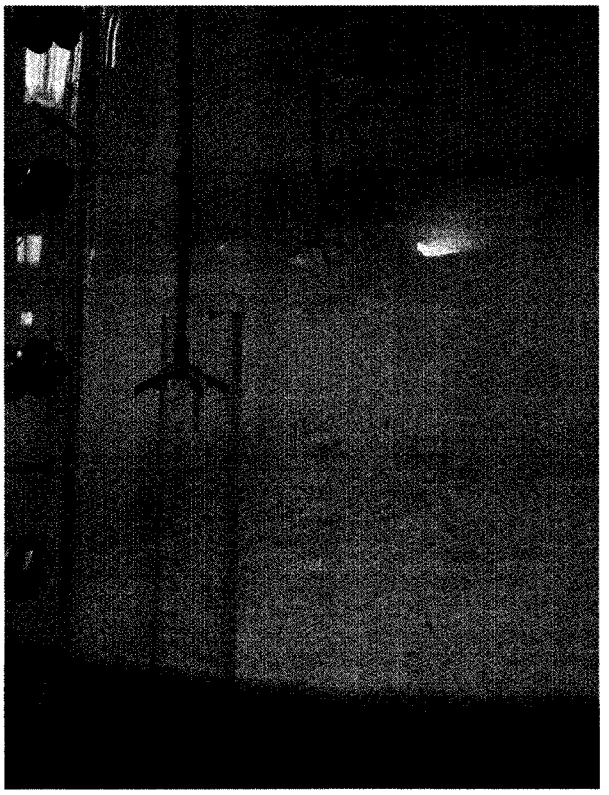

Figure 4-11. Maximum scour magnitude

4.2.5 ADV DATA

4.2.5.1 Introduction

Results from the Tecplot 360 interpolation discussed in Section 3.4.3.2 comprise all figures included in this section. All data derived by the MatLab code for each measurement point are included in Appendix C. To have a clear look at all the results, a total of 23 variables were interpolated to the bathymetry grid and with 3 different overall 3D views, 12 cross-sectional 2D views with both relative and absolute scales have been produced, making for a total of over 700 diagrams. While extremely intriguing, presenting every diagram here would result in too many figures to be sensibly discussed. In this section, then, we will present the overall 3D images, and use the 2D cross-sectional plots in Chapter 5 for discussion. All 2D and 3D plots are included in Appendix C for review.

The terms "relative" and "absolute" are used somewhat arbitrarily to represent the way in which the scales were generated for 2D cross-sectional plots. By scale we are referring to the maximum and minimum values considered for each plot. The term global, then, refers to a scale that

considers the entire range of values over the entire data set, while local indicates that the scale was derived from maximum and minimum values for that cross-section only. This is important for viewing some variables, which, when viewed in relative scales for each cross-section, show very little detail as these data sets are controlled by outliers. For example, two plots of integral time scale in the x-direction, taken at the 10 m cross-section are shown in Fig. 4-12. By examining the scales for both we see that the range of values in the relatively scaled plot (Fig. 4-12a) is somewhat "washed out", while the absolutely scaled plot (Fig. 4-12b) shows much more detail. Thus, both of these scales will be henceforth referred to by this nomenclature when discussing various plots.

In terms of applying scales on the axes for the 2D plots or "slices" the viewpoint can be changed but not the coordinate axes. Thus the x and y axes generated by the software for each plot are not normal to the plane of view (except the straight channel sections at 10 m and 12 m as they are parallel with the y-axis and the 90° cross-section which is parallel with the x-axis) and, when scales on the axes are included, do not give an accurate representation of scale. The reader is reminded, then, that the flume is a constant 1 m when viewing these 2D plots.

Lastly, the ADVs cannot measure velocity in the uppermost 60 mm of the water column. This accounts for the sample volume being 50 mm below the emitting transducer which itself needs to be submerged approximately 7-10 mm to operate properly. Thus, the upper 60 mm of the plots are extrapolated and consequently are cautiously considered, which is less problematic in the location in the pool area, and more problematic near the point bar.

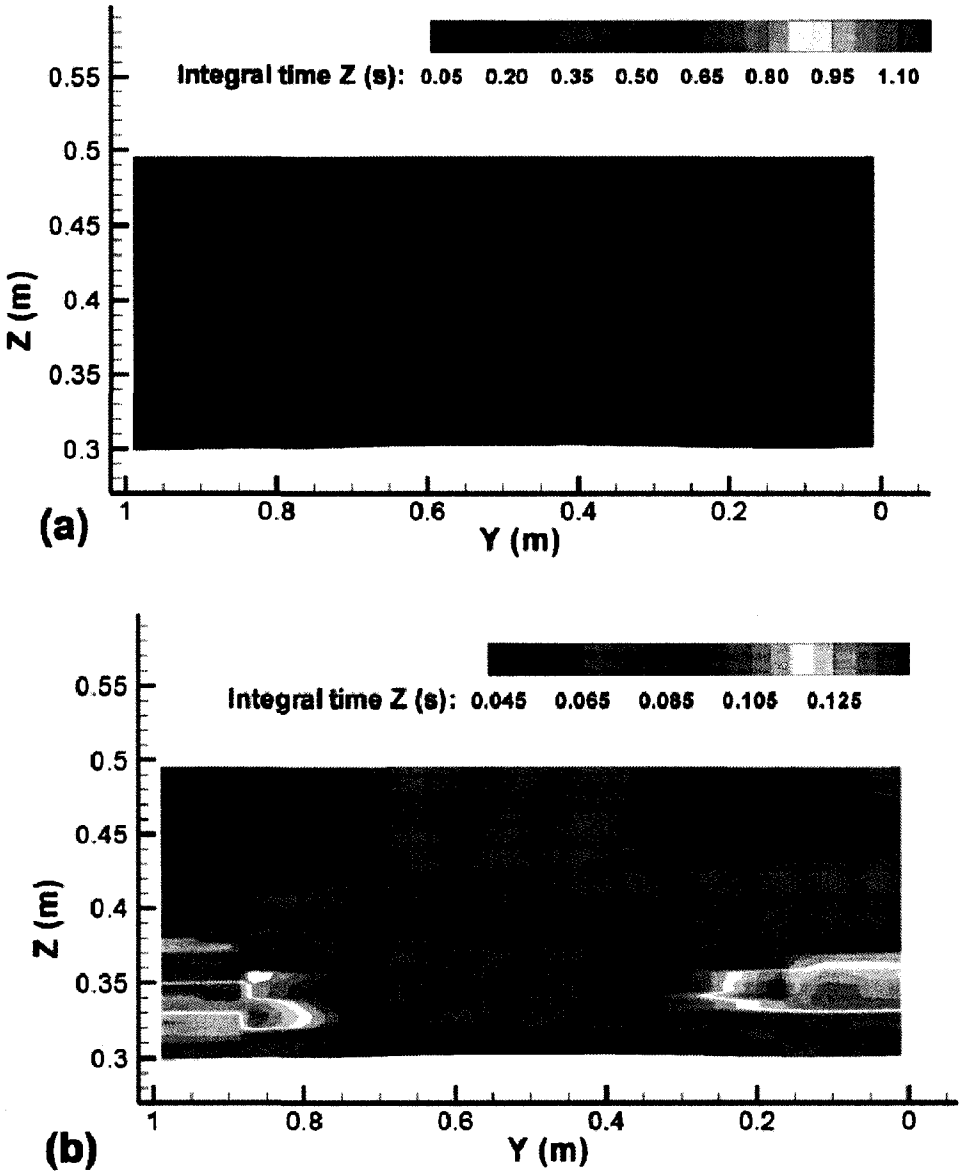

Figure 4-12. (a) Relative scale and (b) absolute scale comparison for 2D plots (taken at 10 m)

4.2.5.2 Performance Metrics

Here we will focus first on presenting metrics by which the overall quality of the measurements can be assessed. MatLab code introduced in Section 3.4.2 was used to calculate the average SNR and correlation for each coordinate axes, as well as the difference in two vertical velocity measurements, *VZ check*, from raw time-series data which is defined here as:

$$VZ\,check = VZ_1 - VZ_2 \tag{4.3}$$

Owing to the four receiver configuration of the Vectrino probes, VZ_1 is measured by the receivers aligned with the flow, and VZ_2 is measured by the cross stream facing receivers. High VZ error, then, indicates these two measures taken from the same sample volume are not showing the same Doppler shift for pulse pairs, which is a clear indicator of error. It is also important to point out that the correlation function, here, is calculated continuously based on cross and autocorrelations for successive pulse pairs as the measurements are being taken, which is not the same as the autocorrelation function used for spectral analyses.

General statistics, of max, min, average and standard deviations, σ, calculated from the average of each time series measurement (from raw data) and are summarized Table 4-7.

Table 4-7. Summary of calculated ADV performance metrics for Run 1 from raw data averaged for each time series

Statistic	*SNR X*	*SNR Y*	*SNR Z1*	*SNR Z2*
Max	24.342	25.270	29.962	24.359
Min	10.656	11.400	12.094	10.602
Mean	21.601	23.005	26.522	21.588
σ (std)	3.586	3.696	4.282	3.169
Statistic	***VZ check (m/s)***			
Max	0.009			
Min	-0.003			
Mean	0.003			
σ (std)	0.002			
Statistic	***COR X (%)***	***COR Y (%)***	***COR Z1 (%)***	***COR Z2 (%)***
Max	96.162	96.009	95.662	96.101
Min	72.330	73.549	77.840	76.221
Mean	91.777	91.495	90.646	91.313
σ (std)	3.200	3.611	3.047	3.139

4.2.5.3 Noise

Another important metric for assessing measurement performance is noise in the streamwise direction. While vertical noise can be computed, noise in the horizontal direction is more likely due to beam configuration. The procedure used to quantify noise was presented in Section 3.4.2, and with the magnitude of streamwise noise calculated from the power spectrum for each time series, basic statistics are calculated as presented in Table 4-8.

Table 4-8. Summary of streamwise noise calculations

Statistic	*Noise U (m/s)*
Max	0.0686
Min	0.0096
average	0.0186
std	0.0058

While Table 4-8 covers all time series considered as a whole, when measurements were analyzed in reference to an individual cross-section, noise was examined more closely using absolute scales to estimate any biasing that may occur locally due to outliers.

4.2.5.4 Mean Velocities

First, the plots of mean velocity in each coordinate direction are presented. Note that the coordinate axes for the ADV measurement follows the channel curvature. Thus, at each cross-section, $\overline{U}$ is positive downstream, normal to the plane, $\overline{V}$ is positive cross stream to the left (facing downstream), and $\overline{W}$ is positive up. It is important to point out again, that the values for the upper 30% of these diagrams are extrapolated.

Mean streamwise velocity, $\overline{U}$ is presented in Fig. 4-13. A view from the outside of the bend is shown in Fig. 4-13a, from the bottom in Fig. 4-13b, and the inside of the bend in Fig. 4-13c. Mean cross-stream velocity, $\overline{V}$, is presented similarly in Fig. 4-14a, b, and c; and mean vertical velocity, $\overline{W}$, in Fig. 4-15a, b, and c.

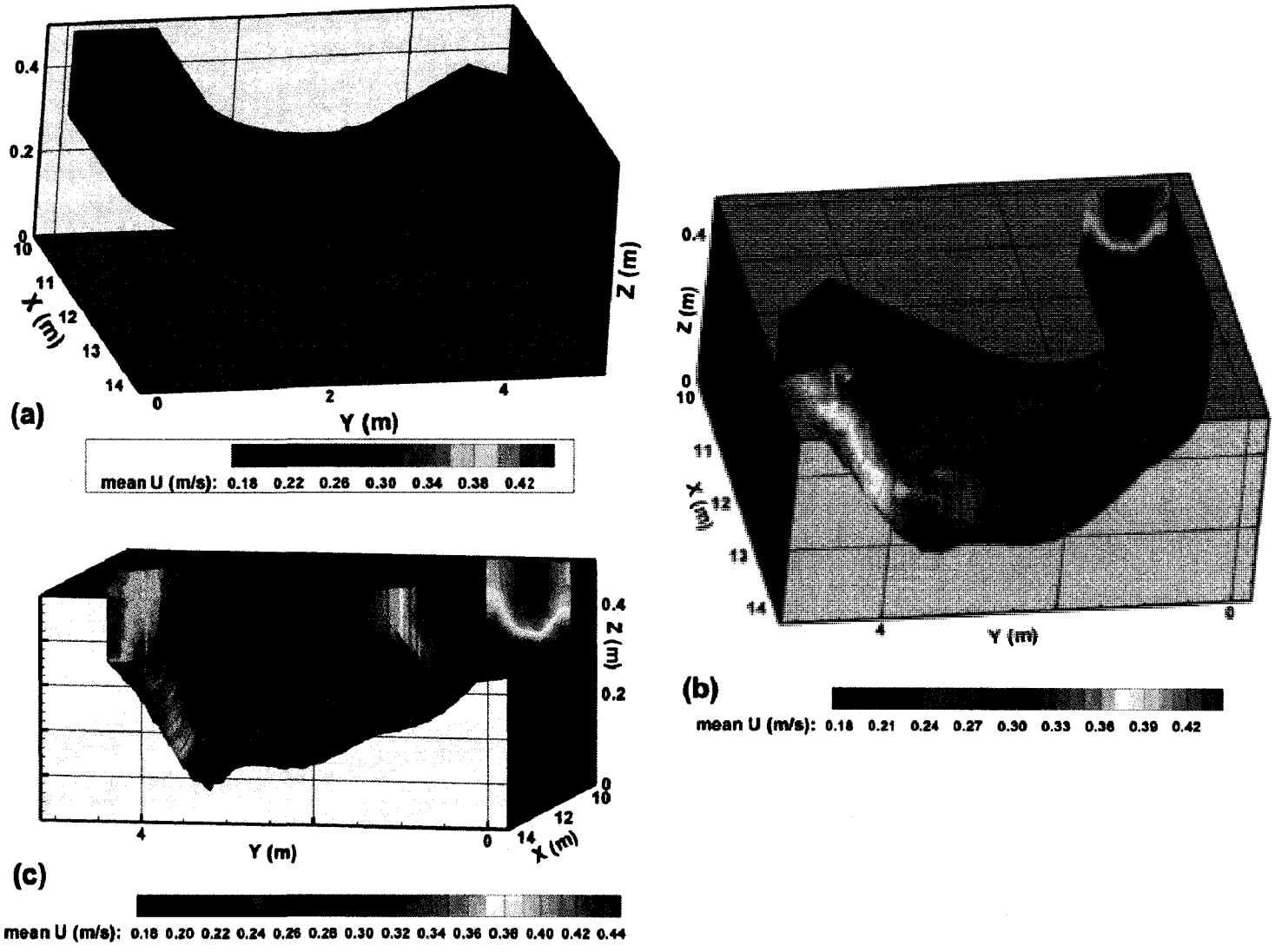

Figure 4-13. Overall 3D views of mean streamwise velocity, $\overline{U}$; (a) outside view, (b) bottom view, and (c) inside view

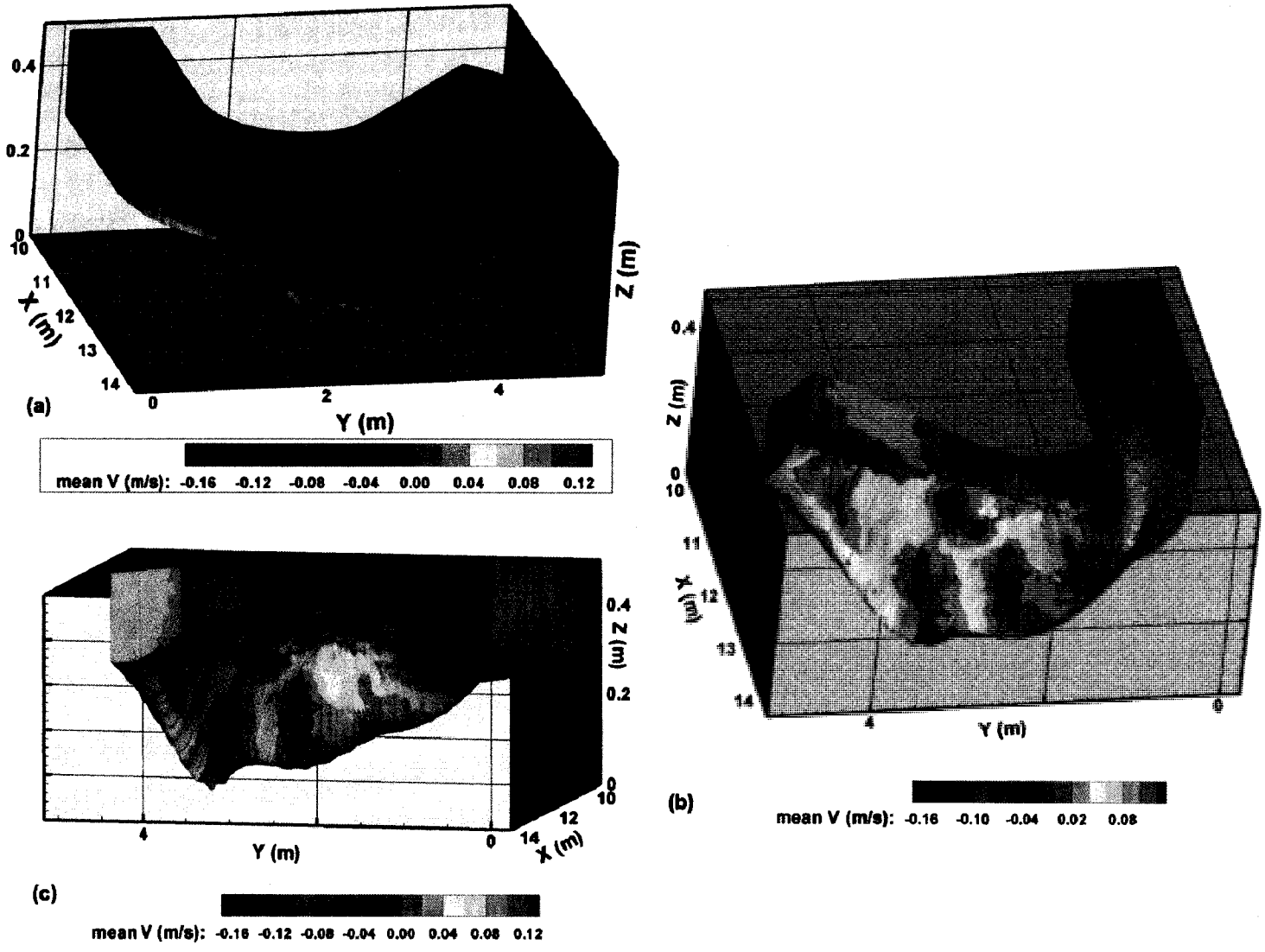

Figure 4-14. Overall 3D views of mean cross stream velocity, $\overline{V}$;(a) outside view, (b) bottom view, and (c) inside view

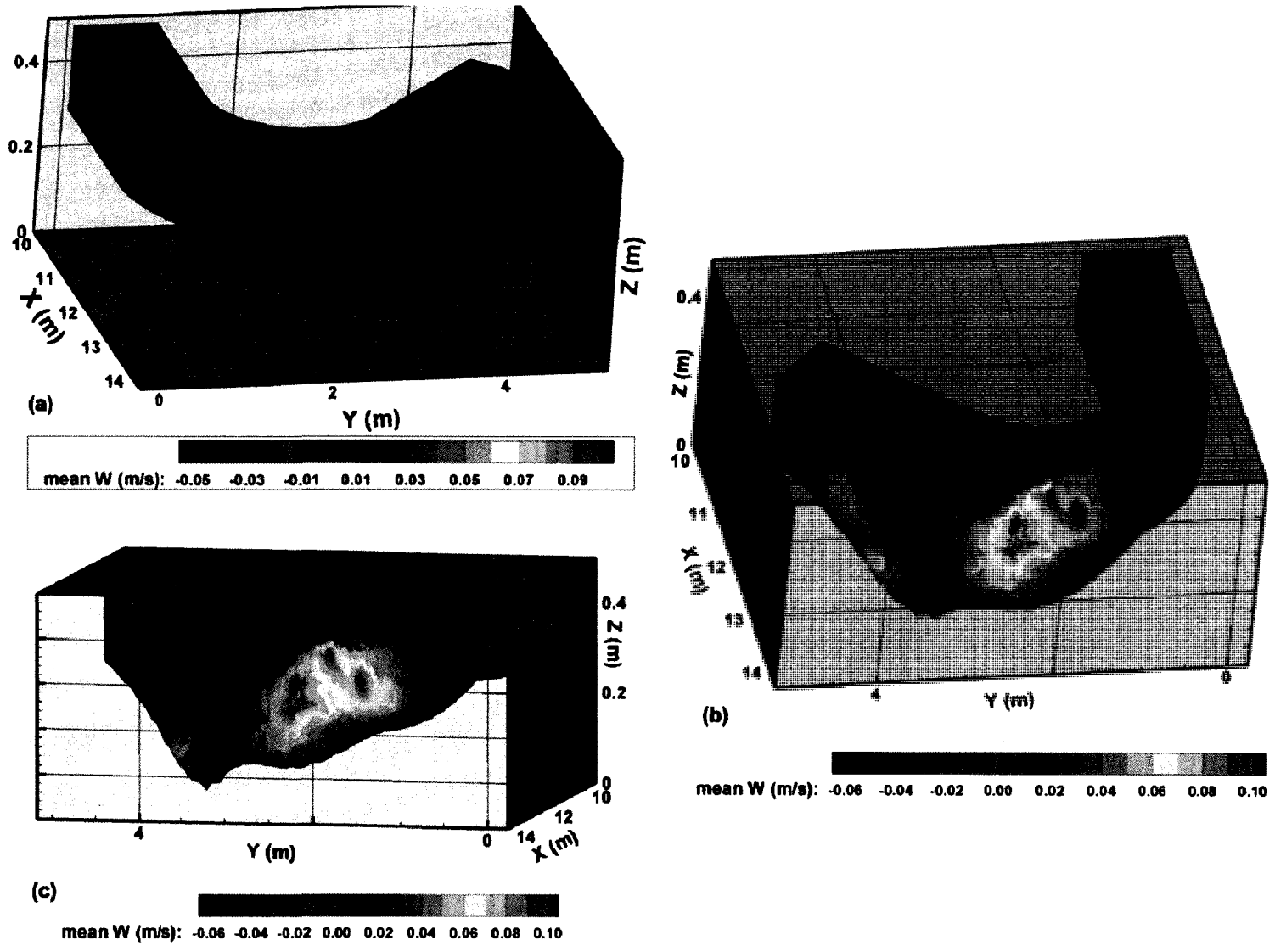

Figure 4-15. Overall 3D views of mean vertical velocity, $\overline{W}$; (a) outside view, (b) bottom view, and (c) inside view

4.2.5.5 Reynolds Stress Distribution

The three components of Reynolds shear stress are the focal point of this thesis. Following the same coordinate translation described in the previous section (i.e., x is constant perpendicular at all cross-sections), streamwise-vertical Reynolds stress, $-\rho\overline{uw}$, is presented first in Fig. 4-16. Note the labels generated by Tecplot 360 do not allow over-bars or special characters, and thus the nomenclature, "*Reynstress uw*", used in the figures should be interpreted as being $-\rho\overline{uw}$, which is to be applied to the other plots of streamwise-cross stream Reynolds stresses, $-\rho\overline{uv}$ (Fig. 4-17), and cross stream-vertical, $-\rho\overline{vw}$ (Fig. 4-18), respectively.

These stresses give an indication of the stress in the fluid due to turbulent fluctuations. In classical theory derived in straight channels, principal or streamwise-vertical Reynolds stress is of paramount importance. With strongly curved helical flow patterns in a river bend, the direction of the bulk flow is not necessarily perpendicular with the channel centerline. Therefore, each of the Reynolds shear stress terms are equally important.

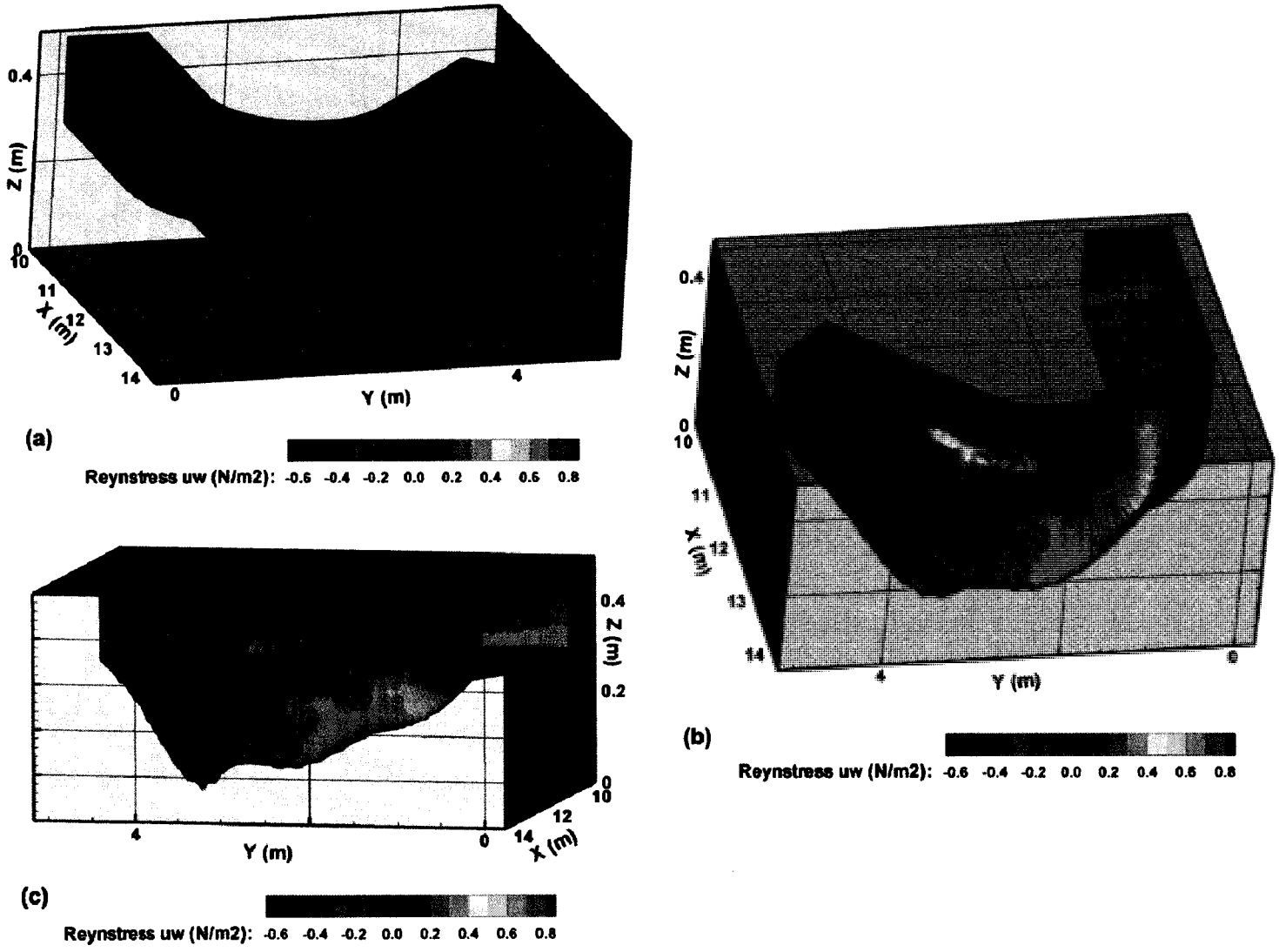

Figure 4-16. Overall 3D views of streamwise-vertical Reynolds stress, $-\rho\overline{uw}$; (a) outside view, (b) bottom view, and (c) inside view

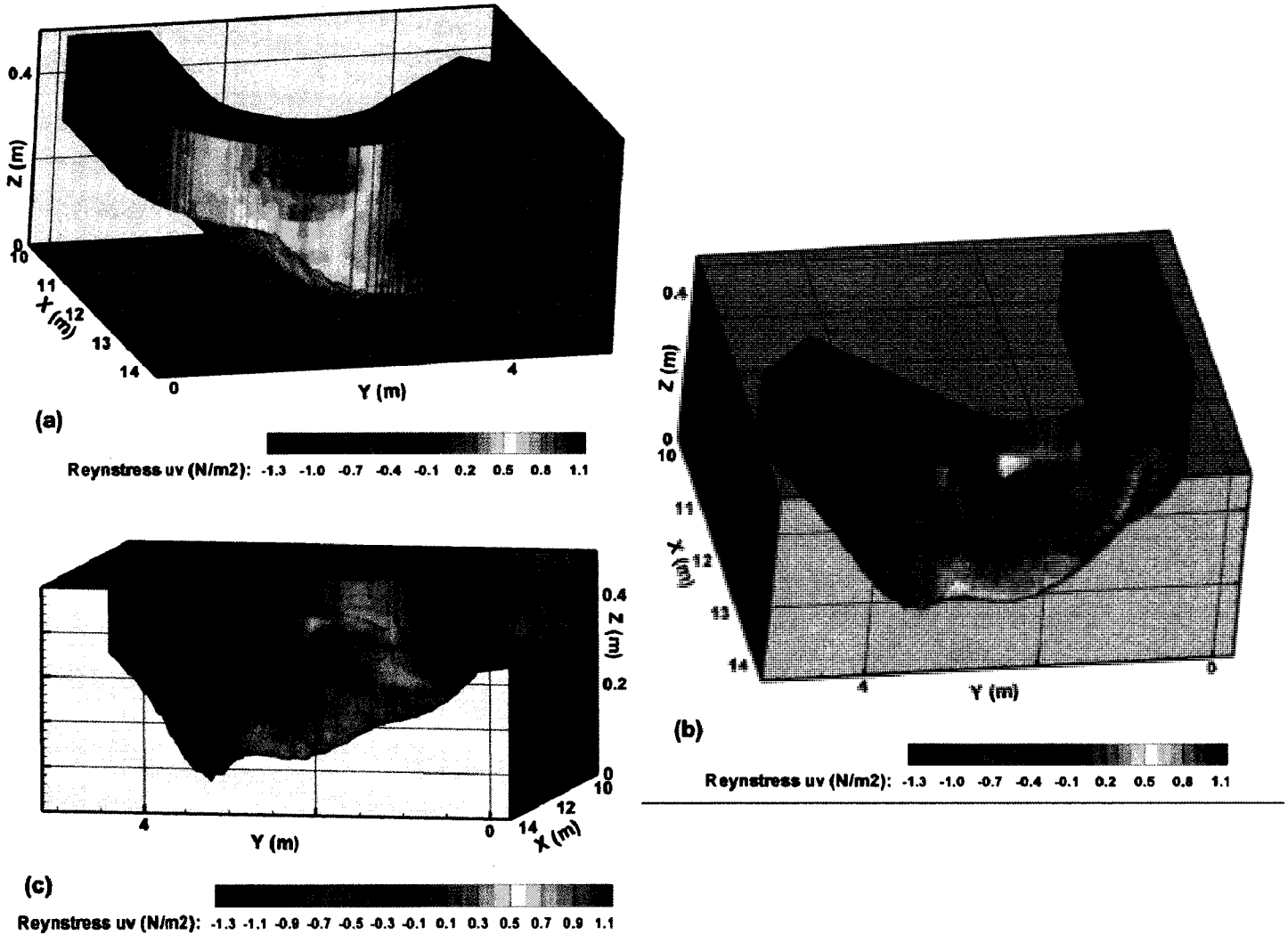

Figure 4-17. Overall 3D views of streamwise-cross stream Reynolds stress, $-\overline{\rho uv}$;(a) outside view, (b) bottom view, and (c) inside view

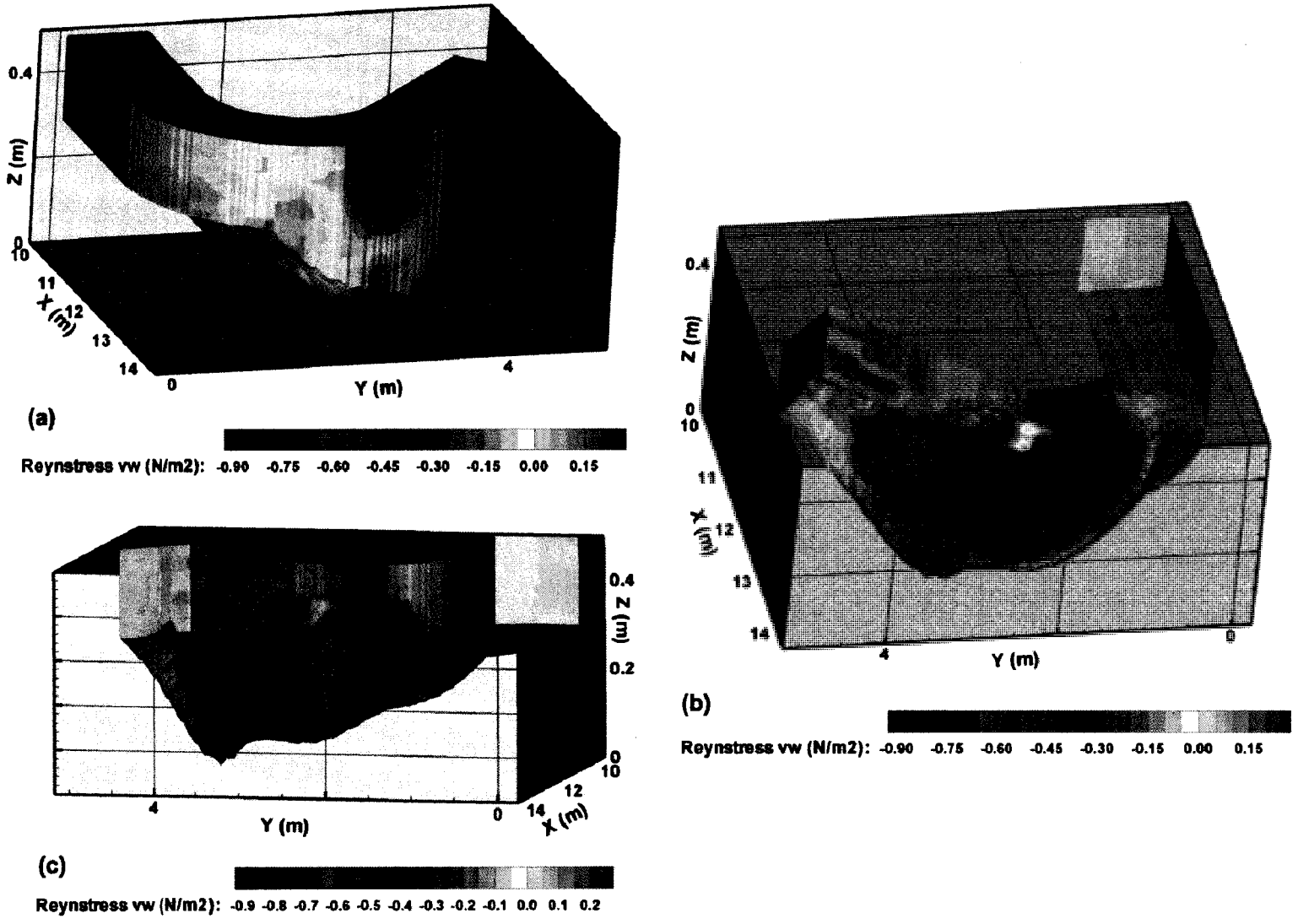

Figure 4-18. Overall 3D views of cross stream-vertical Reynolds stress, $-\overline{\rho vw}$; (a) outside view, (b) bottom view, and (c) inside view

4.2.5.6 Turbulent Fluctuations and Relative Turbulent Intensities

Turbulent fluctuations are represented here by their RMS values in each direction. While the mean of absolute fluctuations is better for acoustic velocimetry, this measure is not classically used. Regardless, this metric gives a good indication of where turbulent activity is greatest which is important for validation of other metrics such as integral time. Figure 4-19 is a plot of "*u rms*" which is the RMS of turbulent fluctuations in the streamwise direction, while Fig. 4-20 is a plot of cross stream fluctuations, and lastly Fig. 4-21 for vertical fluctuations.

Relative turbulent intensities then give an indication of the fluctuations normalized by mean streamwise velocity, $\overline{U}$, in each coordinate direction. Similar to Reynolds stress, Tecplot 360 does not include special characters and using the character $\hat{u}$ in the plots is not possible. Thus the term "*u turb int*" is used to replace the correct label in Fig. 4-22. This same approach applies to the cross stream relative turbulent intensity, $\hat{v}$ (Fig. 4-23), and vertical relative turbulent intensity, $\hat{w}$ (Fig. 4-24). These give us a visual indication of where Taylor's frozen field hypothesis is applicable.

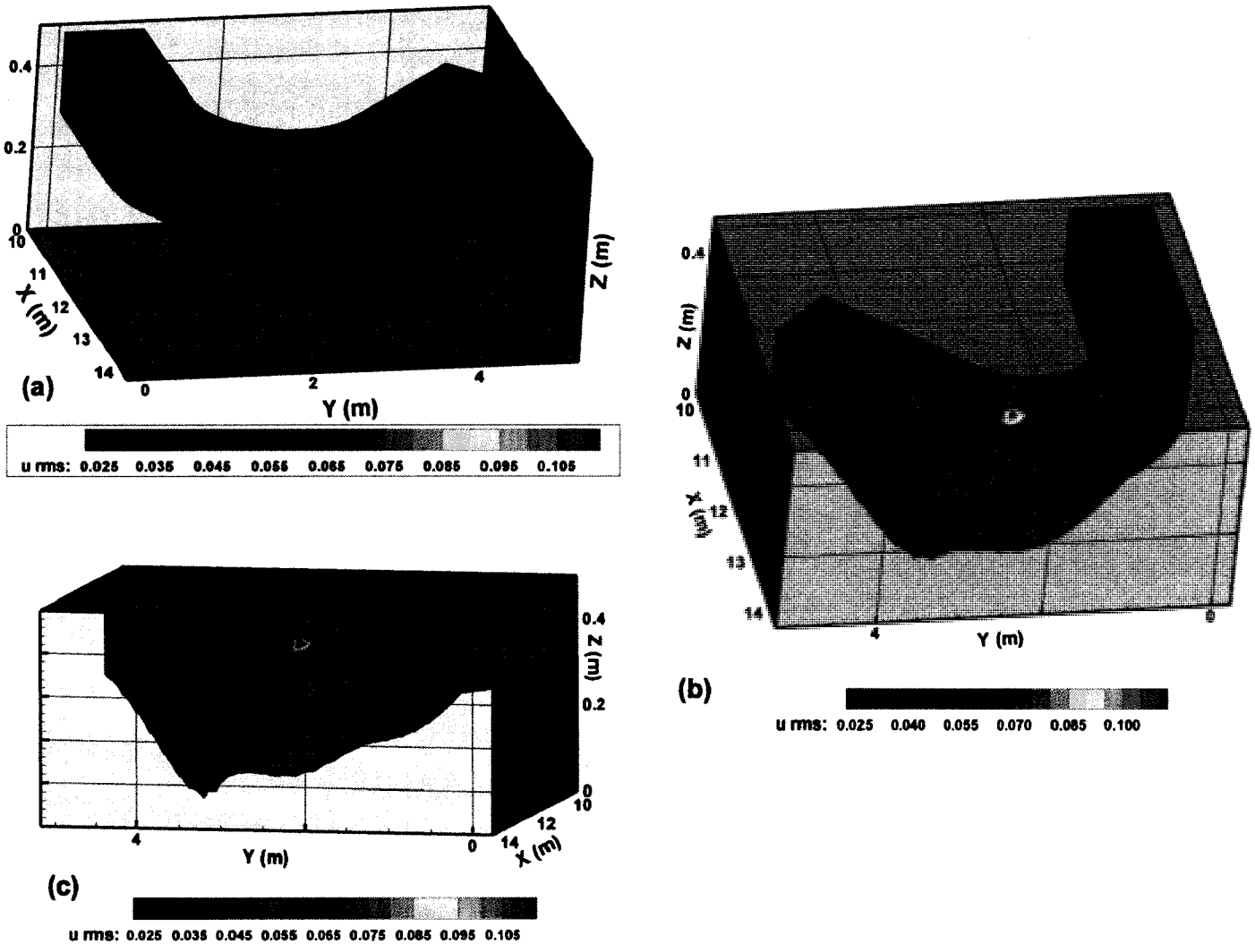

Figure 4-19. Overall 3D views of the turbulent fluctuations in the streamwise direction; (a) outside view, (b) bottom view, and (c) inside view

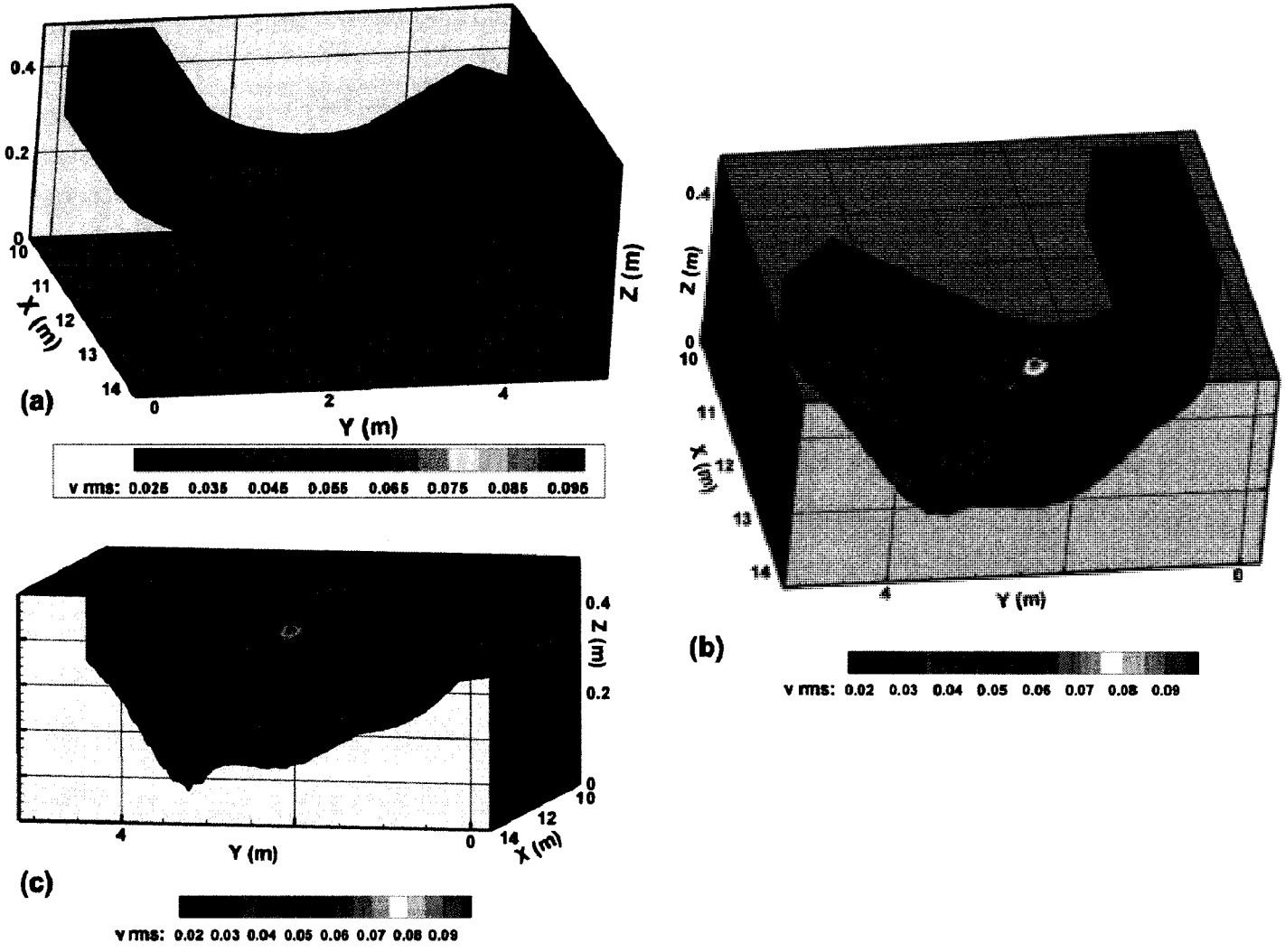

Figure 4-20. Overall 3D views of the turbulent fluctuations in the cross stream direction; (a) outside view, (b) bottom view, and (c) inside view

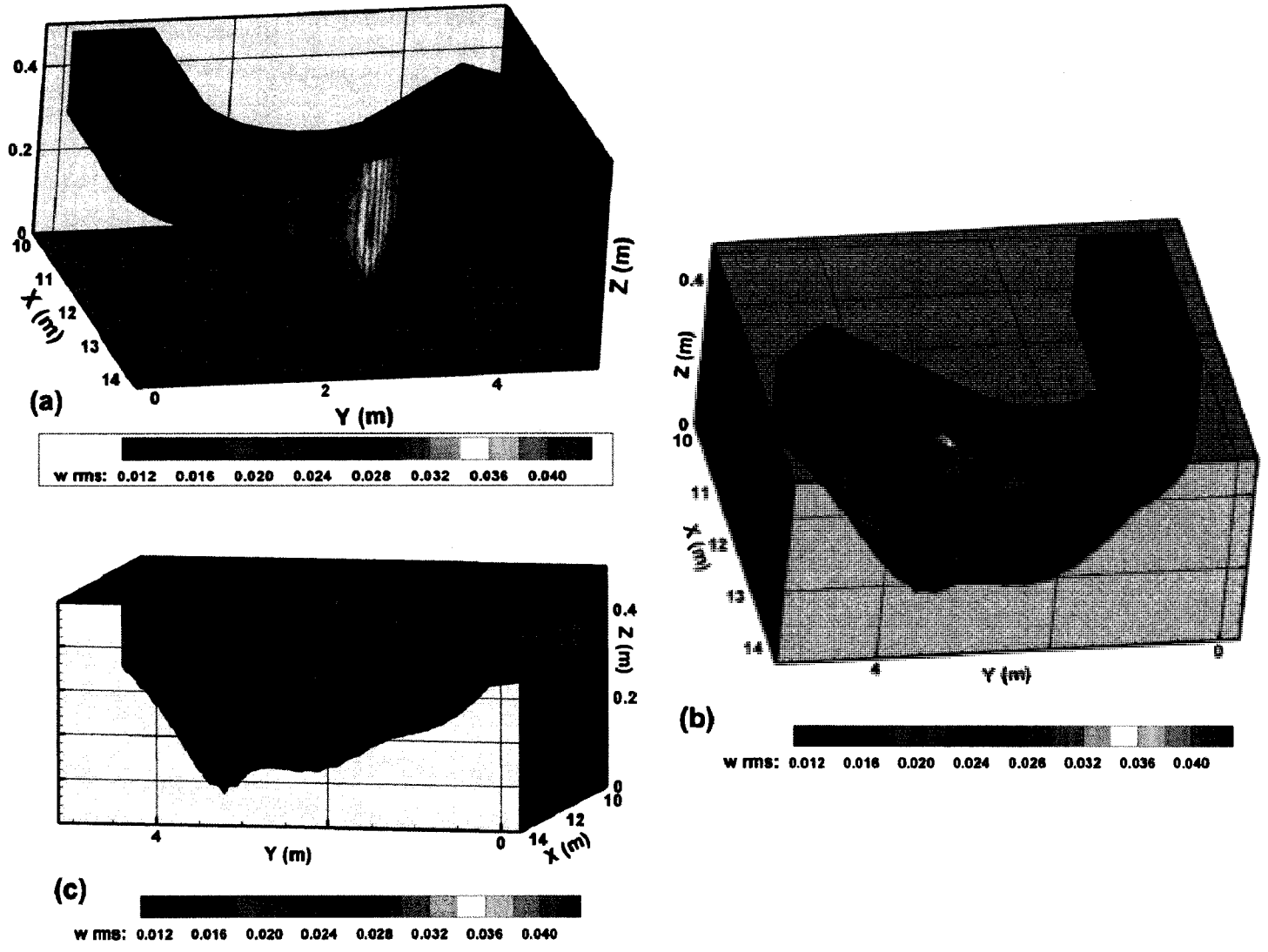

Figure 4-21. Overall 3D views of the turbulent fluctuations in the vertical direction; (a) outside view, (b) bottom view, and (c) inside view

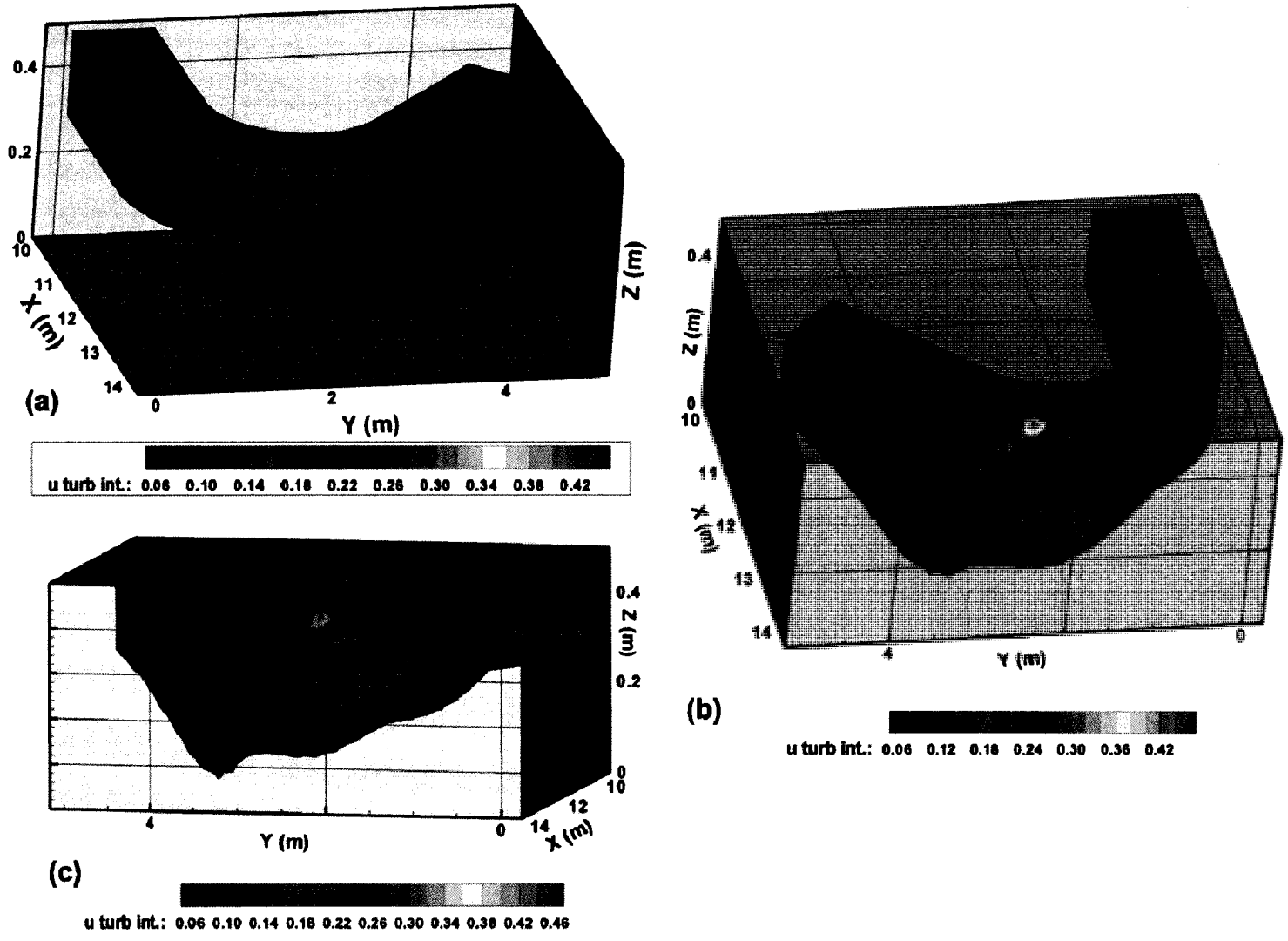

Figure 4-22. Overall 3D views of relative turbulent intensity; $\hat{u}$, in the streamwise direction; (a) outside view, (b) bottom view, and (c) inside view

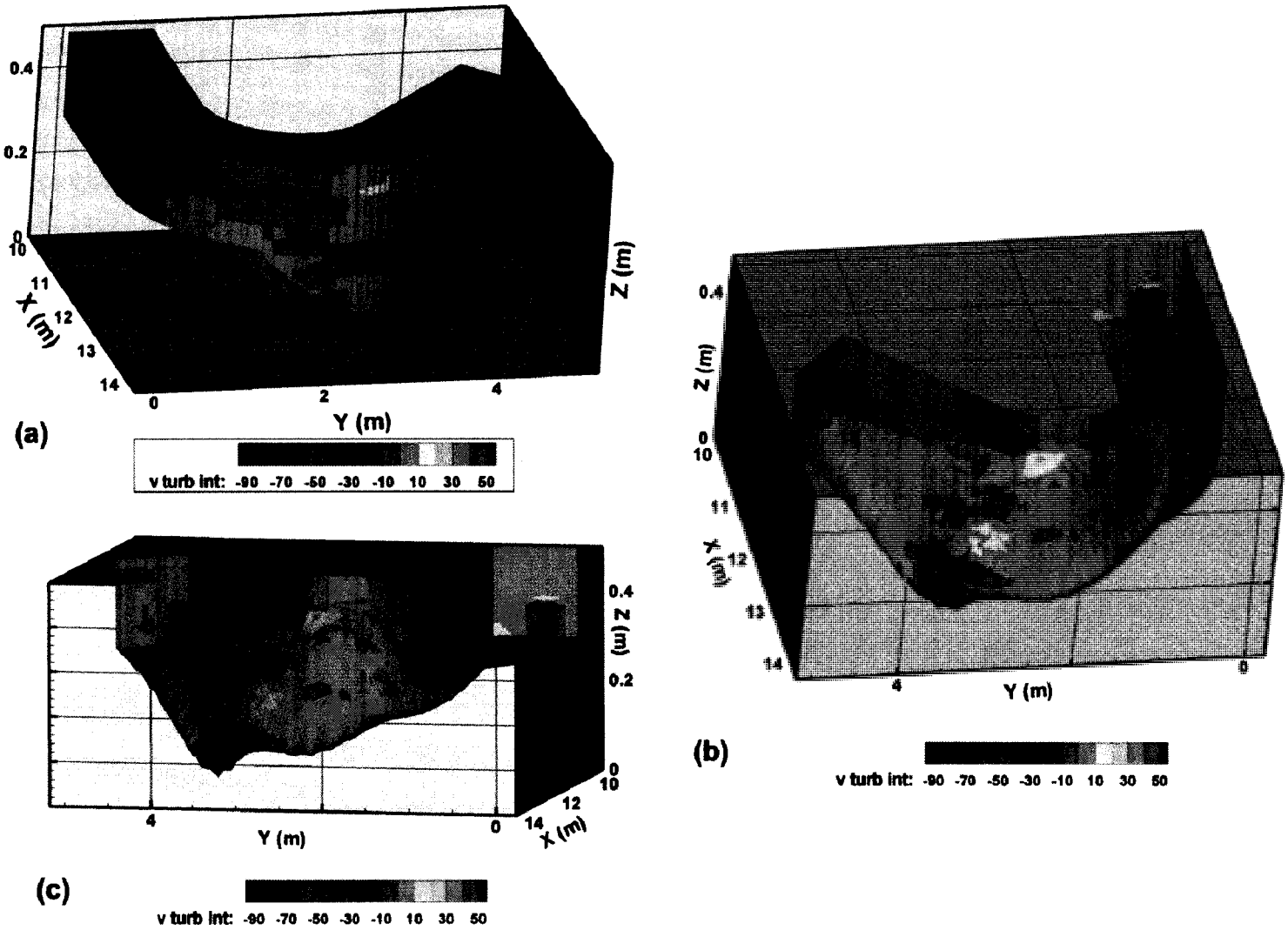

Figure 4-23. Overall 3D views of relative turbulent intensity; $\hat{v}$, in the streamwise direction; (a) outside view, (b) bottom view, and (c) inside view

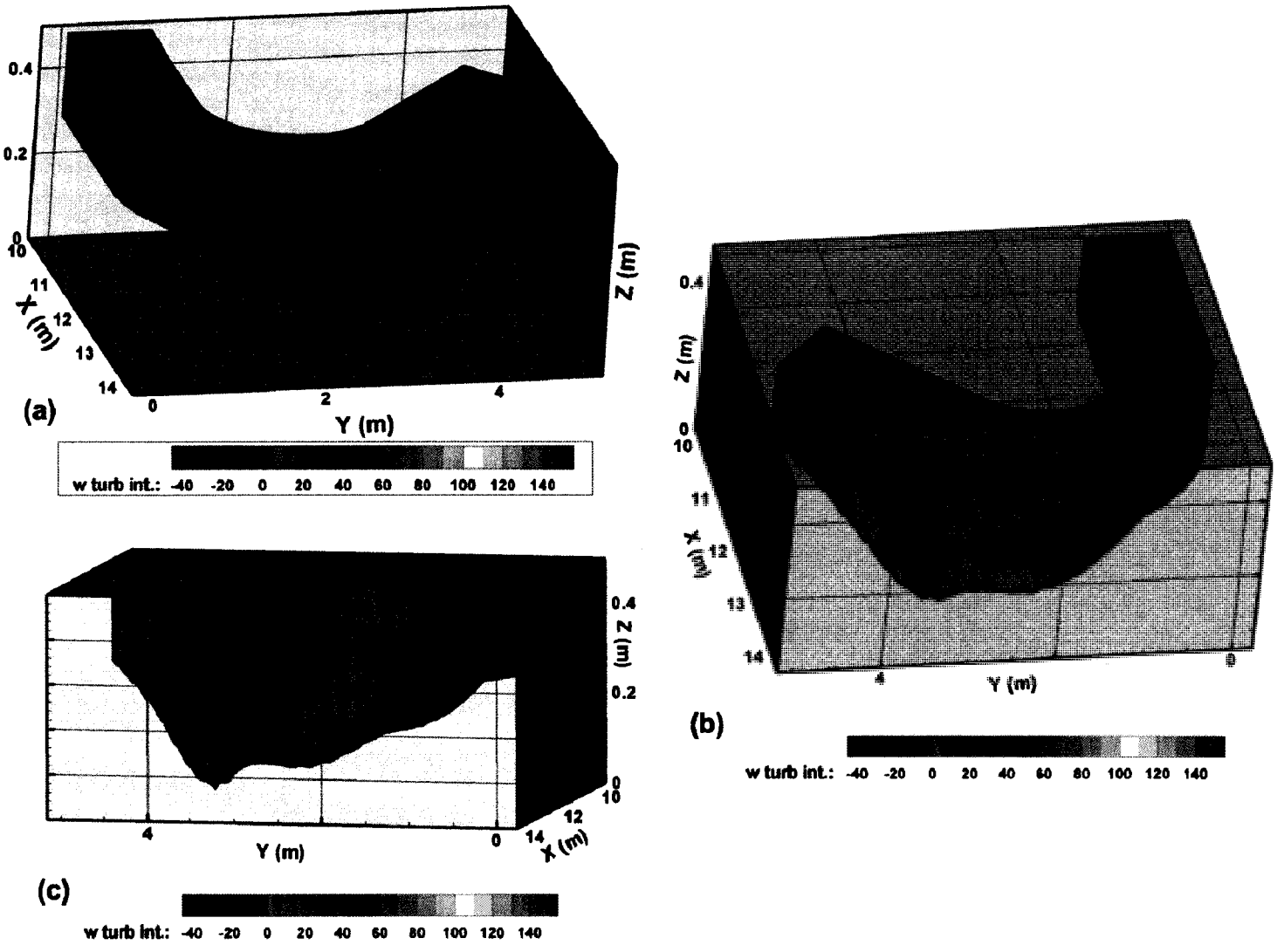

Figure 4-24. Overall 3D views of relative turbulent intensity; $\hat{w}$, in the streamwise direction; (a) outside view, (b) bottom view, and (c) inside view

4.2.5.7 Turbulent Kinetic Energy

This metric gives an idea of the overall turbulent energy in an area, regardless of direction. Notice that these plots are biased by a location of intense activity at the downstream tip of the point bar. Multiple plots are not required as all coordinate axes are represented in the single measure, k, as is shown in Fig. 4-26.

4.2.5.8 Streamwise Noise

As previously discussed in this chapter, noise in the streamwise direction, N, has been estimated using spectral analysis techniques. Overall views of the 3D surficial distribution of noise are shown in Fig. 4-26.

4.2.5.9 Average SNR, Average Correlation, and VZ error

Lastly, the indicators of ADV performance, average SNR and average correlation are presented in Fig. 4-27 and Fig. 4-28, respectively; along with VZ error in Fig. 4-29.

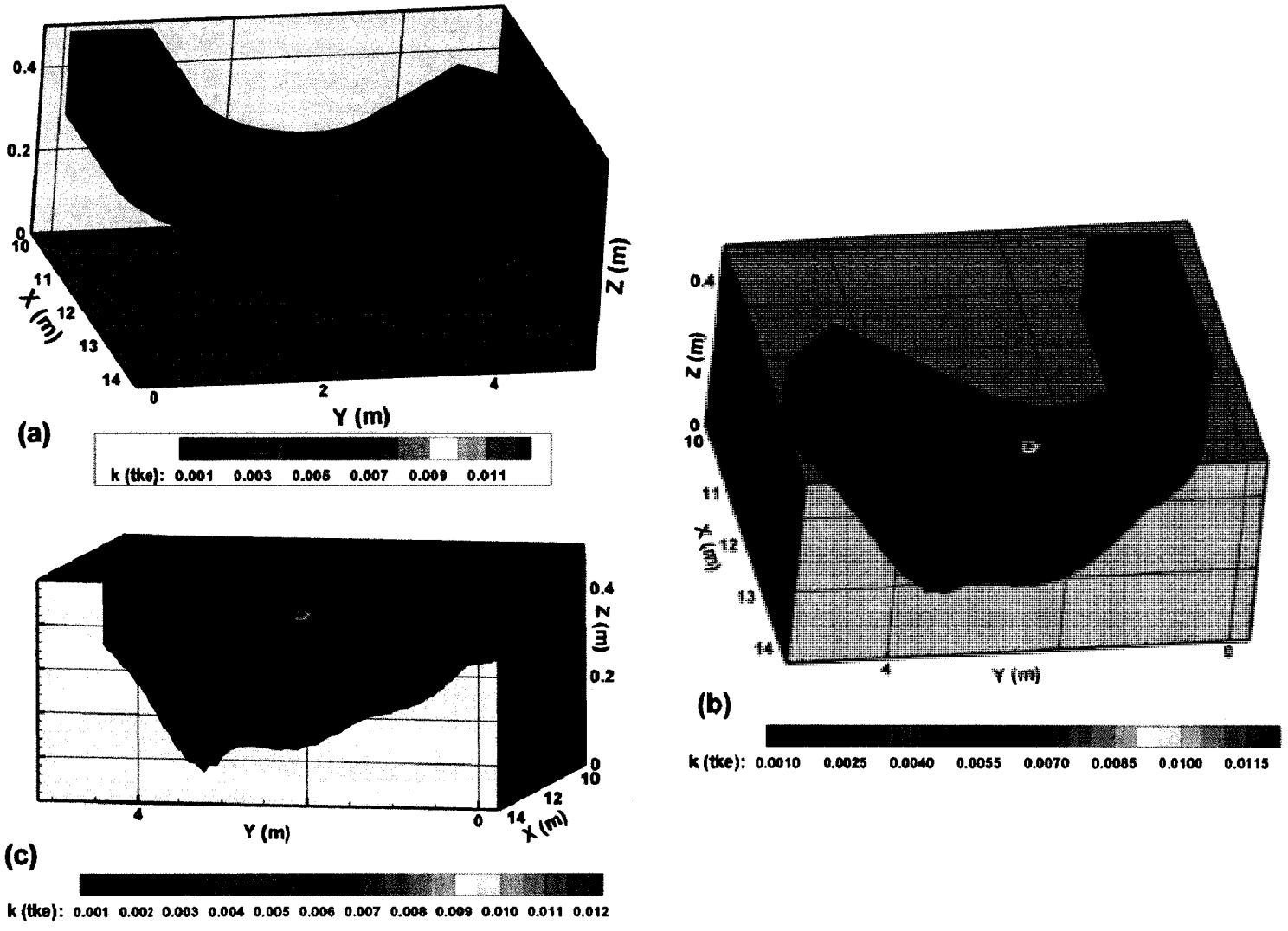

Figure 4-25. Overall 3D views of relative turbulent intensity, *k*, in the streamwise direction; (a) outside view, (b) bottom view, and (c) inside view.

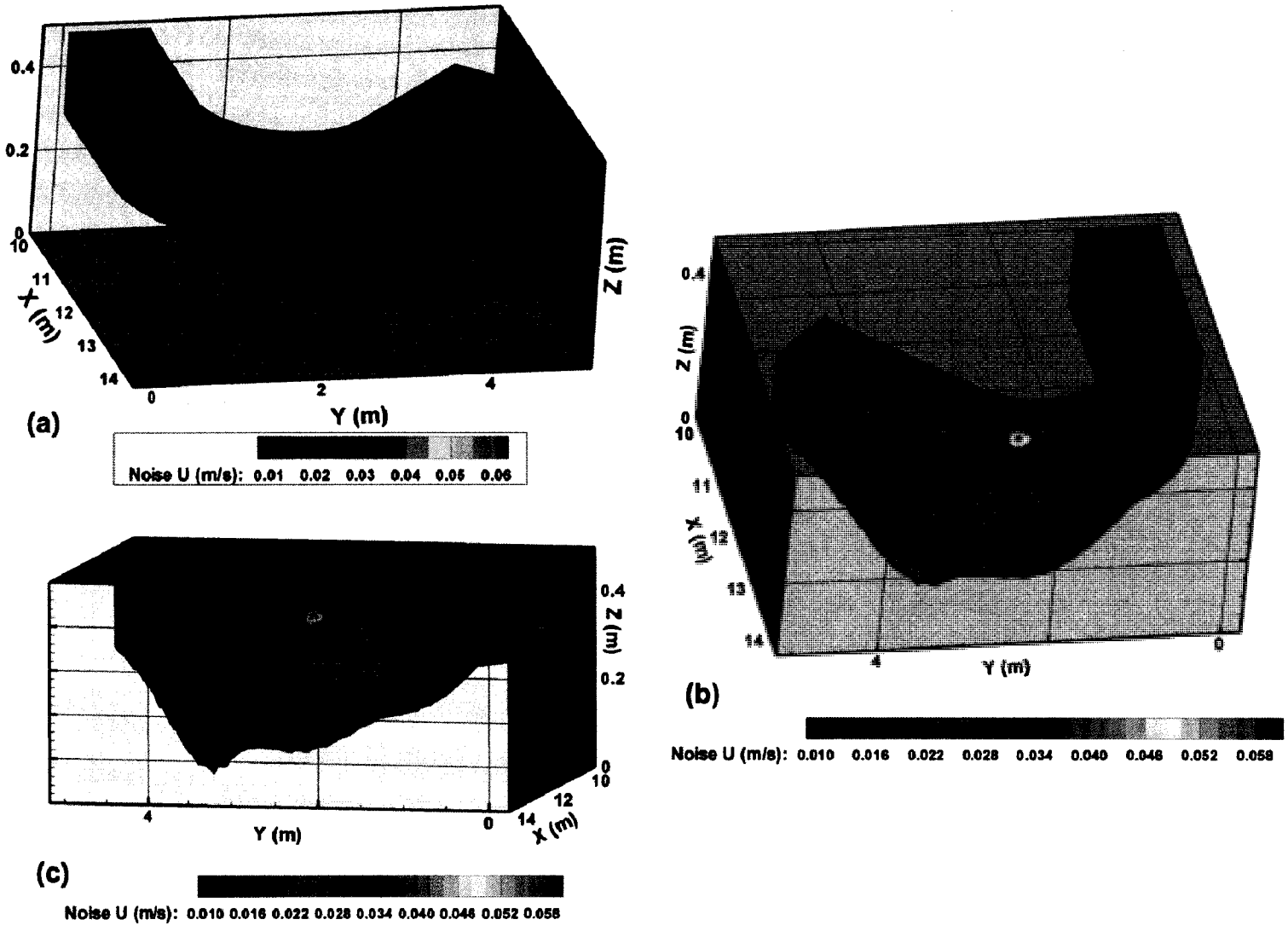

Figure 4-26. Overall 3D views of streamwise Noise, *N*, in the streamwise direction; (a) outside view, (b) bottom view, and (c) inside view.

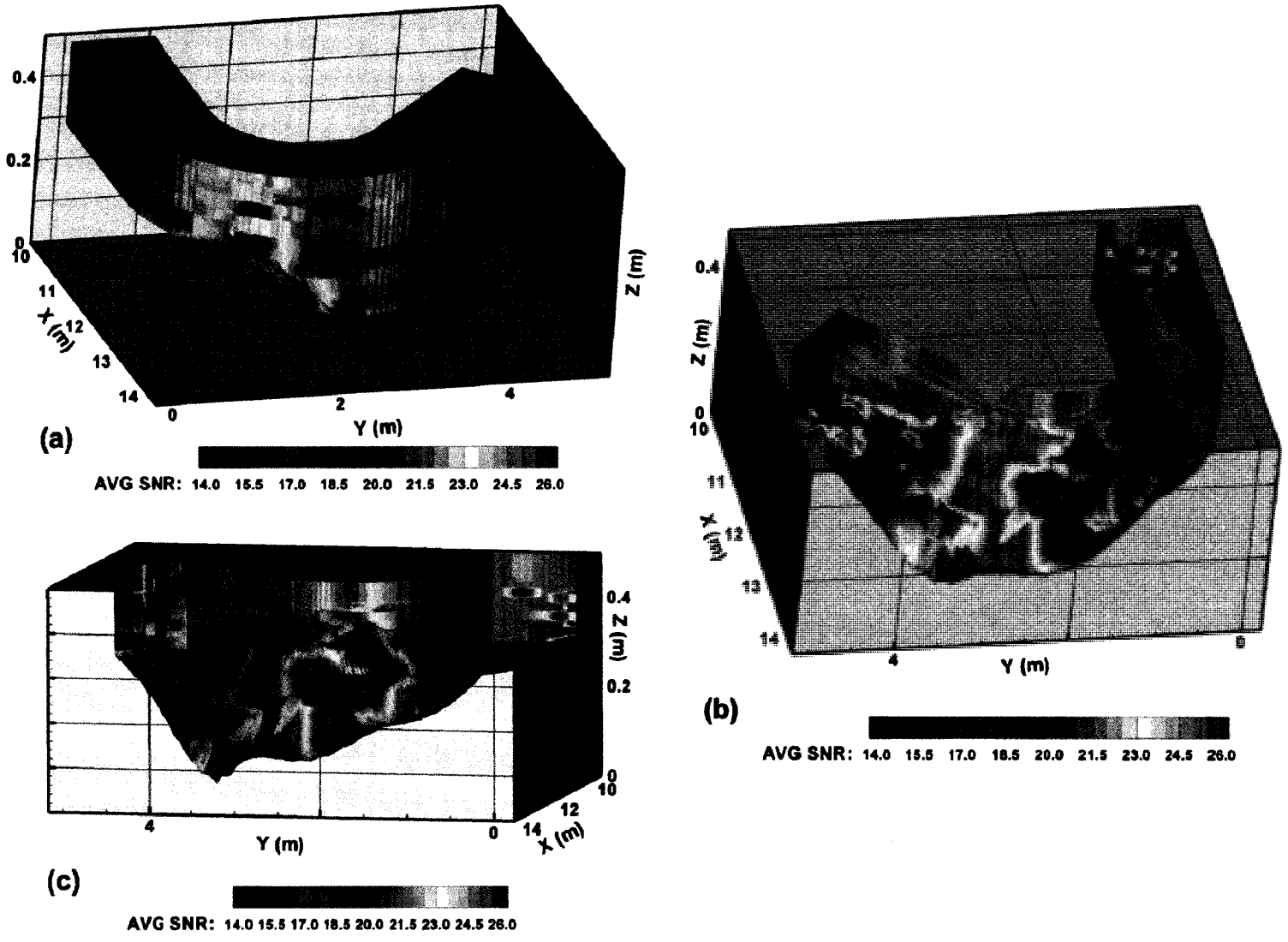

Figure 4-27. Overall 3D views of average SNR; (a) outside view, (b) bottom view, and (c) inside view

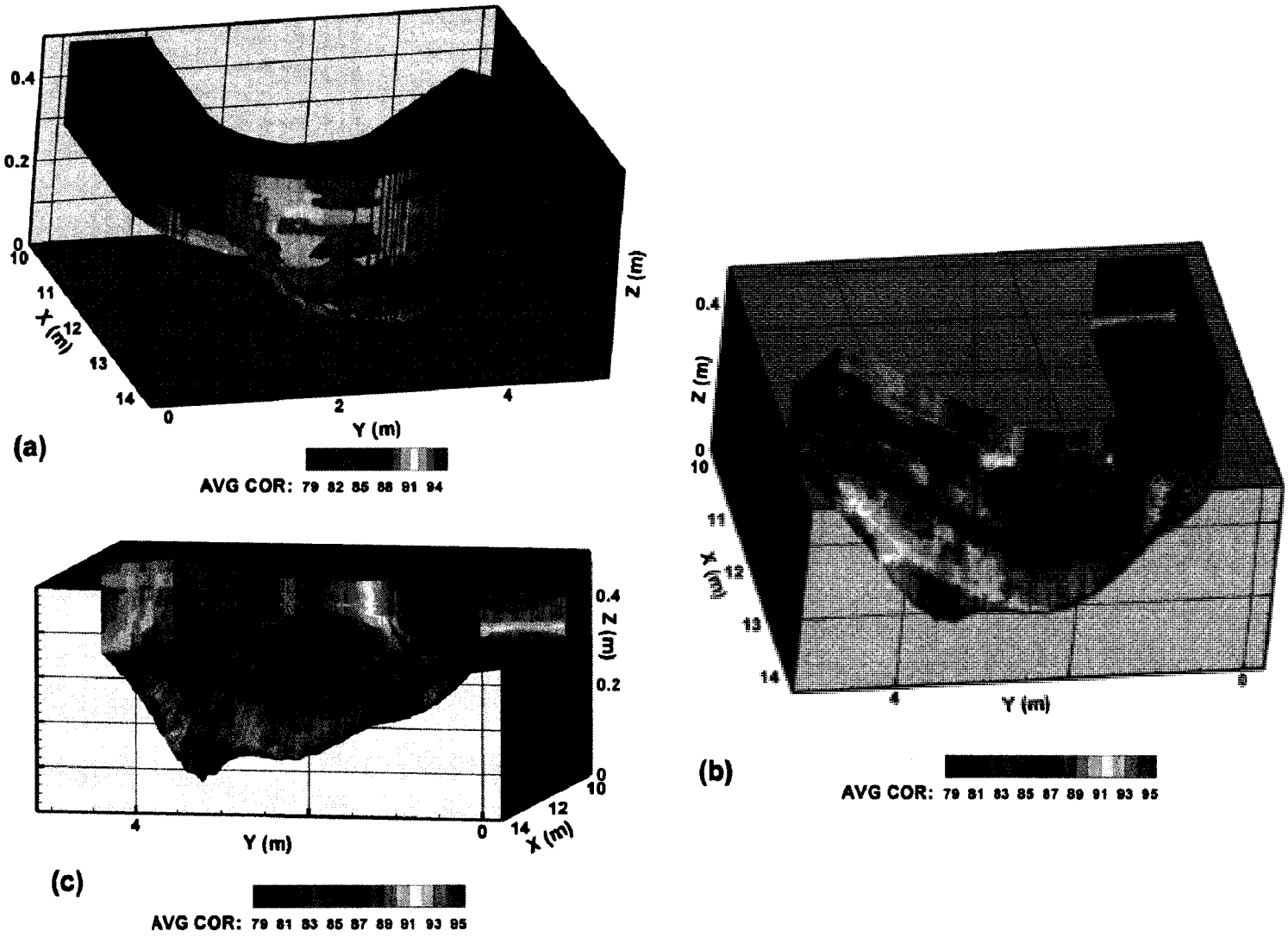

Figure 4-28. Overall 3D views of average correlation; (a) outside view, (b) bottom view, and (c) inside view

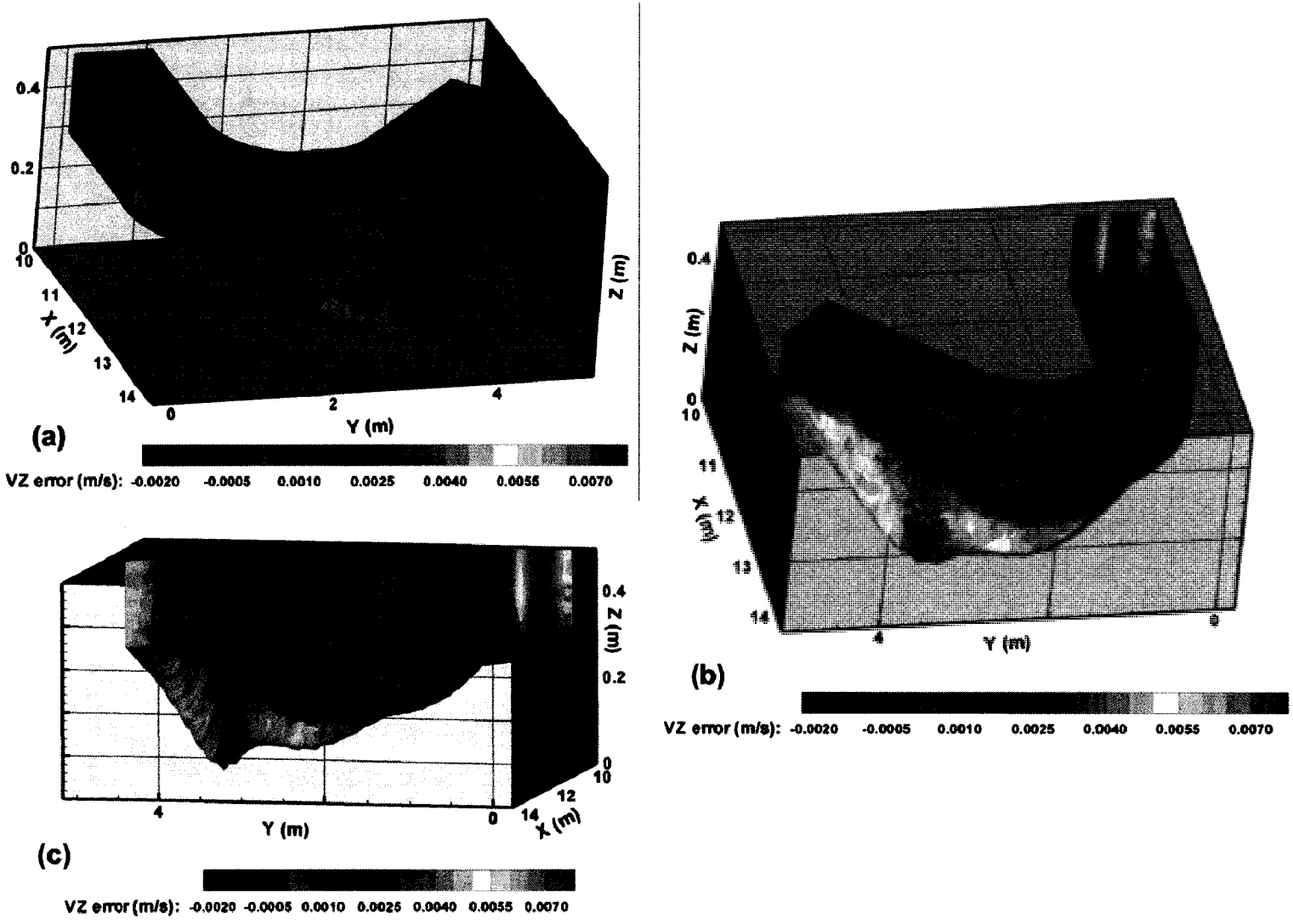

Figure 4-29. Overall 3D views of average VZ error; (a) outside view, (b) bottom view, and (c) inside view

4.2.5.10 Integral Time

Discussed in Section 2.6.3.1, integral time scale, T_E, gives an indication of largest eddy sizes in all three coordinate directions. By definition these are the largest fluctuations that are discernable from spectral analysis of the data, calculated by Eqn. 2.47. First, integral time in the x-direction (streamwise) is presented in Fig. 4-30, then the y-direction (cross-stream) in Fig. 4-31, and lastly, the z-direction in Fig. 4-32.

4.2.5.11 Microtime

This metric is determined by the turbulence dissipation at small scales (whereas integral time is related to turbulence production at large scales) and is calculated with Eqn. 2.48. Microtime is a measure of the time scale at which turbulent dissipation takes place. Longer microtime indicates that dissipation is taking place through relatively large eddies. However, it should be noted that the estimation of microtime is limited by the spatial and temporal resolution of the measurements. Microtime in each direction is presented similarly to integral time where x denotes streamwise and y denotes cross stream microtime, z is vertical and the 3D plots of these are shown in Fig. 4-33, Fig. 4-34, and Fig. 4-35 respectively.

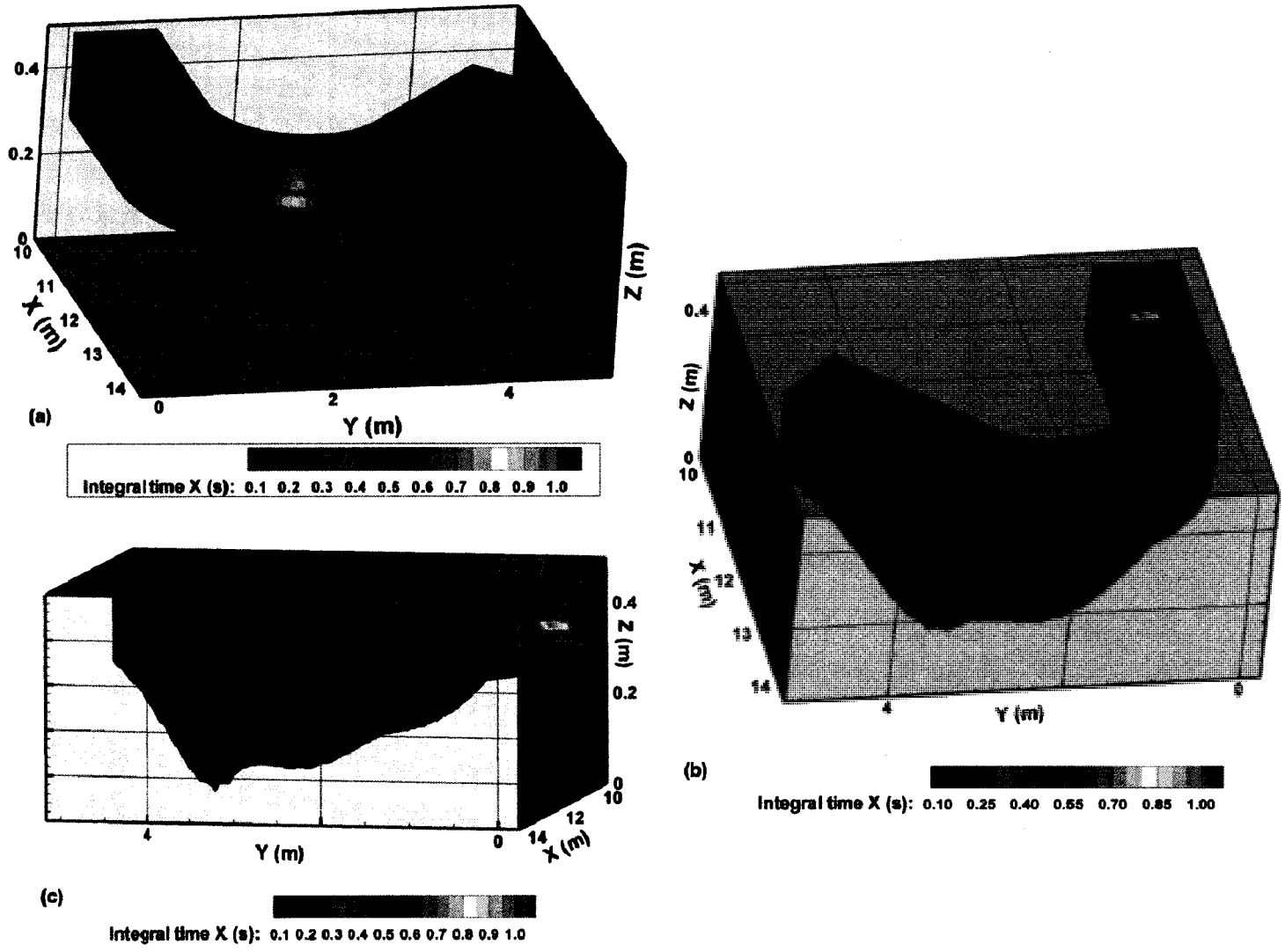

Figure 4-30. Overall 3D views of integral time, T_E, in the x-direction; (a) outside view, (b) bottom view, and (c) inside view

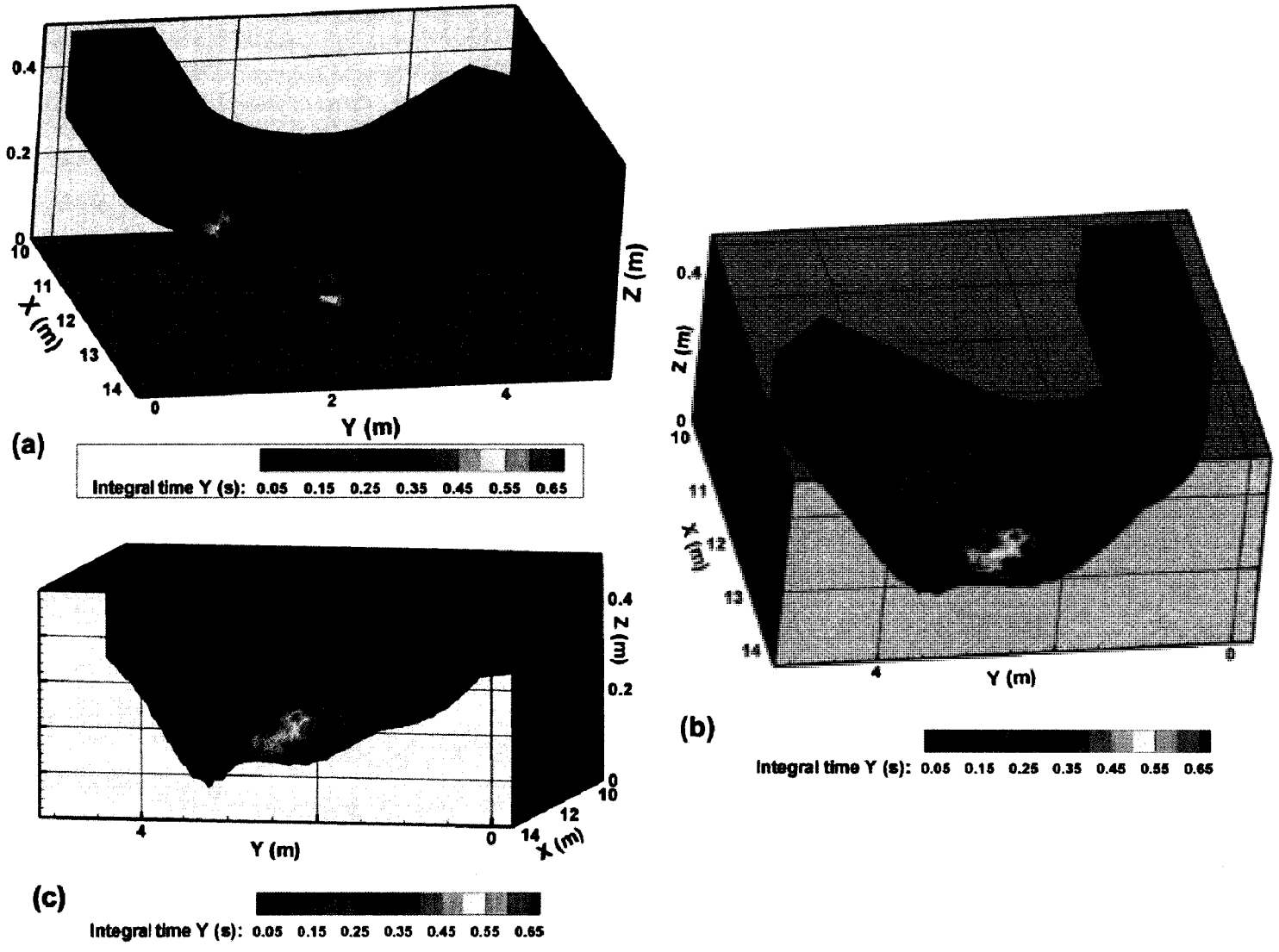

Figure 4-31. Overall 3D views of integral time, T_E, in the y-direction; (a) outside view, (b) bottom view, and (c) inside view

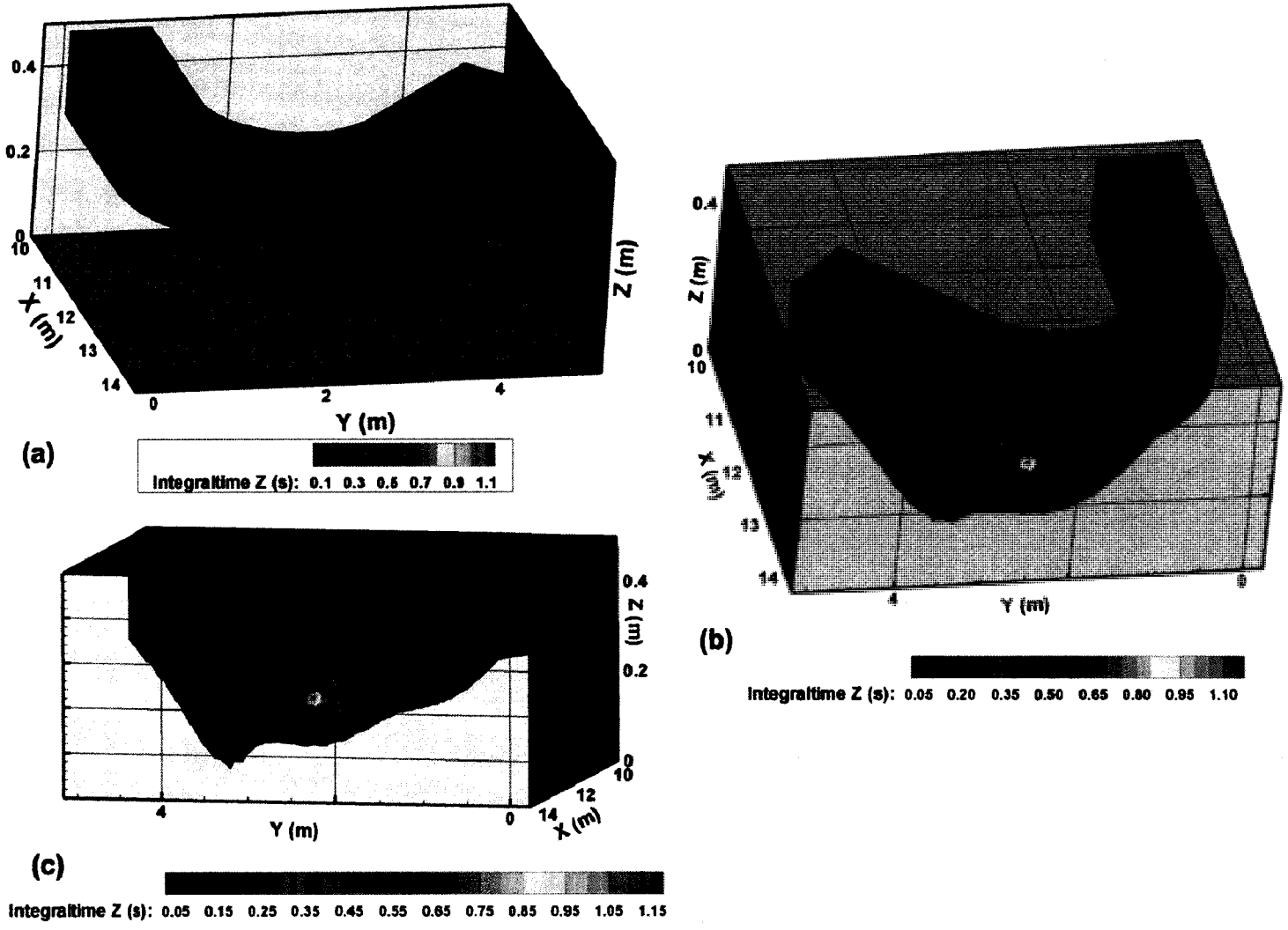

Figure 4-32. Overall 3D views of integral time, T_E, in the z-direction; (a) outside view, (b) bottom view, and (c) inside view

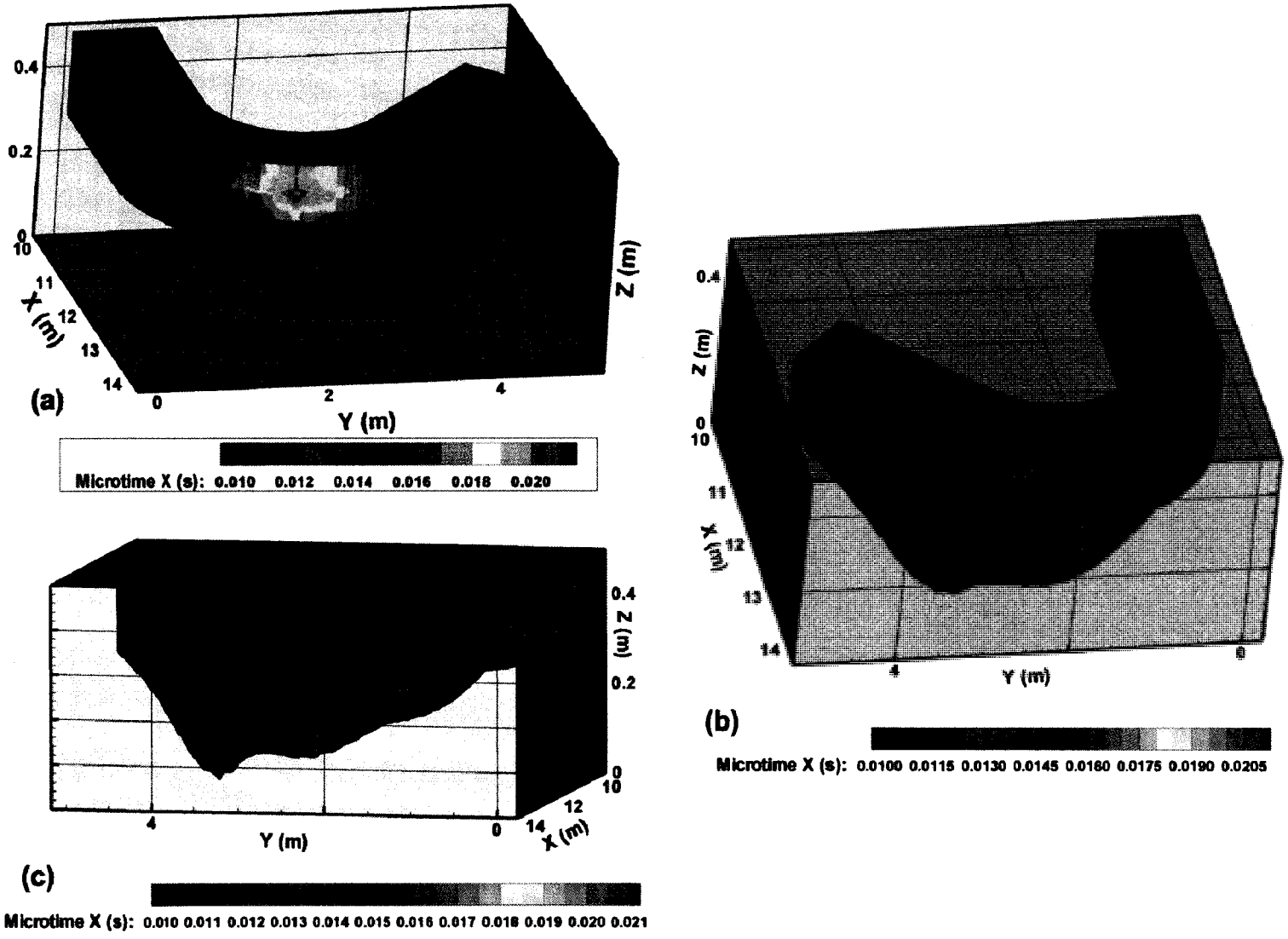

Figure 4-33. Overall 3D views of microtime, τ_e, in the streamwise direction; (a) outside view, (b) bottom view, and (c) inside view

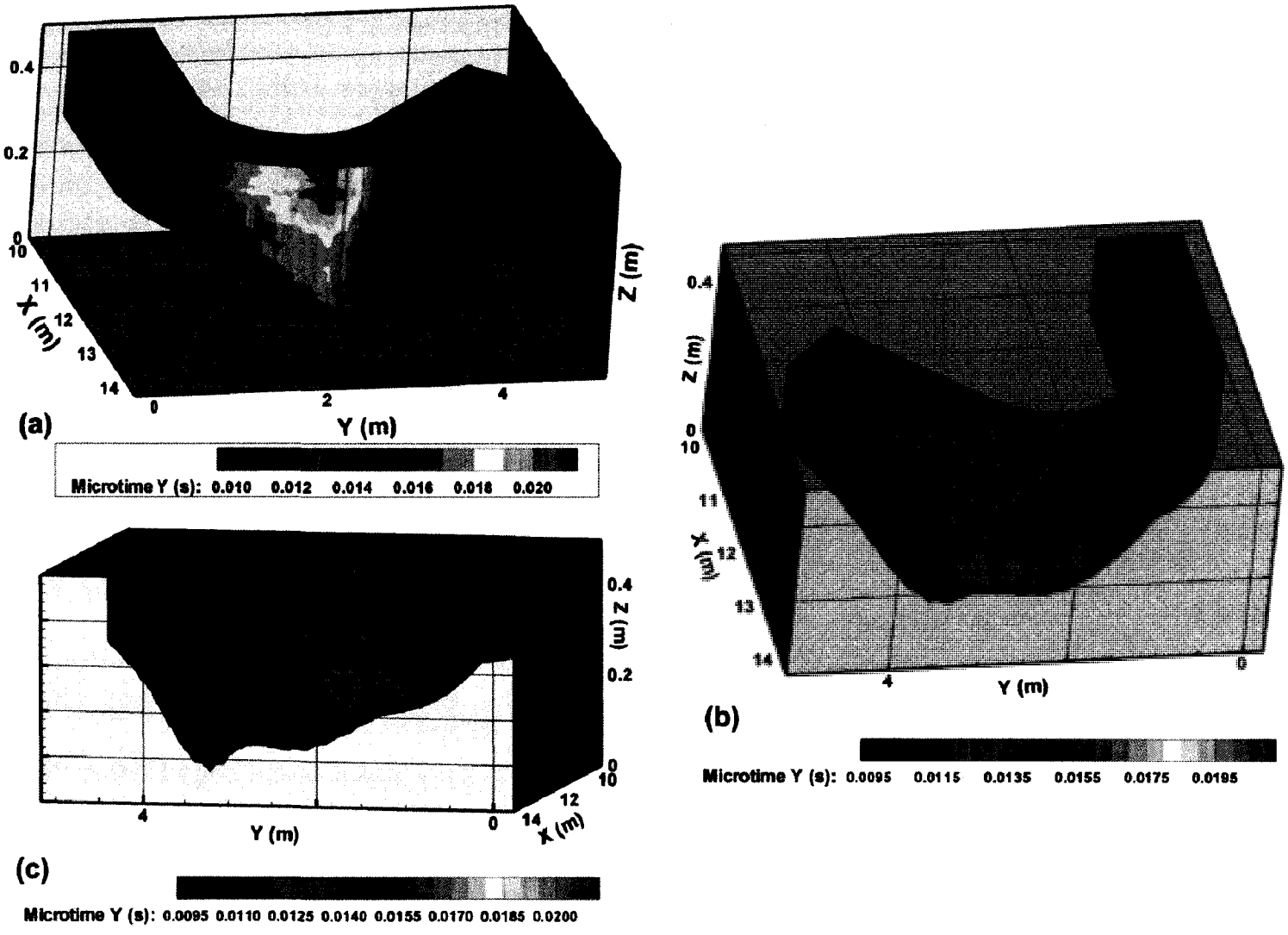

Figure 4-34. Overall 3D views of microtime, τ_c, in the cross-stream direction; (a) outside view, (b) bottom view, and (c) inside view

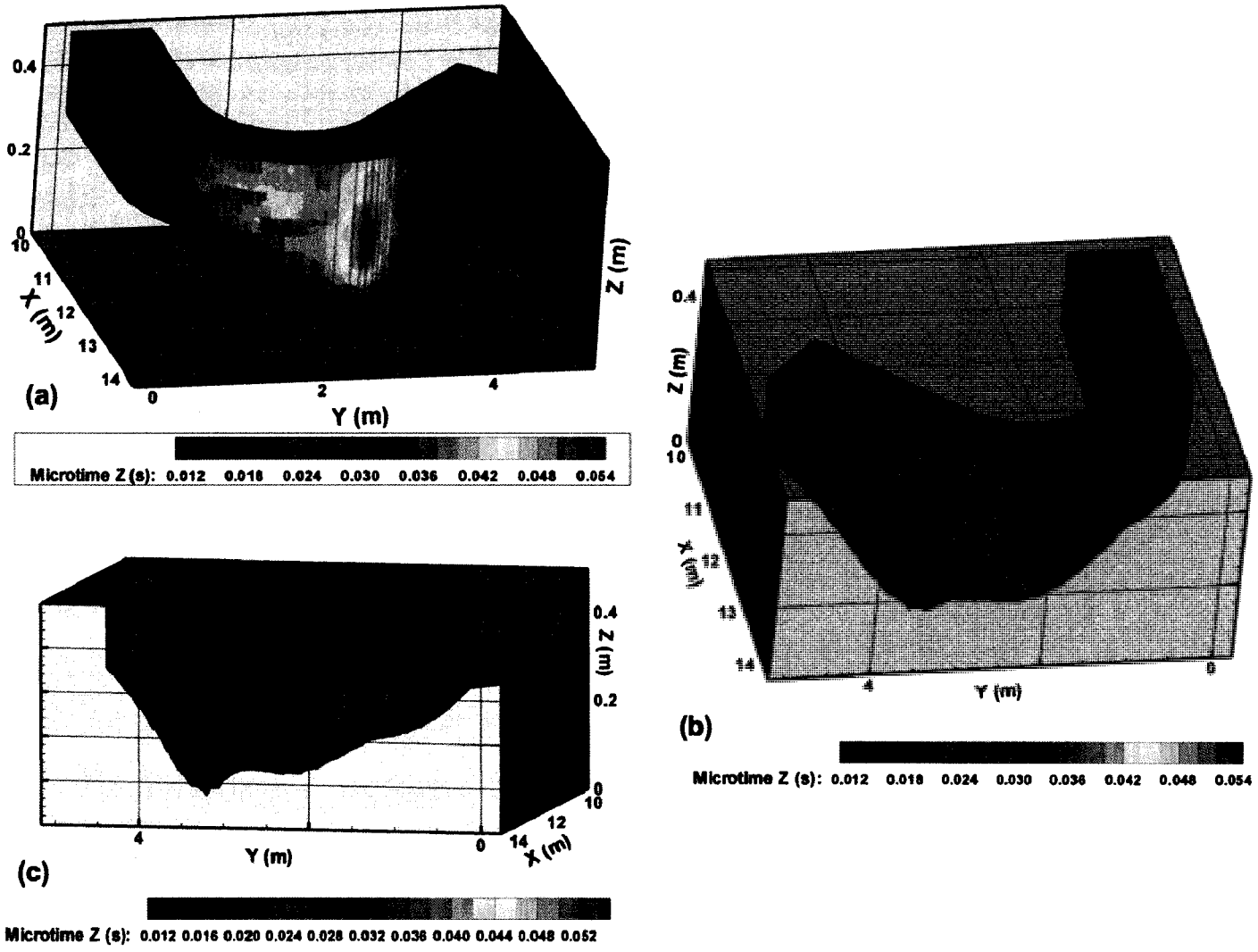

Figure 4-35. Overall 3D views of microtime, τ_e, in the streamwise direction; (a) outside view, (b) bottom view, and (c) inside view

4.2.6 Water Surface Superelevation

Of particular importance to the study of flow in river bends is the superelevation of the water surface slope, *E*, caused by centrifugal force in the bend. In terms of validating the results, slope is a key factor. A single measurement of cross-stream water surface slope was taken at the 75° cross section during the first experiment. The superelevation was measured to be 11 mm, which is very close to 10.5 mm which was predicted by Eqn. 2.57.

4.3 Experiment #2

With the first experiment conducted at clear-water scour conditions, an attempt was made at a second experiment with an increased channel slope resulting in live-bed conditions. This test utilized the novel sediment recirculation discussed in Section 3.2.3.5, and shown in detail in Fig. 3-12. While the observed mode of sediment transport was congruous with our intentions of lower plane bed transport, unfortunately this test did not run until completion due to system failure.

The screens that were used to separate the sand from the water in the first stage of the outlet tank worked well for the first 12 hours of the test. During this time, the system worked properly until the first stage tank started to overflow. Sand grains very close to the screen aperture size became lodged firmly into the screen. As the percent of open area on the screen decreased, velocity increased through the remaining open area increasing turbulent activity in the first stage tank, which restricted sediment settlement necessary for removal by the slurry pump. After a single episode of a large amount of sediment being transported out of the flume due to higher transport rates, the screen allowed no flow. Attempts were made at manually clearing the screen, but these attempts were futile.

Presenting the results of the observed mode of sediment transport in figures is not possible for this test. Evaluating the effect of the recirculated flow being re-introduced downward into the flow was closely monitored, however, and is shown in Fig. 4-36; part a of this figure shows the considerable surface disruption caused by the downward jet, and the protective effect of the bed protection system in part b. While this operated quite well, with the exit gate opened too much, water depth decreased to 16 cm and considerable sediment transport and dune formation was observed once the error was realized. Once uniform flow established again, however, plane bed movement was observed in one area not affected by the period of high shear, which remained constant over the remainder of the test. Procedures have been documented in Appendix A of this thesis, and were developed to avoid these errors.

Figure 4-36. Flow recirculation; (a) strong jet downward into flow (b) mobile bed protection details

This test will be resumed following some modifications to the system. The slurry pump is to be relocated to a section in second stage tank where sediment naturally accumulated during the first experiment. The sand separation screens were not in place during the first experiment and sand was deposited in the second stage tank directly downstream of the tank union. By moving the slurry pump into the location where sediment was accumulated during the first test, a draw will be created in this area making sediment removal possible.

The use of the gate valve on the sediment return line resulted in more effective establishment of uniform flow for the second test because it allows for precise control of flowrate. Also, after the reported period of increased shear, the clear walls of the flume made visual observation of sediment transport possible at all points along the channel. By closely examining the highlighted region of Fig. 4-37 (taken with an exposure time of 1/100 s) sediment trajectory from the dune crest is seen, as well as in the trough just downstream, which is quite similar to the bursting effect of turbulence shown in Fig. 2-17.

No ADV measurements were made during the second test because equilibrium was not established over the 12 hour run.

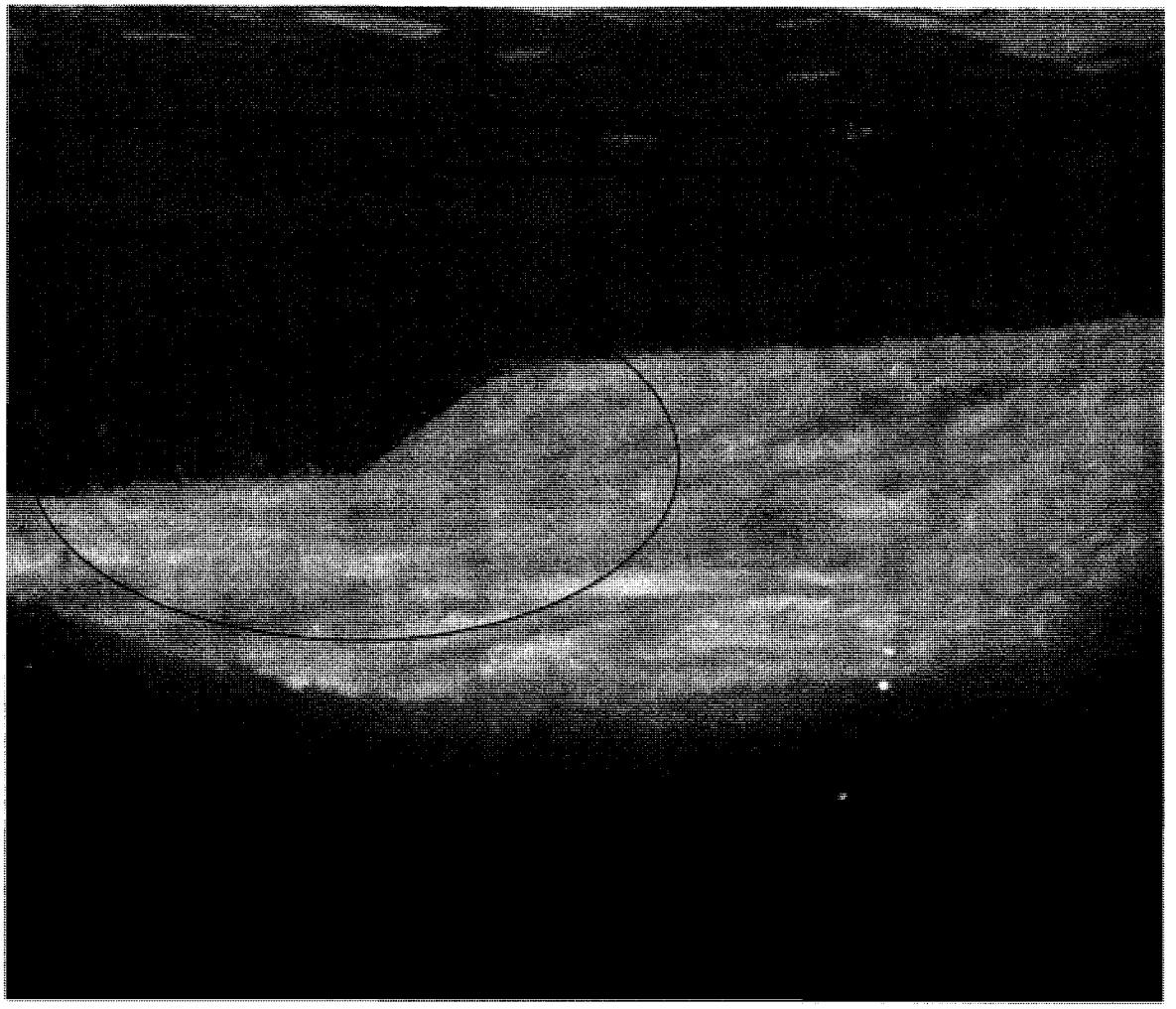

Figure 4-37. Observed sediment transport through clear flume wall in Run 2

Chapter 5 Discussion

5.1 Introduction

While this study was originally intended to be a calibration exercise in determining the performance of the apparatus developed by the author, the results of the first experiment reported in this thesis were successful beyond our expectations. The MatLab code utilized to analyze mean statistics and power spectra provided us with a wealth of information on the flow field, the results of which clearly show the high quality, high frequency ADV measurements are worthy of further analysis. With data being highly congruous in its mean flow properties with our present understanding of flow in bends and secondary currents, the supporting metrics that have been calculated can be analyzed with confidence.

Over 1.4 M individual velocity measurements were taken in 609 measurements lasting two minutes each; for over 20 hours of time-series data, computation time and data management become key factors. Also, the coding generated 33 variables in total, ranging from very tangible physical metrics such as mean velocity and turbulent fluctuations, to the more theoretically based spectral analysis metrics such as integral time and microtime, with several indicators of ADV performance also included. Tecplot 360 has been employed for plotting interpolated values throughout the entire flume bend in three different 3D views. However, because integral length, microlength, and Taylor's microlength are only calculated if relative turbulent intensity is < 0.25, there are then gaps in the data set and thus these values were not interpolated by Tecplot. Also, by averaging the four-beam SNR and correlation values the original 33 variables were reduced to 23. Therefore, with the already mentioned 3D overall views, which have then been "sliced" into 12, 2D cross-sections, each plotted twice with different scales, over 700 figures of the interpolated ADV "volume" have been produced, all of which are included in Appendix C of this thesis.

The production of these figures took a considerable amount of time to accomplish. An attempt is made here to highlight the more significant conclusions which can be drawn thus far, most notably the discovery of a concentration of principal Reynolds stress at the beginning of the scour hole very near the bend entrance, and another at the downstream tip of the point bar near the inside of the bend. Both relative and absolutely scaled figures are provided in two separate groupings sorted by cross-section and by metric, respectively. These are extremely interesting to look through in slide show format. Refer to Fig. 3-19 of this thesis to gain perspective on point measurement locations.

5.2 Boundary Layer Development and Sediment Transport Rates

With two rates of sediment transport "designed" for the experiments reported in this thesis, observed transport was adequately in agreement with expectations. As summarized in Section 3.3.2, for the first experiment, a channel slope of 0.044% was estimated to give a friction velocity, U_*, of 0.0250 m/s which lies directly on the Shields' curve for sediment of this size. Friction velocity was calculated to be 0.0188 m/s as presented in Table 4-3, which explains why very few grains moved in the straight approach section. However, the calculated bed shear at 10 m was less than our predicted values (Table 4-5) because boundary layer development was not complete (77%), which is critical for the accurate application of all concepts outlined in Chapter 2. At the 12 m cross-section, effects of the bend are clearly shown in both velocity plots (Figs. 4-2 and 4-5), most notably in the measurement taken at 0.133 m from the right channel wall where downstream velocity is clearly suppressed. As a consequence, the calculations from straight channel theory presented in Tables 4-4 and 4-6, while not directly applicable, are provided for comparison as they are consistent with expected bend effects.

It is unclear as to whether the turbulent boundary layer became fully developed in the first experiment. At the 10 m section the boundary layer was approximated at being 77% developed, and slightly more developed (81%) at 12 m. No measurements were made at the 11 m section of the flume during the first test, and it is possible that in that region the boundary layer becomes fully developed before being affected by the channel curvature. Again, no velocity measurements were made for the second test and based on the results of the first experiment, it is concluded that the turbulent boundary layer was not fully developed.

During these experiments it was felt that the angularity of the grains indeed increased critical shear values for the sediment due to the packing of grains. However, without a fully developed boundary layer, direct comparison of measured bed shear parameters from the first experiment is not applicable. The second experiment was intended to be at live-bed conditions and more specifically with lower plane bed movement without the presence of dunes as this would complicate analysis.

In determining slope for the second experiment using Fig. 2-10 for a particle size of 1.1 mm, rather than follow the margin for lower plane bed movement with a value of critical dimensionless boundary shear stress ($\tau_{*c} \approx 0.04$), a value of 0.05 was chosen to determine the 0.064% slope. With Fig. 2-10, taking $\tau_{*c} = 0.05$ and a particle size of 1.1 mm, the predicted regime lies in the transition zone between lower plane bed and dunes. This transition zone is interpreted to be primarily plane bed movement with intermittent dunes occurring. For the second

test, uniform plane bed transport was observed in the straight approach which verifies live-bed conditions were achieved. However, the transport regime was less than predicted as no dunes formed at uniform flow conditions. It is hypothesised based on these two tests that the angularity of the grains did indeed increase the critical shear.

5.3 ADV Measurements

5.3.1 SNR, Correlation, and VZ error

Little mention has been made previously in this thesis about the significance of the success using the 200Hz sampling frequency, as typically the reduction in averaging between samples increases the noise in the data. With high quality measurements having average correlations from each beam velocity over 90%, average SNR from each beam measuring over 21 dB, and very low VZ error with an average value of 0.003 m/s, conclusions can comfortably be drawn from the data.

Owing to the use of other lab equipment directly previous to these experiments, which had long lay dormant in the hydraulics lab, the 300 m^3 reservoir contained a high level of suspended particulate in the form of iron oxides. This suspended particulate increases the amount of acoustic pulse energy that is returned to the receiving transducers, thus reducing noise, and increasing SNR and correlation. Also, the acrylic flume walls and silica sand must play a role in the quality of measurements. Owing to a highly elastic behaviour, acrylic materials are ideal for ADV operation as it absorbs stray sound energy well.

5.3.2 Noise and Near Bed Performance

The results of an analysis of streamwise noise calculations were presented in Table 4-8. With an average value of 0.0186 m/s, it is reasonable to conclude that these are high quality measurements as mean noise is less than 5% of the depth averaged velocity of 0.394 m/s at 10 m. By examining Fig. 4-32 we see the area of maximum noise at 0.0686 m/s, near the downstream tip of the point bar at the 105° cross-section, which somewhat dilates the rest of the plot. It should be noted, however, that noise was consistently higher on the sloped point bar surface. With this cross-section observed to show the maximum amount of transport movement along its steep point bar slope, twice the number of vertical profiles was taken. One of the time series taken 0.15 m from the left channel wall at 5 mm from the bed was thought to be erroneous whilst the measurements were taken. However as this was the authors' first extended use of such equipment, these "bad" time series were left unchanged until further analysis could verify this assumption.

If we view several cross-sectional plots of noise, average SNR, and average correlation with relative scales (overall values) as is shown in Fig. 5-1, it is observed that not only is noise high (part c) in the upper left portion of the point bar, but an increase in SNR (part a) and decrease in correlation (part b). It is hypothesized that this is caused by a combination of ADV sampling error related to sediment transport introducing sand grains into the sample volume and/or limited submergence of the transducers. Based on this, these data points were initially thought to be erroneous from a stress and turbulent fluctuation standpoint. However, mean velocities in each direction show little or no effect at the 105° cross section (Figs. 4-13, 4-14, and 4-15). More important is the fact that principal Reynolds stress did not display an outlier at this location, thus the data set was kept intact. However, it should be acknowledged that streamwise and cross-stream turbulent fluctuations (Figs. 4-19, 4-20) were very high at this location, thus the measurement remains suspect.

Introduced in Section 2.3.6, Precht et al. (2006) report a noted lack in ADV performance near a sediment bed from a series of comparative tests with several different ADV models, none of which were the Nortek Vectrino. The sensors in that test were set at a sampling frequency of 8 Hz which is considerably less than the high frequency measurements made for this thesis. For the first experiment noise and correlation are consistently lower along the point bar surface, and SNR seems to be lowest in the locations where maximum sediment transport is likely to occur as shown in Figs. 4-26, 4-27, and 4-28. Regardless of this trend near the bed, no average measurement fell below the commonly accepted minimum values of correlation at 70% and very few below the SNR minimum of 15 dB, respectively.

The ADVs also performed adequately at 0.1 m from the bed which is known to cause error as the bed is exactly twice the sample volume distance to the bed. Also, if the bed is amply sloped, scattered sound from the control volume reflects off the bed toward one transducer with only a small time delay which can cause error. In general, however, it is felt that the noise on the surface is likely due to either: a) bedload transport in the sample volume, or b) higher turbulence. Also, because the latter is also a possible cause for the high turbulent fluctuations near the point bar tip discussed above, the data set was not altered.

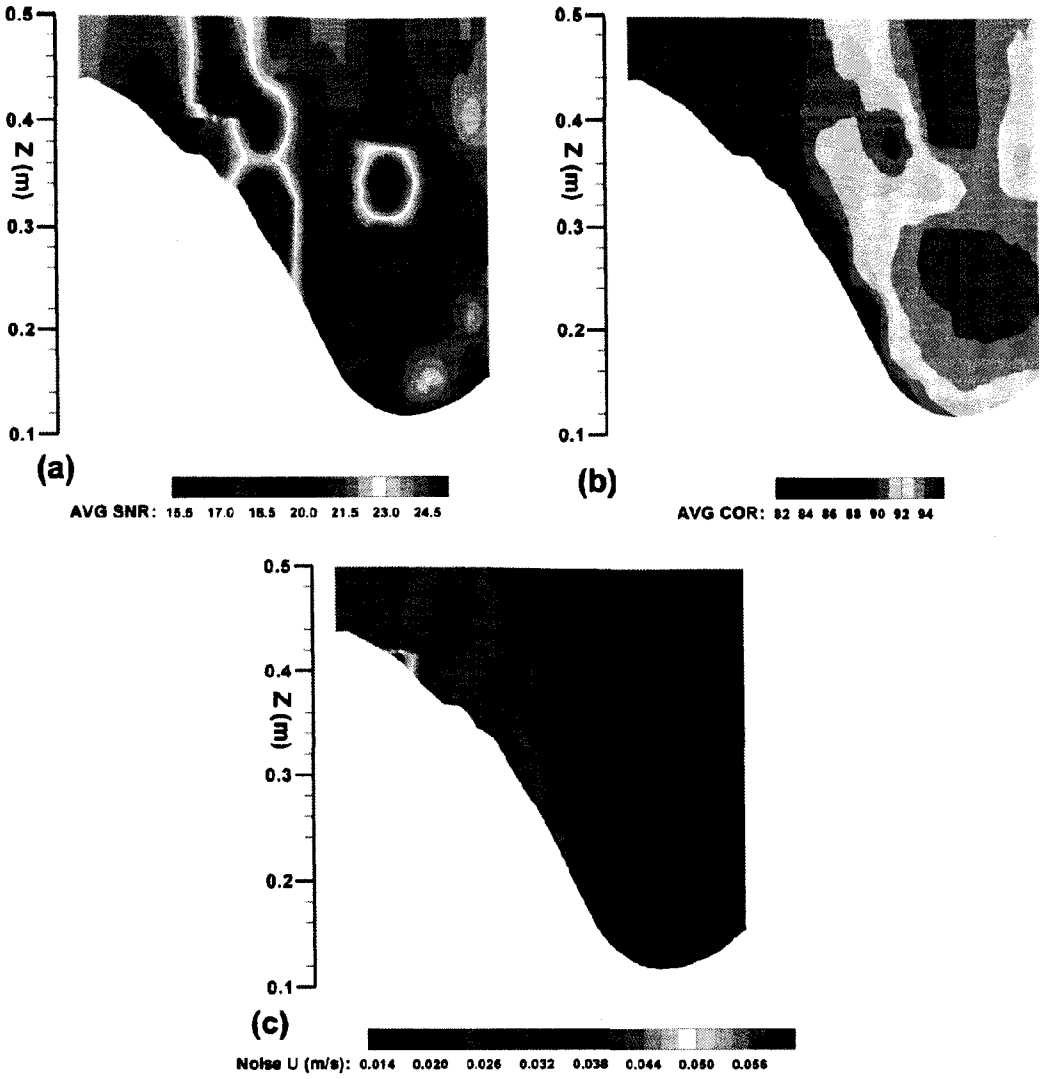

Figure 5-1. Comparison of; (a) average SNR, (b) average correlation, and (c) noise in the streamwise direction (facing downstream) viewed with relative scales taken at 105°

5.4 Velocity Data Interpretation

5.4.1 Mean Velocities and Secondary Circulation

The 3D plots of mean velocities presented in Chapter 4 demonstrate a strong adherence of the results from this thesis to the proven aspects of helical flow and secondary circulation presented in Section 2.8.1. We will use here a combination of references to the 3D plots from Section 4.2.5.4 and a combination of selected 2D plots to support statements.

First, from mean streamwise velocity (Fig. 4-13) we see that the core of maximum velocity is pushed to the inside of the bend as it enters, and is then suppressed until mean flow is increased again in the outside of the bend in the adversely sloped scour hole exit. Figure 5-2

shows a sequence of cross-sections (relative scale) taken in the following order; 10 m, 30°, 75°, and 125° (Fig. 5-2a, b, c, and d, respectively). This shows that the core of maximum velocity was not suppressed uniformly near the apex of the bend, rather the core was shifted first from the inside of the bend, then pushed outward and down into the deepest part of the scour hole near the bend exit. The core of minimum streamwise velocity is also observed in Fig. 5-2b at the right channel wall near the beginning of the scour hole.

Figure 4-14 shows mean cross-stream velocity where positive indicates flow from channel right to left (toward the inside of the bend). In analyzing this plot, one must pay attention to the slight change in colour as hues of green/yellow represent slightly negative and positive cross stream velocities. In this 3D view, secondary circulation is quite apparent. Maximum positive values were measured near the bed throughout most of the scour hole. The maximum negative values, which were deep enough within the water column so as to show outward directed flow up to the interpolated surface, are strongest only up to the bend apex which coincides with the observations made from Fig. 5-2.

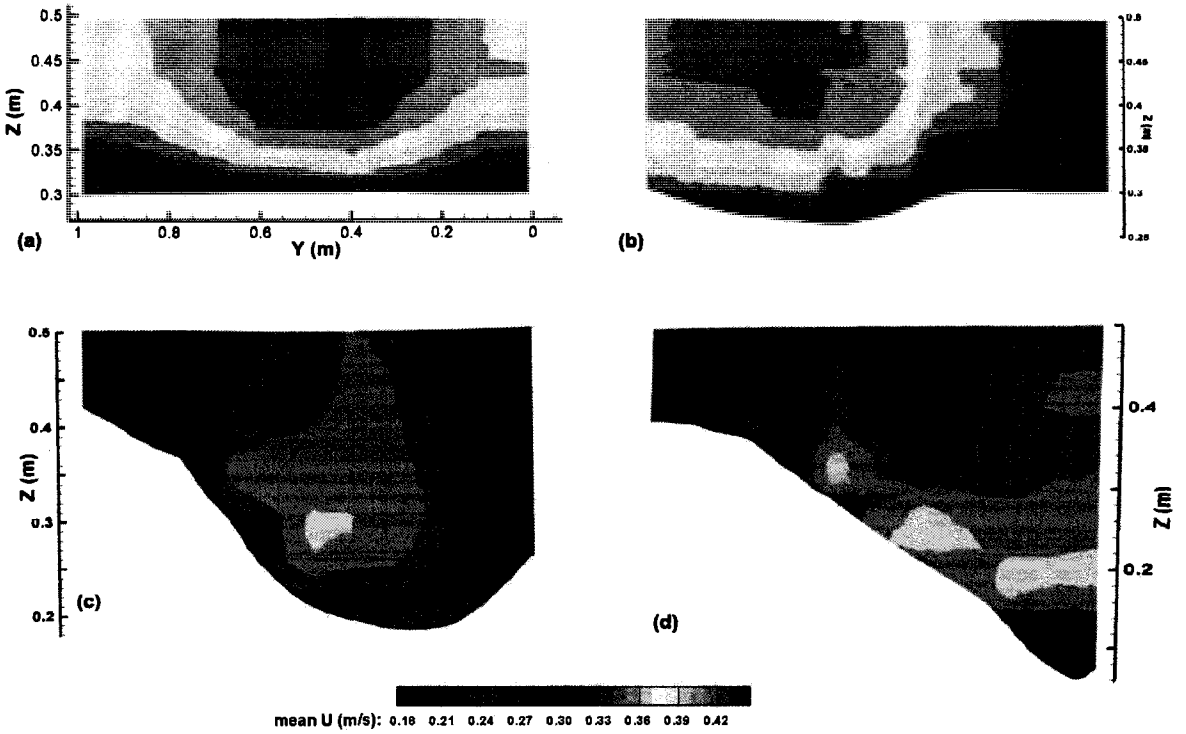

Figure 5-2. Comparison of $\overline{U}$ (facing downstream) with relative scales; (a) 10 m, (b) 30°, (c) 75°, and (d) 135°

Analysis of cross stream processes is affected by the minimum submergence depth of the ADV. Upon first inspection it was thought that cross stream measurements made at 12 m (Fig. 5-3) may be erroneous as they show no negative value. This would indicate a net flow out of the flume which is not physically possible. However, considering that 30% of the flow depth at the 10 and 12 m sections could not be measured, it is possible that surface velocities were indeed negative. There are two other plausible explanations for this; the effect of twisted probe heads was not entirely corrected by resolving measurements, or that the equipment carriage was not precisely perpendicular to the flow.

Figure 4-15 (mean vertical velocity, $\overline{W}$), lends further support to the identification of secondary circulation, and shows the maximum downward velocity occurs on the outside of the bend near the apex, and maximum vertical velocity just past the bend apex. This indicates that the water "somersaults" as it enters the bend creating helical flow, which is congruous with the observations made from the mean streamwise plots in terms of the location of minimum streamwise velocity (Fig. 5-2b). It is postulated that the strong downward flow at the outside of the bend creates its own vortices as it impinges downward on the scour hole crest. This seems to have a protective effect on the bed pushing the core of maximum velocity back toward the inside of the bend.

A more detailed look is provided in Fig. 5-4a-d, which shows cross-sections taken at 30°, 60°, 90°, and 135°, respectively. Figure 5-4c clearly shows that secondary circulation indeed exists throughout the bend, which is further supported when combined with the presented analysis of mean streamwise and cross-stream velocities.

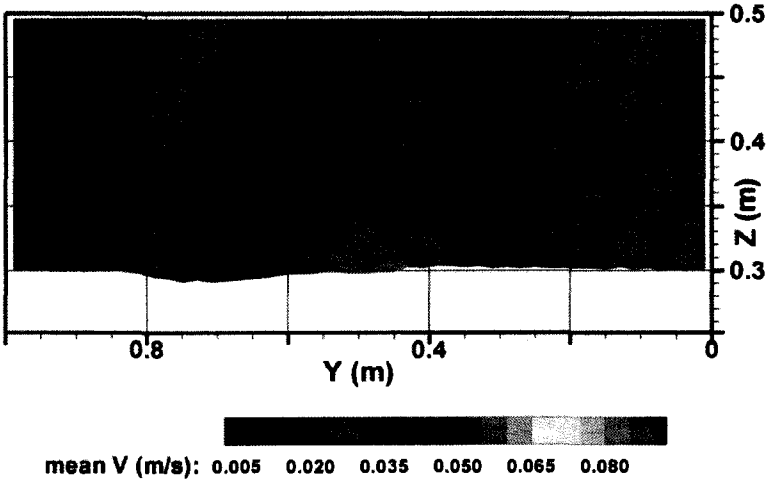

Figure 5-3. Mean cross stream velocity, $\overline{V}$, at 12 m (absolute scale)

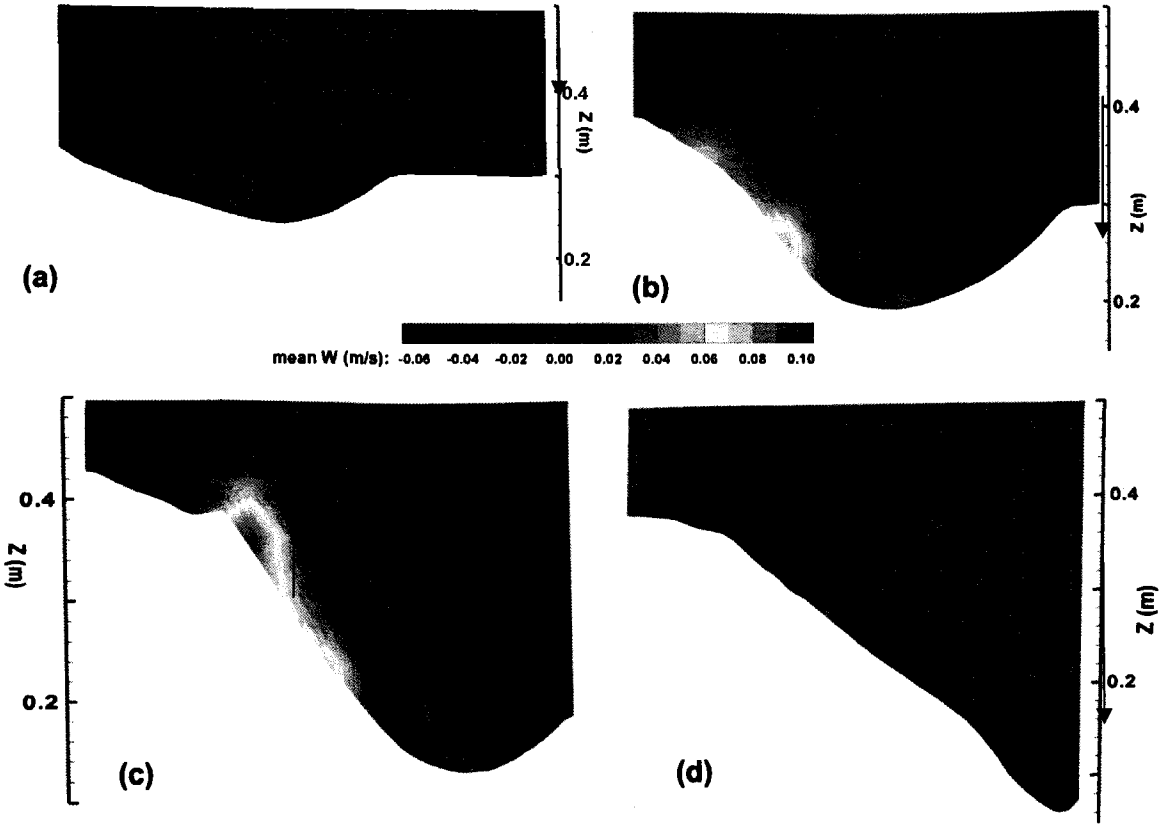

Figure 5-4. Comparison of $\overline{W}$ with relative scales; (a) 30°, (b) 60°, (c) 90°, and (d) 135°

5.4.2 Reynolds Stress Distribution

Outside of their lack of documentation in the literature, and their importance in the calibration and validation of numerical models, the three Reynolds shear stress terms describe the stress on various faces of the fluid particle due to shear from turbulent fluctuations. With respect to relevance in the flow, persistent turbulent structures generate stresses in certain directions at individual locations in the flow, and thus the Reynolds stress distribution provides an indication on the 3D shear in the fluid due to eddies.

The term Principal Reynolds stress has been given to the streamwise-vertical component, $-\rho\overline{uw}$, ("reynstress uw" in figures) because it is directly related to the vertical distribution of horizontal shear in the fluid, which is generated by shear at the bed. As has been shown, shear force on the bed can be determined from the vertical distribution of $-\rho\overline{uw}$. Positive Reynolds stresses occur when strong component fluctuations are of opposite signs (Rennie and Hay, in review), which understandably imparts stress into the fluid.

Figure 4-16 shows that streamwise-vertical stress increases starting at the beginning of the scour hole, near the bend entrance, then follows the point bar slope upward to the location of maximum stress along the peak of the of the point bar tip. At first it was thought that the maximum value may be biased by the poor measurements made at 105°, however; if we view a series of the 2D plots (Fig. 5-5), we can see that this zone occurs further downstream at 135° (Fig. 5-5d). Maximum negative streamwise-vertical Reynolds stress occurs in Fig. 5-5c, and d, directly adjacent to the zone of maximum of positive stress.

Streamwise-cross stream Reynolds stress was presented in Fig. 4-17. The maximum positive stress here is at the impingement point of the main flow along the outside wall shown in Fig. 5-6e. This maximum area seems to be bi-cellular with a stronger cell moving toward the upper outside of the flow field which suggests the presence of the outer circulation cell.

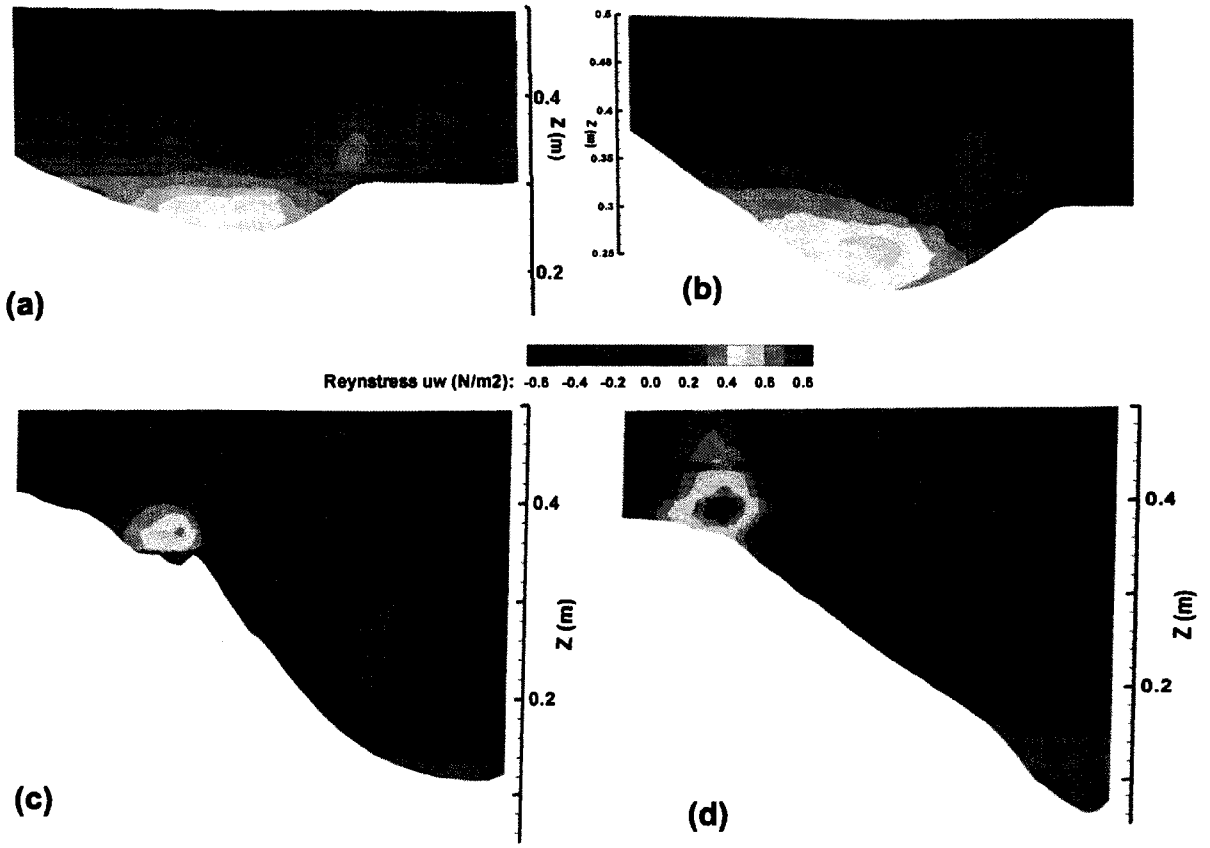

Figure 5-5. 2D (relative) comparison of streamwise-vertical Reynolds stress; (a) 30°, (b) 45°, (c) 120°, and (d) 135°

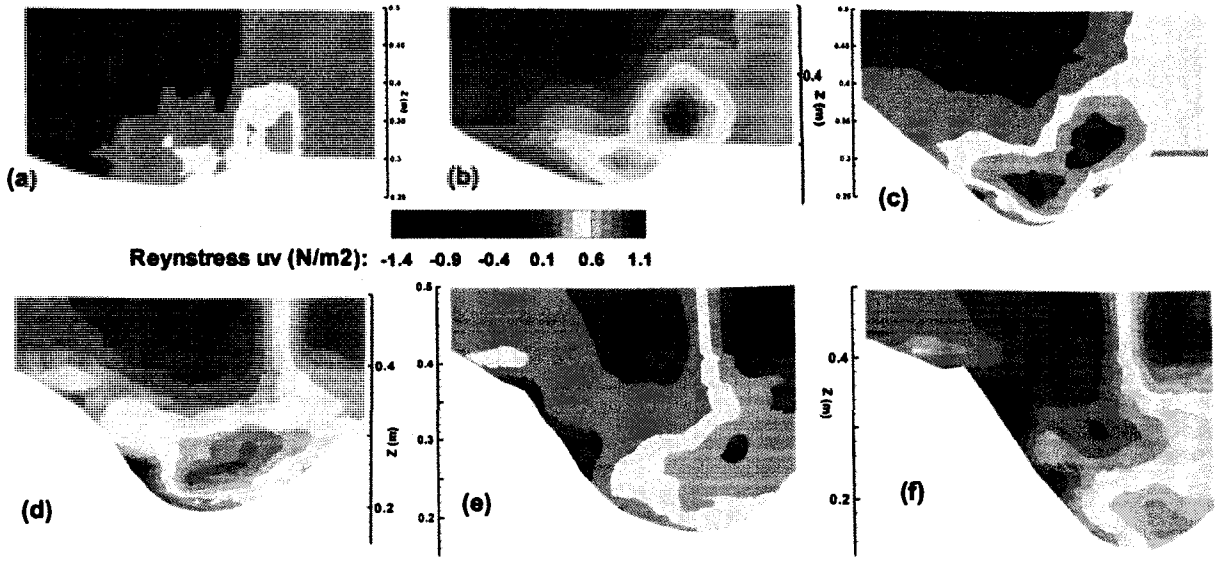

Figure 5-6. 2D (relative) comparison of streamwise-cross stream Reynolds stress; (a) 20°, (b) 30°, (c) 45°, (d) 60°, (e) 75°, and (f) 90°

Cross stream-vertical Reynolds stress shows maximum positive both at the impingement point of the main flow on the outer wall, but larger magnitude maximum negative at the wall and channel centre towards the bend exit as observed in Fig. 4-18. By examining Fig. 5-7 and its succession of 2D plots, it is clearly observed that secondary circulation seems to control the Reynolds stress distribution.

It is interesting to note that the stress distributions presented in this section seem to be controlled by the helical flow pattern through the bend, with the flow forced to turn over itself as it impinges on the bank. This might explain the transitions between positive and negative stresses.

We have shown clearly that the helical flow pattern is based on the mean primary and secondary currents, not their fluctuations. If nothing else, this should confirm that the Reynolds stresses are related to the rate of strain in the flow. The most significant discovery here, however, are the loci of high streamwise-vertical shear at the entrance to the scour hole and near the point bar tip. This is contrary to straight channel theory discussed in Section 2.3.4 in that we expect principal Reynolds stress to increase with depth. Were that the case, maximum values would be found in the deepest part of the flow. This gives insight into the way the scour hole forms during the establishment of equilibrium. With flow acceleration and separation over the cusp of the scour hole, sediment particles are briefly suspended and the helical flow carries the particle from the scour hole diagonally up onto the point bar. Locally, grains are continued to be displaced until bed shear is relatively small. Thus over time the scour hole continues to expand in horizontal dimension upstream until no bend effects are present.

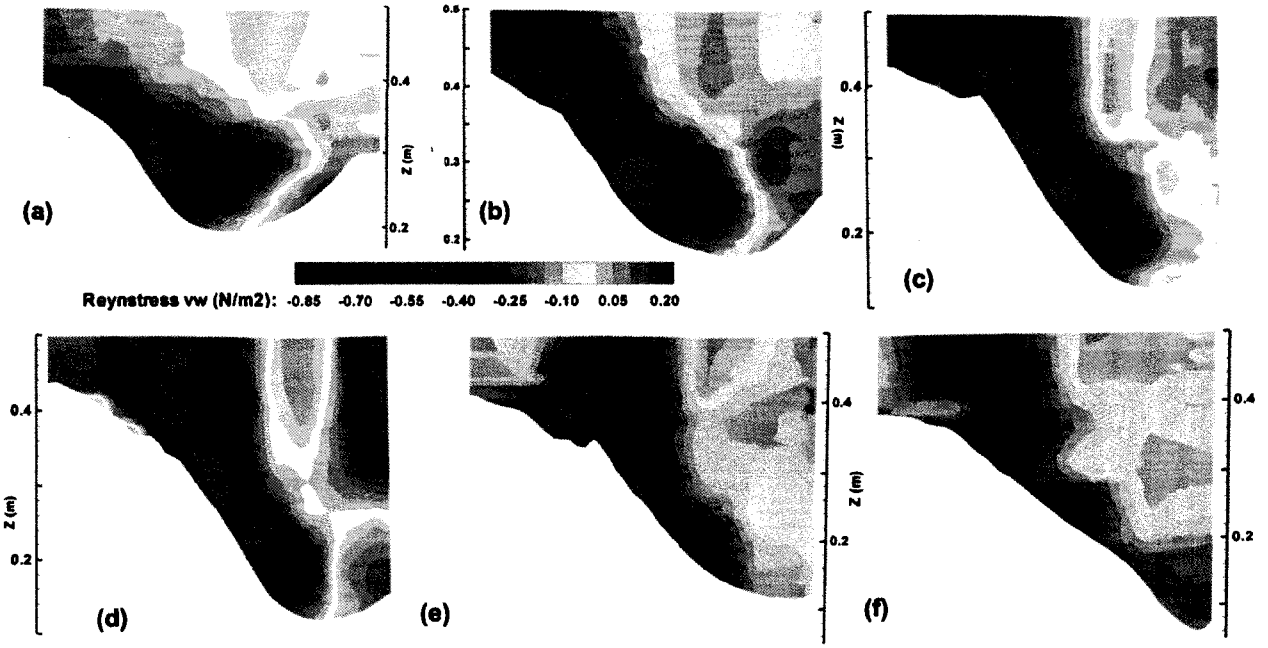

Figure 5-7. 2D (relative) comparison of cross stream-vertical Reynolds stress; (a) 60°, (b) 75°, (c) 90°, (d) 105°, (e) 120°, and (f) 135°

5.4.3 Turbulent Fluctuations, Turbulent Intensities and Turbulent Kinetic Energy

As described in Section 2.6.2, Nezu and Nakagawa (1993) suggest anisotropy to be in the ratio 9:7:5 for *u* rms, *v* rms, and *w* rms respectively. This can be then reduced to *u* rms = 1.8 *w* rms, and *v* rms = 1.4 *w* rms. Average ratio values over the entire data set were *u* rms = 1.97 *w* rms, *u* rms = 1.09 *v* rms, and *v* rms = 1.81 *w* rms. These average values are similar but somewhat higher than Nezu and Nakagawa's predictions. It appears the effect of the bend increases both *u* rms and *v* rms with respect to *w* rms as compared to a straight channel flow, which may indicate an increased presence of vertical axis vortices. Such vortices were observed visually in the vicinity of the bend apex.

The 3D overall images presented for *w* rms (Fig. 4-21) are not affected by the suspected erroneous measurement, and are revealing in that a core of high turbulent energy is evident directly adjacent to the impingement point of the main flow and the channel wall. These fluctuations are interpreted to be a response the main current plunging downward, which is where high vorticity was visually observed during the first experiment.

By viewing the absolutely scaled 2D plots (Appendix C > absolutely scaled > organized by metric) for each coordinate fluctuation parameter, considerably more detail of turbulent fluctuations are apparent and the visual effect of the suspected erroneous measurement is eliminated. The effect of the free surface suppressing turbulent activity is indeed present at the 10

m section for all three directional fluctuations. However as we move into the bend this is not shown to be the case. This is most likely due to the inability of the ADV to measure the uppermost 30% of the flow. Turbulent fluctuations are high in all three coordinate directions near the bed, following the scour hole. Once the bend apex is passed (75°), the presence of the outer circulation cell presented in Fig. 2-18 is observed. Even further past the bend apex turbulent fluctuations show the presence of more complex multi-cellular activity, and the effect of the outer circulation cell does not seem to be quite as consistent as the single cross sectional analysis from Blanckaert and Graf (2001).

By examining the overall plot of turbulent kinetic energy, *k*, (Fig. 4-25) we see that the erroneous measurement affects this diagram significantly, however, if the 2D cross-sections are viewed in their absolute scales (Appendix C), it is apparent that a concentration of high *k* is located near the bed as flow enters the bend. Past the bend apex, at 75°, (Fig.5-8) we have another confirmation of the overall helical flow and the protective outer circulation cell, which is the location observed to have the largest vortices.

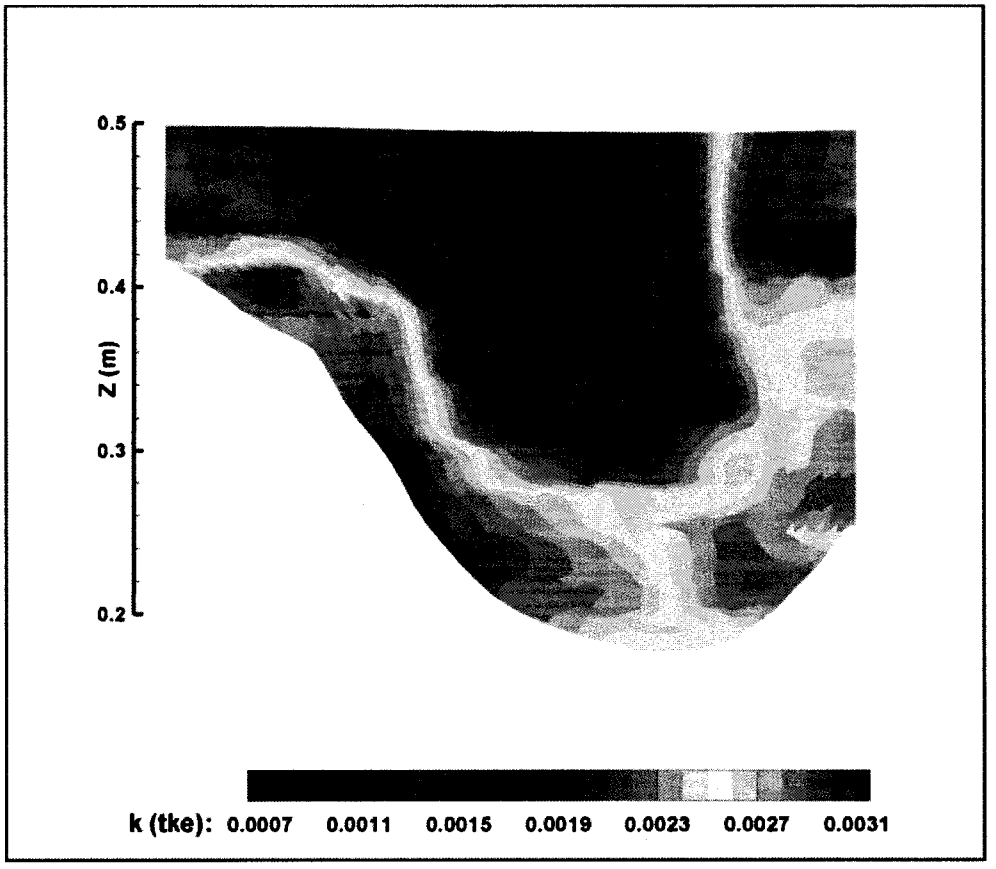

Figure 5-8. Turbulent kinetic energy, *k*, at 75° (absolute)

The relative turbulent intensities for each component direction were normalized with their respective mean velocity. This was contrary to the classical definition of normalizing turbulent intensity in each direction with mean downstream velocity. The respective mean velocity was used for normalization to yield an indication of the fluctuation strength within the sample volume compared to the advection speed through the sample volume in the same direction. However, admittedly, the flow would be advected out of the sample volume most rapidly by the local streamwise velocity. In this sense, local streamwise does not mean perpendicular to the cross-section, but the actual flow direction locally.

With respect to utilizing the relative turbulent intensity as an indicator of the validity of Taylor's Frozen Field Hypothesis to calculate turbulent length scales, only the local streamwise relative intensity and local streamwise length scale should be considered. The Frozen Field Hypothesis relies on the assumption that the advection distance of an eddy during the turbulent time scale equals the turbulent length scale (i.e., the eddy size). This is only true in the direction of advection, i.e. the local streamwise direction. Thus, the Frozen Field Hypothesis is only valid in the local streamwise direction.

5.4.4 Integral Time and Microtime

Integral time and microtime can be used in combination with mean downstream velocity, $\overline{U}$, (Eqns. 2.49 and 2.50, respectively) to estimate eddy length scales for the local streamwise component. For simplicity the streamwise component (perpendicular to the cross-section) is considered here. The estimated streamwise integral length scales (L_x) ranged from 0.02 m to 0.63 m, with an average of 0.09 m (Appendix C). These values correspond reasonably well with the average flow depth of 0.20 m and the maximum flow depth in the scour hole of 0.48 m. When examining Figs. 4-30 and 4-33 we see again that the largest eddies occurred where the flow impinged on the outside wall which was also a locus of high streamwise-cross stream Reynolds stress and turbulent kinetic energy. Observations made visually during the test confirm these results, and large eddies were apparent in this region.

Chapter 6 Conclusions and Future Research

6.1 Conclusions

The data set produced by the first experiment reported in this thesis is quite accurate based on the interpretation provided. Showing acceptably high SNR and correlations, with minimal noise contribution, and few measurements anomalies, we showed that the results are also highly congruous with well proven bend flow studies. In particular, strong helical flow patterns driven by the main flow, and the outer circulation cell were shown.

Most interesting is the discovery of a concentration of principal Reynolds stress near the scour hole margin and at the tip of the point bar has been documented. The other directional Reynolds stresses are also understandable given the displayed multi-cellular activity within the bend, and more specifically past the bend apex. This is supported by the distribution of turbulent fluctuations and turbulent kinetic energy in these areas. More experiments at the same conditions need to be run before these results can be confirmed.

Also, while not directly related to the problem statement, a thorough look into the flume which was designed and manufactured by the author has been made to ensure the reproducibility of these experiments. Procedures have been developed and documented for effective use of the flume and as much information as possible is included about the experiments reported in this thesis.

6.2 Future Research

This is the first set of experiments in a long term study, and again the author was responsible for the flume manufacturing and thus the recommendations for future research are divided into two parts. First, procedural recommendations will be discussed, and then recommendations on what could be done with these results are made.

6.2.1 Procedural

With the high quality results from this test, and the discovery of the zones of high Reynolds stress near the bed at the scour hole beginning and the downstream tip of the point bar, reproduability of results is important. Rather than run multiple tests at different slopes, several runs at one slope should be completed, which, with repeatability of these measurements will truly show their accuracy. It was also realized during the second test that because of live-bed conditions, and recharge of material into the scour hole from the straight approach, that true static

equilibrium of the bed may never establish under those conditions. The problem lies in locating ADV measurements after the test and representing them as a whole.

For the first experiment, the elevation of the sand bed did not change throughout ADV testing. This made it possible to create the images for this thesis as conditions did not change over the 27 hours of measurements. Were the bed topography to be changing constantly throughout the measurements, creating these 3D full flume views would not be possible.

6.2.2 Analytical

The MatLab code utilized for data analysis was developed by Dr. Rennie for his past field experiments. One particularity of the code is the calculation of relative turbulent intensity. Here we utilized normalization by mean streamwise velocity for the respective coordinate intensity. With relative turbulent intensities in the cross stream and vertical directions normalized by the mean velocities in those directions respectively, values were highly variable. Theoretically, mean velocities in these directions should tend to zero and normalizing by near zero value results in excessively large measures of turbulent intensity.

Also, while "commented out" for this analysis, it would have been convenient to have vertical noise calculated using the spectral analysis techniques employed to determine streamwise noise. Again, the M-files used have been provided in Appendix B.

More information needs to be gathered about the Kriging interpolation methods employed by Tecplot 360. It would be worthwhile to check the interpolation by comparing the interpolated section to measured values at each section. If a quick comparison method can be devised, the Kriging parameters can be employed in an iterative process until the interpolations are proven. It is also possible that a more sophisticated 3D interpolation software exists, although none have been identified which have the same level of control that Surfer allowed with the bathymetry data.

Lastly, further data analysis features available in Tecplot 360 should be implemented, including 3D vector plotting, vorticity, and stream trace calculation and plotting

References

Allen, J. R. (1983). River bedforms: process and problems. In J. D. Collinson, & J. Lewin (Eds.), *Modern and ancient fluvial systems* (Vol. 6, pp. 19-33). Oxford: Special Publication of the International Association of Sedimentologists.

Bathurst, J. C., Thorne, C. R., & Hey, R. D. (1977). Direct measurements of secondary currents in river bend. *Nature* (269), 504-506.

Blanckaert, K. (2003). *Flow and turbulence in sharp open-channel bends.* Phd Thesis, EPFL, Department of Civl Engineering, Lausanne, Switzerland.

Blanckaert, K., & De Vriend, H. J. (2005). Turbulent Structure in Sharp Open-Channel Bends. *Journal of Fluid Mechanics , 536*, 27-48.

Blanckaert, K., & Graf, W. H. (2001). Mean Flow and Turbulence in Open-Channel Bend. *Journal of Hydraulic Engineering , 127* (10), 835-847.

Blanckaert, K., & Lemmin, U. (2006). Means of Noise Reduction in Acoustic Turbulence Measurements. *Journal of Hydraulic Research , 44* (1), 3-17.

Born, M. (1965). *Einstein's Theory of Relativity.* New York: Dover Publications.

Bray, D. I., & Davar, K. S. (1987). Resistance to flow in gravel-bed rivers. *Canadian Journal of Civil Engineering , 14* (1), 77-86.

Bridge, J. S. A revised model for water flow, sediment transport, bed topography and grain size sorting in natural river bends. *Water Resources Research , 28* (4), 999-1013.

Buffin-Belanger, T., & Roy, A. G. (2005). 1 min in the life of a river: selecting the optimal record length for the measurement of turbulence in fluvial boundary layers. *Geomorphology , 68* (1-2), 77-79.

Buffington, J. M., & Montgomery, D. R. (1997). A Systematic analysis of eight decades of incipient motion studies, with special reference to gravel-bedded rivers. *Water Resources Research , 33* (8), 1993-2029.

Chow, V. T. (1959). *Open Channel Hydraulics* . Boston: McGraw-Hill.

Coles, D. (1956). The law of the wake in the turbulent boundary layers. *Journal of Fluid Mechanics* , 191-226.

Corney, R. K., Peakall, J., Parsons, D. R., Elliott, L., Amos, K. J., Best, J. L., et al. (2006). The Orientation of Helical Flow in Curved Channels. *Sedimentology , 53*, 249-257.

Dietrich, W. E. (1987). Mechanics of Flow and Sediment Transport in River Bends. In K. Richards, & K. Richards (Ed.), *River Channels* (pp. 179-227). New York, NY: Institute of British Geographers.

Dietrich, W. E., & Smith, J. D. (1983). Influence of the Point Bar on Flow Through Curved Channels. *Water Resources Research , 19* (5), 1173-1192.

Einstein, H. A., & Barbarossa, N. L. (1952). River Channel Roughness. In *Trans. Am. Soc. Civ. Eng.* (Vol. 117, pp. 1121-1146). American Society for Civil Engineers.

Gilbert, G. K. (1914). *Transportation of Debris by Running Water.* U.S. Geological Survey.

Graf, W. H. (1971). *Hydraulics of Sediment Transport.* New York: McGraw Hill.

Hicks, D. M., & Mason, P. D. (1999). *Characteristics of New Zealand Rivers.* Christchurch, New Zealand: National institute of Water and Atmospheric Research Ltd.

Keulegan, G. H. (1938). *Laws of turbulent flow in open channels.* Research Paper 1151, Journal of Research of the National Bureau of Standards.

King, H. W., & Brater, E. F. (1952). *Handbook of Hydraulics.* New York: McGraw Hill.

Kironoto, B. A., & Graf, W. H. (1994). Turbulence characteristics in rough uniform open-channel flow. *Proc. Instn. Civ. Engrs. Wat., Marit. & Energy, 106 (Dec.)*, pp. 333-344.

Knighton, D. (1998). *Fluvial Forms and Processes: A New Perspective.* New York, NY: Oxford University Press.

Millar, R. G. (1999). Grain and form resistance in gravel-bed rivers. *Journal of Hydraulic Research , 37* (3), 303-312.

Minor, B., Rennie, C., & Townsend, D. R. (in press). 3D Numerical Modelling of Flow and Sediment Transport through a Series of 'Barbs' for River Bend Bank Protection. *Canadian Journal of Civil Engineering .*

Nezu, I., & Nakagawa, H. (1993). *Turbulence in Open Channel Flows.* Brookfield, VT.: A.A. Balkema.

Nikora, V. I., & Goring, D. G. (1998). ADV Measurements of Turbulence: Can We Improve Their Interpretation. *Journal of Hydraulic Engineering , 124* (6), 630-634.

Nikuradse, J. (1933). Laws of flow in rough pipes. *VDI Forschungsheft 361 .*

Nowell, R. M., & Church, M. (1979). Turbulent flow in a depth limited boundary layer. *Journal of Geophysical Research , 84(C8)*, 4816-4824.

Odgaard, A. J. (1984). Flow and Topography in Alluvial Channel Bend. *Journal of Hydraulic Research , 110* (4), 521-536.

Odgaard, A. J. (1989). River-Meander Model I: Development. *Journal of Hydraulic Engineering , 115* (11), 1433-1448.

Odgaard, A. J., & Bergs, M. A. (1988). Flow Processes in a Curved Alluvial Channel. *Water Resources Research , 24* (1), 45-56.

Powers, M. C. (1953). A new roundness scale for sedimentary particles. *Journal of Sediment Petrology , 23* (2), 117-119.

Prashun, A. L. (1992). *Fundamentals of Hydraulic Engineering.* New York: Oxford University Press.

Precht, E., Janssen, F., & Huettel, M. (2006). Near-bottom performance of the Acoustic Doppler Velocimeter. *Acuatic Ecology , 40*, 481-492.

Pye, K. (1994). Properties of sediment particles. In K. Pye, & K. Pye (Ed.), *Sediment Transport and Depositional Processes.* Oxford: Blackwell Scientific Publications.

Raju, K. R., Asawa, G. L., & Mishra, H. K. (2000). Flow-Establishment Length in Rectangular Channels and Ducts. *Journal of Hydraulic Engineering , 126* (7), 533-539.

Raudkivi, A. J. (1997). Ripples on a stream bed. *123* (7), 58-64.

Rennie, C. D., & Hay, A. ((in review)). Reynolds stress estimates in a tidal channel from phase-wrapped ADV data. *Submitted to J. Hydraulic Research, December 2006.*

Rennie, C. D., Millar, R. G., & Church, M. A. (2002). Measurement of bedload velocity using an acoustic Doppler current profiler. *Journal of Hydraulic Engineering , 128*, 473-483.

Richardson, L. F. (1922). *Weather Prediction by Numerical Process.* Cambridge University Press.

Rouse, H. (1959). *Advanced Fluid Mechanics.*

Rouse, H., & Ince, S. (1957). *History of Hydraulics.* New York: Dover Publications.

Rouse, H., Appel, D. W., Hubbard, P. G., Landweber, L., Laursen, E. M., McNown, J. S., et al. (1959). *Advanced Fluid Mechanics.* (H. Rouse, Ed.) New York: John Wiley & Sons. Inc.

Rusello, P. J., Lohrmann, A., Siegel, E., & Maddux, T. (2006). Improvements in Acoustic Doppler Velocimetry. *The 7th International Conference on Hydroscience and Engineering (ICHE)*, (pp. 1-16). Philadelphia.

Sharpe, J. J. (1981). *Hydraulic Modeling.* Toronto, ON: Butterworth & Co.

Simons, D. B., & Richardson, E. V. (1966). *Resistance to Flow in and Alluvial Channel.* U.S. Geological Survey.

Simons, D., & Senturk, F. (1992). *Sediment Transport Technology.* Littleton, CO: Water Resources Publications.

Smith, J. D., & McLean, S. R. (1984). A Model for flow in Meandering Streams. *Water Resources Research , 20*, 1301-1315.

Song, T., & Chiew, Y. M. (2001). Turbulence Measurement in Nonuniform Open-Channel Flow Using Acoustic Doppler Velocimeter (ADV). *Journal of Engineering Mechanics , 127* (3), 219-232.

Strickler, A. (1981). Contributions to the question of a velocity formula and roughness data for streams, channels and closed pipelines. (T. b. Brownlie, Ed.)

Townsend, A. A. (1976). *The Structure of Turbulent Shear Flow* (2nd Edition ed.). Cambridge, England: Cambridge University Press .

Townsend, R. D., & Matsuura, T. D. (2004). Stream-barb installations for narrow channel bends — a laboratory study. *Canadian Journal of Civil Engineering , 31* (3), 478-486.

USBR. (1997). *Water Measurment Manual* (3rd Edition ed.). Unites States Bureau of Reclamation.

van Rijn, L. C. (1982). Equivalent Roughness of Alluvial Bed. *Journal of Hydraulic Engineering , 108* (10), 1215-1218.

Voulgaris, G., & Trowbridge, J. H. (1998, February). Evaluation of the Acoustic Doppler Velocimeter (ADV) for Turbulence Measurements. *Journal of Atmospheric and Oceanic Technology* , 272-289.

Wilcox, D. (2000). *Turbulence Modeling for CFD.* La Canada, CA: DCW Industries.

Yalin, M. S. (1992). *River Mechanics.* New York: Pergamon Press.

Yen, B. C., & Yen, C. *Water Surface Configuration in Channel Bends.* American Society of Civil Engineers, Journal of the Hydraulics Division.

Appendix A Procedures

A.1 Channel slope adjustment

A.1.1 Introduction

The main structural support for the straight approach section is a 12.192 m (40 ft) tilting platform. The bend sections are supported by an adjustable "tube-clamp" system to allow for slope adjustments while keeping the cross section level about the centerline through the bend. Were the complete structure housed on the tilting platform, the cross sections in the bend would be tilted with the platform slope, and the outlet would be higher than the bend. However, even with the supporting structures capable of slope adjustments, the process of doing so with the flume body made entirely of acrylic requires great care, and is consequently very time consuming. As an aid to this, an adjustable equipment rail was attached to the sidewall top for changes in bed slope up to one percent.

To achieve different channel slopes of ± 1%, the equipment rail is adjusted and the sand bed screed a fixed distance from the rails. With the sensitivity of flow to channel slope, being able to adjust the channel accurately is important for eliminating error and verifying results. For the desired slope of 0.044% for example, the centerline change in elevation over the 18.2 m length is 8.08 mm, which is reasonable. However, if one takes into consideration the many different points of connection, making precise adjustments along the entire length becomes increasingly difficult. This is especially true in the bend sections; for both the shorter inside and longer outside rails to follow the centerline slope, their individual slopes are respectively steeper and flatter than the centerline slope.

Referring to Fig. 3-1, the equipment rails are constructed of 38.1 mm (1.5") aluminum square tube supported along their length at different points by 12.7 mm (½") stainless steel threaded rod. This threaded rod is attached to the top edge of the acrylic flume wall with nuts and washers on the top and bottom of drilled holes. However simple, this allows for accurate adjustment moving both up and down. The rail system has been designed to permit a one percent range of slopes with the flume body at a set position. Any adjustment outside this one percent range requires the entire supporting structure be adjusted.

A.1.2 Structural Slope Changes

The main structural support for the straight approach section is a large tilting platform which sits 1.6 m from the ground on the pivot side. Along its 12.2 m length, two heavy steel I-

Beams run parallel to each other, spaced 1.5 m apart and act as the girders for the platform. To adjust overall slope, two heavy lateral joists of similar dimensions as the girders are supported at one end on a pivot, and the other joist (at the opposite end) on two jack screws that are used to determine the overall slope of the platform (Fig. A-1a, b). The accuracy and precision of the structural steel used to fabricate this frame is not very good. Thus, the underside of the frame was supported with fabricated jack-screws at points where the frame was deficient.

Through the bend sections the flume body twists with a downward centerline slope and a radius of curvature. As we adjust the bend sections, each cross section must stay level with the centerline slope to ensure the channel walls stay perpendicular to flow. Consequently, the bend section support and the straight exit section support structure needs to be more adjustable than that for the approach section. To accommodate the combined strength, overall geometric complexity, and adjustability requirements for different channel slopes, a "Tube-Clamp" (also known as Kee-Klamp) system was chosen (Fig. A-1c). This highly modular system is based on the use of galvanized steel tube for frame elements, and a variety of different connectors depending on the desired intent of the given joint or connection.

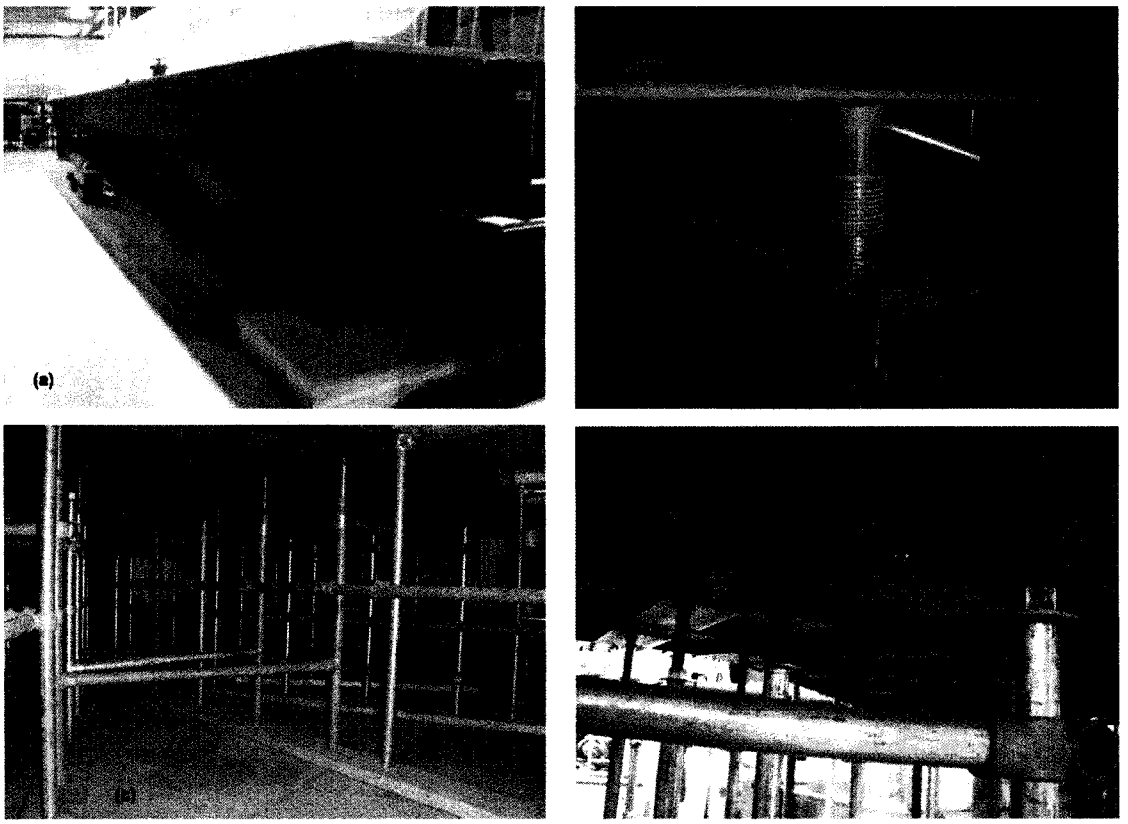

Figure A-1. Support structures: (a) approach section platform (b) adjusting jackscrews for platform (c) overview of bend section support system (d) connection details for bend sections

Steel frames were manufactured from 38.1 mm (1.5") square steel tube, topped with high quality marine grade plywood to support each 45° bend section independently. The frames for each bend section are supported by the tube-clamp system using steel plates welded to the frames with 25.4 mm (1") threaded rod for adjustment (Fig. A-1d). With four connection points laterally, and spacing at 22.5°, there are a total of 28 support points for the bend and exit sections. Each of these support points can be adjusted for a desired slope.

Due the stress that structural slope changes subject the acrylic flume body to, extreme caution should be used. Before attempting to adjust the structural slope it is advisable to remove all sand bed material from the flume, and loosen all the bolts in the joint and equipment rails. To ensure no problems for this thesis, after initially being constructed, the flume was left "as-is". The approach section platform follows precisely a 0.02% slope. With the bend sections being independently fabricated and considering their size and complexity, some error in fabrication exists. Being glued in place with a construction grade adhesive to eliminate any torsion twisting due to centrifugally induced moment on the structure, the bend sections are fastened securely to the plywood support. Again, being water tight, these bend sections were left "as-is" after construction, and follow a slightly adverse slope making for a height gain of approximately 20 mm from the beginning of the bend to the outlet. It is likely that some fabrication may be necessary to ensure the water-tightness of the joints following a structural slope change.

A.1.3 Equipment Rail and Sand Bed Levelling Procedure

Levelling the rails was accomplished using a Topcon GS-223 total-station for height measurements at each connection point. The rail height at each individual bend section attachment point needs to be adjusted to ensure a certain slope along the channel centerline. Again, the slope of each rail in the bend sections is inherently different from the centerline slope, with the inside rail having a steeper slope, and alternately, the outside rail having a gentler slope. A spreadsheet was developed for this and future use, calculating the required height differences of each attachment point in relation to the measured height at the last points on each rail. Future research will not require an adverse slope, therefore the last attachment point of the rails have the shortest threaded rods attached.

A 12" Mitutoyo Combination square precise to 0.254 mm (0.01") was placed so the scale reads directly above each attachment point (Fig. A-2). By utilizing the internal tilt sensing capabilities of the total station, and the sight lines in the lens of the total station, maintaining level at rotations over 180° is ensured. One optimum tripod location which could site all points on the flume was used for all adjustments.

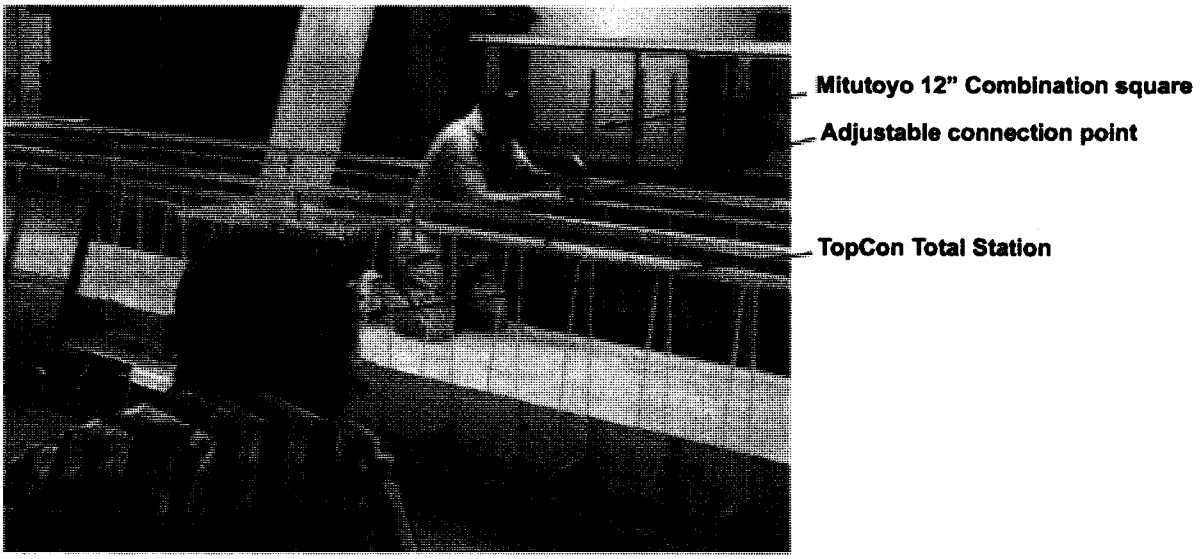

Figure A-2. Equipment rail adjustment method

The step by step procedure for this is as follows:

1. Set up tripod on a sufficiently tall and sturdy platform ensuring full level visibility. This should not be the same platform the operator stands on to look through the Total Station sights. A step ladder was used to access the instrument.
2. Establish level on the total station, and check to see if the cross-hairs in the sight is reading within the 0.3 m of the combination square. If not, the total station height needs to be adjusted accordingly.
3. By taking the height measurement at the last connection point (nearest the exit gate) of the outside rail, and entering this value into the design spreadsheet, the height at each connection point that you expect to read is then calculated.
4. Adjustments are made moving from the exit to the inlet, in a zigzag pattern from one side to the other.
5. One person makes the adjustments to the rail via the top and bottom nuts, and moves the square, marking with non-permanent ink each time a connection point has been measured. If a significant change in slope is to take place, care should be taken to loosen several connection points upstream of the connection point to eliminate error due to bending.
6. At each reading the tilt of the total station should be verified at 90° on the digital readout.
7. With all connection points levelled a check can be made using a precision level placed span-wise perpendicular on top of a straight piece of aluminum bar.

Figure A-3. Screed bar for sand bed levelling

With the equipment rails levelled, the sand bed is then made to follow the same slope by means of a screed bar (Fig. A-3). Sand is raked thoroughly before being screed to reduce any effect of compaction. The outer edges of the levelling blade are outfit with paint brushes to eliminate any scuffs the wooden blade would make on the channel wall.

A.2 Flume Filling Procedure

Care must be taken to fill the flume slowly. It is important that bed shear does not exceed expected maximum test levels during flume filling.

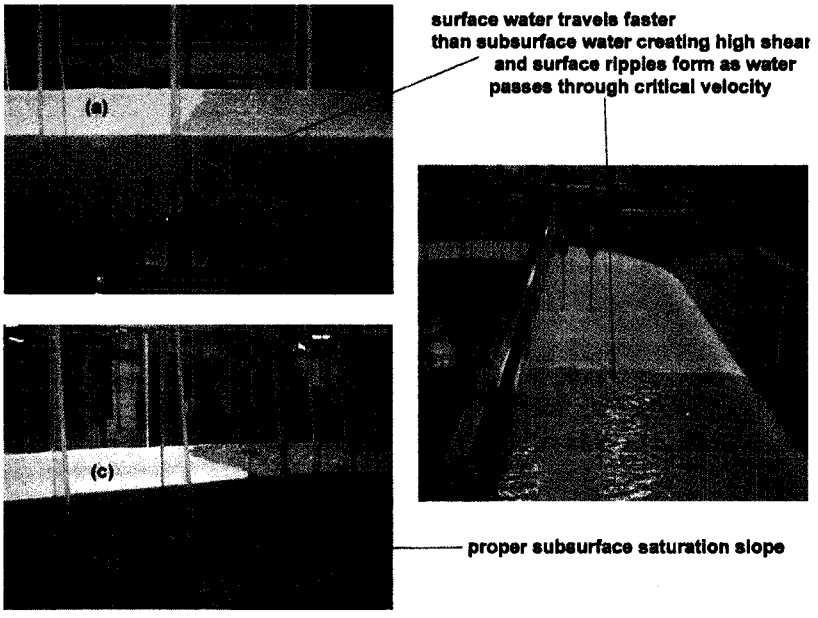

Figure A-4. Flume filling procedure: (a) adverse subsoil water slope (b) surface ripples caused by excessive bed shear (c) optimal subsurface water slope

The easiest way to ensure this is for the water to percolate up through the water column. During preliminary runs of the flume shortly after build completion, the filling procedure used was rather hasty. By rushing to establish uniform flow at 0.2 m of depth, higher than expected bed shear invariably occurs. Depending on the desired rate of sediment transport, unexpected bed deformation can occur under this excess shear period. Shown in Fig. A-4a, an adversely sloped subsurface saturation front is created by filling the flume too fast. With the water driving forward and down into the sand bed, a small, yet strong bore is created which quickly reorganizes the sediment. As the water passes through critical velocity, standing waves are created on the surface, which themselves create a rippling of the sand bed (Fig. A-1b). Proper filling of the flume takes approximately 2-3 hours. When this care is taken, a positive slope of the subsurface water is present. Figure A-4c shows a good image of this subsurface slope (surface ripples still present). Keeping the flat bed intact is possible when 2-3 hours is taken to properly fill the flume. The procedure for properly filling the flume is as follows:

1. To reduce scouring at the entrance and exit gate, hairspray was applied liberally in these regions to help maintain the sand bed structure.
2. Close the ball valve on the drain line which is connected to the inlet tank (Fig 3-6a). Since this valve is old it is rather hard to turn but can be achieved with a little "persuasion".
3. Close both the upper and lower portions of the exit gate. The level of the bottom gate will extend approximately 0.05 m above the sand bed when fully closed.
4. Start supply pump (pump #1) and open the supply valve (Fig. 3-5a) slightly until air is heard bubbling from the diffuser in the inlet tank, and the water level slowly rises.
5. Continue to slowly open the valve so water fills the tank until the level is approximately 0.1 m above the bottom of the sand bed. The saturation front of the sand near the channel entrance can be seen through the clear flume wall. If the water level is constant in the tank, and the water continues to push its way into, and up through the sand bed, the right setting has been reached. If the water level in the inlet tank rises above the top of the bricks, a bore will surely form once the water level enters the flume.
6. Once the entire sand bed is saturated the flow can be increased slightly to fill the flume to the desired depth.

A.3 Establishment of Uniform Flow

A.3.1 Clear-water scour conditions

This is the most difficult portion of the procedure. The goal is to increase the flow rate slowly without letting the water flow until the established test depth is reached. If, for example, the exit gate is opened before reaching test depth, an increase in the water surface slope will occur and consequently shear stress would increase as the drawdown curve works its way upstream. More desirable is the case where the gate is not open enough or not at all, and we have an adverse water surface slope. This is achieved by slowly filling the flume.

Once the flume is at or above test flow depth, the user can incrementally increase flow, and open the exit until uniform flow is reached. Given the large flume dimensions, adjustments made to either the flow supply or the exit gate take a considerable amount of time to equalize. Thus accurately establishing uniform flow can take a long time. Devised through the pre-trials, the following procedure was developed so as to expedite the process. Leaving off the procedure from the previous section as the flume slowly fills:

1. Attach the Dynasonics flowmeter to the supply line (Fig. 3-5b)
2. Place the point gauge near the channel entrance with height preset to the expected depth which in this case is 0.2 m. With the sand bed levelled from the sloped equipment rails and the flowrate in the flume while filling is nil, the water surface will measure deeper at the outlet end.
3. Start first by increasing the flow slightly. Because the valve on the supply line is butterfly style and is connected to a gear box, accurate flow throttling is difficult to achieve. The large gears have a large amount of "backlash" when trying to attenuate the flow. The user is required to sense how much more flow is being delivered by listening to the line. Quickly opening the valve causes the system to become noticeably excited, and a large rush of flow is surely to result. Although signal strength is not great in this situation, the Dynasonics flowmeter attached to the supply line will give a good estimation of flowrate. Intended for full pipe flow conditions, this system takes approximately one minute to deliver accurate readings in this application.
4. Once the water surface is very near the point gauge at the channel entrance, the gate can be opened slightly using the control switch (Fig. A-5). This electrically powered motor for the linear actuator does not have an internal brake, and thus continues movement for a brief moment after the switch is released. In other words, a quick pulse of the switch can result in movement in either direction in the order of 5 mm. The drive mechanism also has a large

magnitude of backlash when changing directions, thus if the gate is opened too much initially it is difficult to smoothly move the gate in the other direction. With the lower gate capable of much smaller increments of movement the upper gate is used for coarse adjustment to flow. With the upper gate opened slightly, the water level in relation to the point gauge should be monitored. At this point, it must be ensured that the water level upstream does not go below the expected flow depth again.

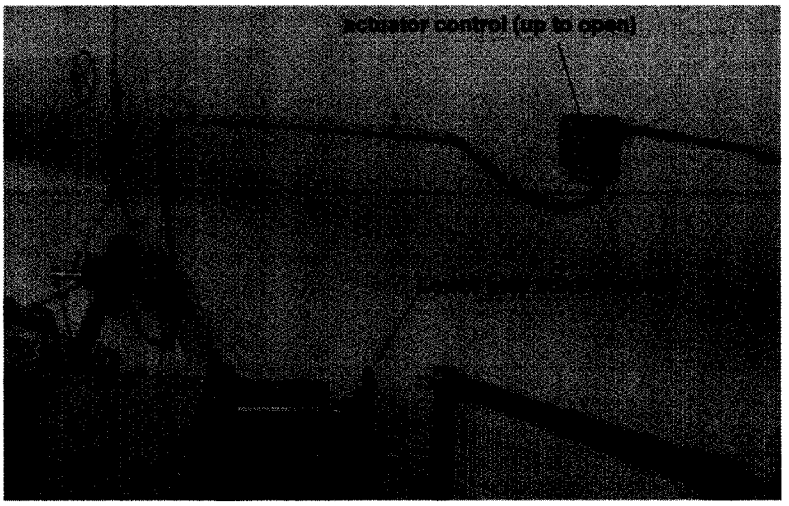

Figure A-5. Exit gate controls

5. Steps 3 and 4 can be repeated several times until the reading from the Dynasonics flowmeter nears the expected flow rate. The outlet tank arrangement and more specifically the V-Notch weir was designed for 85 L/s which was determined before the build started. This is the maximum flow without recirculation that the outlet system can handle.
6. Once the reading on the Dynasonics flowmeter reads within 5-10 L/s of the expected value the lower gate should be used for adjustments. Lowering this gate quickly can induce sudden scour formations at the interface between the sand and gate, so care must be taken to do so slowly. With the flow depth of 0.2 m at the entrance, a meter stick is used to measure the water surface slope at points all along the channel through the flume wall.
7. Gradually move toward uniform flow now by increasing flow and opening the gate by small amounts. Finally, use the point gauge at several points along the channel to precisely verify the water surface slope.

A.3.2 Addendum for Live-Bed Testing Conditions

If the test is to be conducted at live-bed conditions and transport is expected in the straight approach section, the slurry pump is started to recirculate sediment and a portion of the

flow to the channel entrance. The following procedure is a caveat to Step 5 in the previous section. Once the flowrate is at expected rates based on critical shear for a given slope, the slurry pump is started; the gate valve on the return line (Fig. 3-13a) is then used to vary the additional flow.

1. With the Dynasonics flowmeter, detach the cables from the supply line transducers and attach them to the transducers outfitted on the return line (Fig. 3-13a). The basic configuration of the Dynasonics needs to be changed for the smaller diameter pipe and expected maximum flowrate. With this pipe flowing full, and outfitted an appropriate distance away from sources of loss, the signal strength from the flowmeter is stronger, and measurements are more accurate. Now, total flow is the summation of the last reading for flow taken from the supply line and the reading from the return line.
2. Ensuring that the gate valve is fully closed, the slurry pump is started. Flow is now increased using the gate valve attached to the return line. This gate valve allows for very precise flow adjustments.
3. Return to Step 7 above.

A.4 Draining procedure

Equally important in terms of maintaining integrity of the sand bed is the way in which the flume is drained. Ideally, shear stress should not go above testing levels, and draining must be done as smoothly as possible. The following procedure will help ensure this is the case, with the main objective of keeping the water deeper than the expected depth until flow is stopped. Here diagrams and references are not used as the reader should be acquainted with the apparatus by this point:

1. First start by closing the bottom gate slightly;
2. Slightly reduce flow on the return line (if it is running) or the main supply line;
3. Repeat these steps until the gate is closed and the flow is stopped;
4. On the inlet tank drain, open the ball valve half way;
5. Now open the outlet on the bend section drain manifold, ensure it is hooked up to the drain hose;
6. As the flume now slowly drains, bedforms with steep slopes and unique features can also be preserved by using hairspray on the sand once drained.

A.5 Useful Tips for ADV Testing

While the details of operating the ADVs in terms of data acquisition using the Vectrino+ software are available at the Nortek website, www.nortek-as.com; some useful hints learned from this research are provided as follows:

1. In terms of file naming convention, one should be chosen to ensure no problems with post-processing. For example using operators such as, –, or &, can foul MatLab processing. For these tests an example of the filename is "ten333pro7cm.dat" meaning the ten meter cross section, 33.3 cm from the wall, and 7 cm from the channel bed. A possible improvement would be to name measurements so that sorting functions in a spreadsheet program can be used to easily sort all data. Individual sections should be given a whole number, the plan point a letter, and instrument depth an extension of plan point number. For example for the third cross section would be labelled 3, the center plan point would be C (3 of 5) and the depth at 7 cm should be named "3C7".
2. Print a hardcopy of the planned data names in the order they are to be taken and check them off after each measurement. With the measurements for the first experiment taking over 27 hours, any additional double check is useful. Also leave room on these sheets to make comments about the measurements if necessary. Comments about irregularities are useful later.
3. The 0.1 m depth is particularly tricky. Here, the transmitter is exactly twice the height of the sample volume and thus pulses reflected from the bottom bounce back to the transducers. Measurements at this depth are consistently noisy.

Appendix B Matlab M-Files

B.1 processVectrinobatch

```
%assume water temperature in lab is 20degC, therefore
rho=998;%density of water in kg/m3, (note temp changed from 18degC to 22degC during run
writematrixall=[];
%this file will process Vectrino .dat files
%load file

filename={}



for p=1:length(filename)
filescript = ['load ' filename{p} '.dat -ASCII'];
eval(filescript)

dummy=['tvec=' filename{p} '(:,1);'];
eval(dummy);
dummy=['vx=' filename{p} '(:,3);'];
eval(dummy);
dummy=['vy=' filename{p} '(:,4);'];%note vy follows right-hand rule with x forward and z
vertical
eval(dummy);
dummy=['vz1=' filename{p} '(:,5);'];
eval(dummy);
dummy=['vz2=' filename{p} '(:,6);'];
eval(dummy);
dummy=['amp1x=' filename{p} '(:,7);'];
eval(dummy);
dummy=['amp2y=' filename{p} '(:,8);'];
eval(dummy);
dummy=['amp3z=' filename{p} '(:,9);'];
eval(dummy);
dummy=['amp4w=' filename{p} '(:,10);'];
eval(dummy);
dummy=['snr1x=' filename{p} '(:,11);'];
eval(dummy);
dummy=['snr2y=' filename{p} '(:,12);'];
eval(dummy);
dummy=['snr3z=' filename{p} '(:,13);'];
eval(dummy);
dummy=['snr4w=' filename{p} '(:,14);'];
eval(dummy);
dummy=['cor1x=' filename{p} '(:,15);'];
eval(dummy);
dummy=['cor2y=' filename{p} '(:,16);'];
eval(dummy);
dummy=['cor3z=' filename{p} '(:,17);'];
eval(dummy);
dummy=['cor4w=' filename{p} '(:,18);'];
eval(dummy);

headerscript = ['FID = fopen( ''' filename{p} '.hdr'')'];
eval(headerscript)
for k=1:80
fgetl(FID);
end
advhead=fgetl(FID);
fclose(FID);

advheadnum=str2num(advhead(end-3:end));

%based on which adv, correct for twist of probe head.  The actual
%correction will occur after initial filtering in processVectrinocore
xyrotate=0;
if advheadnum==7059
```

```
    xyrotate=2.658*pi/180;
elseif advheadnum==7047
    xyrotate=2.194*pi/180;
elseif advheadnum==7055
    xyrotate=2.497*pi/180;
end

timestep=tvec(2)-tvec(1);

processVectrinocore

spectralVectrinofinalfiltnoisebatch %does spectral analysis, and low pass filters data if
noise observed in spectrum

Vectrinooutput%note this calculates the turbulence scales, as well as the reynstresses
again in case the Vectrino data were low-pass filtered (Vectorfiltflag=1)

writematrix=[meanxraw meanyraw meanzraw uwreynstressraw uvreynstressraw vwreynstressraw
xrmsraw turbintxraw yrmsraw turbintyraw zrmsraw turbintzraw turbkinenergyraw meanxdespike
meanydespike meanzdespike uwreynstressdespike uvreynstressdespike vwreynstressdespike
xrmsdespike turbintxdespike yrmsdespike turbintydespike zrmsdespike turbintzdespike
turbkinenergydespike Vectorfiltflag noisevx meanxfilt meanyfilt meanzfilt uwreynstressfilt
uvreynstressfilt vwreynstressfilt xrmsfilt turbintxfilt yrmsfilt turbintyfilt zrmsfilt
turbintzfilt turbkinenergyfilt integraltimescale microtime integrallengthscale
microlengthscale taylormicrolength integraltimescaley microtimey integrallengthscaley
microlengthscaley taylormicrolengthy integraltimescalez microtimez integrallengthscalez
microlengthscalez taylormicrolengthz];

writematrixall=[writematrixall; writematrix];

save VectrinoOutput writematrixall filename rho p
clear
load VectrinoOutput

end

wk1write('VectrinoOutput',writematrixall)
```

B.2 processVectrinocore

```
%figure
%plot(tvec,vx)
%xlabel('time, s')
%ylabel('raw x vel, m/s')
%figure
%plot(tvec,vy)
%xlabel('time, s')
%ylabel('raw y vel, m/s')
%figure
%plot(tvec,vz1,tvec,vz2)
%xlabel('time, s')
%ylabel('raw z vels, m/s')
%vzerrorraw=vz2-vz1;
%figure
%plot(tvec,vzerrorraw)
%xlabel('time, s')
%ylabel('raw z error, m/s')

%remove bad data
for k=1:length(vx)
    if vx(k)==3276.7 | vy(k)==3276.7 | vz1(k)==3276.7 | vz2(k)==3276.7 |vx(k)==-3276.7 |
vy(k)==-3276.7 | vz1(k)==-3276.7 | vz2(k)==-3276.7
        vx(k)=NaN;
        vy(k)=NaN;
        vz1(k)=NaN;
        vz2(k)=NaN;
    end
end
```

```
%remove bad data
for k=1:length(vx)
    if vx(k)==0
        vx(k)=NaN;
    end
    if vy(k)==0
        vy(k)=NaN;
    end
    if vz1(k)==0
        vz1(k)=NaN;
    end
    if vz2(k)==0
        vz2(k)=NaN;
    end
end

vz=(vz1+vz2)/2;

%Reynolds stress
meanxraw=meanignoringNaN(vx)
meanzraw=meanignoringNaN(vz)
meanyraw=meanignoringNaN(vy)
fluctxraw=vx-meanxraw;
fluctzraw=vz-meanzraw;
fluctyraw=vy-meanyraw;
uwreynstressraw=-rho*meanignoringNaN(fluctxraw.*fluctzraw);%reynolds stress in N/m2
uvreynstressraw=-rho*meanignoringNaN(fluctxraw.*fluctyraw);%reynolds stress in N/m2
vwreynstressraw=-rho*meanignoringNaN(fluctzraw.*fluctyraw);%reynolds stress in N/m2
CDraw=-2*meanignoringNaN(fluctxraw.*fluctzraw)/meanxraw^2;

%statistics
xprsqrraw=fluctxraw.^2;
xrmsraw=sqrt(meanignoringNaN(xprsqrraw));
turbintxraw=xrmsraw/meanxraw;
yprsqrraw=fluctyraw.^2;
yrmsraw=sqrt(meanignoringNaN(yprsqrraw));
zprsqrraw=fluctzraw.^2;
zrmsraw=sqrt(meanignoringNaN(zprsqrraw));
turbintyraw=yrmsraw/meanyraw;
turbintzraw=zrmsraw/meanzraw;
%turbulent kinetic energy
turbkinenergyraw=0.5*(meanignoringNaN(xprsqrraw)+meanignoringNaN(yprsqrraw)+meanignoringNa
N(zprsqrraw));


vzerror=vz2-vz1;
%figure
%plot(tvec,vzerror)
%xlabel('time, s')
%ylabel('z vel error (vz2-vz1), m/s')
vzerrorthresh=0.1;%interpolate data that exceeds vert vel error threshold
for k=2:(length(vx)-1)
    if abs(vzerror(k))>vzerrorthresh
            vx(k)=(vx(k-1)+vx(k+1))/2;
            vy(k)=(vy(k-1)+vy(k+1))/2;
            vz1(k)=(vz1(k-1)+vz1(k+1))/2;
            vz2(k)=(vz2(k-1)+vz2(k+1))/2;
    end
end

%figure
%plot(tvec,vx)
%xlabel('time, s')
%ylabel('x vel after vertvelerrorthresh despike, m/s')
%figure
%plot(tvec,vy)
%xlabel('time, s')
%ylabel('y vel after vertvelerrorthresh despike, m/s')
%figure
%plot(tvec,vz1)
%xlabel('time, s')
```

```
%ylabel('z1 vel after vertvelerrorthresh despike, m/s')

%despike v based on local acceleration (Nortek uses a 1 g filter)
accelthresh=9.81*1.5;% Nortek default is one g acceleration cutoff threshold - I'm using
less severe 1.5
for k=2:(length(vx)-1)
    if abs((vx(k)-vx(k-1))/timestep)>accelthresh & abs((vx(k+1)-
vx(k))/timestep)>accelthresh
            vx(k)=(vx(k-1)+vx(k+1))/2;
    end
    if abs((vy(k)-vy(k-1))/timestep)>accelthresh & abs((vy(k+1)-
vy(k))/timestep)>accelthresh
            vy(k)=(vy(k-1)+vy(k+1))/2;
    end
    if abs((vz1(k)-vz1(k-1))/timestep)>accelthresh & abs((vz1(k+1)-
vz1(k))/timestep)>accelthresh
            vz1(k)=(vz1(k-1)+vz1(k+1))/2;
    end
    if abs((vz2(k)-vz2(k-1))/timestep)>accelthresh & abs((vz2(k+1)-
vz2(k))/timestep)>accelthresh
            vz2(k)=(vz2(k-1)+vz2(k+1))/2;
    end
end
%figure
%plot(tvec,vx)
%xlabel('time, s')
%ylabel('x vel after accel<g despike, m/s')

%despikev by interpolating any values that are more than 4
%standard deviations from the local mean
startlength=10;
stdvx=stdignoringNaN(vx);
for k=(startlength+1):(length(vx)-1)
    if abs(vx(k)-nanmean(vx((k-startlength):(k-1))))>4*stdvx
            vx(k)=(vx(k-1)+vx(k+1))/2;
    end
end
stdvy=stdignoringNaN(vy);
for k=(startlength+1):(length(vy)-1)
    if abs(vy(k)-nanmean(vy((k-startlength):(k-1))))>4*stdvy
            vy(k)=(vy(k-1)+vy(k+1))/2;
    end
end
stdvz1=stdignoringNaN(vz1);
for k=(startlength+1):(length(vz1)-1)
    if abs(vz1(k)-nanmean(vz1((k-startlength):(k-1))))>4*stdvz1
        vz1(k)=(vz1(k-1)+vz1(k+1))/2;
    end
end
stdvz2=stdignoringNaN(vz2);
for k=(startlength+1):(length(vz2)-1)
    if abs(vz2(k)-nanmean(vz2((k-startlength):(k-1))))>4*stdvz2
        vz2(k)=(vz2(k-1)+vz2(k+1))/2;
    end
end

%figure
%plot(tvec,vx)
%xlabel('time, s')
%ylabel('x vel after std despike, m/s')

vz=(vz1+vz2)/2;


%figure
%plot(tvec,vx)
%xlabel('time, s')
%ylabel('x vel after all despike, m/s')
%figure
%plot(tvec,vy)
%xlabel('time, s')
```

```
%ylabel('y vel after all despike, m/s')
%figure
%plot(tvec,vz)
%xlabel('time, s')
%ylabel('z vel after all despike, m/s')

%at least one adv head is twisted, therefore rotate by degree of twist for
%that head
if xyrotate~=0
    vxnew=vx.*cos(xyrotate)+vy.*sin(xyrotate);
    vynew=vy.*cos(xyrotate)-vx.*sin(xyrotate);
    vx=vxnew;
    vy=vynew;
    clear vxnew vynew
end


%calculate statistics.  Note: these are not raw. Rather, they are despiked,
%and rotated for adv head twist.
%Reynolds stress
meanxdespike=meanignoringNaN(vx)
meanzdespike=meanignoringNaN(vz)
meanydespike=meanignoringNaN(vy)
fluctxdespike=vx-meanxdespike;
fluctzdespike=vz-meanzdespike;
fluctydespike=vy-meanydespike;
uwreynstressdespike=-rho*meanignoringNaN(fluctxdespike.*fluctzdespike);%reynolds stress in
N/m2
uvreynstressdespike=-rho*meanignoringNaN(fluctxdespike.*fluctydespike);%reynolds stress in
N/m2
vwreynstressdespike=-rho*meanignoringNaN(fluctzdespike.*fluctydespike);%reynolds stress in
N/m2
CDdespike=-2*meanignoringNaN(fluctxdespike.*fluctzdespike)/meanxdespike^2;

%statistics
xprsqrdespike=fluctxdespike.^2;
xrmsdespike=sqrt(meanignoringNaN(xprsqrdespike));
turbintxdespike=xrmsdespike/meanxdespike;
yprsqrdespike=fluctydespike.^2;
yrmsdespike=sqrt(meanignoringNaN(yprsqrdespike));
zprsqrdespike=fluctzdespike.^2;
zrmsdespike=sqrt(meanignoringNaN(zprsqrdespike));
turbintydespike=yrmsdespike/meanydespike;
turbintzdespike=zrmsdespike/meanzdespike;
%turbulent kinetic energy
turbkinenergydespike=0.5*(meanignoringNaN(xprsqrdespike)+meanignoringNaN(yprsqrdespike)+me
anignoringNaN(zprsqrdespike));
```

B.3 spectralVectrinofinalfiltnoisebatch

```
%spectralVectrinofinalfiltnoisebatch

%this algorithm will do spectral analysis on Vectrino data, will filt if
%noise level exceeds a threshold, and will then output final stats

    %first, fill in missing values
    vxwoNaN=interpolateNaN(vx);
    vywoNaN=interpolateNaN(vy);
    vzwoNaN=interpolateNaN(vz);

SampleRate=timestep;%200Hz sampling max for Vectrino

%spectrum
Ts = timestep;%sampling rate;
Hs = 1/Ts;%sampling frequency
Hn = Hs/2;%Nyquist frequency
nwindows=4;%number of windows
```

```
nfft=floor(length(vxwoNaN)/nwindows);%length of data for each window
noverlap=floor(nfft/2);%overlap of each window
window=hanning(nfft);
[P,F]=spectrum(vxwoNaN,vzwoNaN,nfft,noverlap,window,Hs);
fftvx=P(:,1).*2.*Ts;%area under curve should equal variance of data, so this is correct
conversion (Steve Ponds)
fftvz=P(:,2).*2.*Ts;%ie divide by Nyquist
fftcross=P(:,3);
%find -5/3
fivethirds=F.^(-5/3);
scaledfivethirds=fivethirds.*fftvx(10)./F(10).^(-5/3).*5;%just to show a five thirds line
on plot
scaledfivethirdsz=fivethirds.*fftvz(10)./F(10).^(-5/3).*5;%just to show a five thirds line
on plot
meanvxspecdensity=mean(fftvx);
meanvzspecdensity=mean(fftvz);
meancrossspecdensity=mean(fftcross);
coherencevxvz=P(:,5);
lowerconflimitvx=(P(:,1)-P(:,6)).*2.*Ts;
upperconflimitvx=(P(:,1)+P(:,6)).*2.*Ts;
lowerconflimitvz=(P(:,2)-P(:,7)).*2.*Ts;
upperconflimitvz=(P(:,2)+P(:,7)).*2.*Ts;
lowerconflimitcross=P(:,3)-P(:,8);
upperconflimitcross=P(:,3)+P(:,8);

%figure(21), clf
%figure
%subplot(3,1,1)
%loglog(F,fftvx,'k-',F,lowerconflimitvx,'g-',F,upperconflimitvx,'g-
',F,meanvxspecdensity,'r',F(10:end),scaledfivethirds(10:end),'c')
%ylabel('x, m^2/s')%units are units^2/frequency
%legend('original','~ conf',0)%note this is matlab 95% conf interval - not Nuttal for
windows
%title([filename{p} ' spectral density and coherence'],'FontSize',14)
%subplot(3,1,2)
%loglog(F,fftvz,'k-',F,lowerconflimitvz,'g-',F,upperconflimitvz,'g-
',F,meanvzspecdensity,'r',F(10:end),scaledfivethirdsz(10:end),'c')
%ylabel('z, m^2/s')%units are units^2/frequency
%legend('original','~ conf',0)
%subplot(3,1,3)
%semilogx(F,coherencevxvz,'k-')%note coherence is the normalized cross-spectrum, where
complex is eliminated by taking absolute
%therefore coherence has value between 0 and 1
%xlabel('frequency, Hz')
%ylabel('coherence vxvz,')


%fit a noise level to spectrum
%determine where inertial range should be.  Assume starts at 1 Hz, but
%certainly at 5 Hz.  Therefore, find F=5
ftest=1;
while F(ftest)<5
    ftest=ftest+1;
end
Fforfit=(F(ftest:end));
fftvxforfit=(fftvx(ftest:end));
fftvzforfit=(fftvz(ftest:end));

         xdata = Fforfit;
         ydata = fftvxforfit;
         xo=[fftvx(10)./F(10).^(-5/3) fftvx(end)];
        fun = inline('x(1)*xdata.^(-5/3)+x(2)','x','xdata');
        x = lsqcurvefit(fun,xo, xdata, ydata)
        xfit=x(1).*xdata.^(-5/3)+x(2);

         %find noise in m/s by integrating over spectrum
        N=x(2);
        noisevx = sqrt(N*F(end))%noise vx in m/s


        y2data = fftvzforfit;
```

```
         xo2=[fftvz(10)./F(10).^(-5/3) fftvz(end)];
        fun2 = inline('x2(1)*xdata.^(-5/3)+x2(2)','x2','xdata');
        x2 = lsqcurvefit(fun2,xo2, xdata, y2data)
        zfit=x2(1).*xdata.^(-5/3)+x2(2);

                %find noise in m/s by integrating over spectrum
        N2=x2(2);
        noisevz = sqrt(N2*F(end))%noise vx in m/s

        %look for total variance in spectrum
varspec=sum((fftvx)*(F(2)-F(1)))
varvx=var(vxwoNaN)%this is a problem - it appears to be off by a factor of about 3

%filter data if noise too high
%noisecutoff=0.3;
%noiseratio=abs(noisevx/Vectormeanx);
noisecutoff=0.75;
meanabsfluctx=mean(abs(fluctxraw));

noiseratio=abs(noisevx/meanabsfluctx);%this might make more sense: if fluctuations are due
to noise, then reynolds stress unreliable

Vectorfiltflag=0;
if noiseratio>noisecutoff%perform lowpass filter
    Vectorfiltflag=1;
    [b,a]=butter(10,.1);%might need to adjust this to determine frequency cutoff for
filtering
    filtvx = filtfilt(b,a,vxwoNaN);
    filtvy = filtfilt(b,a,vywoNaN);
    filtvz = filtfilt(b,a,vzwoNaN);

    vxwoNaN=filtvx;%rename so I can use same code again
    vywoNaN=filtvy;
    vzwoNaN=filtvz;

[P,F]=spectrum(vxwoNaN,vzwoNaN,nfft,noverlap,window,Hs);
fftvx=P(:,1).*2.*Ts;%area under curve should equal variance of data, so this is correct
conversion (Steve Ponds)
fftvz=P(:,2).*2.*Ts;%ie divide by Nyquist
fftcross=P(:,3);
%find -5/3
fivethirds=F.^(-5/3);
scaledfivethirds=fivethirds.*fftvx(10)./F(10).^(-5/3).*5;%just to show a five thirds line
on plot
scaledfivethirdsz=fivethirds.*fftvz(10)./F(10).^(-5/3).*5;%just to show a five thirds line
on plot
meanvxspecdensity=mean(fftvx);
meanvzspecdensity=mean(fftvz);
meancrossspecdensity=mean(fftcross);
coherencevxvz=P(:,5);
lowerconflimitvx=(P(:,1)-P(:,6)).*2.*Ts;
upperconflimitvx=(P(:,1)+P(:,6)).*2.*Ts;
lowerconflimitvz=(P(:,2)-P(:,7)).*2.*Ts;
upperconflimitvz=(P(:,2)+P(:,7)).*2.*Ts;
lowerconflimitcross=P(:,3)-P(:,8);
upperconflimitcross=P(:,3)+P(:,8);

%figure(22), clf
%figure
%subplot(3,1,1)
%loglog(F,fftvx,'k-',F,lowerconflimitvx,'g-',F,upperconflimitvx,'g-
',F,meanvxspecdensity,'r',F(10:end),scaledfivethirds(10:end),'c')
%ylabel('x, m^2/s')%units are units^2/frequency
%legend('original','~ conf',0)%note this is matlab 95% conf interval - not Nuttal for
windows
%title([filename{p} ' spectral density and coherence'],'FontSize',14)
%subplot(3,1,2)
%loglog(F,fftvz,'k-',F,lowerconflimitvz,'g-',F,upperconflimitvz,'g-
',F,meanvzspecdensity,'r',F(10:end),scaledfivethirdsz(10:end),'c')
%ylabel('z, m^2/s')%units are units^2/frequency
%legend('original','~ conf',0)
```

```
%subplot(3,1,3)
%semilogx(F,coherencevxvz,'k-')%note coherence is the normalized cross-spectrum, where
complex is eliminated by taking absolute
%%therefore coherence has value between 0 and 1
%xlabel('frequency, Hz')
%ylabel('coherence vxvz,')

%fit a noise level to spectrum
Fforfit=(F(ftest:end));
fftvxforfit=(fftvx(ftest:end));
fftvzforfit=(fftvz(ftest:end));

         xdata = Fforfit;
         ydata = fftvxforfit;
         xo=[fftvx(10)./F(10).^(-5/3) fftvx(end)];
        fun = inline('x(1)*xdata.^(-5/3)+x(2)','x','xdata');
        x = lsqcurvefit(fun,xo, xdata, ydata)
        xfit=x(1).*xdata.^(-5/3)+x(2);

         %find noise in m/s by integrating over spectrum
        N=x(2);
        noisevxfilt = sqrt(N*F(end))%noise vx in m/s


        y2data = fftvzforfit;
         xo2=[fftvz(10)./F(10).^(-5/3) fftvz(end)];
        fun2 = inline('x2(1)*xdata.^(-5/3)+x2(2)','x2','xdata');
        x2 = lsqcurvefit(fun2,xo2, xdata, y2data)
        zfit=x2(1).*xdata.^(-5/3)+x2(2);

                %find noise in m/s by integrating over spectrum
        N2=x2(2);
        noisevzfilt = sqrt(N2*F(end))%noise vx in m/s
        else
        noisevxfilt=NaN;
        noisevzfilt=NaN;
end

%recompute statistics with filtered data.  Note, if no filtering applied,
%these should be the same as despiked.
    %Reynolds stress
    meanxfilt=meanignoringNaN(vxwoNaN)
    meanzfilt=meanignoringNaN(vzwoNaN)
    meanyfilt=meanignoringNaN(vywoNaN)
    fluctx=vxwoNaN-meanxfilt;%leave these names, so can use correlation code next
    fluctz=vzwoNaN-meanzfilt;
    flucty=vywoNaN-meanyfilt;
    uwreynstressfilt=-rho*meanignoringNaN(fluctx.*fluctz);%reynolds stress in N/m2
    uvreynstressfilt=-rho*meanignoringNaN(fluctx.*flucty);%reynolds stress in N/m2
    vwreynstressfilt=-rho*meanignoringNaN(fluctz.*flucty);%reynolds stress in N/m2
    CDfilt=-2*meanignoringNaN(fluctx.*fluctz)/meanxfilt^2;

    %statistics
    xprsqr=fluctx.^2;
    xrmsfilt=sqrt(meanignoringNaN(xprsqr));
    turbintxfilt=xrmsfilt/meanxfilt;
    yprsqr=flucty.^2;
    yrmsfilt=sqrt(meanignoringNaN(yprsqr));
    zprsqr=fluctz.^2;
    zrmsfilt=sqrt(meanignoringNaN(zprsqr));
    turbintyfilt=yrmsfilt/meanyfilt;
    turbintzfilt=zrmsfilt/meanzfilt;
    %turbulent kinetic energy

turbkinenergyfilt=0.5*(meanignoringNaN(xprsqr)+meanignoringNaN(yprsqr)+meanignoringNaN(zpr
sqr));
```

B.4 interpolateNaN

```
%this function fills in values for NaN values, by taking the average of the values before
and after the series of NaN values
function [ebtwonan] = interpolateNaN(ebt)
ebtwonan=ebt;
badebtindex=find(isnan(ebt));
for k=1:length(ebt)
   btprofilecount(k)=k;
end
goodebtindex=setdiff(btprofilecount,badebtindex);
if ~isempty(badebtindex)
   if ~isempty(goodebtindex)
   countgood=1;
   countbad=1;
   if length(badebtindex) == 1
      stoplooping=1;
   else
      stoplooping=0;
   end
   k=1;
   while k <= badebtindex(end)
      if goodebtindex(countgood)<badebtindex(countbad)
         if countgood < length(goodebtindex)
            countgood=countgood+1;
         end
         k=k+1;
      else %I need to find how many bad points occur contiguously
         t=1;
         if stoplooping ~= 1
            while ((badebtindex(countbad+t)-badebtindex(countbad+(t-1)))==1 & (countbad+t-
1)<length(badebtindex))
               t=t+1;
               if (countbad+t)>length(badebtindex)
                  break
               end
             end
         end
         for s=1:t %now increment the bad points by taking the average of the good points
before and after bad data
            if (k-s)<=0 %only take latter point if NaN at start of series
               ebtwonan(k)=ebt(k-s+t+1);
            elseif (k-s+t+1)>length(ebt) %only take earlier point if NaN at end of series
               ebtwonan(k)=ebt(k-s);
            else
               ebtwonan(k)=(ebt(k-s)+ebt(k-s+t+1))/2;
            end
            if countbad < length(badebtindex)
               countbad=countbad+1;
            end
            if countbad == length(badebtindex)
               stoplooping=1;
            end
            k=k+1;
         end
      end %end of if statement to check for good or bad index
   end %end of while loop through k
end %end of initial if statement that there be some good points
end %end of initial if statement that there be some bad points
```

B.5 meanignoringNaN

```
function [means] = meanignoringNaN(input)
%This is function 'meanignoringNaN', that will determine the mean of an array
%while ignoring NaN values or non-values
%find average, but remove bad (NaN) points first
badindex=find(isnan(input));
count=1;
```

```
sums=0;
countzeros=0;
 %find sum without bad points
 if length(badindex) > 0
   for k=1:length(input)
      if k~=badindex(count)
         sums=sums+input(k);
      else
         if count ~= length(badindex)
            count=count+1;
         end
      end
   end
   means=sums/(length(input)-length(badindex));
else
   means=sum(input)/(length(input));
end
```

B.6 stdignoringNaN

```
function [stdignoringNaN] = stdignoringNaN(input)
%This is function 'sdignoringNaN', that will determine the standard deviation of an array
%while ignoring NaN values as non-values.  Note: this uses std, which normalizes by N-1.
badindex=find(isnan(input));
count=1;
counter=1;
if length(badindex)>0
   for k=1:length(input)
      if k~=badindex(count)
         inputwithoutNaN(counter)=input(k);
         counter=counter+1;
      else
         if count ~= length(badindex)
            count=count+1;
         end
      end
   end
   stdignoringNaN=std(inputwithoutNaN);
else
   stdignoringNaN=std(input);
end
```

B.7 Vectrinooutput

```
%Vectrinooutput
%this now just calculates turbulence scales from the correlation function
%as it is written now

%find correlation coefficient (R)
cnt=length(tvec);
num=floor((cnt-1)/2);
for tau=0:1:(num-1)
    N=0;
    sumx=0;
    sumy=0;
    sumz=0;
    for N=1:1:(cnt-tau-1)
        sumx=sumx+fluctx(N)*fluctx(N+tau);
        sumy=sumy+flucty(N)*flucty(N+tau);
        sumz=sumz+fluctz(N)*fluctz(N+tau);
    end
    corltnx(tau+1)=sumx/(cnt-tau-1);
    corltny(tau+1)=sumy/(cnt-tau-1);
    corltnz(tau+1)=sumz/(cnt-tau-1);
    taup(tau+1)=tau*timestep;
end
Rxmine=corltnx/meanignoringNaN(xprsqr);
```

```
Rymine=corltny/meanignoringNaN(yprsqr);
Rzmine=corltnz/meanignoringNaN(zprsqr);

%do x,y,z scales separately

%x
%find integral time scale, and if turbintensity<0.25, integral length scale
%(using Taylor's frozen field hypothesis)
%first, integrate Rx until Rx<0
k=1;
while Rxmine(k)>0
    if k<length(Rxmine)
        k=k+1;
    else
        break
    end
end

Rfit=Rxmine(1:(k-1));
integraltimescale=Rfit(1)*timestep/2+sum(Rfit(2:end))*timestep%in s
%find microtimescale - note the sample volume may be too large
derivx=diff(fluctx)/timestep;%approximate derivative of x fluctuations
derivxsq=derivx.^2;
microtime=sqrt(2)*sqrt(meanignoringNaN(xprsqr))/sqrt(sum(derivxsq)/cnt)
if abs(turbintxfilt)<0.25
    integrallengthscale=meanignoringNaN(vx)*integraltimescale;
    microlengthscale=meanignoringNaN(vx)*microtime;
    taylormicrolength=microlengthscale/sqrt(2);
else
    integrallengthscale=NaN;
    microlengthscale=NaN;
    taylormicrolength=NaN;
end

%y
%find integral time scale, and if turbintensity<0.25, integral length scale
%(using Taylor's frozen field hypothesis)
%first, integrate Ry until Ry<0
k=1;
while Rymine(k)>0
    if k<length(Rymine)
        k=k+1;
    else
        break
    end
end

Rfity=Rymine(1:(k-1));
integraltimescaley=Rfity(1)*timestep/2+sum(Rfity(2:end))*timestep%in s
%find microtimescale - note the sample volume may be too large
derivy=diff(fluctY)/timestep;%approximate derivative of x fluctuations
derivysq=derivy.^2;
microtimey=sqrt(2)*sqrt(meanignoringNaN(yprsqr))/sqrt(sum(derivysq)/cnt)
if abs(turbintyfilt)<0.25
    integrallengthscaley=meanignoringNaN(vy)*integraltimescaley;
    microlengthscaley=meanignoringNaN(vy)*microtimey;
    taylormicrolengthy=microlengthscaley/sqrt(2);
else
    integrallengthscaley=NaN;
    microlengthscaley=NaN;
    taylormicrolengthy=NaN;
end

%z
%find integral time scale, and if turbintensity<0.25, integral length scale
%(using Taylor's frozen field hypothesis)
%first, integrate Rz until Rz<0
k=1;
while Rzmine(k)>0
    if k<length(Rzmine)
        k=k+1;
```

```
    else
        break
    end
end

Rfitz=Rzmine(1:(k-1));
integraltimescalez=Rfitz(1)*timestep/2+sum(Rfitz(2:end))*timestep%in s
%find microtimescale - note the sample volume may be too large
derivz=diff(fluctz)/timestep;%approximate derivative of x fluctuations
derivzsq=derivz.^2;
microtimez=sqrt(2)*sqrt(meanignoringNaN(zprsqr))/sqrt(sum(derivzsq)/cnt)
if abs(turbintzfilt)<0.25
    integrallengthscalez=meanignoringNaN(vz)*integraltimescalez;
    microlengthscalez=meanignoringNaN(vz)*microtimez;
    taylormicrolengthz=microlengthscalez/sqrt(2);
else
    integrallengthscalez=NaN;
    microlengthscalez=NaN;
    taylormicrolengthz=NaN;
end
```